INTEGRATED GEOCHEMICAL - GEOPHYSICAL STUDIES OF SEDIMENTARY RESERVOIR ROCKS

Thesis submitted for the degree of
Doctor of Philosophy
at the University of Leicester

by

Jeremy C. Lofts BSc (Leicester)
Department of Geology
University of Leicester

February 1993

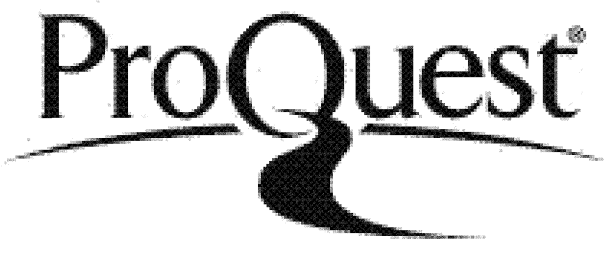

ProQuest LLC
789 East Eisenhower Parkway
P.O. Box 1346
Ann Arbor, MI 48106-1346

TO MY FAMILY...

Mum, Dad,
Margot, Guy, Simon.

Acknowledgements

Acknowledgement must first of all go to *Dr. John Locke* and *Dr. John Butler* at the UKAEA whom with my supervisors *Dr. Peter Harvey* and *Dr. Mike Lovell,* were the brain-child of my project and whom have provided input throughout. I gratefully acknowledge the funding for the project through the auspices of Winfrith Petroleum Services and the EUROPA project.

Many thanks to *Peter* and *Mike* for their 'supervision', especially *Peter* for many stimulating 'geostats' and 'computing' discussions and *Mike* for making the Atlantic Ocean, that separated us during my final year, seem like the length of the office.

I also acknowledge, with thanks, *Caroline Bajsaiowicz* and *Don Milne* at BP, Glasgow for their great help in providing core data for Thistle Hole 211/18-a50(40); *Dorrik Stow* at Southampton for providing the Statfjord core samples and data; *Bernard Humphreys* and *Graham Lott* at the BGS for Thistle 211/18a-a33 core material; *Mike Herron* at Schlumberger, Ridgefield, for re-processing the a50 GLT data; *John Adams* (*ex* Schlumberger, Aberdeen) and *Stuart Burley* for their helpful discussions. Thanks also to *Jeremy McNab* and *Nirmala* at Exxon, Houston and *Rick Wendlandt* in Colorado (CSM) for additional log data.

Thanks very much to the "borehole boys" *Jim, Rich, Ceri*; especially *Jim Bristow* for all our lengthy discussions on boreholes and women, *Rich Pelling* for discussions on boreholes, beer and women; also *George Christidis* for discussions on clays and Greek women. Thanks to *Andy Mcnight & Ian Warren* for XRD and microprobe tips and *Ceri Williams* and*Gail Williamson* for your last minute help in preperation of the final draft.

Acknowledgement must also go to *Giles, Ceri, Stuart,* my house-mates, for many cups of tea whilst 'writing up'; *Catrin J.* and *Paul D.* for dragging me from work to play squash and to go clubbing. Thanks to *Emma M.* and *Ceri W.* for insisting on 'last orders' while 'writing up'; *Nick C.* for promising but never-making-it to them and *Fran C.* for serving them. I must also thank the rest of the "Flaming Beavers" band - *Andy, Darren, Mac and Tim* for putting up with my guitar solos that were induced by stress from my writing.

Last, but by a long way not least, I would like to thank *Rhiannon* for all her help and encouragement throughout the project and for urging me to become more of a *geophysical* geologist, although I will never admit to being a geophysicist!

I would like to spare a thought for *Paul Metcalfe,* who can't be here today to see me go through what he endured only a few months before his tragic death.

****

Table of Contents

Chapter contents

page

Chapter 3, Part 2. Laboratory assessment of mineral transform models

Chapter 4. Mineral modelling of the Brent Group

Chapter 5 . Strategies for overcoming the problems faced by mineral transform models

Chapter 6. Mineral transform modelling & evaluation of GLT data from the Thistle hole 211/18-A50(40)

Chapter 1.
Introduction

1.1 Preamble

Advances in subsurface nuclear logging techniques in recent years have resulted in the ability to determine the abundance of the *major* elements that constitute most lithologies. These include Si, Al, Ti, Fe, Ca, K, S (indirectly Mg + Na), as well as the *minor* elements Gd, Th and U (Hertzog *et al.*, 1989). Elements are measured continuously down-hole using a string of four separate logging tools that exploit various nuclear reactions and measurement techniques; in particular - *neutron induced capture, activation* and *passive gamma-ray spectroscopy*. The only commercially available tool is the Geochemical Logging Tool (GLT) of Schlumberger.

Appropriate calibration and conversion of the initial elemental yields to weight percent elemental (or oxide) form allows a continuous measurement of chemistry, typically at 0.15m intervals, down-hole, with the exception of the volatile phases H2O and CO2. Virtually all of these elements measured by the GLT tool reside exclusively in the minerals that make up sedimentary rock sequences, and not in the fluid brine or hydrocarbon phases. Measurements therefore are primarily the response of the solid matrix lithology (H and Cl are in fact measured but they represent responses, primarily, from the borehole fluid).

Tools such as the GLT therefore provide a whole new set of previously unavailable data related to down-hole rock chemistry. The use of these data in the study of sediments, particularly its application in *reservoir characterisation* and *formation evaluation*, is still at an early stage. Different ideas exist on how to use these data to best advantage.

One of the more straight-forward applications of continuous down-hole *geochemical* logs is as an indication of *lithological variation* in a sedimentary sequence. Conventional wireline logging tools, routinely used to estimate lithology, offer neither the accuracy, dynamic range or independence from porosity (fluids) that can, potentially, be provided by these geochemical measurements. This is because tools, such as bulk density, neutron porosity and acoustic travel time, are primarily sensitive to changes in porosity. As porosity varies and formations become more compositionally complex, interpreting lithologies from these logs becomes more difficult or impossible. Geochemical concentrations, as primary responses of the solid matrix, offer greater diagnostic qualities for lithological evaluation.

Herron and Herron (1990) use the elemental ratios of three of the eleven possible elements, Si, Al and Ca as a '*rapid screen* ' to distinguish carbonates, from sandstone and shales in the borehole environment. Their contribution illustrates the enhanced diagnostic strengths possible, especially in complex shaly-sand lithologies, when compared with conventional tools.

In an alternative approach, elemental data have been employed to *classify* siliciclastic (and carbonate) lithologies. Such a system has been employed in geology for three decades

(Middelton 1960; Garrels & McKenzie 1971; Pettijohn *et al.,* 1972). In the scheme of Pettijohn *et al.,* (1972), oxide ratios SiO2/Al2O3 and Na2O/K2O are used to differentiate between the various sandstone classes. SiO2/Al2O3 is used to distinguish the pureness of sandstone (maturity), while Na2O/K2O is used to distinguish greywackes from arkosic sands. A more specific '*Sandclass*' system was employed by Herron (1988), for concentrations derived from the GLT tool. Primary ratios, for this scheme include the SiO2/Al2O3 ratio used in a similar context to the *Pettijohn scheme*, to separate arenites from shales, with a plethora of intermediate sandstones between. However, as Na is not measured directly by the GLT tool the ratio Fe2O3/K2O is used in place of Na2O/K2O. This in effect separates lithic sandstones (with relatively high levels of Fe) from feldspathic sandstones. A third, (carbonate) axis is also deployed to distinguish non-calcareous, calcareous and carbonate lithologies. Both schemes, however useful, do have pitfalls in the assumptions that define the classes. For example, in the *Pettijohn scheme* the Na2O/K2O is not well suited to distinguishing greywackes from arkosic arenites when albite is abundant, while the *sandclass scheme* incorrectly identifies sandstone when shaly clasts are abundant (Herron, 1988).

In a slightly different context, multivariate statistical analysis techniques, such as non hierarchical cluster analysis (INCA) and Principal Components Analysis have been employed to better understand element relationships (Brewer *et al.,* 1990). These techniques allow oxide or element data to be classified into geochemically similar groups. Interpretation of such elemental data can be made in terms of geological processes that give rise to a particular abundance or pattern. Attempts at deriving the *chemostratigraphy* from such geochemical groups, derived from geochemical logs in an igneous environment, have been made by Pelling *et al.* (1989, 1991). Similar statistical techniques have been employed for the evaluation of mudrocks (Primmer *et al.,* 1990).

One of the most potentially useful ways, however, of using elemental data derived from logging tools, especially for reservoir characterisation, is to convert geochemical data into quantitative estimates of *mineralogy*.

There are no simple relationships that exist between elemental abundances and petrophysical parameters traditionally sought by petrophysicists for reservoir characterisation. A relationship often exists, however, between the mineralogy of a rock and these parameters. Therefore, resulting estimates of accurate *mineralogy*, besides being valuable in their own right for formation evaluation, can in effect allow the direct estimation of many of physical and chemical parameters important in reservoir characterisation. Potential applications include the measurement of grain (matrix) density, porosity, cation exchange capacity (Chapman *et al.,* 1987; Herron, 1987; Herron & Grau, 1987), thermal conductivity (Dove & Williams 1987), heat flow (Anderson & Dove, 1987), magnetic susceptibility (P. Harvey *pers.comm.*), fluid saturation (Hastings, 1988), neutron capture cross-section (Herron, 1987), source rock evaluation (Herron, (S.), 1987), enhanced measurement of Archie's exponent '*n*' through improved resistivity estimates (Herron *et al.,* 1990) and, *tentatively*, estimates of permeability (Herron, 1987(b)).

1.1.1 The norm

The conversion of geochemical data to mineral abundances (mineral transformation or inversion) has long been employed as an investigative technique by geologists. One possibility is to re-compute a chemical analysis to a fixed set of minerals (usually with ideal or 'theoretical' compositions) to produce a *norm.* The CIPW norm (Cross *et al.,* 1902; Kesly, 1965), still widely used today by igneous petrologists, is probably the best known procedure of this type. Similar ideas have been used for metamorphic rocks, using Niggli's normative procedures (Burri, 1964; Barth, 1969); and for sediments (Imbrie & Poldervaart, 1959; Nicholls, 1962; Cohen & Ward, 1991).

The CIPW norm and Niggli schemes are *subtractive norms* in that the chemical analyses are assumed to be correct and minerals are subtracted one at a time from the analysis, usually with one chemical constituent acting as a limiting concentration. Subtractive norms were originally developed for the classification or 'pigeon holing' purposes much like the *sandclass* or *Pettijohn* scheme. Niggli's scheme is considerably more versatile and can approach the mode if mineral analyses are incorporated. Such a *normative* approach has been tailored, by Herron and Herron, 1990 (chem-modes), for geochemical logging measurements.

1.1.2 The Mode

The chemical *mode*, on the other hand (Wright & Doherty, 1970), represents the *actual* mineral phases present in a given rock sample, unlike the *norm* which represents the percentage of theoretical mineral phases calculated from a given analysis. It is the *mode* (or modal proportion) that should be sought after if accurate estimates of mineralogy are to be made. The mode is usually estimated in the laboratory by techniques such as X-ray diffraction, thin section point-counting or infra-red spectroscopy.

The estimation of a *mode* is considerably more involved than computing a simple *norm* where the rules of calculation are fixed. For the *mode* the relationship between the composition of a formation, at a given point, and the amount of each phase (both fluid and mineral), and constituent compositions must be considered. In borehole sequences, with new elemental data measured every 15 cm, it is possible the mineral assemblage and composition of phases will vary. Each depth interval must therefore be regarded as new problem requiring independent solution.

Various approaches at estimating an accurate mode from elemental data have been attempted. These have employed various algebraic procedures such as solution to sets of simultaneous equations, linear programming, factor analysis and constituent analysis. Most techniques can be easily manipulated in terms of matrices and therefore easily handled and programmed on computer. In the context of sediments such techniques have been attempted by Imbrie and Poldervaart (1959); Pearson (1978); Miesch, (1962); Gold *et al.,*(1983), and Kornder (1984), although none are considered in the context of the logging-borehole environment.

1.2 Aims and objective of this study

The aim of this study is a thorough investigation and evaluation of the process of mineral transformation (or inversion) in sediments. A selection of techniques have been developed and programmed for this exercise that *transform* (or *invert)* elemental oxides, derived from the GLT tool string, into a set of geologically 'viable' mineral phases. Primarily, this study assesses the implementation of these *mineral transform models* on elemental data derived from nuclear logging measurements and it addresses the question ...*'can an accurate mineralogy be successfully obtained from geochemical logging instruments?'* A secondary objective assesses the potential for the application of such mineralogy in reservoir characterisation. These objectives are summarised in Figure 1.1.

If a model is to be proved successful in producing an accurate *modal mineralogy* at each sample or depth interval, it must be provisionally assessed using well constrained data, free from the random and systematic errors associated with nuclear logging data. Emphasis is therefore placed on evaluating transform techniques using constrained laboratory and core data, before using nuclear logging data. The evaluation procedure adopted is summarised in Figure 1.2.

Each transform model is firstly evaluated using a) numerically 'produced' data and b) laboratory measurements from synthetically 'produced' rock samples which cover a wide variety of lithologies. Core from an almost continuous 40m section of reservoir through the Brent Group of the North Sea Thistle Field is then used, in a further stage, to evaluate *transform models* in an 'actual' reservoir lithology. The Ness, Etive and Rannoch formations of the Brent Group, sampled here, offer an excellent range of lithologies in which to evaluate these *inversion* techniques; with lithologies ranging from quartz-rich arenites through subarkose sandstones to micaceous-subarkosic arenites, siltstones and mudstones.

It is only when these models are fully evaluated should they be applied to real logging data. In this context, nuclear logging data, including geochemical measurements, from a nearby hole in the Thistle Field are used for the final step in the evaluation procedure. Strategies and conclusions developed from previous modelling are applied in an attempt to best model this data. A critical look at the quality of the tool measurement and the processing required to produce geochemical (elemental) concentrations is undertaken, as any errors in either will ultimately affect the estimate of mineralogy.

The potential for *derived mineralogy* to be applied in reservoir characterisation is assessed; firstly as a correlative tool in *inter-well correlation* and secondly to produce estimates of *matrix density* and *porosity* for petrophysical characterisation. Examples from the Thistle data used through the study are included in addition to a *case example* from the Statfjord Field, UK North Sea.

Throughout this investigation emphasis is placed on further understanding the relationship between nuclear measurements and the mineral phases present in a rock formation. Such a close study of nuclear logging data, as undertaken in the final evaluation

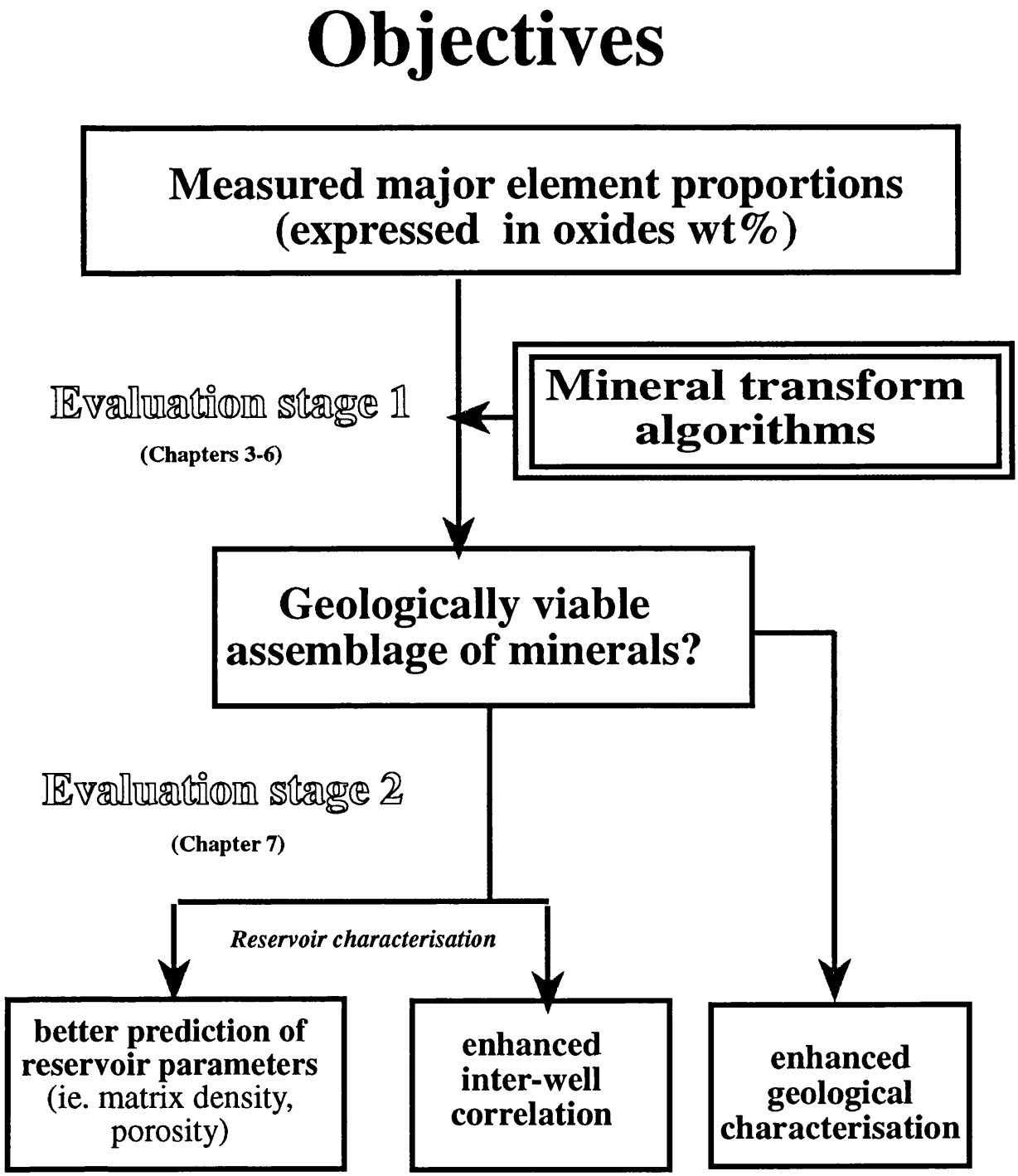

Figure 1.1. Flow diagram depicting the objectives of this study.

here, allows a further insight into the relationship between the two. This is a very important step in the assessment of the usefulness of nuclear tools in reservoir characterisation.

1.3 Structure of this thesis

After a review of the methods of obtaining elemental concentrations from spectroscopy measurements made by the GLT tool (Chapter 2), the theory and philosophy of each mineral model is reviewed (Chapter 3). Careful evaluation and identification of inherent problems are then addressed, using a set of synthetic rocks produced from mixtures of minerals. In Chapter 4 reservoir core from the Thistle Field is used to evaluate techniques in an attempt to validate and extend earlier conclusions. For this exercise extensive core analysis was performed to determine the modal mineralogy, mineral composition and elemental analysis of all sample intervals. A section at the beginning of the chapter is therefore dedicated to the introduction to the Brent Group and a full *characterisation* of the studied section, including wireline log interpretation.

Strategies developed which alleviate some of the problems faced in mineral inversion are introduced in Chapter 5. These are demonstrated by examples from the *synthetic* and *Thistle* data sets and a successful case study, employing a combination of these strategies, is detailed at the end of the chapter.

In Chapter 6, the modelling procedures developed over chapters 3 - 5 are applied to *real* geochemical logging data acquired from the Thistle Field. This includes a critical assessment of the quality of data from post processing and possible enhancements to processing. Models and associated strategies are then evaluated using measurements from core and are discussed. Chapter 7 critically demonstrates two different applications possible from a direct knowledge of modal mineralogy down-hole. Examples are taken from data modelled during this study in an attempt to assess the feasibility of these applications. The final chapter draws together conclusions and suggestions for further work.

In summary....

Can we produce meaningful mineralogy from chemical analysis of elements? Can this be attempted successfully in a borehole environment ? and can these data be relied on to use in subsequent applications?

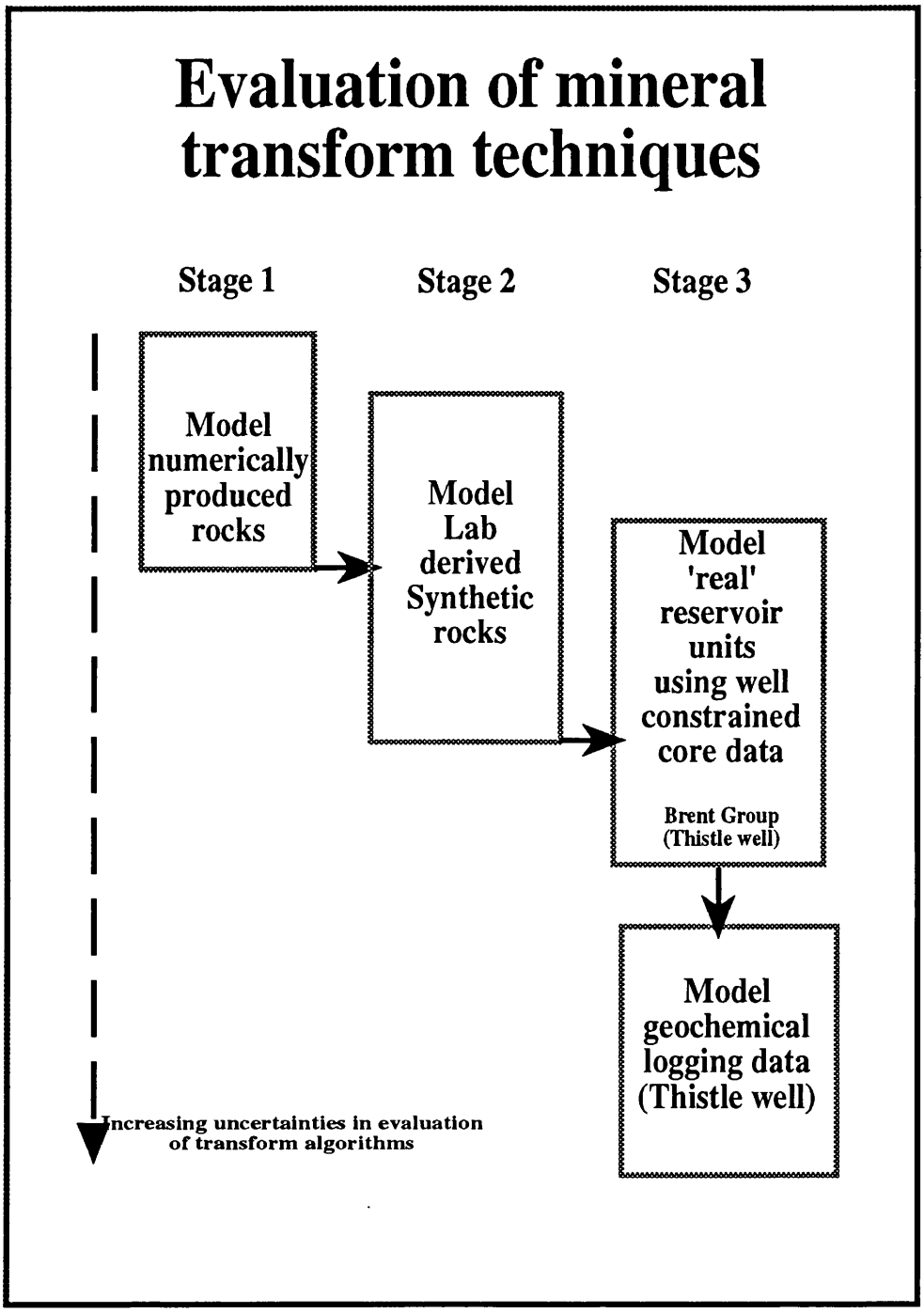

Figure 1.2 Stages in the evaluation of mineral transform models

Chapter 2

Elemental measurements from the Geochemical Logging Tool (GLT)

2.0 Introduction

Down-hole logging measurements can be used to characterise the geophysical, geochemical and intrinsic structural properties of a borehole sequence. After drilling and coring, various different *sondes* are lowered down-hole on a wireline and each of several measuring devices continuously monitor properties adjacent to the formation. The advantages of these quasi-continuous, in-situ measurements of formation properties are well recognised *in comparison* and *as a complement* to core-based measurements.

These may be summarised as:

-Logs are effectively continuous over an entire interval and independent of core disturbance or loss or incomplete recovery.

-Logs are representative of sampling a much greater volume of rock.

-Log acquisition is very efficient in terms of measurement time and turn around.

-Logs measure properties at in-situ conditions (ie, temperature and pressure).

Geochemical logs do, however, suffer from disadvantages:

-Not all elements can be determined

-Precision and accuracy of laboratory analysis, such as XRF are well known and high, while that of geochemical logs is still relatively unknown and because of the hostile environment, inevitably lower.

The Geochemical Logging Tool String (GLT[1]) of Schlumberger is currently the only commercially available tool capable of measuring a comprehensive elemental analysis of a subsurface formation. Although most techniques were pioneered for the petroleum industry, the tool is routinely deployed in the *Ocean Drilling Program*, ironically, well ahead of any routine deployment in hydrocarbon exploration.

This chapter aims to review the procedure in which elemental measurements are derived by the GLT tool string and subsequently processed to derive estimates of the major element oxides. It serves to illustrate this state-of-the-art logging technology with a view to summarising the performance and behaviour of such a tool. An idea may then be perceived of the levels of accuracy and confidence of the derived estimates for use in applications such as mineral transformation.

The GLT integrates three separate modes of gamma-ray spectroscopy to obtain elemental measurements. This is a result of a complex interaction of physics and chemistry. The tool uses *natural* gamma-ray activity to detect the abundance of K, U, Th; *delayed neutron activation* to detect Al, and the *prompt capture* gamma-ray spectrum to measure relative concentrations of Si, Ca, Fe, S, Ti, Gd (H & Cl). These relative concentrations are then converted to absolute weight percent using a *geochemical oxide closure model*, which in

[1] All logging tool acronyms used in this thesis are summarised in Appendix AA.

essence, assumes all elemental oxides present sum to unity. Mg and Na are not directly measured by the tool but can be inferred, in favourable conditions, from the photoelectric factor derived from the Litho-density tool. The GLT tool is described in detail by Hertzog *et al.*, (1989); the theory by Hertzog & Plesek (1979), Hertzog (1980), Serra (1984), Schweitzer *et al.*, (1988), Grau *et al.*, (1987, 1988, 1989); and in review by Ellis (1987) and Herron (S) *et al.*, in press;. Critical views and independent test work include Anderson *et al.*, (1988), Wendlandt and Bhuyan (1990), Van den Oord (1991), Georgi (1991), Jarrard and Lyle (1992), Bristow & deMenocal (1992) and Pelling (1992).

2.1 Fundamentals of gamma-ray spectroscopy

Reconfiguration of an unstable, excited atom into a stable form often results in energy in the form of gamma-rays being emitted. The laws of Quantum mechanics govern the amount of energy emitted by this gamma-ray *photon*. In general the energy is equivalent to the difference in the energy states of the initial and final energy shells an electron, in a particular atom, has moved between to gain stability. Emitted gamma-rays thus have energies that are characteristic or unique to a particular atomic species.

Only three of the elements present in the earth's crust, K, U and Th, contribute a large enough *natural* gamma-ray signal (by the spontaneous natural emission of gamma-rays), to allow detection in the borehole environment. This is due essentially to the naturally occurring concentrations and the length of half life of their isotopes and the associated decay series. Concentrations of these elements can therefore be measured from their natural gamma-ray signature. For other elements that make no significant contribution to the natural gamma-ray flux, it is necessary to *artificially* create instability within atoms to induce the emission of gamma-rays that can then be measured. This is achieved by bombarding a formation with high energy neutrons (Hertzog & Plesek, 1979). The exploitation of several possible nuclear reactions which are the consequence of bombardment by neutrons, allows *characteristic gamma-rays* to be measured as an indication of the abundance of that particular element. Such measurements were recognised as possible in the borehole environment and implemented in the current GLT tool by Hertzog *et al.* (1989). Two groups of useful neutron *interactions* include a) moderation and b) absorption.

a) Moderating interactions

These reactions occur when neutron collision with a target nuclei results in a reduction in neutron energy (speed). These collisions include (1) inelastic scatter and (2) elastic scatter.

(1) In *inelastic scatter collisions*, a proportion of the incident energy from the neutron manifests in the excitation of the target nucleus. Besides reducing the energy of the incident neutron, it induces the *target* nucleus to produce and emit one or more gamma-rays. Such an interaction only occurs at high neutron energies ('*fast*' neutron speeds), shown in Figure 2.1.

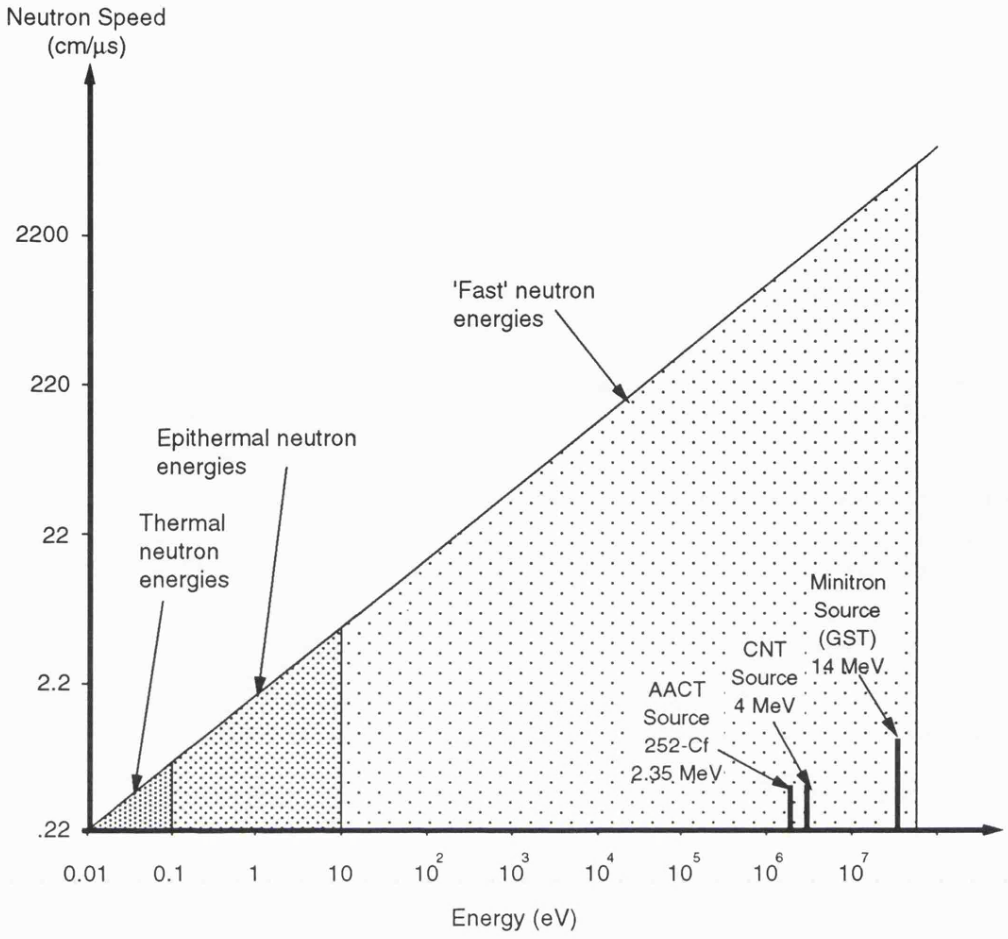

Figure 2.1 (a) Classification of neutrons according to broad energy ranges and their corresponding velocities. The vertical lines represent the average neutron energy produced from the various tool sources. Adapted from Ellis, 1987.

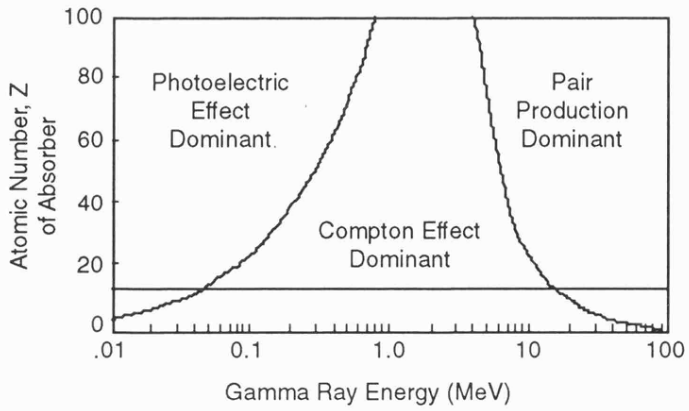

Figure 2.1 (b) Regions of dominmance of the three principal gamma-ray interactions as a function of energy and the atomic number of the scattering material. Adapted from Ellis,1987.

Common elements with identifiable gamma-rays include C, O, Si, Ca, Fe, S and Cl (Hertzog, 1980).

(2) *Elastic scatter* is the primary interaction which occurs to *fast* neutrons leaving tool sources. This is where neutron collision results in a reduction in its energy before continuing to travel with a reduced velocity and modified direction of propagation. The energy of a fast neutron is reduced more efficiently in collisions with nuclei similar in mass, such as H. It is the sensitivity of elastic scatter energy loss due to hydrogen that is exploited by neutron *porosity* devices (Ellis, 1987).

Another useful interaction is *activation*, where neutron collision promotes the transformation of the target nucleus to an unstable intermediate isotope which decays with a relatively long half life (2.3 minutes for Al) to another isotope with the simultaneous production of a gamma-ray. Elements that produce resolvable gamma-rays by activation include Al, Mn, F, I and O (Scott & Smith, 1973).

b) Absorption interactions

These involve the capture of a neutron by a target nucleus that results in an unstable nucleus and annihilation of the neutron. The unstable nucleus reacts in two categories - *Radiative capture* and *reactions which produce nuclear particles*. The former is exploited in logging. *Radiative capture* ('prompt capture') occurs when neutrons reach *thermal* energy levels (due principally to *elastic scatter* moderating interactions). The neutron is absorbed then by a target nucleus which produces an unstable *compound* nucleus. Electrons in this nucleus jump temporarily to higher energy shells and the instantaneous decay of electrons back to their original stable shell results in the emission of characteristic *gamma-rays of capture* (Scott, 1973; Hertzog & Plesek, 1979). It is this *prompt capture* reaction that is exploited by the GST (Gamma-ray Spectroscopy Tool) component of the GLT string (see Section 2.2.3).

All these interactions are therefore dependent on neutron energy; inelastic scatter only occurs at high energies, elastic scatter reactions occur reasonably consistently through 'fast' energies, and prompt capture reactions only at low *thermal* energies, as summarised in Figure 2.1. Strength of the neutron source and logging speed are therefore important parameters.

All of neutron (and gamma-ray) interactions have *cross-sections* which describe the probability of their occurrence. For geochemical logging and neutron tools involving capture reactions the cross-section at *thermal* energies is most significant. A useful parameter in nuclear logging is the *macroscopic thermal neutron absorption cross-section* of the formation (Σ_{Fm}) and of the borehole fluid (Σ_{bh}), Ellis (1987). This is simply the sum of individual elemental thermal neutron cross-sections multiplied by the number of atoms per cm^3. It therefore describes the probability of a prompt capture reaction occurring.

Other useful parameters are the neutron *slowing down length* (L_s) and the *diffusion length* (L_d). L_s is the computed average distance a neutron travels (in cm) at *fast* energy levels

before it is slowed down to *thermal* energies (0.025 eV) and is related to the neutrons initial energy and the probability of a moderating reaction occurring (*neutron slowing down density*). During this slowing down process the neutrons direction of propagation will be modified. The actual penetration distance of a fast neutron into a formation will approximate L_S. The diffusion length (L_d) describes the distance a neutron travels at thermal energies before it is involved in a capture reaction and it is dependent on the Σ_{Fm}. The *total migration length* (L_m) describes the total slowing down and diffusion length of a neutron from its birth to capture, calculated as the square root of ($L_s + L_d$).

Gamma-ray interactions

Since *gamma-ray interactions* are commonly exploited in nuclear logging (for bulk density and PEF measurement [photoelectric absorption factor]) it is worth a note on the three main types; these include two absorption interactions, the *photoelectric effect* and *pair production;* and a scattering interaction, *Compton scatter.* The regions of dominance of these reactions are shown in Figure 2.1 (b).

The *photoelectric effect* results from the interaction of a very low energy gamma-ray with an atom of the incident material. This take place at energies below which the other two reactions can usually occur, becoming the dominant reaction below gamma-ray energies of 100 keV. In this process the incident gamma-ray disappears and transfers its energy to a bound electron. If this energy is enough then the electron is ejected from the atom and interacts with the adjacent material. An ejected electron will be replaced with a less tightly bound electron and an accompanying emission of an X-ray (with an energy dependent on the atomic number of the material). The cross-section for the photoelectric effect is strongly dependent on the incident gamma-ray energy and more importantly the atomic number of the absorbing medium. The Lithodensity tool measures the photoelectric absorption factor (PEF) which is proportional photoelectric cross-section per electron (Pe). Since this is very sensitive to the average (mean) *atomic number* it is important for distinguishing lithologies. It is also used to determine Mg and Na; refer to Section 2.2.4.

Compton scatter is an interaction whereby only part of the gamma-ray energy is imparted to the electron, resulting in a reduction in the gamma-ray energy. The attenuation of gamma-rays by Compton scattering is a function of the *bulk density* and the ratio between the atomic number (Z) and the atomic mass (A). This process is not so dependent on energy and its upper and lower limits are non-exclusive with other reactions. The fact that Z/A is constant for most elements of interest (= 1/2) is the basis for the determination of *bulk density* by the density tools.

Pair production involves gamma-ray interaction with the electrical field of the incident nucleus at high energies. If the gamma-ray energy is above a threshold of 1.022 MeV, it will disappear and a electron/positron pair will form. The positron is subsequently annihilated resulting in the emission of two gamma-rays (at 511 keV each).

Gamma-ray detection

The gamma-rays emitted as a result of neutron interactions are recorded by a crystal that reacts or 'scintillates' when incident photons deposit energy into the atomic lattice of the crystal, such that the intensity of the scintillation is related to the energy of the incident gamma-ray, which in turn is related to the concentration of the contributing element and its capture cross-section. It is possible then to amplify and produce, through a photo multiplier tube, an electrical pulse which is proportional to the magnitude of the gamma-ray. By recording the energy distribution of a number of gamma-rays, which enter the crystal, it is possible to interpret the gamma-ray signal from a formation as an energy spectrum from which specific elements and their concentration yields may be determined.

For an element to be detected by prompt capture its thermal neutron absorption cross-section (Σ) must be sufficiently large to make the reaction possible and it must emit enough gamma-rays to contribute to a resolvable signal. The *sensitivity* of a device in detecting a given element is therefore a function of the abundance of the element and the distinctiveness of the emitted gamma-ray spectrum. The latter pertains to the combined effect of other interfering spectra and the resolution of the detector. Table 2.1 details the typical abundance and capture cross-sections for common elements in formations along with typical *sensitivity products*. The sensitivity product expresses the detectability of an element and it is the product of the elements typical concentration and thermal neutron cross-section, divided by it's atomic weight (Hertzog *et al.*, 1989).

Table 2.1 Common prompt capture elemental sensitivities. (from Hertzog *et al.*, 1989). Sensitivity provides an indication of the 'detectability' of an element through gamma-ray spectroscopy. Note the very low sensitivity products for Na and Mg

Element	typical abundance (wt %)	capture cross-section (barns)	typical sensitivity product		typical abundance (wt%)	capture cross-section (barns)	typical sensitivity product
Si	40	0.16	0.23	K	1	2.1	0.054
Ca	20	0.43	0.21	Al	3	0.23	0.026
Fe	5	2.55	0.23	Gd	0.0005	49000.0	0.16
S	2	0.52	0.030	Na	1	0.053	0.002
Ti	0.2	6.1	0.025	Mg	1	0.063	0.002

An additional consideration is that of similar or overlapping gamma-ray spectra of individual elements. Good detection sensitivities occur when elements have very different spectra; however, those with similar spectra are hard to resolve into individual components with any precision. Such is the case with Gd and Sm and as a consequence they can only be determined together (Gd + Sm).

2. 2 Tool configuration

The basic configuration of the GLT tool is shown in Figure 2.2. It consists of a *string* of four main tool components. At the top of the string is the first tool, the Natural Gamma-ray Spectrometry Tool (NGT- *acronym of Schlumberger, see Appendix AA*).

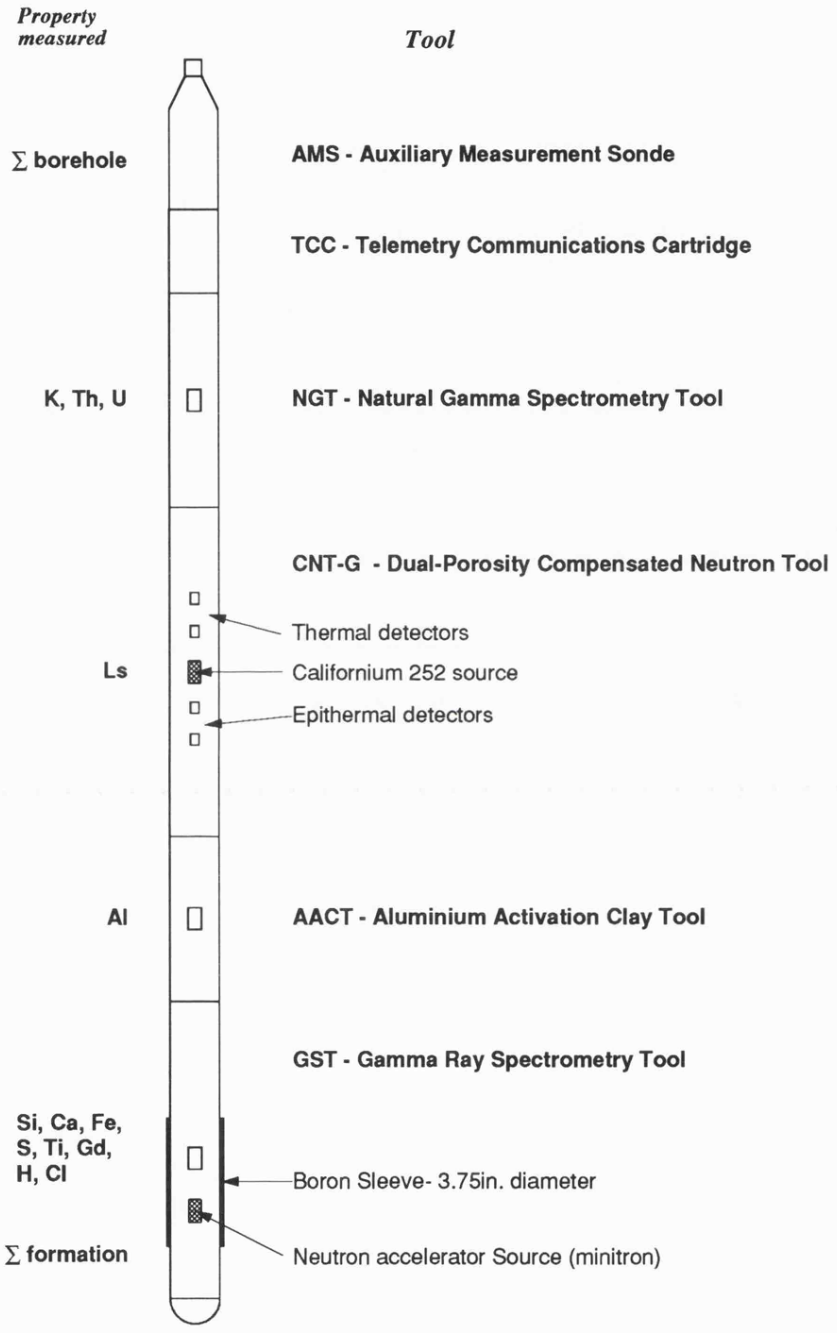

Figure 2.2 Schematic representation of the geochemical logging tool (GLT)
(Note: drawing not to scale, length of tool 23m)

2.2.1 The NGT tool

This tool measures the *natural* gamma-ray radiation signal of a formation, due to ^{40}K, isotope and the complex isotopic decay series of ^{238}U and ^{232}Th (Lock and Hoyer, 1971). With a prior knowledge of the individual contribution each of these three isotopes make to the natural gamma-ray spectrum, it is possible to resolve the measured gamma-ray spectrum from the rock into components attributable to K, U and Th (Serra, 1984). The incident gamma-ray spectrum is divided into five discrete windows (energy ranges), see Figure 2.3. Three windows lie in the high energy part of the spectrum (windows 3 - 5) and cover the characteristic peaks of K, U and Th. Contributions from two additional 'low' energy windows (windows 1 & 2) help to reduce statistical variations. The number of gamma-rays emitted from each isotope is proportional to its abundance, and after suitable calibration (Mathews *et al.*, 1987) it is possible to convert counting rates from each window into absolute abundances. This tool is positioned at the top of the tool string so that the measurement is taken before any irradiation of the formation from the sources below.

2.2.2 The AACT tool

The next component of the GLT tool string is the Aluminium Activation Clay Tool (AACT) which measures the concentration of Al in the formation (Scott & Smith, 1973; Hertzog *et al.*, 1989). Unfortunately Al does not contribute a resolvable signal to the *prompt capture* gamma-ray spectrum (described next), but is suitably detected by *delayed activation.* Gamma-rays are produced by delayed activation when the stable ^{27}Al atom absorbs a low energy *thermal* neutron and is transformed into its unstable ^{28}Al isotope, emitting a 1779 keV gamma-ray as it decays to stable ^{28}Si. The half life of this reaction is 2.24 minutes and so at normal logging speeds (500-600 ft/hr) a delay of 40-50 seconds is required between emitting the neutron and measurement of the gamma-ray. A Californium (^{252}Cf) natural source is used to generate neutrons at 2.35 MeV. This is housed in a conventional *neutron* tool (the CNT-G), positioned above the AACT in the string. The actual AACT tool is itself a modified natural gamma-ray tool (NGT) adapted to detect induced gamma-rays as well as the natural gamma-ray signal. The net spectrum from Al is then determined by subtracting the NGT contribution determined from the NGT tool above. The Al gamma-ray peak falls into window 4 of the energy spectrum. Interference is possible due to the ^{56}Mn activation, causing a gamma-ray peak at 1811 MeV which, due to detector resolution, can not be resolved from Al. An additional spectral window between 800-900 keV(window 6) is incorporated over the lower energy peak of Mn which allows correction for any Mn. This is usually a minor problem as Mn is not common and Al abundant; it may cause a problem, however, when logging through drill pipe. The choice of a source below the more conventional 4 MeV (AmBe) source is due to spectral interference from Si which is activated by fast neutrons above 3.9 MeV(Hertzog *et al.*, 1986, Grau *et al.*, 1989). Even with the Cf source a proportion of neutrons may be emitted above 3.9 MeV threshold and it may be necessary to correct the Al count rate after estimation

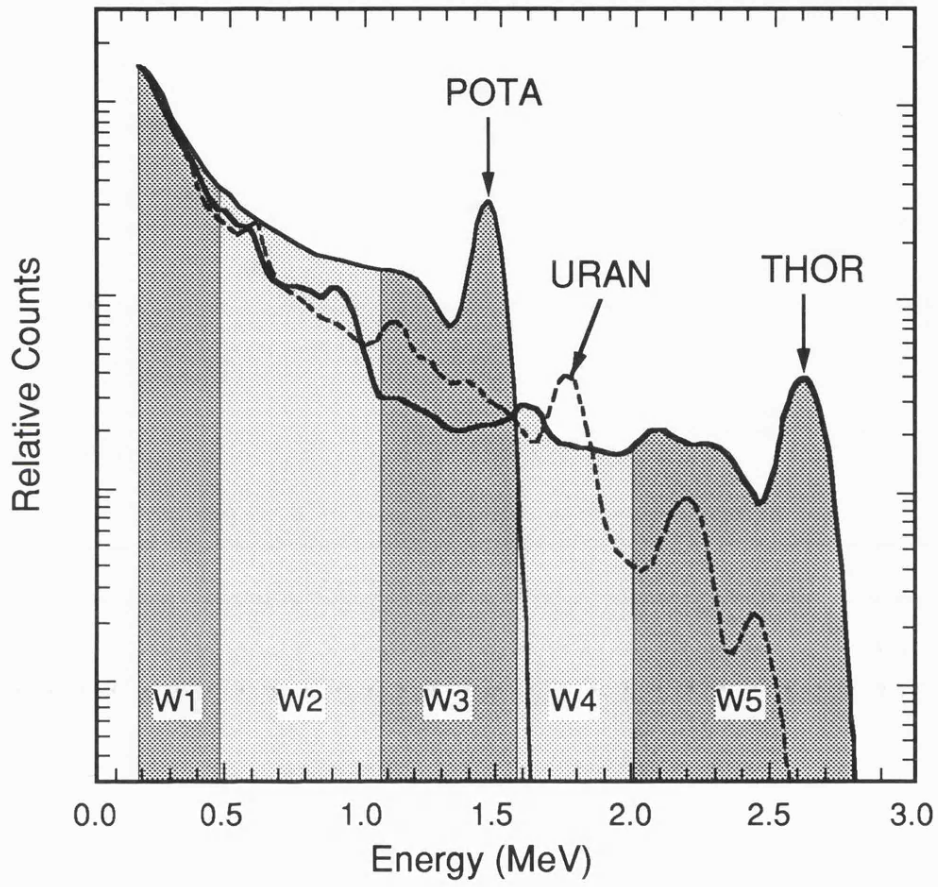

Figure 2.3 Standard spectra from a natural gamma-ray spectrometry tool (NGT) showing the relative counts of incident gamma rays versus their energy. The spectra are split up by the tool into five energy windows indicated by the shading. Windows 3, 4, and 5 cover the characteristic peaks of K, U and Th, respectively.

of Si (Schweitzer, 1991). The tool can be pressed against the formation wall to increase gamma-ray signal emitted from the formation.

2.2.3 The GST tool

The third component of the GLT tool string is the Gamma-ray Spectrometry Tool (GST) - carried at the base of the tool string. This consists of a 'minitron' tritium source producing pulsed 14 MeV neutrons and a gamma-ray scintillation detector. The GST exploits the *prompt neutron capture* reactions induced after bombardment of the formation with *fast* neutrons. Fast neutrons lose energy through moderating scatter *interactions* (Section 2.1) and on reaching thermal energy levels are captured by elemental nuclei causing 'element specific', gamma-rays of capture to be emitted. It is possible to resolve the spectral *'yields'*, or contributions, of the elements Si, Fe, Ca, S, Ti, (Gd+Sm) in addition to Cl and H (Hertzog *et al.,* 1989).

The pulsed nature of the GST 'minitron' source allows for multiple spectral measurements to be made. These measurements are 'gated' at different times to the neutron pulse, to optimise sensitivity to the gamma-ray signals produced by the various neutron reactions and optimise the signal-to-noise ratio. (Serra, 1984; Schlumberger, 1982, Ellis, 1987). The use of 'minitron' neutron accelerator source is advantageous for safety reasons as it can be turned off, but due to factors such as *down-hole* temperature variation and varying capture cross-sections, the neutron accelerating voltage, and therefore neutron flux produced, is not constant. For this reason it is not possible, like the AACT tool (where the neutron flux is constant), to directly convert count rates from the GST into absolute abundances. The elemental yields derived from *spectral stripping* of the total recorded spectrum, are used in conjunction with elements derived from the NGT and AACT tools to derive the weight percent of all these elements in the *geochemical oxide closure model* (described later in Section 2.5).

Elements with similar or overlapping gamma-ray spectra are hard to resolve into individual components with any precision (ie, detection sensitivities). Such is the case with Gd and Sm and as a consequence they can only be determined together (Gd + Sm). Al suffers from partial interference with the Fe spectra and is difficult to separate due to the low resolution of the scintillation crystal. Luckily Al can be detected, as shown, by delayed activation.

H and Cl both contribute significantly to the measured gamma-ray spectrum, but are not determined as part of the rock chemistry as they are primarily the response of the borehole fluid. Their spectral contributions are included, however, in the processing to calculate the other elements. Cl (and H) has a very large thermal neutron capture cross section (Σ) and is also an effective *fast* neutron stopper. If it is present in the borehole fluid it has a great effect on the neutron flux entering the formation, the gamma-ray signal returned and therefore the elemental yields measured. The addition of a boron sleeve to the tool reduces the signal from the borehole. Boron effectively reduces the number of capture reactions in the borehole

induced by Cl, and in the tool housing by Fe, by 'mopping up' thermal neutrons, thereby increasing the signal derived from the formation and improving the signal-to-noise ratio (Schweitzer, 1984).

2.2.4 Additional tools

In addition to the three gamma-ray spectrometry devices, two other tools are coupled at the top of the string. The Auxiliary Measurement Sonde (AMS) records the resistivity and temperature of the borehole fluids. This allows the borehole fluid salinity and consequently the abundance of Cl to be determined. It therefore provides an idea of the borehole neutron capture cross-section (Σ_{bh}). Σ_{bh} is an important parameter for the calculation of the neutron flux entering the formation and is essential in the calculation of elemental abundances by delayed activation. A Telemetry Cartridge is coupled beneath the AMS with the sole purpose of relaying digitised log measurements up the wireline to the surface. This offers a superior quality of data in comparison to sending analogue data for digitising at the surface. A compensated neutron tool CNT-G (as previously mentioned in Section 2.2.2) is deployed to carry the ^{252}Cf source for the AACT tool and also to measure the apparent neutron slowing down length (L_s) for input to the aluminium measurement.

The only major elements not measured are Mg and Na. Neither has a large enough capture cross section relative to their typical abundance (sensitivity product) to be detected by the GST (See Table 2.1). An estimate of their concentration can, however, be derived from the photoelectric factor (PEF) measured by the Litho-density tool. PEF is an estimate of the probability of photoelectric absorption (Pe), a reaction induced by *gamma-ray* bombardment of a formation at very low energies (<100 keV) below which *Compton Scatter* reactions can occur, see Figure 2.1 (b) and Section 2.1. Pe is very sensitive to the average atomic number of a formation , and is especially sensitive to the low atomic number elements, most of which have been recorded by the GLT (except Mg and Na). Thus the recorded PEF log estimate is compared to a PEF estimate derived from the summation of all the photoelectric contributions of elements measured by the GLT tool. Any difference is attributed to the un-measured major elements Mg + Na. (Hertzog *et al.*, 1989).

2.2.5 The detection of gamma-rays

All of the spectrometry tools in the GLT employ a NaI Thallium (Tl) doped scintillation crystal. This is the most commonly used detector in spectrometry tools. Tools such as the NGT and AACT divide the energy spectrum from this crystal into broad energy windows aimed at detecting specific, target peaks. In contrast, the GST records counts-rates through a series of 256 energy channels, covering the energy spectrum from 1 to 8 MeV. It should be theoretically possible to measure the total spectrum from either situation and decompose it, quite simply, into the relative spectral components of each element. However, NaI(Tl) crystals have some factors that may compromise their performance. In the first instance,

discrete gamma-ray peaks are broadened as a result of a) *Doppler Shift*, due recoil and vibration in the crystal (Serra, 1984); b) *Compton Scatter* resulting in degradation of gamma-ray energies (Ellis, 1987); c) the production of three, triplet *peaks* for each gamma-ray, due to nuclear interactions in the crystal (Willard, 1988); and finally d) the finite energy *resolution* of the detector. Scintillation *deadtime* must also be short to allow operation at high count rates and to avoid *pile up peaks* (Ellis, 1987). The result is an indistinct 'bumpy' spectrum as illustrated in Figure 2.4.

The resolution of the detector crystal is a function of its size and scintillation efficiency. Typical crystals have resolutions of between 6 -10%, which suggests that even a sharp, full energy peak can lie within +/- 5% of its true intensity. A *poor* resolution (>9%)will result in allocation of a gamma-ray to the wrong energy window, leading to its mis-identification and contaminating that window. This will decrease the differences between individual spectra being resolved, and will increase the signal-to-noise ratio. It is therefore necessary to ensure that gamma-rays are being counted in the correct window by monitoring *gain* in the crystal. Crystal *gain* is monitored by a secondary gamma-ray source and feed-back loop (Bateman, 1985), and appropriate changes accounted for.

Unfortunately the scintillation crystal is also sensitive to temperature effects which will reduce resolution and scintillation efficiency. An operational maximum temperature for a typical 50 x 150 mm NaI(Tl) crystal is 150°C (Schlumberger, 1982). Scintillation crystals also degrade through time (Grau, 1980) resulting in a loss in resolution. Appropriate calibration can be used, however, to check for bad crystals. Cable speed and crystal size will also affect the counting statistics from a detector. For this reason cable speed and crystal size are *input* to the operators signal-processing routine, and can be corrected. Problems do occur, however, when a tool gets stuck and continues to record. Figure 2.4 illustrates the broad spectrum created by a NaI(Tl) crystal. In Figure (a) the difference in resolution due to temperature is illustrated and Figure (b) the difference between a 'good' and 'bad' crystal. As long as the aforementioned effects are considered in processing, they can be accounted for under normal logging conditions, however; a bad crystal will have to be replaced.

Future advancements in detector technology, especially with high resolution germanium based detectors, will allow much more accuracy and better spectral de-convolution to be achieved. The dramatic improvement in peak detection makes it practical to analyse elements which do not make vast contributions to the gamma-ray signal. The detection of ^{24}Na, ^{27}Mg, ^{56}Mn and ^{52}V as wt% concentrations, from a *pilot* germanium logging tool, has recently been achieved through delayed activation (Schweitzer & Peterson, 1992).

2.3 Processing of log data

Processing is required to transform GST derived elemental yields to more familiar wt% elemental oxide fractions. This processing requires the addition of the independent tool derived measurements of K, Al (and Σ). Preliminary *field* processing is performed 'on site' to

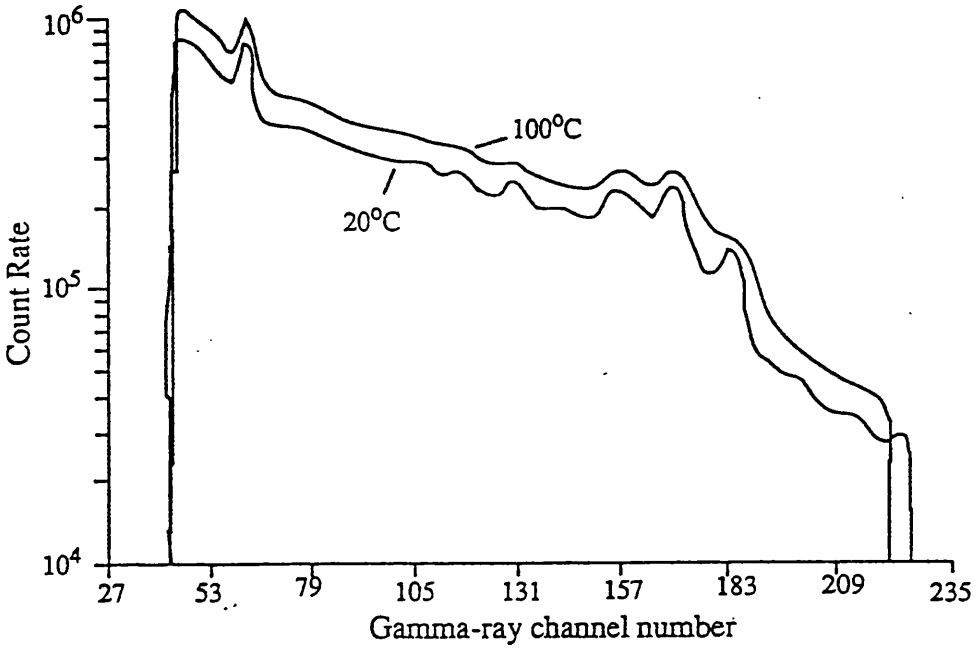

Figure 2.4a Difference in the recorded spectra from a NaI(Tl) crystal at 20 degrees C and 100 degrees C. A sharp decrease in resolution of the crystal is seen at higher temperature.

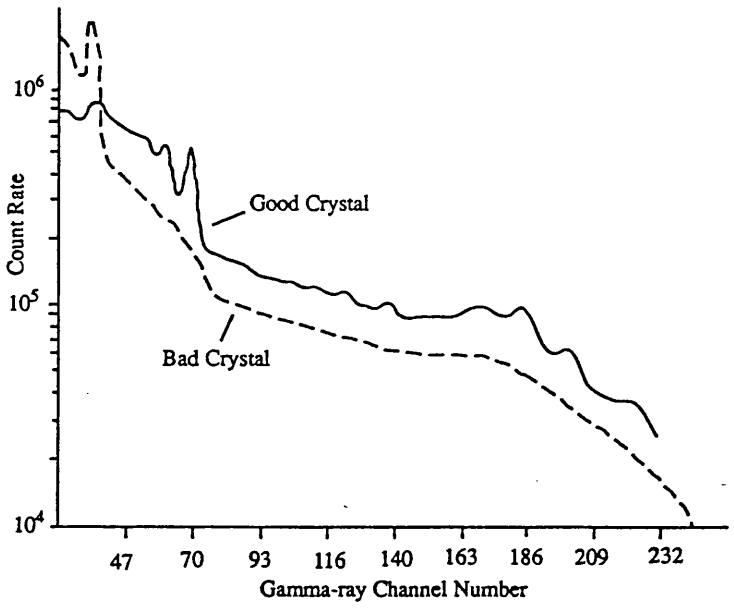

Figure 2.4b An example of the difference in resolution of two NaI(Tl) scintillation crystals (spectra are slightly offset for clarity) modified from Grau et., al., (1980).

produce 'working logs'; later post *acquisition* processing is performed to allow a more comprehensive correction for temperature, borehole size, logging speed, borehole fluid salinity and drill pipe effects. This processing is performed using a series of programs implemented by Schlumberger (Bristow *et al.,* 1992). These are now summarised. A flow diagram of these routines, depicting the integration of tool measurements, is illustrated in Figure 2.5.

2.3.1 Spectral stripping - derivation of GST elemental yields

The assumption taken in this first step of the processing is that the acquired gamma-ray spectrum from the GST at each depth interval can be represented by a linear combination of a number of *standard* spectra (Grau *et al.,* 1980). These standard spectra, shown in Figure 2.6, approximate to the contributed spectrum of each element. Spectral standards are combined together, and matched with the recorded spectrum, in an inversion routine that *best fits* the two spectra, and the relative elemental yields determined. *Field processing* conventionally has a six-element inversion which include the elements Si, Ca, Cl, H, S and Fe. Three additional spectra - Ti, Gd and K, are added in subsequent processing to substantially improve the fit of the elements to the recorded spectra (Grau & Schweitzer, 1989). In some environments elements may occur below the detection capability of the tool (Jarrard & Lyle 1991, Bristow & deMenocal, 1992); removal and insertion of other *elemental* standards is possible at this stage to improve the fit and reduce instability in the inversion process. A simple 7 point (3.5') arithmetic averaging is then applied to yields to reduce statistical noise levels.

2.3.2 Depth shift

In the course of geochemical processing data from different tool *runs* are combined. It is important to depth correlate all data to one reference run. By deploying the NGT on all tool strings run, the natural gamma-ray curve is used to match and correlate depths; and the reference run selected on the basis cable tension. This indicates the tool speed and whether any tool sticking occurred, and thus the quality of the run. The Lithodensity tool (measuring bulk density and PEF) is usually run separately to the GLT tool due to differences in the optimum measurement speed of each tool and tool string lengths.

2.3.3 Calculation of potassium

This stage of the processing involves the calculation of potassium in wet wt% from the natural gamma-ray spectrum obtained from the NGT tool (in addition to U and Th in ppm). Total gamma-ray ([SGR], K + U + Th) and computed gamma-ray curves([CGR], Th + K) are also derived. Counts from five energy windows utilised in the recording of the spectrum (see Section 2.2.1) are inverted at each depth interval to give the concentrations of K, U, Th, using

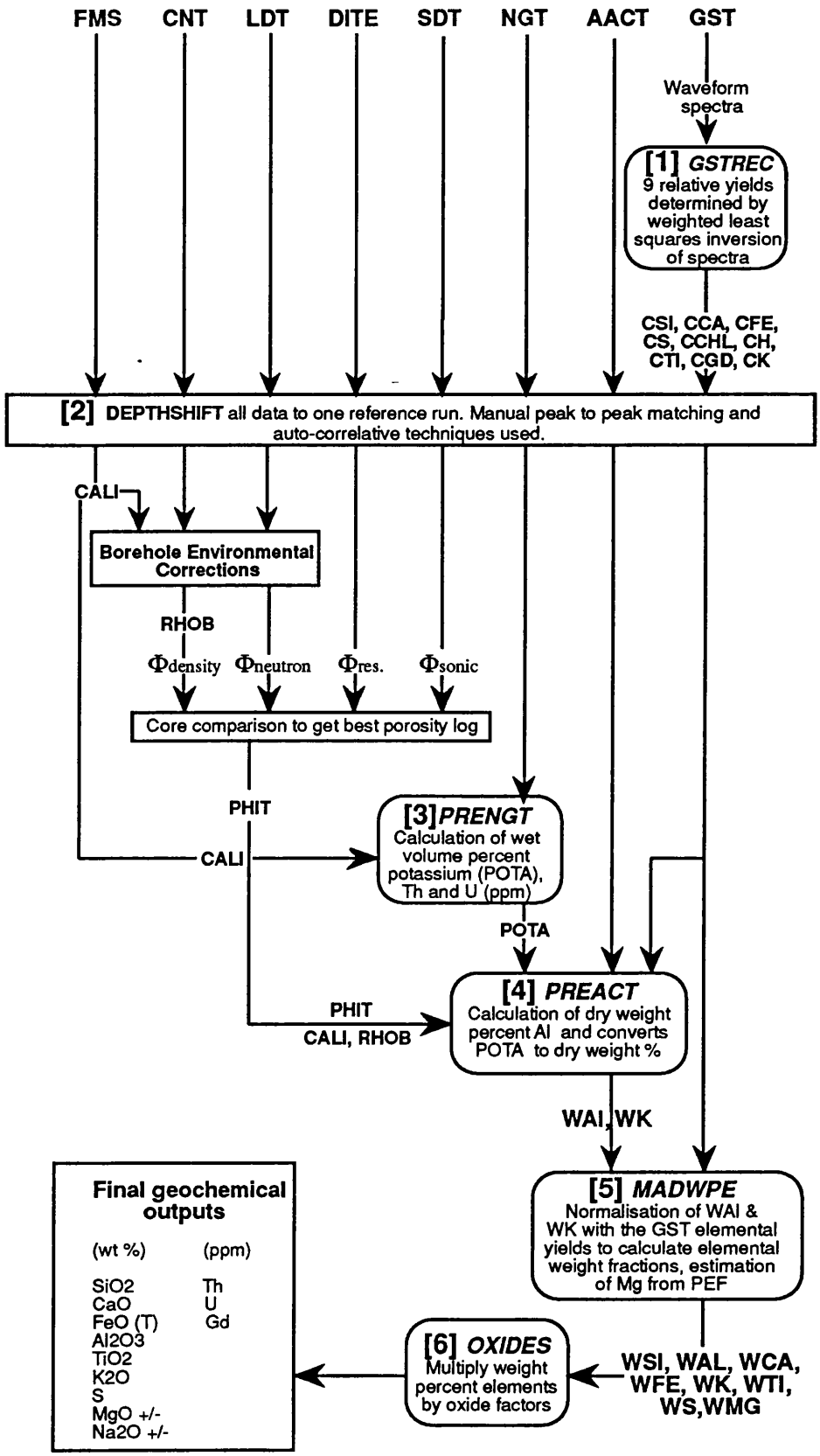

Figure 2.5 Flow diagram summarising the processing of geochemical logging data. Schlumberger tool acronyms: FMS - formation microscanner, CNT - compensated neutron porosity tool, LDT - lithodensity tool, DITE - dual induction tool, SDT - digital sonic tool, NGT - natural gamma spectrometry tool, AACT - aluminium activation clay tool, GST - gamma spectrometry tool. CALI - caliper, RHOB - bulk density. Bold names in italics refer to processing routine names.Numbers refer to these routines as described, in order in the text (Adapted from Bristow et., al., 1991).

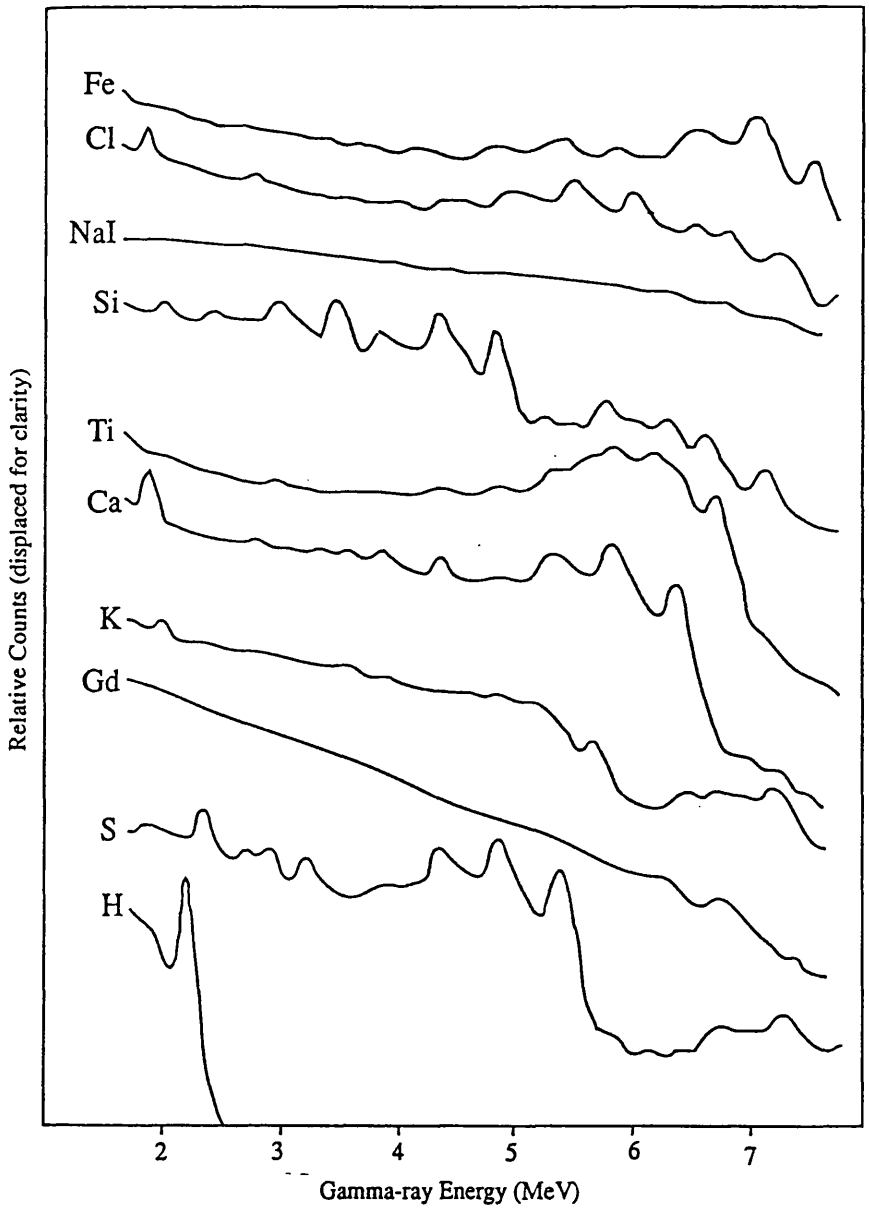

Figure 2.6 Standard spectrum of each commonly recorded element as used in GST spectral stripping and determination ofelemental yields. Modified from Schweitzer (in press)

calibration coefficients derived from laboratory spectral standards. Inclusion of caliper and temperature data and the correction for the presence of potassium and barite in drilling fluid (KCl is added to inhibit clay swelling) compensates for any un-wanted environmental perturbations. The NGT spectrum is often derived from the GLT tool run, not from other runs, as this is deployed at the slowest logging speed (*viz.* 500 ft/hr) facilitating the best gamma-ray count statistics. K is converted to dry wt% in the next routine.

2.3.4 Calculation of Aluminium

The fourth processing routine calculates the concentration of dry wt% Al, from the Aluminium Activation Clay Tool (AACT) measurement. The count rates from the natural gamma-ray contribution of the spectrum are subtracted by combining the spectrum from the NGT tool with that from the AACT tool; the residual spectrum is attributed to Al wet wt%. The ^{252}Cf neutron source strength is fundamental for derivation of Al measurement; this is calculated in the routine from calibration data. Raw data are corrected for environmental effects such as borehole fluid, borehole diameter, in addition to Σ_{Fm} and Σ_{Bh}, formation density and neutron slowing down length (L_s), which all have a large effect on the neutron flux entering the formation.

Porosity and density logs, derived from separate logging runs, are then used to convert both Al and K to dry weight percent. Porosity can be derived from induction logs using Archie's Law (Archie, 1942) or more commonly from the density (LDT), neutron (CNT) or sonic logs (SDT) (Ellis, 1987). Comparison with core porosity indicates the best log to use. The final step in the routine makes a correction for Si activation and transformation to ^{28}Al, induced by the fast neutron interactions (Section 2.2.2.). This reaction affects the Al spectrum. Any background Si interference is calculated by combining Al data from the AACT with the elemental yields from the GST, and K from the NGT; and the contributions from Si, subsequently subtracted out.

2.3.5 The geochemical oxide closure model

Due to the variable neutron flux generated by the GST minitron source, it is not possible to directly convert elemental spectral count rates into absolute abundances. *Relative* concentrations of the GST derived elemental concentrations can be determined, however, by dividing each elemental yield by a relative spectral *sensitivity* factor S_i. (Hertzog *et al.*, 1989; Grau *et al.*, 1989). This parameter is related to the thermal neutron cross-section of each element (Σ_i), as well as detection and transport efficiencies, and it is a laboratory derived *tool constant*. Relative elemental concentrations are then related to absolute concentrations by an interval/depth dependent *normalisation factor*, F, as defined in the relationship:

$$Wt_i = FY_i / S_i \qquad (..1)$$

where Wt_i is the absolute elemental concentration, F = normalisation factor, Y_i = the relative elemental yield, and S_i = the spectral sensitivity factor. F is a complex function of

almost every physical variable in the borehole environment. It cannot be determined directly due to the variable and unknown neutron source strength. The approach adopted therefore is to calculate F on the basis that the sum of all the elemental weight fractions is unity (100 wt%). The approximation that each element combines, or is locked up, in an oxide or carbonate allows this *closure* model to cope with the absence of carbon and oxygen, which are not measured by the tool but are abundant. K and Al concentrations (dry wt%), derived from previous routines, are then normalised with the reconstructed elemental yields to determine F at each depth interval from the following equation:

$$F\left[\sum_i X_i\left(\frac{Y_i}{S_i}\right)\right] + X_K Wt_K + X_{Al} Wt_{Al} = 1.0 \qquad (..2)$$

Where: X_i is the weight of the oxide or carbonate divided by the weight of element i; Wt_K and Wt_{Al} are the independently determined weight fractions of K and Al from there respective tools. In effect, F forces the equation to closure at each depth interval. Only elements contained in the formation (and formation fluids) are therefore included in the model, and those that may be present in the borehole fluid (Cl & H) are excluded.

An enhancement in processing is provided by comparing the relatively poor GST derived potassium spectrum with an estimated spectrum for K, back-calculated through the closure model from the wt% K NGT measurement. Any difference between the two spectra is *redistributed* amongst other elemental yields. This in turn produces an improved estimate of F leading to improved elemental abundances (Grau & Schweitzer, 1989). By nature of the closure relationship the model compensates automatically for tool standoff and washouts by increasing F .

2.3.6 Calculation of Mg + Na

This closure model as it stands does not take into account Mg and Na which may be present, due to their poor spectral contribution (detectability). If a large amount of MgCO3 is present the normalisation factor (F) will be over estimated, possibly by up to a factor of 2 in pure dolomite (Hertzog *et al.*, 1989). It is possible to make an estimation of Mg (see section 2.2.4) from the difference in the PEF values measured from the Lithodensity tool and a value for PEF determined from the initial elemental abundances gained from the closure model. The assumption is that this difference is Mg (or Na) as they are the most abundant elements not measured by the GLT. Any estimate of Mg (or Na) can be included into the closure model of Eqn. (2) and the other variables are re-normalised, thus obtaining a better estimate of F. Caution must be exercised when using the Mg+Na estimate as its derivation is compromised by the borehole environment especially when barite mud (BaSO4) is used; this masks formation PEF. It should only be attempted when quality of the GLT and LDT data are high, or Mg is present in large quantities.

2.3.7 Final calculation of oxide percentages

The final routine converts the elemental abundances (wt %) into oxide percentages by multiplying each element by its associated *oxide factor* as used in the previous normalisation step. Table 2.2 summarises the oxide typical oxide factors employed for this routine. Discretion is needed in determining which oxide or carbonate species is deployed, depending on the minerals present and geological environment being logged.

Table 2.2 Elemental oxide factors used for different geological environments as deployed in the geochemical oxide closure model. From Hertzog *et al.*, 1989 and J. F. Bristow *pers. comm.*, 1992. Values relate to different geological environments. sst - sandstone, sed-carb - carbonate environment.

element	oxide	theoretical	igneous	sed-carb	sst/mixed
Si	SiO2	2.139	2.139	2.139	2.139
Ca	CaO	1.399	1.399	2.497	1.399<6
	CaCo3	2.497			2.497>12
Fe	FeO	1.287	1.358	2.075	2.075
	Fe2O3	1.43			1.43
	FeCo3	2.075			
S	CaSo4	1.125	1	0.064	0.064
	FeS	0.064			
K	K2O	1.205	1.205	0.615	0.615
Al	Al2O3	1.889	1.889	2.741	2.741
Mg	MgO	1.658	1.658	3.472	1.658
	MgCo3	3.472			

2.4 Volume and depth of investigation.

The distance that a fast neutron travels through a material is governed by the neutrons initial energy and nuclear properties of that material. Considering the AACT tool source is 2.35 MeV and the GST tool is 14 MeV, it is likely that the distance that a neutron slows down to induce a capture reaction and therefore the distance a neutron flux penetrates into a formation, will vary. Simulation studies (Pelling, 1992) show that differences in slowing and migration lengths (thus area of rock measured) between the two source strengths will occur above a certain threshold of porosity. In a simulated *fresh water filled sandstone* this is at 15% porosity, and in a limestone it is 10%. In general, this is where the 14 MeV slowing down distance (L_S, see section 2.1) and 2.35 MeV migration distance (L_m) cease to overlap, see Figure 2.7 (a & b). An increase in porosity is seen also to have a greater effect on reducing the total *migration length* of lower energy (2.35 MeV) neutron sources. This is such that in a simulated sandstone with 40% porosity, 14 MeV neutrons slow to a capture reaction over a distance of 13.8 cm, while a 2.35 MeV source will slow in only 8.1 cm (Pelling, 1992). Figure 2.6 a & b illustrate (from Pelling, 1992) the neutron distances travelled in a sandstone and limestone for two neutron sources and the effect porosity has on both. Porosity and source strength clearly affect neutron distance travelled thus the area and the volume of investigation. The AACT tool does not necessarily have the same investigation depth as the GST tool.

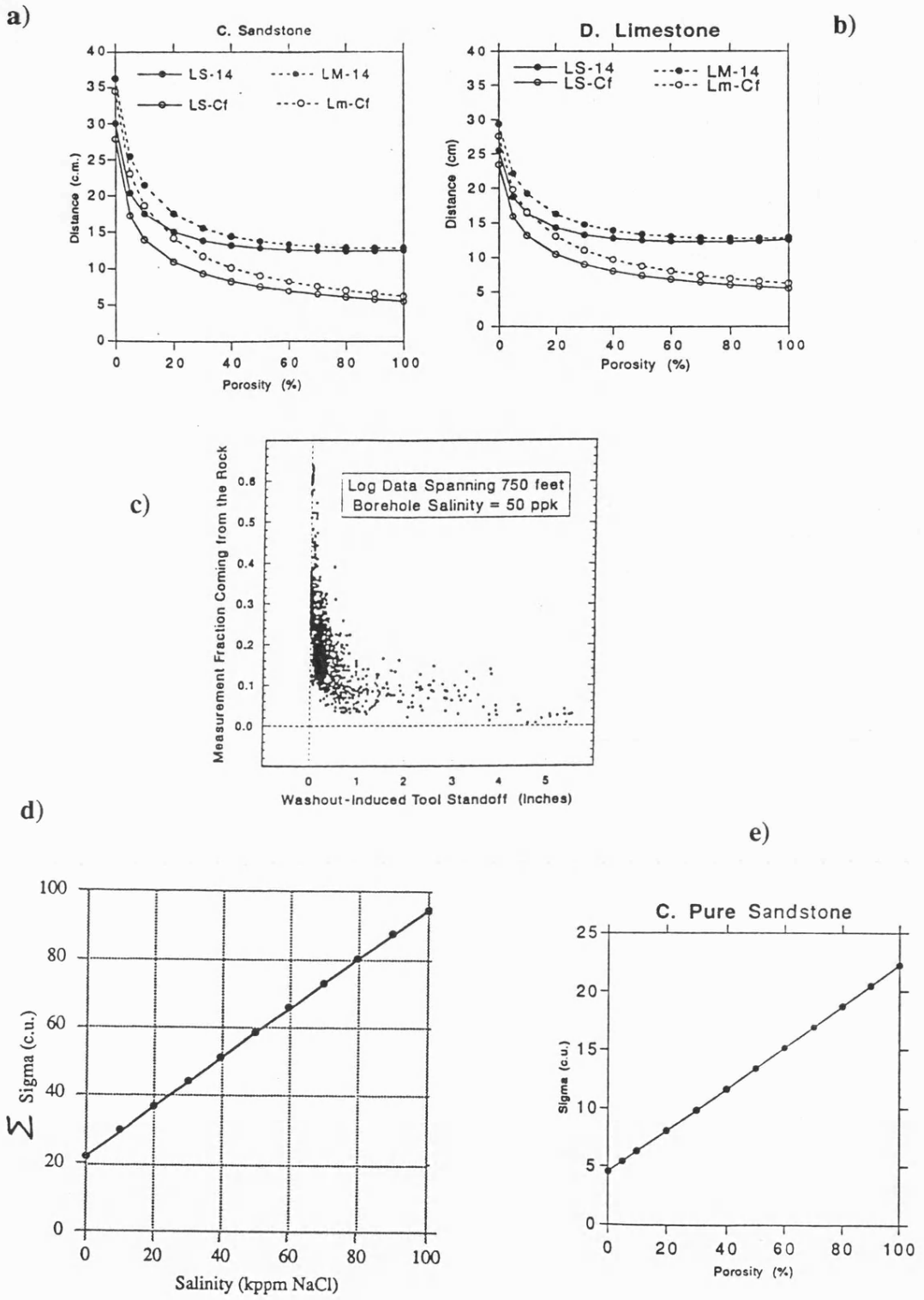

Figure 2.7: Figures a + b, Effect on neutron propagation distance, (thus volume and area of tool investigation), due to neutron source strength and porosity. Figure c). The effect of an increase in volume of saline borehole fluid (greater Σ) on the proportion of the total gamma-ray signature coming from the formation (induced, here, by tool standoff). Figures d-e - The effect of salinity and porosity on the macroscopic thermal neutron capture cross-section (Σ), see text. All neutron transport distances and Σ calculations are simulated models (after - Pelling, 1992).

Figures a + b - Ls -14 and Ls-Cf represent the neutron Slowing down length (Ls) for a neutron source of 14 MeV and 2.35 MeV, respectively, and Lm the migration length. Threshold porosities, where porosity will noticeably effect migration length between the two source strengths, occur at 15% for simulated sandstone and 10% for simulated limestone. This may affect the volume of investigation. Fresh water fluid modelled.
Figure c - Washout induced standoff represents an increased distance between the logging tool , See Text. **Figure d + e** - Σ , measured in capture units. Porosity in Figure e is fresh water filled.

The volume of investigation of GLT data is also partially dependent on lithology. Most formations do not have high neutron capture cross sections (ie, sandstone and limestone) and therefore have a lower probability of capturing a neutron and inducing a measurable gamma-ray, in comparison with, for example, a basalt. This may mean that any signal from a rock matrix may be overshadowed by reactions taking place in the formation fluids. This is especially so for high porosity formations and must be considered in processing.

The *borehole fluid*, in terms of the thermal neutron cross-section that it exhibits (Σ_{bh}), will also have an effect on the neutron transport behaviour. This tends to be influenced by the salinity of the fluid, due essentially to Cl - with its extremely large neutron capture cross-section. Figure 2.7 (c) shows the effect of the increased volume of saline borehole fluid, (in this case by tool standoff) on the percentage of total gamma-ray yield contributed by the formation. It is clear that with 5 inches of saline fluid between the tool and the formation, the contribution of gamma-rays from the formation is 2 - 3% of the total gamma-ray yield. Figure 2.7 (d & e) demonstrate the effect of salinity and porosity, respectively, on the thermal neutron cross-section (Σ). A boron sleeve helps to alleviate this problem.

Hertzog *et al.* (1989) quote the average volume of investigation of the GLT tool to be in the order of $1m^3$, presiding as a spherical geometry. Theoretical simulation of neutron transport in the borehole environment by Pelling (1992) suggests that such a volume is reduced to 0.3 m^3 in some rocks (in his case a basalt) and the geometry, in adverse conditions, takes on a bell shape with the apex of the bell furthest into the formation, perpendicular to the borehole axis. The best data quality will be derived where the matrix material predominates the gamma-ray signature. This is more likely to happen in low porosity formations where the borehole diameter is uniform and close to the tool and a boron sleeve deployed.

2.5 Accuracy and precision of GLT measurements

2.5.1 Precision

Through a series of multiple pass evaluations in a siliciclastic test well, Hertzog *et al.* (1989) have predicted estimates of the precision of the GLT tool. These estimates of precision, quoted in Table 2.3, column 2, are 1 sigma standard deviations for typical concentration ranges expected for each element (column 1). Grau *et al.* (1989) looked at predicted uncertainties of GLT measurements in more detail using a different approach. They suggest such uncertainties in GLT measurements depend weakly on elemental abundance itself, and strongly on other measurement and environmental parameters. They considered the statistical uncertainties associated with elemental determination by numerically simulating a number of spectra, for different concentrations; and then deriving elemental concentrations by processing each spectrum using the closure model. By applying noise they could simulate different environmental perturbations in the spectra. In this way different environmental effects could be simulated and uncertainties in each elemental measurement calculated.

Standard deviations, as measures of precision, derived from 2000 simulations are summarised in Table 2.3, column 3 + 4. In summary, their results suggest typical uncertainties under normal logging conditions of between 2 - 3 wt% for Ca and Si, just over 1 wt% for S, a few tenths of a percent for Fe and Ti, and 0.2 ppm for Gd. Adverse effects such as tool standoff and abnormally large borehole fluid Σ, will increase these uncertainties. In such conditions they advocate use of slower logging speeds or multiple passes.

Table 2.3 GLT precision from multiple pass evaluations (Hertzog *et al.*, 1989), columns 1 & 2; and uncertainties calculated from 2000 numerical simulations (Grau *et al.*, 1989), columns 3 + 4; column 3 shows the standard deviation of simulated measurements (SD_m), column 4 - $SD_{(no\ K\ or\ Al)}$ - shows calculated uncertainty without K and Al in the closure model. Al* from Grau *et al.*, 1989. K* from Chapman *et al.*, 1987.

	Range	Precision	SD_m	$SD_{(no\ K\ or\ Al)}$
Si	25 - 47wt%	2.3 - 6.4 wt%	2.76 wt%	3.67 wt%
Al	0-15	0.1 - 0.8%	-	-
Al*	2		0.2%	-
Al*	18		0.9%	-
Ti	0.1 - 0.3	0.1 - 0.3	0.19	0.19
Fe	1 - 5	0.3 - 0.8	0.41	0.46
Ca	0 - 40	1.6 - 4.2	2.29	2.52
Gd	0 - 10ppm	0.4 - 1.1 ppm	0.99 ppm	0.70 ppm
S	-	-	1.29	1.28
K*	0 - 4	0.25	-	-

Georgi (1991) also looks at precision estimates using time-series analysis of multiple-pass data. From this he produced estimates of the signal-to-noise ratios and vertical resolution for restricted set of elements in two high porosity (33%) heavy oil wells. Signal-to-noise ratio should, of course, be maximised to reduce error from noise in the spectral measurement. His conclusions suggest that the quality of the signal from each element is not equal, an observation also made by Pelling (1992) and Jarrard & Lyle (1991) who also consider the problem. In Georgi's data, Fe has a reasonable signal to noise ratio of 6:1 and a vertical resolution of 0.55m while Si and Ca are of less quality, with 5.1:1 and 2:1 ratios respectively, and both a resolution of 1m. Estimates of S, however, have the best resolution of 0.3m and signal-to-noise ratio of 64:1.

Lower estimates of precision are generally encountered in ODP logging environment, (Jarrard & Lyle, 1991; Pelling, 1992; Bristow *et al.*, 1992), where harsh borehole conditions and a tool string compromised by modifications for the drilling environment increse uncertainties.

2.5.2 Accuracy

In theory, it is extremely difficult to test the accuracy of GLT measurements in the borehole environment. The best available test is to compare elemental weight fractions obtained from logging measurements with laboratory elemental analyses of sidewall plugs or core such as by XRF spectrometry. This has been performed for a number of wells in an attempt to establish limits of accuracy. There are, however, two potential problems that must be considered when comparing such data. First is the substantial disparity in the volumes of

rock measured, the GLT measurement being hundreds of times larger. The GLT typically samples a volume between 0.3 and 1.0 m^3, while a typical XRF sample maybe as little as 10^{-6} m^3. The second is the problem of correlating core samples, of relatively low frequency, with the abundant, high frequency, measurements from the GLT.

Through a series of published examples Pelling (1992) studied the performance of the GLT data in the ODP environment. He revealed mixed results, which point to the GLT being restricted to detecting gross changes in geochemistry compared with XRF, which are none-the-less sufficient to allow geochemical classification of sedimentary rocks. The most comprehensive, non ODP study (besides Schlumberger *in house* studies), was undertaken by Van Den Oord (1991) who used core sampled specifically to accommodate, as best as possible, sample volume disparities. These results, presented in Table 2.4, fall, *surprisingly*, within those predicted by Schlumberger. Results from other independent field tests by Anderson *et al.* (1988) Wendlandt & Bhuyan (1991) and Carpenter and Ryan (1991) are also listed. Anderson *et al.* also employed a rigorous sampling procedure, which may reflect the good results, but they made no effort to quantify accuracy. Values for these data are derived from visual inspection of core-log cross plot data, as are data from Wendlandt & Bhuyan (1990) and Carpenter and Ryan (1991). Wendlandt & Bhuyan (1991) found that K, Fe and Si are determined most accurately, followed by Al, Ca and Ti, with Mg+Na the least accurate. Jarrard & Lyle (1992) illustrate poor quality of results obtained from the *'compromised'* tool deployed in the ODP.

Table 2.4 Reported accuracy of GLT wt% elemental data from different field tests. Values for Van Den Oord are standard errors derived from a number of sub-populations. Values in brackets indicate the typical range of abundances. Standard deviations for each sub-population will be less than these values quoted here. Schlumberger data is from promotional material.

	Van Den Oord (1990)	Schlumberger (1988)	Anderson *et.al.* (1988)		Wendlant & Bhuyan (1990)		Carpenter& Ryan (1991)	
Si	2.0	1.6 - 6.5	2.33	(50 - 75%)	5.0	(0 - 50%)	2.74	(14-40%)
Ti	0.2	0.1 - 0.6	0.18	(0.2 - 1.2%)	-	-		(0-0.6%)
Al	0.8	0.1 - 0.8	2.11	(10 - 20%)	3.0	(0 - 12%)	1.15	(0-10%)
Fe	0.4	0.2 - 0.6	1.55	(1 - 10%)	2.0	(0 - 5%)	1.23	(0-7%)
Ca	2.0	0.7 - 3.1	2.86	(0 - 10%)	3.0	(0 - 10%)	1.62	(0-12%)
K	0.3	0.3	0.83	(0 - 4%)	1.0	(0 - 3%)	0.26	(0-4%)
Mg+Na	2.0	1.0 - 2.0	2.4 - 2.9	(3 - 10%)	-	-	-	-
S	0.8	0.1 -1.8	-	- -	-	-	-	-

Even with these poor data they conclude that real geochemical changes could be detected above the following limits: Si 2 - 6 wt%, Al 0.4 wt%, Fe 0.5 wt%, Ca 2 wt%, K 0.5 - 1.0 wt%. One example from Chapman *et al.* (1987), shown in Figure 2.8, demonstrates a relatively close tracking of core and GLT elemental estimates that may be obtained in a clastic reservoir with favourable hole conditions. In this case it is for a range of siliciclastic lithologies from the Conoco test well, Ponco City, Oklahoma.

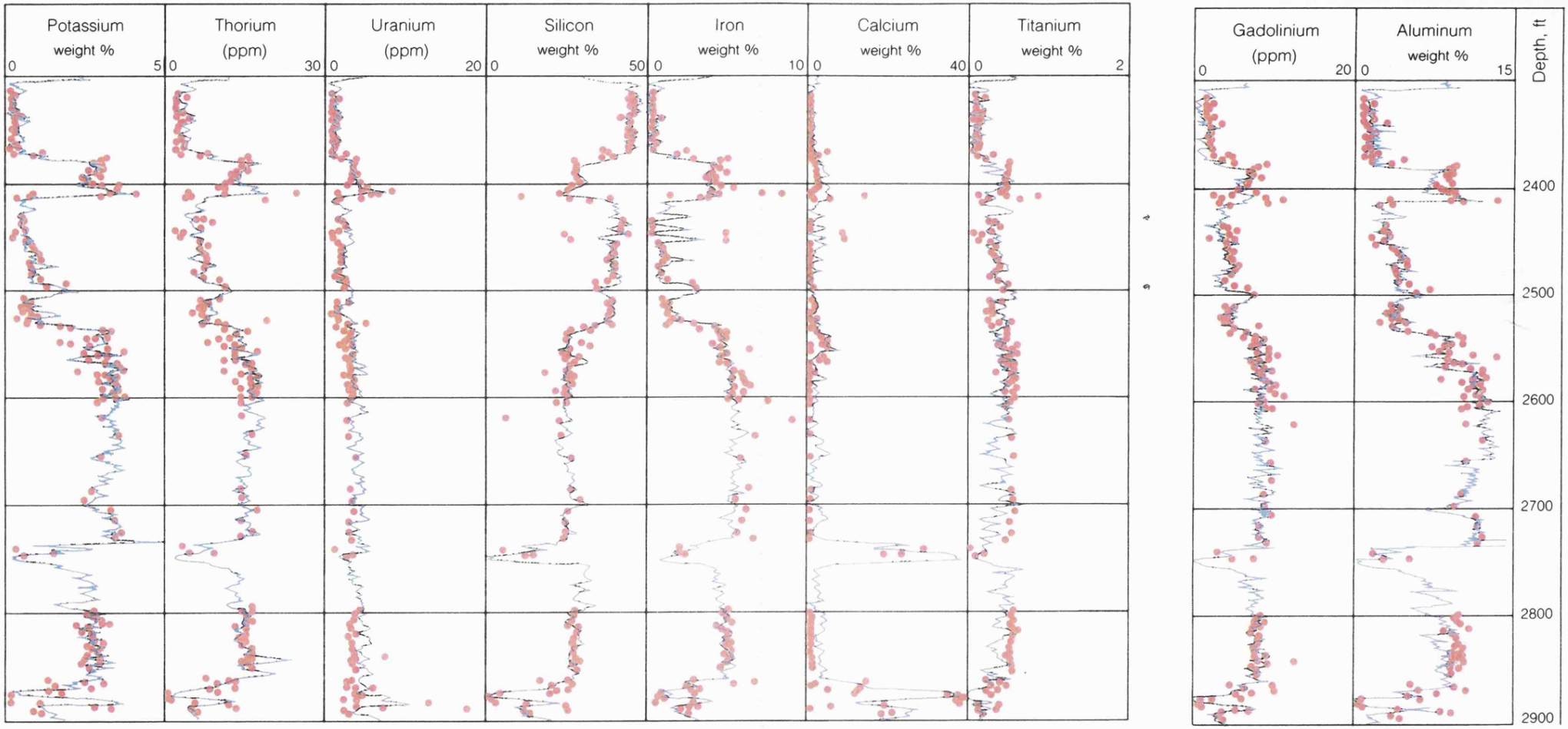

☐ *Elemental concentrations measured by instrumental neutron activation analysis on cores (dots) and by the geochemical tool string (solid lines) in the Conoco, Inc. test well in Ponca City, Oklahoma. From left, potassium, thorium, and uranium measured by the Natural Gamma-Ray Spectrometry (NGS) tool and core analysis; silicon, iron, calcium, titanium, and gadolinium measured by the Gamma-Ray Spectrometry (GST) tool and core analysis; aluminum measured by the Aluminum Activation Clay (AACT) tool and core analysis.*

Figure 2.8

2.6 Errors

Any attempt at the appraisal of a new technique must include identifying the source of potential errors. The potential sources of error in terms of the GLT tool can manifest as errors related to the *data acquisition* or as errors in *post acquisition processing*. In the data acquisition phase, the quality of gamma-ray signal in the borehole may be caused by poor count rates and detector resolution as well as poor signal-to-noise ratios caused by environmental effects. Post-acquisition spectral analysis and processing of GST data, will suffer as a result of such errors, in addition to possible signal contributions and interference effects from unmeasured elements which are likely to manifest as an incorrect spectral inversion and element re-partitioning. The geochemical oxide closure model will then suffer from erroneous input yields and any errors passed from independent measurement of K, Al and Mg+Na, as well as any oxide assumptions that do not hold true for the particular lithology being logged. In any assessment of the quality of GLT elemental data it is therefore important to gain as much of an insight into the magnitude or severity of such errors. This is demonstrated with *data acquisition* and post *acquisition errors* in Chapter 6.

2.7 Synopsis

It is hoped that this chapter has not just introduced the method of gathering elemental data in the logging environment, which as can be seen is a tortuous exercise. It also identifies certain aspects which may compromise, or improve, measurements. This is in addition to gaining an appreciation of the accuracy and precision, as we currently know it, of the tool. The study of elemental data from the GLT will now be left until Chapter 6 and in the meanwhile *well constrained* laboratory data will be used to introduce and independently evaluate mineral transform models developed to handle such elemental data as derived from the GLT.

Chapter 3.

Part 1. Mineral transform models

3.1 Introduction

The Geochemical Logging Tool (GLT) provides seven or more elemental concentrations, and when converted to oxide form, the problem posed is what approach is available to convert these data to useful, accurate estimates of mineralogy. In determining such an approach it is important to re-emphasise the distinction between the calculation of a *norm* and *mode*. The mode, as previously introduced, is the proportion of '*actual*' mineral phases occurring in a rock. This is what is required for this exercise. The norm is a hypothetical assemblage that may or may not be a true reflection of mineralogy, but is rather a scheme used for the distillation of elemental data into more useful 'groups' for subsequent comparison (classification). In the well constrained case the norm may approach the mode with considerable accuracy if a) the minerals to be subtracted match the mode, b) the mineral compositions vary significantly for each phase, and c) they remain correct.

This chapter is concerned with establishing several different approaches available for producing as accurate an estimate of the *mode* as possible (Part 1). A selection of different techniques (*models*) that attempt this transformation of element chemistry to modal mineral proportions are introduced here. These models have been developed with particular attention to their application to downhole geochemical measurements. As part of this development, models are critically compared and evaluated in this chapter using numerically produced samples and synthetic rock samples produced in the laboratory (Part 2). This allows a 'first stage' assessment of the usefulness of each model. The data are well constrained, with minimal or no measurement error to construe the relative performance of each model. A quantification of the limitations and inherent problems of individual techniques can therefore be attempted before more general application to *real* rocks (the 'second stage'), where the introduction of measurement errors, inhibit any *formal* evaluation. Models introduced here, in their current algorithms, have been used previously only in brief attempts to calculate modal mineralogy in sediments and basement rocks (Harvey *et al.*, 1990; Harvey & Lovell 1992). These attempts in the early stages of development, however, offer no formal or extensive evaluation of the performance of each model on laboratory or sediment data. An attempt is therefore made to evaluate these further in the sedimentary *reservoir* environment.

3.2 Assumptions for mineral modelling

Any attempt to accurately represent the bulk chemical composition of a rock in terms of an accurate assemblage of mineral and fluid phases is a complex problem. Indeed it is more complex than generating a subtractive *norm* which follow pre-defined rules.

Minerals have different habits and origins, such as well preserved *detrital* minerals, secondary *authigenic* minerals and leached detrital minerals. All may be present in one rock.

In addition to these minerals, fluids can be freely circulating in the connected pore space of a permeable rock, or bound within mineral structures. All of these are part of the *modal* mineralogy and should be considered in a calculation.

In consideration of the possible complexities of generating a continuous mineralogy from borehole measurements, some assumptions need to be made about the relationship between the bulk chemistry of a sample and its constituent phases. These include:

1) The first and the most important when attempting mineral modelling is the assumption that a linear relationship exists between the bulk geochemical composition of a sample and the mineral and fluid phases present in that sample. Total rock composition is assumed then to be related to mineral and fluid phases by the relationship:

$$c_i = \sum_{j=1}^{m} x_{ij} \cdot p_j \qquad j = 1, n. \qquad (..1)$$

Where $\mathbf{x_{ij}}$ is the weight percentage of the ith oxide in the jth constituent phase; $\mathbf{p_j}$ the proportion of the jth phase present in the mode, and $\mathbf{c_i}$ is the weight percentage of the ith oxide in the rock; **n** being the number of oxides analysed and **m** the number of phases present. The rock is considered to be made from no more than **m** mineral phases and the sum of minerals equals one. Thus:

$$\sum_{i=1}^{m} \mathbf{p_j} = 1. \qquad (..2)$$

A linear system may not fully exist, however, for every single sedimentary rock type encountered; at least in terms of total geochemistry measured by the geochemical logging tool. Examples of this include the metaliferous ores, such as galena (PbS), or uranium oxide deposits (uraninite - UO_2), where a large proportion of the bulk chemistry is composed of the elements that are not measured by the GLT tool.

Table 3.1 shows the average sedimentary rock composition in terms of the four dominant mineral groups (in sediments) and the typical abundance of each of the major elements. On average >99% of crustal rocks consist of the major elements which can be measured by the GLT tool (Table 3.1(b)). In addition a wide variety of sediments are dominated by only ten or so minerals (Table 3.1(a); Pettijohn, 1975; Blatt *et al.*, 1972); these effectively contribute all of a major element analysis. Together, these observations draw some validity to our assumption and make the task of mineral modelling seem more feasible. It at least provides an initial framework in which to begin mineral modelling. The ten most common minerals include quartz; the four clay minerals kaolinite, illite, chlorite and smectite; three end-member feldspars (k-feldspar, albite and anorthite); as well as two carbonates, calcite and dolomite.

2) A second assumption takes into account the lithological changes that occur through a sedimentary sequence. The assumption here is that the assemblage of *constituent* phases in a sample (the paragenesis), implicit in the first assumption, may vary between individual sample intervals in a borehole sequence.

3) A third assumption follows that the *composition* of each individual constituent mineral phase, even in two samples with identical mineral assemblages, may differ between each sample interval in a borehole sequence.

Table 3.1 (a)The average mineral composition of common sedimentary rocks, (after Blatt *et al.*, 1972; Pettijohn, 1975). (b) Typical major element composition of the earth's crust (weight percent & volume percent), from Carmichael, 1989.

(a)	Mineral	Sandstone	Shale	Carbonate
	quartz	65-70	20-30	0-5
	feldspar	10-25	5-20	0
	clay	5-10	50-60	0-5
	carbonate	0-5	0-10	95

(b)	Element	Wt%	Volume %
	O	46.40	94.04
	Si	28.15	0.88
	Al	8.23	0.48
	Na	2.36	1.11
	Ca	4.15	1.18
	Fe	5.63	0.49
	Mg	2.33	0.33
	K	2.09	1.49
	total	*99.34%*	*99.99%*

4) A fourth assumption is one of *error* in the geochemical analysis. Both systematic and random errors from geochemical measurements (the latter being especially a problem in nuclear logging tools, see Chapter 2) will propagate through to the modal analysis and final solution. This will have the effect of degrading the modal estimate or in extreme cases rendering it totally erroneous. In a similar fashion measurement error can also be expected in the mineral composition analysis. This is a subject discussed in the previous chapter and will be discussed again in the context of 'real' logging data.

To generate an accurate mineralogy within these constraints a model must treat each sample as a new problem requiring independent solution. While the basic assumptions may not hold true for *every* rock type measured, they will apply to the vast majority of sediments and it may be a matter of geological 'common sense' to exclude samples which do not conform.

3.2.1 Model parameterisation - setting up a transform model

Given the assumption that a linear relationship exists between total rock chemistry and the mineral/fluid phases present in a rock, they can be related by a set of physical parameters or *model parameters.* In this situation the *model parameters* will be the possible minerals and their compositions that may be found in the mode, denoted X_{ij} in Eqn. 1. The mineral transform problem is summarised in Figure 3.0. Initial elemental *yields* as measured by the GLT logging tool are processed through the oxide closure model to gain oxide estimates (Chapter 2). These are input as the *response logs* (called the input *response vectors*) for mineral modelling (denoted c_i in Eqn. 1). For each sample interval it is necessary to choose an appropriate mineral assemblage in addition to compositional values of each mineral (X_{ij}). These act as the input *model parameters* to the mineral model (called here, the *components matrix*). With the *response vector* and the *components matrix* known, the problem is then one

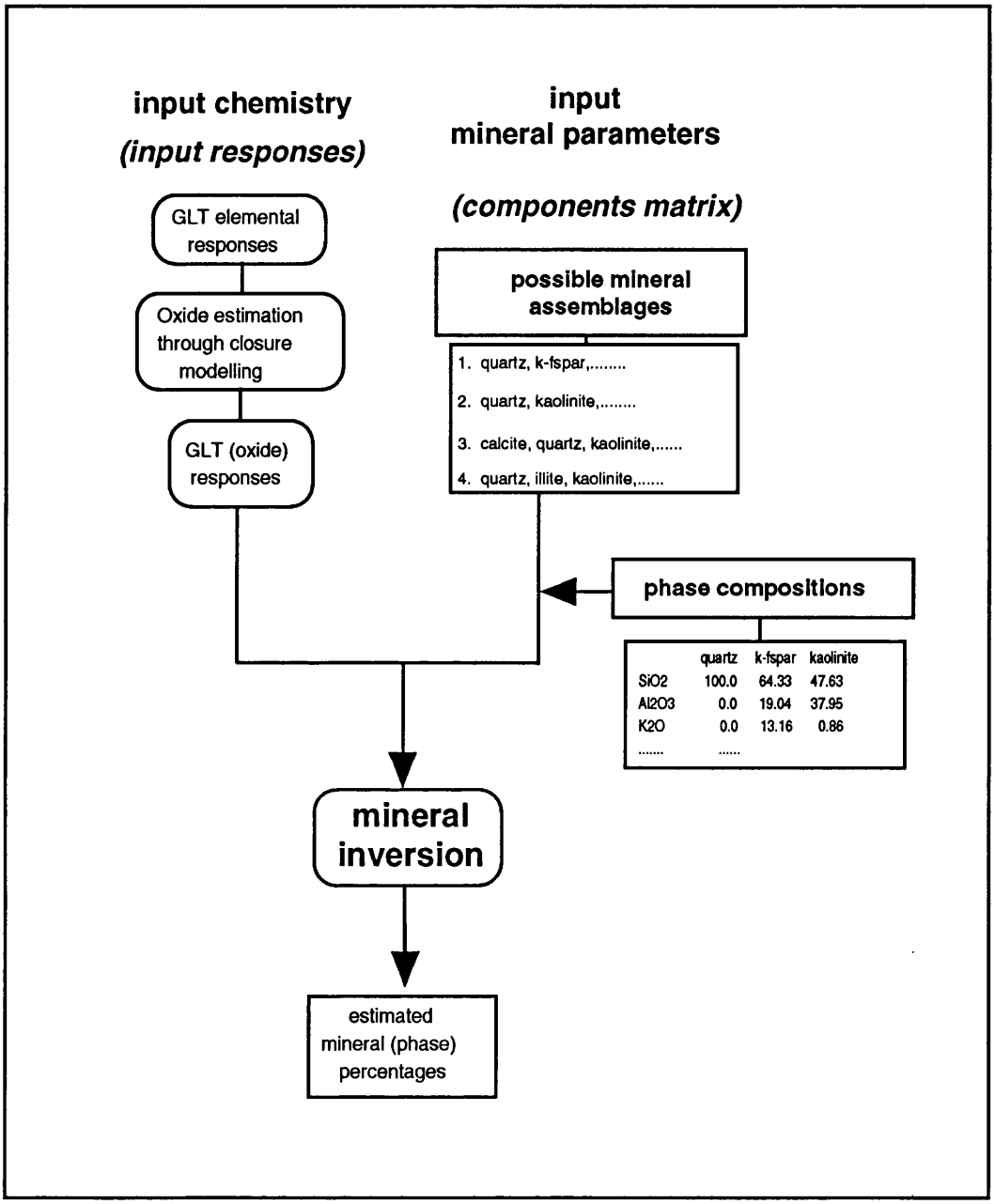

Figure 3.0 Flow diagram depicting the input parameters required for the mineral inversion process

of performing an *inversion*, using an algebraic procedure, to produce a mineral proportion in weight percent.

3.3 Models for mineral transformation

Various approaches to the calculation of an accurate mode have been investigated over the last twenty-five years. These have involved a plethora of algebraic procedures such as solution of sets of *simultaneous equations* (often by matrix inversion) (Marquardt, 1962; Perry, 1967; Bryan *et al.*, 1969; Wright & Doherty, 1970; Reid *et al.*, 1973; Albarede & Provost, 1977; Doveton, 1986); *Linear Programming* (Gass, 1975; Wright & Doherty, 1970; Banks, 1979; LeMaitre 1982; Walsh 1985); *constituent analysis* and *euclidian geometry* (Fuh, 1973) and *factor analysis* (Miesch, 1976; Klovan and Miesch, 1976; Full *et al.*, 1981 & 1982). Fortunately procedures such as the solution to simultaneous equations or Linear Programming can be easily manipulated in terms of matrices and therefore easily handled and coded on computer. In the context of sediments such techniques have previously been attempted by Pearson (1978), Miesch (1962), Gold *et al.* (1983), Kornder (1984) and Ehrlich and Full (1991), although none pertain to the borehole environment.

Having assumed the calculation of a mode as a linear problem, the basic limitation will be the number of oxides (input responses) available for modelling. This limitation, as seen commonly in conventional geophysical and log analysis inversion problems, means that the number of responses should at least match the number of unknowns (mineral proportions) and the system is *fully-determined.* In many instances this condition is not always met, the number of responses (oxides) being insufficient to provide a unique solution. The system is then *under-determined.* In contrast, if the number of responses is greater than unknowns the system is *over-determined.* The determinacy of the solution will predict the model or algebraic approach that may be taken in calculating the mode. In general, with eight available oxides (from the GLT tool), or more, and considering that the vast majority of sedimentary lithologies contain 5-10 mineral phases, models must be at least capable of handling fully and over-determined systems.

A selection of *models* aimed directly at transforming elements to minerals have been developed as computer algorithms. These are simply alternative algebraic procedures to the problem, each having individual features that are useful. Until now no particular transform has been deemed more superior. The evaluation of these techniques forms the basis for this study. The philosophy of each technique is now reviewed as a reasoning for its deployment.

Modelling is performed in oxide form, in preference to elemental form, as it offers a more geologically familiar way of handling geochemical data and the ultimate GLT tool output is in oxide weight percent. These *models* could, however be performed using *element* concentrations through appropriate conversion of oxides using the oxide factor in Table 2.4 (Section 2.3).

3.3.1 Basic linear algorithms (*fully-determined systems*).

If, as in Eqn. 1, we assume a linear relationship between the minerals present and their elemental compositions, then for a system with three minerals, each of which may be characterised by their concentration of *two* oxides, the proportions of the minerals necessary to satisfy a whole rock analysis are given more fully by:

$$p_1 \cdot X_{1,1} + p_2 \cdot X_{1,2} + p_3 \cdot X_{1,3} = c_1$$
$$p_1 \cdot X_{2,1} + p_2 \cdot X_{2,2} + p_3 \cdot X_{2,3} = c_2$$

to which may be added the 'geological' constraint that the proportions must sum to unity:

$$p_1 \cdot 1.0 + p_2 \cdot 1.0 + p_3 \cdot 1.0 = 1.0 \quad (c=3)$$

These three simultaneous equations may then be solved *directly* to yield *exact* solutions for the proportions, p_1, p_2, and p_3 (*direct solutions* involve the elimination of unknowns one by one, using *elementary* operations). Any error in the analysis (c1, c2), however will be passed directly to the derived proportions.

The more normal way of expressing these equations is in a matrix form:

$$\begin{bmatrix} X_{1,1} & X_{1,2} & X_{1,3} \\ X_{2,1} & X_{2,2} & X_{2,3} \\ 1.0 & 1.0 & 1.0 \end{bmatrix} \bullet \begin{bmatrix} p1 \\ p2 \\ p3 \end{bmatrix} = \begin{bmatrix} c1 \\ c2 \\ c3 \end{bmatrix}$$

or in conventional *matrix* format:

$$\mathbf{X\ p = c} \qquad \text{where } \mathbf{p} \text{ is the unknown vector.} \qquad (..3)$$

A solution can be obtained, in contrast to the *direct solution*, by the *inversion* of the matrix X and the multiplication with **c** will give the *indirect* solution to **p**:

$$\mathbf{p = X^{-1} \cdot c} \qquad (\mathbf{X^{-1}} \text{ being the inverse of X}) \qquad (..4)$$

Straight forward (indirect) *inversion* such as this will only work when the number of 'descriptive' oxides (in the response vector) equals the number of phases in the unknown vector, and the system is *fully-determined.*

Indirect inversion has been in use for some time in *log analysis* for the conversion of physical logs to lithological logs (Savre, 1963; Doveton, 1986; Marret and Kimminau, 1990). The physical *components matrix* (typical values of each tool response for a particular lithology) is set up and inverted once and simply multiplied with the response vector at each depth interval to yield the result. However, this approach requires that the mineral assemblage and compositions are the same at every interval and the small probability that equal numbers of oxides and minerals will always be present for an exact solution. Our previously discussed assumptions indicate that a different approach is, however, needed.

A plethora of *Direct inversion* methods also exist for solving the system of equations in Eqn. 3, of which Gaussian elimination is probably the most widely used (Forsythe & Moler,

1967). Although the computational details are not within the remit of this study, they offer a different, and often preferred, approach to the *indirect* solutions shown in Eqn. 4.

3.3.2 Error Minimisation (over-determined systems)

Fortunately, lithologies will often contain fewer mineral phases than available oxides and the system will be *over-determined* , with more knowns than unknowns. In this situation more equations will be defined and a large number of possible solutions available (Quirein, 1986, Harvey *et al.,* 1990). For example, where six oxides are measured on a sample containing three mineral phases, equations will appear as for a fully-determined system except there are now seven equations, instead of three, and a large number of possible solutions to **p** if the equations are taken three at a time.

One computational method, in this situation, is to attempt to match the composition of a rock sample, $\mathbf{c'_i}$, 'back' calculated from an estimated mineralogy, to the composition of the *actual* rock ($\mathbf{c_i}$) determined by the logging instrument. Success of the modal analysis can be defined by the misfits ($\mathbf{d_i}$) between the two:

$$\mathbf{c_{i'} - c_i = d_i} \qquad (..5)$$

The mathematical problem therefore to be solved in modal analysis is that of finding a solution - $\mathbf{p_j}$ of Eq. (1), which minimises the misfit ($\mathbf{d_i}$). The *proportions* ($\mathbf{p_j}$) of three minerals are determined by direct or indirect inversion and estimates of the composition vector (**c**) calculated from three equations at a time. These are compared with the original values in **c** and good estimates of **p** accepted if the difference between the calculated vector (**c'**) and measured vector (**c**) is small. The most common method of this *Error Minimisation* approach employs a Least Squares solution (Wright & Doherty 1970; Reid 1973, Bjerhammar 1973). This approach aims to estimate **p** in such a way that **e** is minimised, where **e** is the sum of the squares of the differences between **c'** and **c,** and in matrix format is defined by:

$$\mathbf{e = (c' - c)^T \ (c' - c)} \qquad \text{(T denotes a transpose)} \qquad (..6)$$

The best fit values of **p** are chosen in such way that the difference between **c** and **c'** is as small as possible. The Least Squares solution for **p** is :

$$\mathbf{p = (X^T . X)^{-1} . X^T . c} \qquad \text{(T denotes a transpose)} \qquad (..7)$$

One *indirect inversion* method and three *direct* methods were deployed for evaluation in this study; these include *Gaussian Elimination* (most commonly used), *Choleski decomposition* (for computational *speed*), *Gauss-Jordan* direct solutions (advantageous in *sparse* matrices). They are included, simply, as alternatives on-a-theme. Details of these techniques can be found in Forsythe & Moler (1967) and Fox (1964).

3.3.2.1 Weighted Least Squares model

An addition to the previous model allows weights of uncertainty to be applied to the input response vector (**c**). These weights (**w**) can be implemented, for example, if uncertainties in measurement of a particular response are known. In the context of the geochemical measurements from the GLT, the inverse elemental precisions, calculated from calibrated tool measurement variances, may be used as weights (Herron & Herron, 1990, Van Den Oord, 1990); refer to Section 2.5.1.

Using the first example, a weighted model would be defined, where weights associated with each response are w_i , and n the total number of responses, as:

$$\begin{aligned} p_1 \cdot X_{1,1} + p_2 \cdot X_{1,2} + p_3 \cdot X_{1,3} &= w_1 C_1 \\ p_1 \cdot X_{2,1} + p_2 \cdot X_{2,2} + p_3 \cdot X_{2,3} &= w_2 C_2 \\ p_1 \cdot 1.0 + p_2 \cdot 1.0 + p_3 \cdot 1.0 &= w_n 1.0 \end{aligned}$$

The weighted Least Squares solution in matrix form is then

$$\mathbf{p} = (\mathbf{X}^t \mathbf{w} \mathbf{X})^{-1} \cdot \mathbf{X}^t \cdot \mathbf{w} \cdot \mathbf{c} \qquad (..8)$$

Where **W** = Diagonal matrix of elements, (with elements of the weight vector in the main diagonal).

3.3.3 Potential problems with Least Squares - Error Minimisation models

When modelling minerals, error in any analysis is most likely to be in the *response vector* and an explicit solution can be readily sought without validation of the linearity assumption from Section 3.2. In the area of conventional field geophysics there is often a degree of experimental error in the *components matrix* as well, which can cause the linearity of the model to break down. This is usually not a problem with mineral transforms since compositions, in general, are better constrained than field geophysical measurements. Extensions to the Least Squares methods can be implemented which take into account the uncertainty of all the derived coefficients in both constrained and unconstrained systems. This is often by way of calculating bounding errors for all model parameters *postiori*, to ascertain where doubtful data exists. An attempt to apply this approach to petrologic problems has been made using *maximum-likelihood minimisation* (Albarede & Provost, 1976) and in more conventional geophysics - such as iterative *Most-Squares* solutions, a modification of a Least Squares solution (refer to Marquardt, 1970; Jackson, 1976; Meju & Hutton, 1992; Meju, 1992). For general mineral modelling purposes it is not considered necessary at this stage.

One problem with Least Squares solutions is that derived mineral proportions can either be positive or negative, with the constraint of unity still in place. In the context of a modal analysis a negative mineral estimate is a physical impossibility and such a solution therefore meaningless. This could arise from errors in the response vector (rock analysis) but usually results from the use of an incorrect mineral assemblage, or incorrect choice of mineral composition.

This is demonstrated using an example where silica (SiO2) and alumina (Al2O3) exist in terms of two minerals - quartz (100% [SiO2]) and Kyanite (represented as 50% [SiO2] & 50% [Al2O3] *brackets notate molecular proportions*). Figure 3.1 shows the region of acceptable (the stippled region) and impossible solution for this system (after Harvey *et al.*, 1990). The stippled region represents the unconstrained solution. With a summation to unity constraint implied, a *modelled* analysis must lie on the line XY (a constrained solution). Acceptable results occur between X and K, with negative, meaningless values for quartz between Y and K. Changing the composition of an end-member will move this point. If the sample is incompatible it can move completely into the negative region rendering a useless solution. In a multivariate system with six or more oxides, the line XY becomes a hyper-plane and adding or removing minerals will totally alter the position of such a plane. Unfortunately with a Least Squares solution there is no way to prevent negative values.

3.3.4 Linear Programming - Optimisation transform models.

This method is intended as an alternative method primarily to overcome the negative phase proportions commonly predicted in Least Squares methods. Wright & Doherty (1970) suggested the use of Linear Programming as a *primary stage* in selecting a paragenesis for eventual solution by Least Squares methods. However, Banks (1979) advocates the use of Linear Programming as a stand-alone method for modal estimation. Stochastic approaches have also been proposed (Vajda, 1961), but are not considered here.

Linear Programming itself is designed to solve in an *under-determined* system. Such an under-determined system can have an infinite number of solutions. Linear Programming, however, uses a set of implied *constraints* to limit the number of solutions, and a solution is chosen that maximises (or minimises) some specified *objective function*. This is compatible with mineral modelling as the objective function, and in this sense, can be used to maximise the proportion of modal minerals estimated. The constraints implied are that the oxides used to make the mineral proportions do not exceed the total amount available in the original analysis, and mineral proportions cannot become negative or in turn collectively exceed unity. The definition of the *objective function* to be maximised is then:

$$z = p_1 + p_2 + p_3, \ldots\ldots, p_m$$

with the constraints :

$$\begin{aligned}
p_1 \cdot X_{1,1} &+ p_2 \cdot X_{1,2} + \ldots + p_m X_{1,m} \geq c_1 \\
p_1 \cdot X_{2,1} &+ p_2 \cdot X_{2,2} + \ldots + p_m \cdot X_{2,m} \geq c_2 \\
&\ldots\ldots\ldots\ldots\ldots\ldots\ldots\ldots\ldots\ldots \\
&\ldots\ldots\ldots\ldots\ldots\ldots\ldots\ldots\ldots\ldots \\
p_1 \cdot X_{n,1} &+ p_2 \cdot X_{n,2} + \ldots + p_m \cdot X_{n,m} \leq c_n
\end{aligned}$$

with the *closure* constraint:

$$\sum_{i=1}^{m} p_j \leq 1.$$

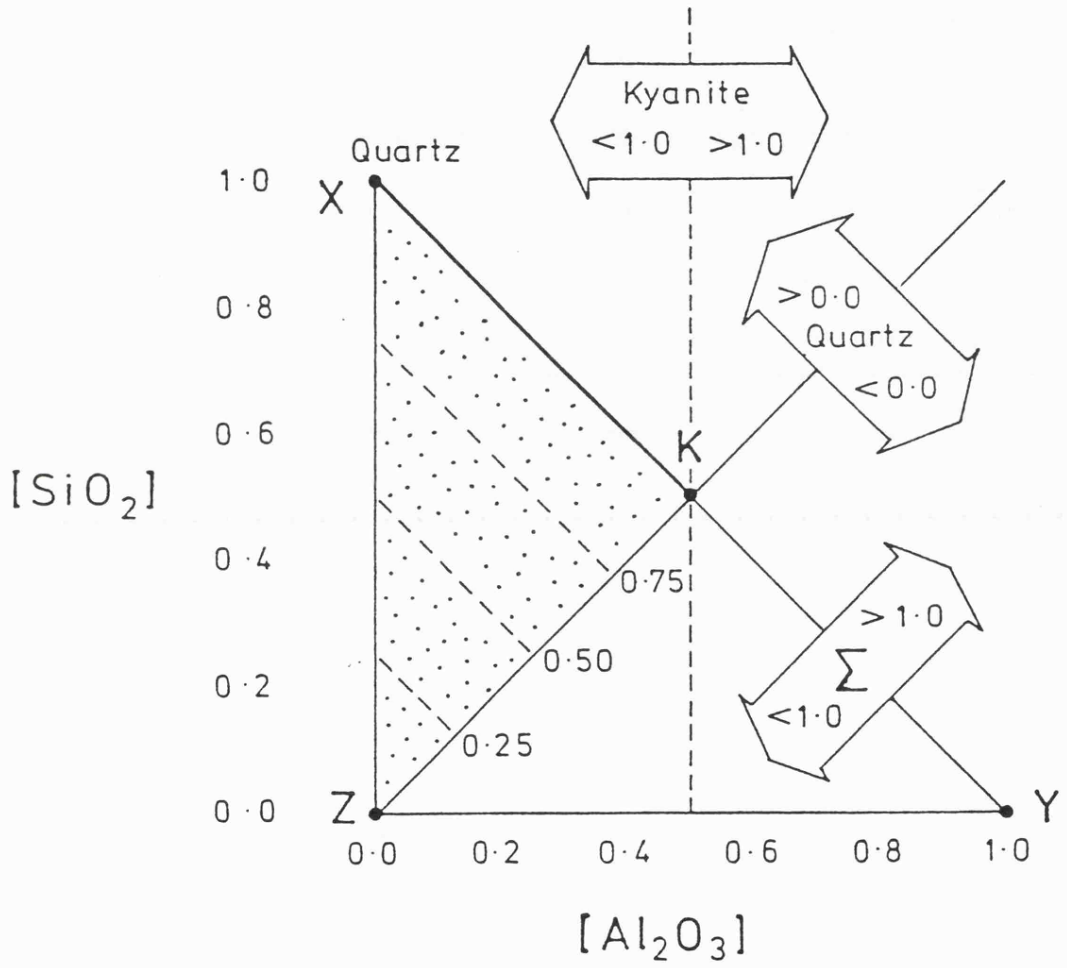

Figure 3.1 Regions of acceptable and impossible solutions for a simple system where only silica and alumina are present. See text for full explanation. Kyanite plots at point K. Possible solutions may occur within the stipled region.Sigma is the sum of the normative quartz plus kyanite. Contours within the stippled region are sigmas of 0.25, 0.5 and 0.75 Brackets infer molecular proportions (not wt%) (from Harvey *et. al.*, 1990).

and: $$\sum_{i=1}^{m} p_j \geq 0.$$

where individual mineral proportions (p_j) themselves: $p_j \geq 0$

In this sense the constraints do not allow negative assemblages to occur as p_j is constrained to be positive, and whilst the sum of the mineral proportions is maximised, it can not exceed unity. Other constraints can be added to the model, a useful one being to ensure a constant ratio of a number oxides between coexisting minerals (Harvey & Lovell, 1992).

In a model, if a mineral does not fit, it is simply determined as a zero proportion. Any residual chemistry not used in the solution (d_i in Eq. (5)), while by definition of the objective function this is minimised, allows a useful direct measure of the effectiveness of the solution. It may be helpful in determining where errors may lie in mineral choice, compositional choice or not so easily, error in input response measurements. One problem, however, with this model is that there is no way of incorporating any uncertainties in the components matrix or of weighting input responses, although it is reported possible (Harbaugh & Bonham-Carter, 1981). Linear Programming can be performed in a variety of ways of which the *Simplex* algorithm is most commonly used (Walsh, 1985). This algorithm is employed in this study.

3.3.5 Euclidian Distance model

An alternative technique applies a different approach to the estimation of modal mineralogy - one used conventionally in metamorphic petrology; and which employs the principle of *constituent analysis* (Fuh, 1973). In essence, this algorithm treats the *input chemistry* (response vector) in terms of the normalised Euclidian distances between mineral phases (end-members) present in the *components matrix* and therefore takes advantage of the multi-dimensional geometry inherent in the components matrix. Figure 3.2 best explains the methodology of this technique. Taking the system quartz (SiO2), sillimanite (Al_2SiO_5) and k-feldspar ($KAlSi_3O_8$), with ideal compositions, they can be represented in a three dimensional compositional space (simplex) defined by the axes: SiO2, K2O and Al2O3 (Figure 3.2). A rock composed of these three minerals (point +) will lie on the plane that contains these minerals, and at the same time within the two dimensional *compositional triangle* defined by them. In terms of the minerals quartz-sillimanite-k-feldspar (qsk), acting as the apices of this two dimensional triangle, the composition of the rock (+) is directly related to the normalised Euclidian distances between itself and these apices. Samples which lie outside of this compositional simplex will produce negative results. For example, if there was sufficient silica to form sillimanite and k-feldspar but not enough remaining to produce quartz, then the sample would plot outside the compositional triangle (qsk) beyond the s-k join, away from the q corner. A solution from this composition based on these three minerals would therefore give a negative quartz abundance.

Although it is hard to illustrate, (although much easier in mathematical (matrix) form) this can be extended from the three dimensional space, illustrated here, to multi-component

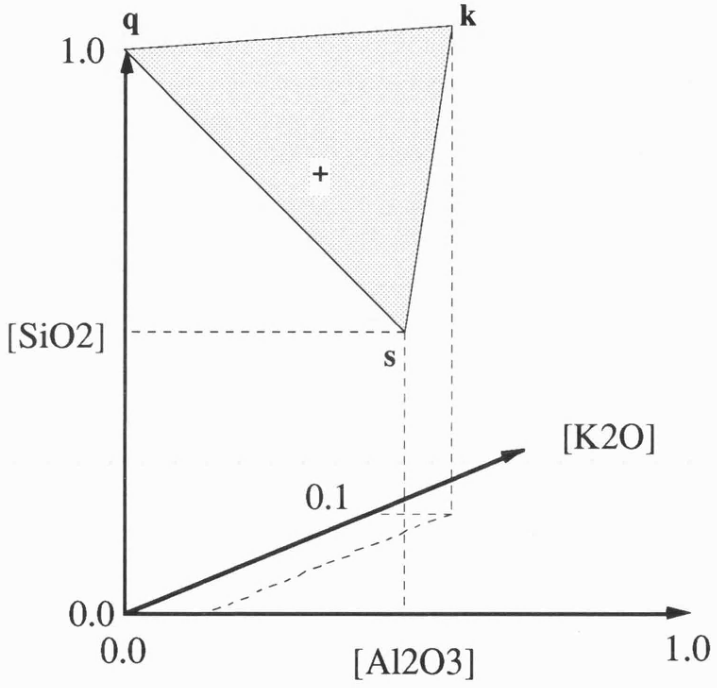

Figure 3.2 Geometric distance relationships within the system [SiO2] - [Al2O3] - [K2O]. q:quartz,s: sillimanite, k: potash-feldspar. Axes are in molecular proportions. (after Harvey and Lovell, 1992).

systems involving a hyper-polygonal space. Such a system is the *components matrix* from our transform model. The model algorithm used here allows up to the same number of minerals as oxide components (fully and over-determined systems) and the constraint implied, as in other models, is that the sum of the derived mineral proportions does not exceed unity. In computational terms, the chemical analysis (response vector) is input within the multidimensional geometry of the components matrix and the Euclidian distances calculated between the end-member minerals and the analysis. Appropriate mineral proportions are then calculated from the resulting geometry.

In a similar sense to Least Squares solutions, negative mineral proportions are possible from this model. Typically this occurs when wrong minerals are present, when minerals are compositionally similar, or as a result of measurement error in the response vector.

3.4 A summary of transform models

Error Minimisation and Euclidian Distance models both have the disadvantage that they can derive negative mineral proportions. On the other hand, negative phases do draw the attention to a problematical solution which can then be investigated. Both models have the slight advantage that they contravene the assumption that there is no error in the analysis; and in the *weighted* form, Least Squares models allow *apriori* estimates of uncertainty to influence the solution. Whilst having the advantage of being constrained not to derive negative proportions, the Linear Programming, Simplex algorithm employed here does assume an input analysis to be correct. Meanwhile residual estimates (d_i) from Linear Programming are useful as a *direct* measure of excess chemistry. This is advantageous, as it provides a good measure of the success of the solution and also indicates where errors lie; for example, in the choice of the mineral assemblage or individual mineral composition.

Having considered the strategy of each transform model, it is worth elaborating on the subtractive *norm* procedure as a contrast to these models. In the normative approach, fractions of chemistry in the form of minerals are subtracted successively from the original analysis until the entire analysis is 'exhausted'. For example, if apatite ($Ca(PO_4)_3F$) is to occur in the norm then the percentage of normative apatite becomes a function of P_2O_5 and a corresponding stoichiometric amount of Ca subtracted; P_2O_5 is then set to zero. In this way a set of pre-defined minerals are in turn removed in a 'hierarchical' order until no chemistry remains. The rules determining such an order must allow procedures, such as the partitioning of certain elements, like Fe and Mg, between coexisting phases. As stated previously, there is a wide initial choice of minerals which could be selected for inclusion in a calculation. In a ridged scheme the minerals chosen will, to some extent, be determined by the rules chosen. The main problem lies in the order in which minerals are removed. For igneous rocks this may be straight forward, but for sediments, (which are not necessarily in equilibrium), it becomes considerably more difficult. There is also no room for error in the chemical analysis and such error will be passed to the resultant *norm*. Data produced from subtractive procedures, however, will either be positive or zero even from under-determined systems.

Originally intended as a useful distillation of elemental data for classification, some 'tailor made' schemes, involving actual analyses, such as Niggli's norms (Burri, 1964), do in a very constrained situation allow the *norm* to be compared with the *mode* in igneous/metamorphic rocks. They do, however, prove unfeasible for large volumes of logging data as they are almost impossible to code in a completely general way in sediments (P. Harvey *pers. comm.* 1992).

3.4.1 Ten mineral normative and modal transformation model

A model developed by Herron and Herron (1990) use both subtractive-normative and modal methods in an attempt to determine the ten most common minerals in sediments from GLT data (termed *chem-minerals*). Their model involves three normative steps that assume pyrite, illite, and siderite are present, if the appropriate chemistry is available. The first normative stage involves the calculation of excess S, after S is used to calculate pyrite. A second stage involves the calculation of excess Fe, after subtraction for pyrite, to estimate the abundance of illite, and the corresponding stoichiometric proportions of K2O, Al2O3 and SiO2 are subtracted. Any excess Fe is taken to be siderite. Thirdly, a calculation to remove minerals with bound water (clay minerals) is included. Finally, the determination of mineral abundances of seven or eight other 'pre-defined' minerals is achieved by the solving of 9 or 10 simultaneous equations which relate the remaining chemistry from the GLT tool to mineral abundance.

These normative minerals will agree with the mode if two assumptions are valid (Herron, 1986). The first assumes a constant chemical composition for each mineral and that each mineral is chemically distinct from the rest. The second assumption is that all minerals residing in the formation will be present in the model. Problems with using this model to predict accurate mineralogy lie with these two assumptions. Mineral compositions of the ten defined minerals in reality can and do vary. Herron uses the average composition of mineral families, ie, for feldspars, a mix of k feldspar, albite and anorthite is taken (Al 10%, Si 30% and Ca 1% (Na is not determined). Providing the elemental input data is accurate, and the algorithm to compute excess Fe is correct the most common problem lies with the second assumption - the choice of minerals. Formations may contain minerals which are absent (due to mis-identification) from the model, and yet still contribute to the total element chemistry. For example, if chlorite was not recognised although present in an analysis, its chemistry would appear as a combination of kaolinite, illite and siderite. In this respect there is no room for the possibility of residual chemistry from minor phases or an error in the analysis. Another problem is with the large influence of the excess Fe calculation. If less Fe is attributed to siderite, then more illite will be calculated (Van den Oord, 1990). Small changes in the calculated percentage of excess siderite will result in large changes in the calculated amount of illite. These problems are recognised by Herron (1990) who advocates that this normative sequence be used as a *start* and minerals be replaced which are appropriate to the local regional geology. This demonstrates, itself, the lack of a completely general approach.

In a similar fashion Harvey *et al.*.(in press) use this approach to remove the minor oxides - TiO2, BaO, ZrO2, P2O5 and S, which are assumed each to lie *exclusively* in minor mineral phases. The advantage of this procedure is to reduce the sparseness introduced to the components matrix, which occurs when a large number of single-oxide, exclusive phases are present. Each of these oxides is removed by subtracting the ideal stoichiometric compositions of the common minerals rutile, barite, zircon, apatite, and pyrite, respectively. This leaves the remaining oxides to be input in to a modal transform model.

Herrons normative model does not strictly adhere to the assumptions defined at the beginning of the chapter and as a part consequence suffers the problems just discussed. For the purposes of estimating an accurate mode this procedure is not considered further.

3.5 Measurement of errors and assessment of models

It is imperative when examining estimates of mineralogy derived from a mineral model to have an idea of the measure of the quality of the solution, or an *estimate of error*. No true statistic, it seems, is present that serves to provide a discrete 'error log' for all the mineral models described. A number of error estimates are partially successful in achieving this goal, especially when combined.

Assessment of error in a modal analysis can either be based on (1) the derived mineral proportions (p_i), or (2) comparison of the difference (d_i) between the original analysis (response vector) c_i and the estimated vector c_i', commonly termed the *error vector* (e).

Two common statistics exist that are based on the mineral proportions:

(1) Proportional Variance (*Pvar*) is related to the maximum entropy (variance) in the system and is defined as

$$Pvar = \frac{m}{m-1}\left(1-\sum_{i=1}^{i=m} p(i)^2\right). \qquad (..9)$$

Where m is the number of minerals and P(i) the derived mineral proportions. Pvar will vary between 0 and 1. Larger estimates of Pvar indicate greater variance and will equal one at maximum variance, this is when equal mineral proportions are present. This statistic is useful in under-determined systems (Doveton, 1986) but is considered in the context of over-determined systems with less reverence.

(2) The Absolute Sum Error (*ASE*), can be useful for exact or fully-determined systems where it indicates the presence of negative proportions. It is defined as:

$$ASE = \left(\sum_{i=1}^{i=m}|p_i|\right)-1 \qquad (..10)$$

Small values of ASE may suggest minor measurement error while large values suggest gross measurement errors, or more commonly, an incorrect mineral assemblage.

In a similar way the negative sum error (NSE), the sum of all negative proportions (p_i), while having no true statistical significance, can be of equal use in over-determined systems

(Error Minimisation and Euclidian Distance models) where negatives can be common. Another error estimate (also lacking any true statistical significance) is the Sum of Proportions (p_i) (SUMP). In a constrained system such as Error Minimisation, SUMP will equal one; however deviations from unity indicate an unstable solution. This is useful for Linear Programming which although constrained not to exceed unity or become negative can vary between the two values. A measure of SUMP in terms of percentages, called *P%acc*, is used in this study.

Perhaps more useful quantitative measures of error are estimates that involve the error vector (e). There are two common estimates which indicate a general measure of fit and can be applied to mineral modelling. These are the Standard Error of the Estimate (SE) and the Mean Absolute Deviation (Mad). From the error vector calculated in Eqn (6) Standard Error is computed, where n is the number of oxides, m the number of minerals and e_j the difference between c_i and c_i' for oxide j :

$$SE = \sqrt{\frac{\sum_{j=1}^{j=n} e_j^2}{(n-m)-1}} \qquad (..11)$$

In terms of geochemical fit, SE is most appropriate for Error Minimisation and Euclidian Distance models and can viewed in terms of units of standard deviation of the chemistry, as estimates of the error vector can be positive or negative. It varies from zero (a perfect fit, ie, $d_i = 0$) upwards, but experience with mineral modelling suggests values greater than 1-1.5 imply a poor fit and inevitably a poor solution. It must be noted that a perfect fit, (zero Standard Error value), although impractical in reality due to measurement and rounding errors, does not necessarily imply a correct *derived* mineralogy, simply a good fit. SE is not a meaningful error for Linear Programming due to the constraint imposed that the residual vector can not be negative (ie, c_i' can not exceed c_i).

Mean absolute deviation (Mad) is a similar statistic to SE but is more meaningful and appropriate for optimisation methods (Linear Programming). It is defined as the absolute sum of the error vector divided by the number of variables (**n**), such that:

$$Mad = \frac{\sum_{j=1}^{j=n} |e_j|}{n} \qquad (..12)$$

Mad offers an almost equivalent measure to SE for comparing Linear Programming with Error Minimisation and Euclidian Distance models. Mad does have the advantage that it can be computed for all models, but values must be compared between models with caution.

As an example of the use of these errors in evaluation of a models solution, Table 3.2 demonstrates two sets of calculated chemistry (c_i') for a modelled gabbroic rock (from Harvey *et al.*, 1990). c_i' in column 2 is from an Error Minimisation model , and c_i' in column 4 from a Linear Programming model. The observed chemistry (c_i) from the input response vector is shown in column one. The difference (d_i) is shown for each solution in columns 3 and 5. For

the Error Minimisation model differences are both negative and positive (column 3) and Se therefore has some statistical significance.

Table 3.2 Example gabbro solution illustrating the different errors calculated for the Least squares - Error Minimisation and Linear Programming models. See Text.

		Error Minimisation		Linear programming	
	observed(c_i)	**calc (c_i')**	**diff (d_i)**	**calc (c_i')**	**diff (d_i)**
	1	2	3	4	5
SiO2	46.55	46.53	-0.019	45.31	1.237
Al2O3	18.93	18.96	0.025	18.93	0.000
TiO2	1.46	1.46	0.002	1.46	0.000
Fe2O3	10.64	10.67	0.028	10.73	0.000
MgO	8.89	8.93	0.041	8.89	0.000
CaO	10.77	10.84	0.070	10.77	0.000
Na2O	2.31	2.51	0.198	2.31	0.000
K2O	0.28	0.00	-0.280	0.00	0.280
MnO	0.080	-0.080	-0.080	0.00	0.080
SE		0.083		-	
Mad		0.182		0.177	
P%acc		-		98.40	

The differences (d_i) from Linear Programming (column 5, *compare both K20 values*) are all positive (as the result of the constraint of the method) and Se therefore meaningless. Mad can be calculated for both solutions as a comparative measure. In absolute terms, Mad is not as meaningful for the Error Minimisation model because negatives, as in this example, are often present. P%acc (SUMP) is very high indicating that a lot of the chemistry has been used in the models solution.

It can be seen that there are a number of errors that can be used to assess the quality of a mineral model, but no clear single statistic that can be broadly used. In summary, for fully-determined inversion models, as well as over-determined Error Minimisation and Euclidian Distance models, SE is very useful in assessing the geochemical fit of the data, and NSE important as an indication of negative phase proportions.

For optimisation models, Mad allows a similar measure with which to compare other models and P%acc (or SUMP) provides a very useful measure of residual or 'unused' chemistry. Table 3.3 summarises the available estimates of error and their application to the transform models.

3.6 Validation of a mineral model

Perhaps the single largest problem common to all proposed mineral transform models is that of validation of the solution. Rejection may be obvious due to negative mineral proportions (an impossibility in reality) and an appropriate measure of error used to detect this, ie, *NSE* or *ASE*. Rejection may also be obvious from a geologically 'silly' or meaningless solution and can be discarded. It is almost impossible, or at least very hard, to validate the accuracy of a *reasonable* solution directly during routine processing. Yet, we must have some idea of the severity of any problems that might arise from modelling a particular assemblage and recognise these at an early stage in processing.

Any evaluation procedure must involve comparing the *model derived mineralogy* with a value derived from independent physical measurements on the sample. Similarly, comparison of the differences between a chemical analysis, *'back calculated'* from the derived estimate of the mode, with the initial chemical analysis will assist in validation.

Table 3.3 Summary table of available estimates of error for mineral modelling and their application to appropriate models

Error Estimate	PVAR	ASE	SUMP (P%acc)	NSE	SE	Mad
	Proportional variance	Absolute Sum Error	Sum of Proportions	Negative Sum Error	Standard Error of the Estimate	Mean Absolute Deviation
Mathematical Determinacy	Under determined	Fully determined	All	All	Fully & Over determined	Fully & Over determined
Range of values	0 - 1 Possible negatives	0 unless negative	0 - 1 1 if proportions equal unity	0 unless negative	0 upwards zero = perfect >1.5 poor	0 upwards zero = perfect
Model most suitable for	none	Exact inversion model	Linear Programming	Error Min. & Euclidian Dist models.	Error Min. & Euclidian Dist models.	Error Min. & Euclidian Dist models., Lin. Prog. models
Comments			Useful for assessing residual chemistry	Useful for assessing erroneous solutions	Good measure of geochemical fit. Seen in terms of a Standard Dev.	Comparison of Lin. Prog to other models. More meaningful for Lin. Prog.

Physical methods readily available for the analysis of a *mode* (on core samples) include whole-rock or orientated X-ray diffraction (XRD), thin-section point counting and infra-red spectroscopy (MINERALOG[1]). Unfortunately these techniques are often neither precise or accurate enough for *absolute* verification of the mode, especially at low concentrations. There also exists a difference in sample volume of typical core and GLT derived elemental measurements (or *geostatistical support*; Clark, (1984)) which may seriously complicate any comparison. These factors must be considered in any comparative exercise (refer to Sections 2.5.1 and Chapter 6, 6.7.1). Physically derived modal estimates provide, however, as close as possible an estimate (in the absence of any other procedure), in which to validate a solution and through necessity they are deployed, *with caution*, in this study.

---

[1] Trade mark of Corelabs Inc.

Chapter 3, Part 2.

Laboratory assessment of mineral transform models

3.7 Introduction

For the reasons outlined in Section 3.6 the initial evaluation stages of the relative performance of transform models, demonstrated next, have been undertaken on 'numerically' produced rocks - rock analyses synthesised by mixing together the compositions of a number of minerals. This allows no error in the analysis and provides a strict validation that each model actually works.

A second procedure adopted is to crush and analyse pure minerals and make up a series of *synthetic 'rocks'* by mixing together known amounts of the minerals in the laboratory. All parameters, including the *mode*, are known to within the laboratory analytical, weighing and mixing errors. In this way the evaluation of each transform model is free of any bias or inaccuracy of tool measurement while remaining realistic. The rest of this chapter is devoted to using this synthetic data set to evaluate the behaviour of these different transform models and establish the problems associated with element to mineral transformation in sediments.

3.7.1 Behaviour of algorithms: numerical modelling of the synthetic data-set

Knowing the XRF derived chemical analysis of each mineral and the proportion of each mineral mixed in the synthetic rock it is possible to 'back-calculate' a rock analysis numerically. Computed analysis for the synthetic rocks were used here in the 'numerical' modelling exercise as the *input response vector*. Eleven oxides were modelled, including SiO2, TiO2, Al2O3, Fe2O3, MgO, CaO, Na2O, K2O MnO, P2O5 and S. The system is therefore *over-determined* (as there are between 2 and 6 minerals to solve) and all models can be evaluated. Two decimal places have been kept throughout to assist evaluation, although this level of accuracy is never expected to be seen in a normal modal analysis. Standard Error and Mean (absolute) deviation of the residuals are quoted as comparative measures of geochemical fit, as is P%acc, for the Linear Programming solution. The actual or 'target' mineralogy is quoted in the results as a direct measure of accuracy and for validation of the correct mineral assemblage.

3.7.1.1 Results of numerical modelling

Table 3.4 shows the estimated mineral proportions from all models for synthetic 'pelite' and 'arenite'. Transform models employed include three Error Minimisation models (an *indirect* 'inversion' solution and two *direct* solutions), Linear Programming and the Euclidian Distance models. Table 3.4 demonstrates the accuracy in estimation of the mineral proportions by all models. Standard Error is negligible and is due only to rounding in computation. This exercise demonstrates that the five different models being evaluated, under ideal conditions, solve perfectly.

Table 3.4 Modelling performed on numerically produced 'arenite' and 'semi pelite' rocks to demonstrate estimation of mineral proportions by different mineral transform techniques.
Key for tables: **Target** - Target mineral proportions, **Lsq-INV** -Least Squares (indirect) model, **Lsq-Chol** - Least Squares (direct) Choleski model, **Lsq-Gj** -Least Squares (direct) Gauss-Jordan model, **LP** - Linear Programming, **Euc** - Euclidian Distance model. **SE** -Standard Error of the chemical fit, **Mad** -mean (absolute) difference of the residuals, P%acc - Percent of chemistry accounted for.

Arenite	**Target**	**Lsq-INV**	**Lsq-GJ**	**Lsq-chol**	**LP**	**Euc**
quartz	80.00	80.01	80.01	80.01	80.16	80.01
muscovite	10.00	10.03	10.03	10.03	10.10	10.00
K-feldspar	5.0	4.97	4.97	4.96	4.76	4.96
dolomite	2.50	2.50	2.50	2.50	2.50	2.50
calcite	2.50	2.50	2.50	2.50	2.51	2.50
SE		0.003	0.003	0.003	-	0.003
Mad		0.002	0.002	0.002	0.00	0.002
P%acc		-	-	-	99.97	-
Semi Pelite						
albite	15.00	15.00	15.00	15.00	14.85	15.00
kaolinite	15.00	15.05	15.04	15.04	15.09	15.03
quartz	40.00	39.97	39.97	39.97	39.20	39.97
k-feldspar	15.00	15.09	15.09	15.08	15.12	15.08
muscovite	10.00	9.91	9.91	9.91	10.06	9.91
dolomite	5.00	5.01	5.01	5.01	5.24	5.00
SE		0.005	0.003	0.003	-	0.005
Mad		0.003	0.002	0.002	0.005	0.002
P%acc		-	-	-	100.00	

3.7.2 The production of synthetically produced rocks in the laboratory

Six 'rock' mixtures have been produced in the laboratory by mixing together pure minerals in proportions that span the range of the most common argillaceous-arenaceous-carbonate sedimentary rocks. These six 'rocks' include a 'shale/pelite', a 'semi pelite', a pure 'arenite', a 'carbonate' (calcite-dolomite mix) and two mixes of minerals that are *compositionally colinear*. These are referred to as Mix 1 and Mix 2. Compositions of the synthetic rocks were taken from average values for sediments quoted in Carmichael (1989; p 105) and are given in Table 3.5. 'Illite' is replaced, however, by muscovite as a respectable *illite* standard was unobtainable. The intention of this data set is to reflect a range of lithologies from a simple two mineral 'rock' to a more complex six mineral rock.

Carefully selected mineral phases were picked and crushed using a flypress, then re-picked to remove any weathering or possible contaminants. 50g of each *picked* mineral was reduced to a size of approximately 50 μm using an agate tema mill for 8 minutes. A 15g *subsample* was split and removed for elemental analysis. Each synthetic rock was then accurately weighed (to 4 decimal places) in the proportions of minerals shown in Table 3.5, and mixed thoroughly for 30 minutes in a mechanical shaker. The sample was subsequently split and 8g reduced in a microniser to 5μm for whole-rock X-ray diffraction analysis (XRD).

Careful major element analysis of the chosen minerals before mixing (the mineral analysis) and of the synthetic 'rock', after mixing (the rock analysis), were conducted using X-ray fluorescence spectroscopy (XRF). Verification of the mineral proportions was performed by whole rock XRD analysis and infra-red spectroscopy, MINERALOG. Details of all analytical techniques are given in Appendix 2.0, and XRF results in Appendix 1.0.

Table 3.5 Minerals and their proportions used to make 'synthetic' mixtures (wt %)

	quartz	K-feldspar	albite	kaolinite	muscovite	calcite	dolomite
pelite	20	15		15	45		5
semi-pelite	40	15	15	15	10		5
arenite	80	5			10	2.5	2.5
carbonate						50	50
mix 1	60	10	20	10			
mix 2	30			45	25		

3.7.3 Evaluation of models using laboratory measured data

The synthetic data set is now used more extensively to demonstrate the accuracy of each model. In this exercise, unlike the numerical modelling the *input response vector* comprises XRF measurements of real rock material, where measurement error (accuracy & precision) and other errors (for example, effects of weathering) are included in the data. In this sense, the system is more realistic although better constrained than logging data.

3.7.3.1 Accuracy of the models

Table 3.6 shows solutions for the six synthetic mixtures derived from the same models deployed in the numerical exercise. The overall prediction of mineral proportions is very good, ranging between 0.5% and 10% from the 'target' mineralogy. Rock 'Mix 1' shows a very accurate prediction of mineral mode, within 0.5% of the target value for quartz and kaolinite, <1% for albite and K-feldspar. 'Semi pelite' with the largest assemblage of minerals (6) shows the largest discrepancy, 7 wt% for muscovite (10% for Linear Programming), 5.5% for k-feldspar and other phases <2%. The other four rocks have minor differences between calculated and observed modal proportions of < 2.0%.

3.7.3.2 Comparison of models

All Least Squares models behave in an identical fashion deriving the same proportions and errors. The Euclidian model shows only a slightly less accurate estimate of mineralogy (mostly less than 0.1 of a percent) and a slightly larger error estimate as a result. The Linear Programming model tends to be the least accurate in the more complex (5-6 mineral) mixtures - pelite and semi pelite. Although the P%acc statistic is good (between 97.5% and 99%) for all rocks (ie, most of the chemistry has been used up), discrepancies in mineral prediction occur, up to 10%. Linear Programming estimates of other rocks (Mix 1, Mix 2, arenite and carbonate) are within 2.5% of the target, which is similar to the other models.

Table 3.6 Estimated mineral proportions, 'modes' of the six synthetic rocks calculated by the different mineral transform techniques (11 oxides used SiO2, TiO2, Al2O3, Fe2O3, MgO, CaO, Na2O, K2O, MnO, P2O5, S) Diff% - percent difference between target and Euclidian model mineralogy.

Key for tables: **Target** - Target mineral proportions, **Lsq-INV** -Least Squares inversion model, **Lsq-Chol** - Least Squares direct choleski model, **Lsq-Gj** -Least Squares direct Gauss-Jordan model, **LP** - Linear Programming, **Euc** - Euclidian Distance model. **SE** -Standard Error of the chemical fit, **Mad** -mean (absolute) difference of the residuals, **P%acc** Percent of chemistry accounted for.**mode diff%** is the percent diference between calculated and observed Euclidian model estimates.

Pelite	Target	Lsq-INV	Lsq-GJ	Lsq-chol	LP	Euc	mode diff%
Kaolinite	15.00	13.42	13.44	13.44	15.87	13.47	-1.53
Quartz	20.00	20.54	20.53	20.53	24.06	20.50	+0.50
K-feldspar	15.00	14.38	14.40	14.39	5.74	14.45	-0.55
Muscovite	45.00	46.88	46.85	46.86	48.751	46.81	+1.81
dolomite	5.00	4.78	4.74	4.74	2.964	4.77	-0.23
Standard error		0.307	0.307	0.307	-	0.330	
Mad		0.143	0.142	0.142	0.003	0.144	
P%Acc					98.04		
Semi Pelite							
albite	15.00	14.83	14.82	14.82	12.95	14.82	-0.18
kaolinite	15.00	18.71	18.70	18.70	22.21	18.74	+3.74
quartz	40.00	38.08	38.08	38.08	38.05	38.06	-1.94
k-feldspar 15.00	20.47	20.47	20.47	22.70	20.53	+5.53	
Muscovite	10.00	3.04	3.03	3.03	0.00	2.98	-7.02
dolomite	5.00	4.86	4.86	4.86	3.158	4.89	-0.11
SE		0.35	0.35	0.35	-	0.38	
Mad		0.146	0.144	0.144	0.002	0.146	
PAC					99.05		
Arenite							
qtz	80.00	78.30	78.30	78.3	79.09	78.26	-1.74
K-feldspar	10.00	10.35	10.35	10.35	8.65	10.42	+0.42
muscovite	5.00	6.87	6.86	6.87	7.25	6.88	+1.88
dolomite	2.50	2.07	2.07	2.07	1.15	2.16	-0.34
calcite	2.50	2.27	2.27	2.07	2.1	2.28	-0.22
SE		0.260	0.260	0.260	-	0.294	
Mad		0.167	0.167	0.167	0.001	0.176	
PAC					98.20		
Mix 1							
albite	20.00	19.22	19.22	19.22	18.62	19.38	-0.62
kaolinite	10.00	9.71	9.71	9.71	9.95	9.68	-0.32
quartz	60.00	59.85	59.85	59.85	60.56	59.68	-0.32
k-feldpsar	10.00	11.06	11.06	11.06	10.19	11.27	+1.27
Standard error		0.246	0.246	0.246	-	0.276	
Mad		0.120	0.120	0.120	0.011	0.133	
PAC					99.34		
MIX 2							
Kao	45.00	44.96	44.96	44.96	44.71	44.92	-0.08
quartz	30.00	30.61	30.61	30.61	30.63	30.59	+0.59
muscovite	25.00	24.38	24.38	24.38	24.47	24.49	-0.51
Standard error		0.204	0.204	0.204	-	0.219	
Mad		0.088	0.088	0.088	0.00	0.092	
PAC					99.81		
CARBONATE MIX							
dolomite	50.0	50.01	50.01	50.01	50.00	50.01	+0.01
calcite	50.0	49.99	49.99	49.99	50.00	49.99	-0.01
Standard error		0.001	0.001	0.001	-	0.001	
Mad		0.002	0.002	0.002	0.000	0.002	
P%acc					100.00		

3.7.4 Behaviour of algorithms with a reduced input data (oxides)

The above solutions from these models, in general, show very accurate mineral estimates, with low Standard Error estimates. It is very rare, however; that eleven oxides are available to model a particular rock, especially in the logging environment. P2O5, MnO and occasionally Na2O and MgO will not be available. The next exercise illustrates the prediction of mineralogy when fewer oxides are present, such as may be expected from a logging tool. The same *synthetic data* set is used except fewer oxides are made available for solution. Table 3.7 shows the solution from five models for the 'pelite' synthetic rock. 'Target' mineralogy is included, as is the previous Euclidian solution with full 11 oxides, for comparison. Between 5 and 7 oxides have been used in this modelling, these being the oxides measured specifically by the geochemical tool. The effect of different oxides on the solution is demonstrated by adding or subtracting different oxides Fe2O3 and MgO, CaO and Na2O.

3.7.4.1 Results of modelling with fewer oxides

Example (a), Table 3.7, shows no change in the solution when minor oxides P2O5, MnO, S, TiO2 removed. Example (b) shows a reasonably close estimate with six oxides, worst estimates being within 5% of the target. The most affected phases are the compositionally 'colinear' minerals - muscovite, k-feldspar and kaolinite. The important missing oxide, MgO in this example, clearly is important in constraining the solution of these colinear minerals. Improved estimates can be seen in example (c) if the missing oxide, MgO, is substituted in place of CaO and Na2O. CaO and Na2O are clearly less important oxides for solving this mineral transform. Example (d) shows that with Fe2O3 and MgO missing the solution has deteriorated further than with just MgO missing, indicating the importance of Fe2O3. Again all solutions for the Linear Programming model are *inferior* to the Error Minimisation and Euclidian distance models.

Table 3.8 illustrates how a simple mineral assemblage (Mix 2) comprising muscovite, k-feldspar and quartz can be determined accurately from only three or four oxides, (but only if the relevant oxides that consitiute the minerals are present). The three oxide example, column 4, is close in its modal estimation (<0.5% from the observed values); the addition of a fourth oxide, Fe2O3, (column 3) however improves the estimation.

Table 3.8 Estimated mineral proportions, 'modes' calculated for synthetic 'mix 2' using a reduced set of oxides. Euclidian distance model used . **Column 3** Fe203, Al2O3, K2O, SiO2 oxides used; **column 4** - Al2O3, K2O, SiO2 oxides used.

	1 Target	**2** 11 oxides	**3** 4 oxides	**4** 3 oxides
kaolinite	45.00	44.92	44.74	44.54
quartz	30.00	30.59	30.58	30.58
muscovite	25.00	24.49	24.68	24.79
SE		0.219	0.139	0.103
Mad		0.092	0.064	0.058

Table 3.7 Estimated mineral proportions, 'modes' calculated for synthetic 'pelite' by different mineral transform techniques using a reduced set oxides.

Key for table: **Target** - Target mineral proportions,**Euc-full** - Euclidian Distance model with 11 oxide modelled, **Lsq-INV** -Least Squares inversion model, **Lsq-Gj** -Least Squares direct Gauss-Jordan model, **LP** - Linear Programming, **Euc** - Euclidian Distance model. **SE** -Standard Error of the chemical fit, **Mad** -mean (absolute) difference of the residuals, **P%acc** Percent of chemistry accounted for.

Example a 7 oxide s Oxides: SiO2, Al2O3, Fe2O3, MgO, CaO, Na2O, K2O

	Target	Euc-Full	Lsq-inv	Lsq-Gj	Euc	LP
kaolinite	15.00	13.47	13.54	13.53	13.57	15.87
quartz	20.00	20.50	20.47	20.47	20.44	24.06
K-feldspar	15.00	14.45	14.56	14.62	14.55	5.74
muscovite	45.00	46.81	46.66	46.60	46.67	48.75
dolomite	5.00	4.77	4.74	4.77	4.74	2.97
SE		0.330	0.467	0.466	0.573	0.538
MAD		0.140	0.212	0.210	0.213	0.003
P%acc						97.38

Example b 6 oxides Oxides: SiO2, Al2O3, Fe2O3, CaO, Na2O, K2O *i.e., no MgO*

kaolinite	15.00	13.47	11.17	11.17	11.17	43.42
quartz	20.00	20.50	21.99	21.99	22.00	22.62
K-feldspar	15.00	14.45	10.79	10.79	10.78	11.61
muscovite	45.00	46.81	50.80	50.80	50.80	15.05
dolomite	5.00	4.77	5.34	5.34	5.26	7.40
SE		0.330	0.384	0.347	0.508	
MAD		0.144	0.149	0.148	0.152	0.699
P%acc						100.00

Example c 5 oxide Oxides: SiO2, Al2O3, Fe2O3, K2O, MgO

kaolinite	15.00	13.47	14.08	14.07	14.22	38.11
quartz	20.00	20.50	19.86	19.86	19.76	7.66
K-feldspar	15.00	14.45	15.97	15.98	16.23	49.22
muscovite	45.00	46.81	45.59	45.61	45.33	0
dolomite	5.00	4.77	4.36	45.61	4.46	4.09
SE		0.330	0.485	0.486	0.521	-
MAD		0.144	0.182	0.182	0.196	0.261
P%acc						99.07

Example d 5 oxide Oxides: SiO2, Al2O3, CaO, Na2O, K2O *ie no Fe2O3 or MgO*

kaolinite	15.00	13.47	7.55	7.57	7.63	3.06
quartz	20.00	20.50	23.84	23.81	23.81	25.90
K-feldspar	15.00	14.40	5.78	5.88	5.88	0.00
muscovite	45.00	46.81	57.53	57.51	57.51	66.15
dolomite	5.00	4.77	5.32	5.32	5.32	4.89
SE		0.330	0.497	0.484	0.484	
MAD		0.144	0.167	0.156	0.156	0.120
P%acc						97.38

Standard Error is much lower than with 11 oxides, due simply to there being less oxides present to contribute to the error. This is a pertinent observation; and the number of oxides used must therefore be taken into account when using Standard Error. This exercise demonstrates that the choice of the oxides is very important for a correct solution. As long as the system has the same number of oxides or more (fully-determined) and the oxides are relevant to the minerals to be estimated, a good solution is possible.

3.8 Potential problems with mineral inversion

3.8.1 Effect of mineral composition on a models solution.

The fact that the agreement of *model derived* and *known* mineralogy is good in the synthetic rocks is hardly surprising (if the models do work), because the correct mineral assemblage, and 'true' mineral compositions have been used. In a real situation the mineral assemblage will generally not be known, though from core or other studies a list of possible mineral assemblages can be collated, and each fitted in turn. In practice the mineral compositions are very important and rarely known, and model solutions can deteriorate rapidly if these are incorrect.

In choosing mineral compositions the possibilities are to use a) 'ideal' (theoretical) compositions, b) 'typical' or 'average' compositions, c) the actual mineral compositions. Ideal compositions are only really appropriate for minerals with very limited ranges of composition, such as quartz or rutile. Some minerals belong to (ideal) *binary systems*, or can be treated as such for modelling purposes. The modelling of olivines (system: forsterite-fayalite) and Fe-Ti oxides (system: magnetite-ilmenite), for example, has worked well in igneous rocks (Harvey *et al.*, 1991) by iterating between the binary end-members. This approach could be applicable to feldspars in sediments, using either albite-anorthite (plagioclase) or albite-k-feldspar (alkali-feldspar) binaries and is discussed later.

Due to the natural variation in composition that can occur, ideal compositions are not appropriate for other minerals, such as micas, chlorites, clays and carbonates, which are common constituents of sediments. For these minerals, in the absence of any specific knowledge about a formations mineralogy, the normal procedure would be to use 'typical' or 'average' compositions. Unfortunately mineral chemistry, particularly of clay minerals, is not easy to determine, and there is a paucity of appropriate data available in the literature from which meaningful 'average' compositions can be derived. Hertzog and Herron (1990) illustrate these problems in their attempt to provide such average compositions.

The effects of varying the mineral compositions can be illustrated using the synthetic rock data-set where the actual mineral compositions are known, at least within the range of analytical accuracy. In the examples which follow, solutions were obtained using the Euclidian Distance model, and all 11 major element oxides modelled. Table 3.9 shows four different solutions for the synthetic 'Mix 1'. Solution 1 uses the 'actual' mineral compositions, and as might be expected has the smallest Standard Error of all four solutions. Solution 2,

with largest Standard Error, uses 'ideal' (theoretical) mineral compositions for all four minerals. For solutions 3 and 4, the *actual* k-feldspar and quartz compositions have been used respectively in the two models, along with *'ideal'* compositions for the other minerals. It is clear from Table 3.9 that the differences between the solutions are quite small. The largest discrepancies are with the albite and kaolinite abundances in Solution 3, where the actual k-feldspar composition was used. In this example all four solutions are acceptable in the sense that they could not be distinguished in a 'real' case, and this arises from the fact that the four minerals involved are chemically distinct and do have close to 'ideal' or 'theoretical' compositions.

Table 3.9 The effect of *swapping* observed input compositions for typical (theoretical or 'ideal') compositions in Mix 1, Euclidian model used.

Solution 1 Using actual mineral compositions.
Solution 2 Using theoretical mineral compositions.
Solution 3 Using theoretical values except K-feldspar.
Solution 4 Using theoretical values except quartz.

	Target	1	2	3	4
quartz	60.00	59.68	58.00	58.20	59.59
k-feldspar	10.00	11.27	10.42	10.85	11.42
albite	20.00	19.38	20.37	17.40	18.98
kaolinite	10.00	9.680	11.21	13.55	10.01
SE		0.280	0.386	0.356	0.346
Mad		0.133	0.215	0.201	0.179

In the next example, the synthetic "Mix 2', composed only of kaolinite, quartz and muscovite, is used. The muscovite is phengitic in composition, and further from its 'ideal' composition than are the other two minerals. Five solutions for this sample are summarised in Figure 3.3, where somewhat greater variation in the estimated mineral percentages is seen. Solution 1, using the actual mineral compositions, again shows the closest agreement with the target composition, and the lowest Standard Error. For solutions 2, 3 and 4 either 'average' or 'ideal' compositions have been used for the muscovite, *actual* compositions being used for the other two minerals. While the quartz figures remain essentially constant throughout all the solutions, kaolinite varies between 40% and 50%, while muscovite ranges between 20% and 28%.

Slightly greater discrepancies are seen in models for the synthetic 'arenite' shown in Figure 3.4. Solutions 1 and 2 were obtained using the 'actual' and 'ideal' compositions respectively for all minerals. The other solutions were generated using 'ideal' or theoretical values throughout except for one of the phases, for which the 'actual' value was used. It is clear that there is generally good agreement between the models, particularly with respect to the calcite and dolomite. Significant differences do, however, occur where muscovite and K-feldspar are involved. Indeed, the best of solutions 3 to 7 is obtained where the actual muscovite composition is included, while the greatest deviation from the target composition is solution 6, involving the actual k-feldspar composition.

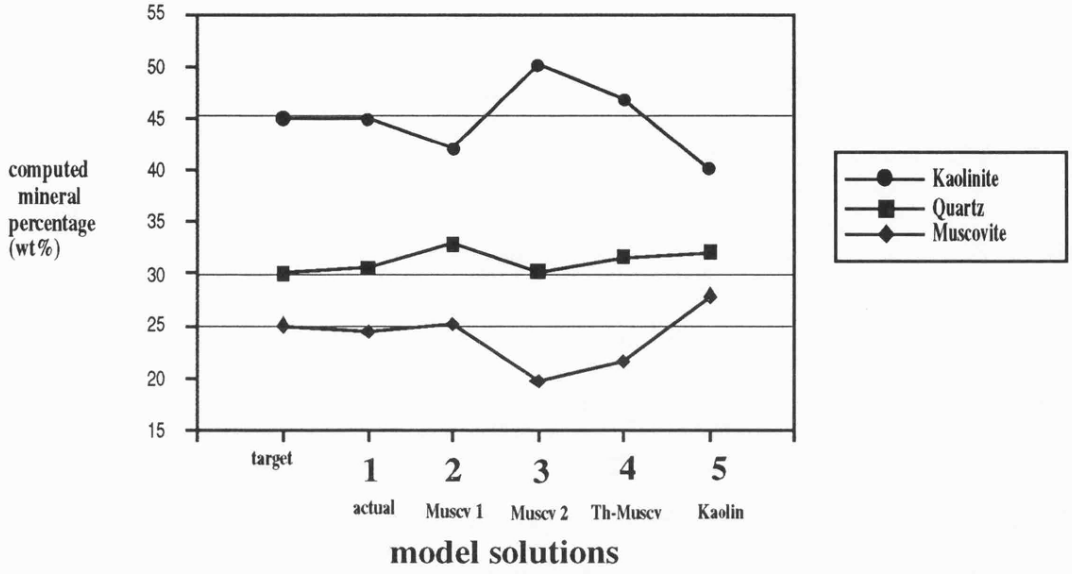

Figure 3.3 Change in modal mineralogy due to the use of varying compositions. Solution 1, actual compositions used, solution 2, using theoretical compositions, solution 3, using theoretical compositions except a different muscovite is substituted, solution 4, 'actual' compositions except muscovite, solution 5, as solution 4 but using theoretical kaolinite. See text for explanation.

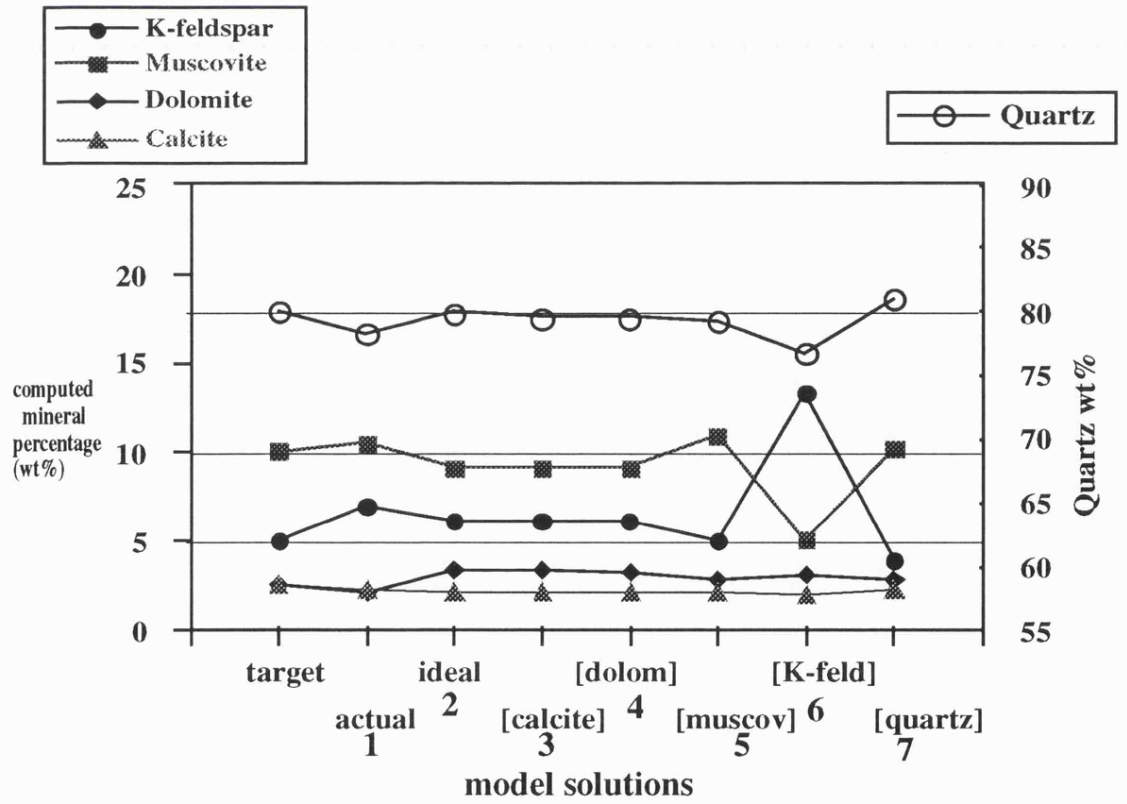

Figure 3.4 Change in modal mineralogy due varying compositions. Solution 1, actual compositions used, solution 2, using theoretical compositions, solution 3, theoretical compositions except calcite, solution 4-7, as solution 3 but using 'actual' dolomite, muscovite, K-feldspar and quartz respectively. See text for explanation.

More serious are the effects of mineral composition in the case of the synthetic 'pelite'. This rock contains kaolinite, quartz, k-feldspar, muscovite and dolomite. Muscovite has already been seen to vary somewhat from its ideal composition though the other minerals have compositions close to their theoretical values. Figure 3.5 shows a number of solutions for the pelite. The use of the actual mineral compositions shows a result close to the target composition. The second solution uses ideal mineral compositions throughout. This solution is totally erroneous with a high negative estimate for muscovite, and a slight negative estimate for quartz. For solutions 1 to 5 ideal compositions have been used except for one mineral for which the *actual* composition has been employed. Only solution 2 (using the actual muscovite composition) and 3 (using the actual k-feldspar composition) are valid in that they contain no negative estimates; only then does solution 2 approach the 'target' composition, though the difference remains significant for k-feldspar.

In the pelite example of Figure 3.5, besides the 'actual' solution, the closest solution to the target composition is solution 2 which utilised the 'actual' muscovite composition. Compared to the target composition, it is a relatively poor fit with muscovite too high by 6%, k-feldspar low by over 5% and kaolinite by 3%. However, that this solution is significantly better than the alternatives, implies that the main problem lies in the composition of the muscovite in this particular example. This is illustrated further in Figure 3.6 where a further set of solutions for the pelite are given. For these solutions the 'actual' mineral compositions have been used throughout except for muscovite, where a variety of different muscovite compositions have been employed. In Figure 3.6 the kaolinite and k-feldspar estimates are seen to be consistently higher than the target composition, while quartz and muscovite are consistently lower. Only dolomite is determined correctly within about 1% absolute by all models. For most solutions kaolinite is too high by a factor of about two; the factor for k-feldspar is slightly higher. To balance, quartz is low by a factor of about two while muscovite varies upwards from a negative estimate. It is notable that one solution (1) is significantly better than all the others. A wide range of solutions result, despite the fact that all muscovite compositions used for modelling are, except for the 'ideal' solution, naturally occurring compositions. It is clear that the compositions of the minerals used in modelling are of particular importance and the models very sensitive to variations in mineral composition. The corollary is that if the model mineral composition is close to the actual composition then the model fit will be excellent.

3.8.2 Compositional colinearity

One problem, in particular, that was addressed in the choice of 'synthetic' samples was that of *compositional colinearity*. This is potentially one of the most serious problems in mineral inversion.

Compositional colinearity occurs when three or more minerals included in a model lie on, or close to, the same compositional plane or vector. Where three phases lie precisely on the same compositional vector any input response vector can be inverted to give a result with

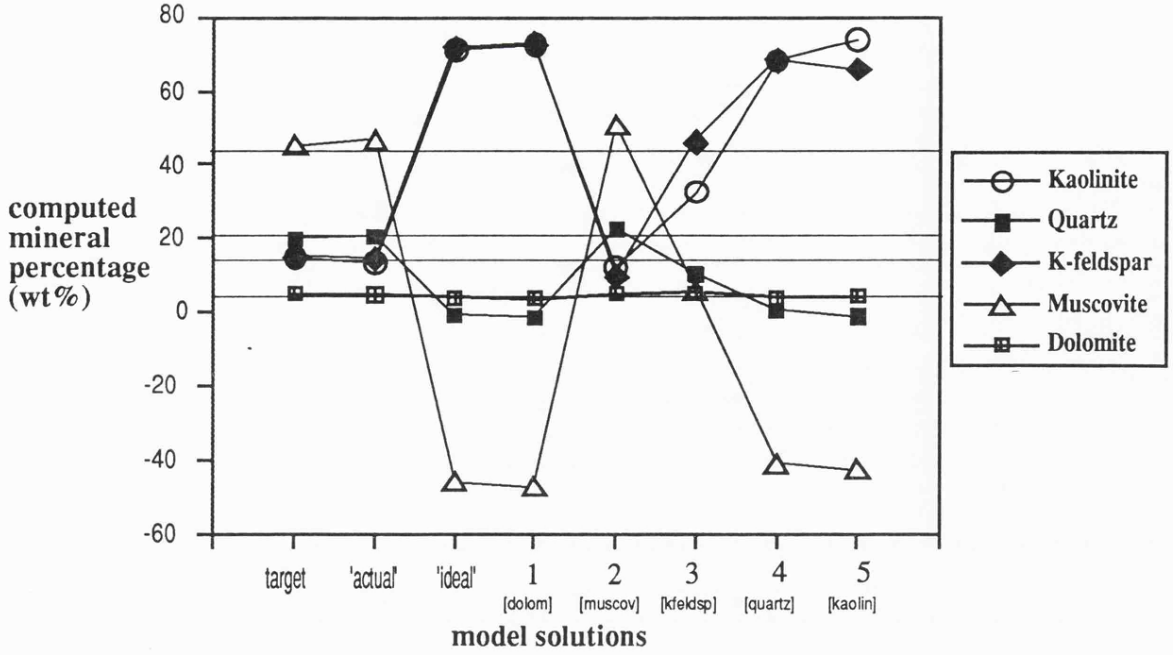

Figure 3.5 - Change in predicted mineralogy due to different compositions in the synthetic 'pelite'. Solutions 1- 5, theoretical compositions used except minerals in brackets (which are actual compositions). " ideal" uses theoretical compositions, "actual" uses laboratory measured compositions. "Target" are the known mineral proportions.

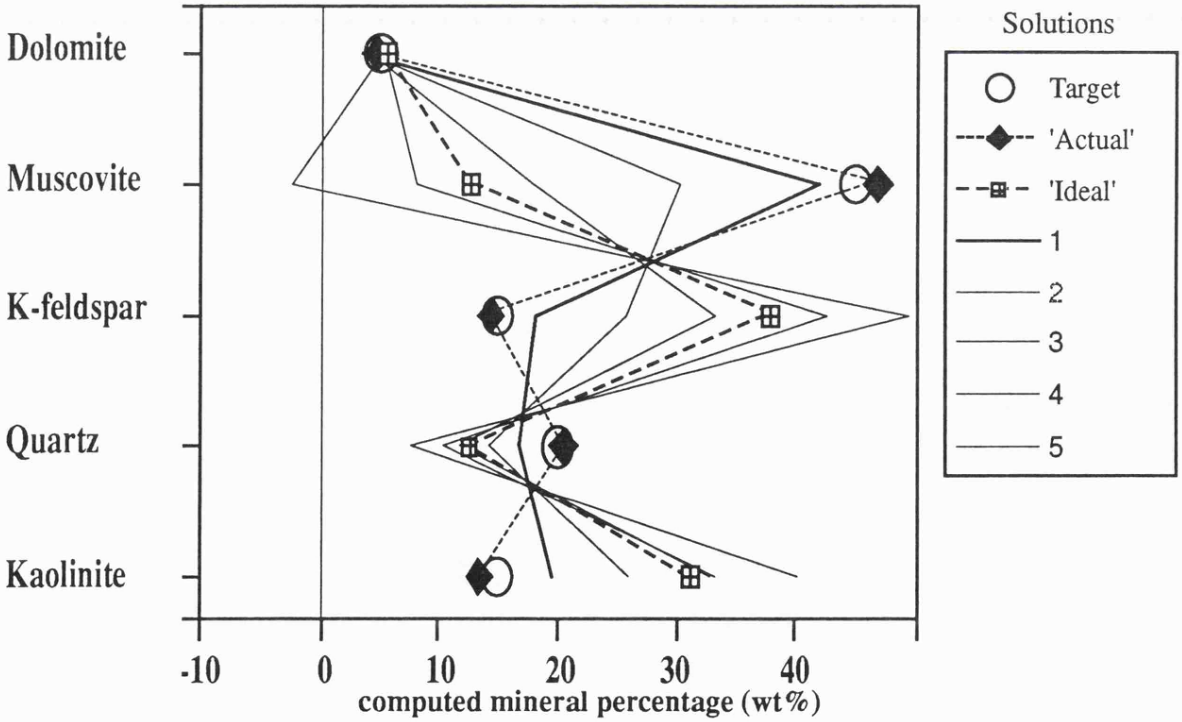

Figure 3.6 Effect on ' pelite' mineralogy due to varying muscovite compositions. Solutions 1-5, various muscovite compositions substituted into the model.See Text.

respect to any two of the phases. With respect to all three phases, however; an infinite number of solutions will be possible. The latter situation, produces a matrix singularity, and a resulting solution failure. More realistically the phases do not lie *exactly* on the such a compositional plane and the effect may not be seen so vividly, but will produce an inherent *instability* in the system.

This problem becomes particularly important in sedimentary rocks where chemical equilibrium is not generally achieved. For example, consider the system (SiO_2-Al_2O_3-K_2O-H_2O) which in clastic sediments could involve quartz, muscovite, illite, k-feldspar and kaolinite. The 'ideal' compositions of all these minerals consist of at least three of the oxides: SiO_2, Al_2O_3, K_2O and H_2O. Water is often not available as a discrete measurement in the laboratory or from logging tools. Figure 3.7 illustrates the problem of compositional colinearity in the system [SiO_2-Al_2O_3-K_2O]. Theoretically there are four possible mineral reactions within this system, as follows:

k-feldspar + kaolinite = illite

k-feldspar + kaolinite = muscovite + quartz

quartz + muscovite + kaolinite = illite
quartz + muscovite = k-feldspar + illite

The problem arises because, taking the first reaction, and appropriate chemistry, an algorithm cannot allocate the chemistry in a unique way between the phases (an *indeterminate* solution). As [k-feldspar + kaolinite] is, in effect, equivalent to [illite], there are an infinite number of solutions possible, for the same chemical composition, between the two 'end-member' phase assemblages. If the mineral compositions are precisely colinear, as may occur if theoretical mineral compositions are used, then it may simply not be possible to solve the algorithm. In natural rocks fortunately, complete compositional colinearity of this type rarely occurs. In clastic sediments, however, where minerals are not necessarily in equilibrium, the problem may occur. Fortunately, clays and micas may vary significantly from their ideal compositions and therefore become *drawn-off* the colinear plane. This can often offer the extra degrees-of-freedom to enable a sensible solution. The latter may or may not be geologically meaningful as some of the 'pelite' solutions in Figure 3.6 demonstrate. It was for this reason, the pelite and semi-pelite compositions were chosen to contain four colinear minerals of the system K2O-SiO2-Al2O3. Compositional colinearity is the major cause of the inaccuracy of these two solutions as shown in Table 3.5.

3.8.3 The contribution of minerals to the total oxide proportion in a sample.

In the light of compositional colinearity it is pertinent, at this stage, to consider the contribution that each mineral, present in a rock, makes towards a particular oxide in a chemical analysis. Figure 3.8 (A & B) illustrates the contribution that certain potassic minerals, commonly found in the sediments, make to the *total* K2O contribution in a sample

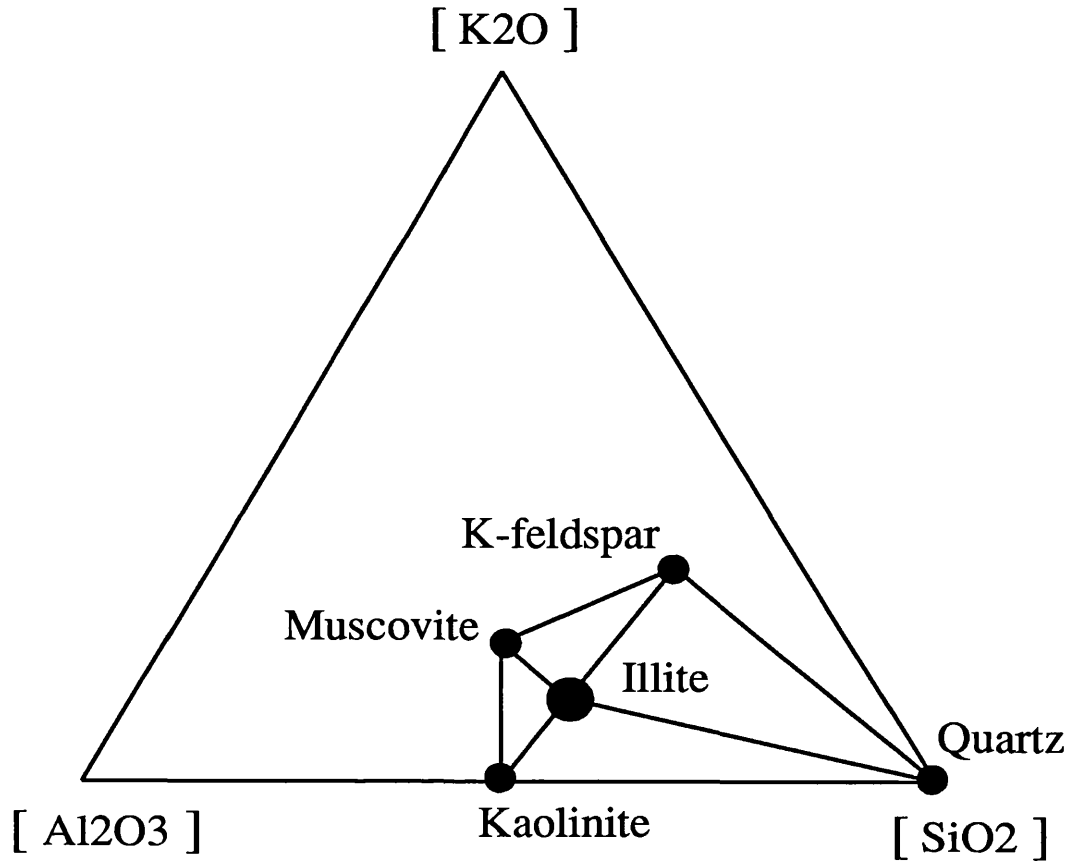

Figure 3.7 Compositional colinearity in the system [SiO2] - [Al2O3] - [K2O]. (after Harvey and Lovell, 1992)

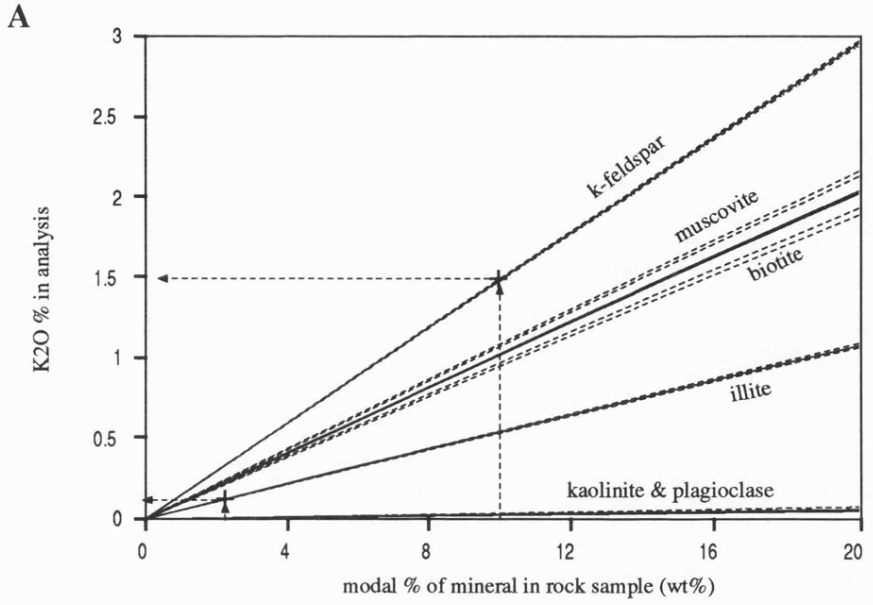

Calculated from data compiled by Hertzog & Herron (1992) bounding lines are standard error of the mean estimate(as this data was compiled from various sets of data). The SE of the mean represents the Standard deviationof all the means of these groups, and acts an estimate of the variance in the compositional data.

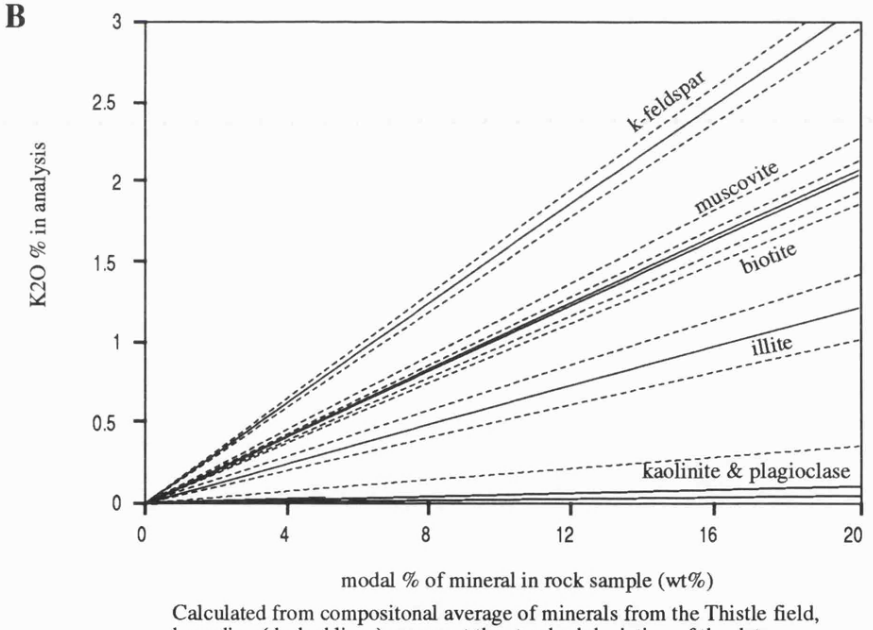

Calculated from compositonal average of minerals from the Thistle field, bounding (dashed lines) represent the standard deviation of the data.

Figure 3.8 Typical contributions that each of the common potassium rich minerals make to the total concentration of K2O in a sample analysis. (a), from 'global ' averages from a compilation of sedimentary data by Hertzog and Herron (1991), and in comparison (b) a specific data set, from the North Sea, Brent Group (this study). Concentrations in wt%

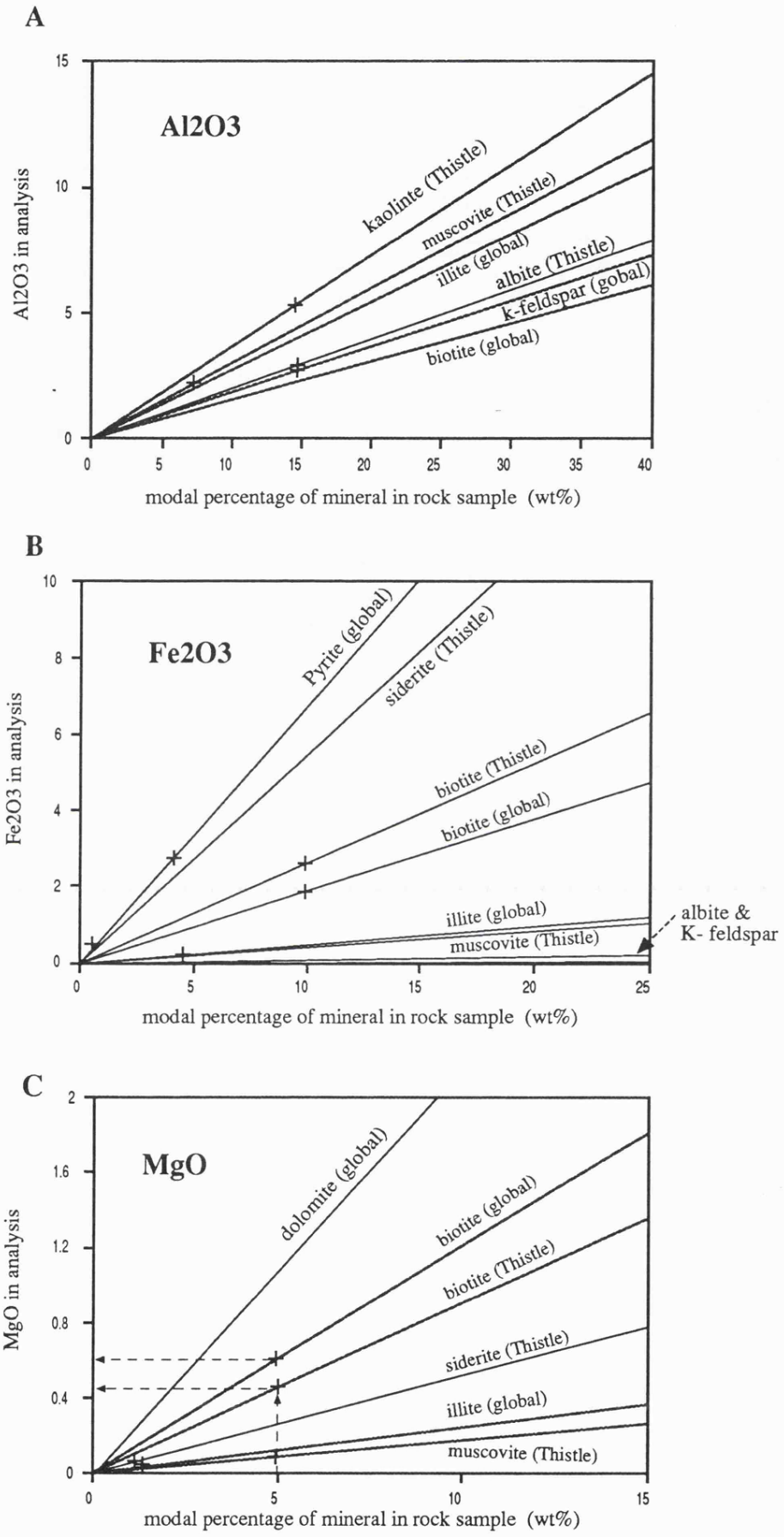

Figure 3.9 Contribution of Al2O3, Fe2O3 and MgO oxide from common minerals. Global values from Hertzog and Herron 1991, Thistle values- microprobe data from the North Sea, Brent Group. Crosses mark average contribution in a Thistle Field sub-arkosic sandstone, see text. concentrations in wt%

analysis. Data is represented from a large 'global' compilation (Figure A) and a specific compilation from one stratigraphic unit, the Brent Group (Figure B).

In terms of mineral transforms, where compositionally colinear minerals are present and a solution is indeterminable, the relationships seen in Figure 3.8 are destroyed, and no possible distinction can be made between the contributions of two minerals.

This sort of data also helps, in the logging scenario, to understand the contribution that certain minerals make to tool measurements. For example; K2O may be dominated by one mineral in a rock, say K-feldspar at 10 wt % of the sample. If another potassic mineral phase were also present, say illite (at 2 wt%); because of the difference in the K2O concentration of each mineral, illite would have to be present in a proportion a factor of four times greater than the K-feldspar concentration to make the same contribution to K2O. In terms of the natural gamma-ray spectrometry logging tool (NGT, Section 2.2.1), if 10 wt% K-feldspar were present, the contribution of gamma-rays recorded from any illite present would be masked until illite reached a value >40 wt%. Illite discrimination by the NGT alone (as has been advocated possible) in the presence of K-feldspar is therefore impossible (Hurst, 1990).

Diagrams such as Figure 3.8 are useful in mineral modelling for understanding the relationship of a minerals oxide contribution to the total oxide composition of a sample. Figure 3.9 a, b and c show similar plots calculated for the oxides Al2O3, MgO and Fe2O3. Such relationships are, of course, inherent in the components matrix.

3.9 Synopsis and conclusions

The early part of this chapter introduced the different philosophies adopted for mineral transformation and appropriate measures of error assessment. The exercises in the later part of the chapter are concerned with the evaluation of a well constrained, idealised data set as a means to test the accuracy and predictive power of the different mineral transform techniques. The main problems that can seriously affect a solution are also established. As a summary, a comparison of the main features of each mineral transform model are presented in Table 3.10.

Numerical modelling verifies that each of the mineral transform models can produce a perfect solution (and therefore work!). Estimates of error indicate the closeness of fit of the solution. In the 'numerical' evaluation these errors are negligible and due only to rounding.

The use of real mineral data, from a range of synthetically produced rocks that span the spectrum of sedimentary lithologies, provides a more realistic, yet well constrained indication of how each transform model 'behaves'. With the correct input mineral compositions all models except Linear Programming, solve almost identically (to 1 decimal place). Accuracy of the solution ranges through the data set from within 0.2% of the target mineralogy to 7% (10% for Linear Programming). Semi pelite, with the largest number of phases (6) and consisting in part of minerals that are *compositionally colinear*, produces the least accurate modal estimate.

When a *reduced number of oxides* are available to model, as is the case in the logging environment, it is possible to gain similar estimates of mineralogy as long as the correct oxides are chosen for the minerals being solved.

Compositional colinearity is a serious potential source of error. It can result in modal estimates that are only slightly in error (as in the semi pelite solution), or estimates with large negative values and the 'silly' solutions of Figure 3.6. In the case of slightly inaccurate solutions, these are probably the most dangerous as they can go undetected. The gross instability in the pelite solutions of Figure 3.5, while sensitive to the mineral compositions, are primarily the effected by compositional colinearity in the system.

Care must be taken in the choice of correct mineral composition for each mineral in the components matrix. This especially so for the clay minerals and mica minerals where compositional variation, due to ionic substitution, is common.

The inherent problems identified in this chapter are now investigated on reservoir core material in the next chapter. Strategies that address the problem of compositional colinearity, identification of correct mineral phases, and the correct mineral composition for solution are then dealt with in Chapter 5.

Table 3.10 A summary comparison of the different mineral transform models. (adapted and updated from Harvey *et al.*, 1990). Subtractive (norm) model is also included for completeness. (*) Depends on inclusion of additional constraints to the unity constraint. (@) Linear Programming is deterministic although other optimisation techniques may allow for uncertainties.

	Error minimisation models	Linear programming model	Euclidian Distance model	subtractive (norm) model
Maximum no of minerals	No. of components +1	(*) No. of components +1	No. of components +1	Effectively no limit
Errors in the chemistry	minimised as part of model	(@)not considered	averaged out.	not considered
Weighting	straightforward	possible with extra constraints	not possible	not possible
Negative minerals	possible can be common	none possible	possible can be common	none possible
stability of solution	colinearity - ill conditioned matrix problems not uncommon	colinearity is a problem	colinearity is a problem	no problem
Useful error measures	ASE, NSE SE (MAD)	P%acc(SUMP) MAD	ASE, NSE SE (MAD)	none
Constraint of unity in place	yes	yes	yes	not necessarily

Chapter 4.
Mineral Modelling of the Brent Group.

4.0 Introduction

The aim of this chapter is evaluate the performance of mineral transform models on a range of lithologies from a real sedimentary environment. The use of a data-set derived from laboratory measurements of core, rather than logging tool measurements, is the next step in evaluating how transform models behave. It is used here as an important intermediary step between an evaluation of well constrained *synthetic rock* data (Chapter 3) and less well constrained log derived data (Chapter 6). Obtaining *carefully measured* laboratory data from core allows us to accumulate all the variables required to evaluate the mineral inversion problem; namely the sample geochemistry, mineral assemblage, mineral composition and for the purpose of evaluation, the mineral proportions, in a manner similar to that used in the previous the synthetic rock exercise.

The familiarity, through previous research, coupled with the variable lithology of the Brent Group (northern North Sea), provide an excellent example of a reservoir in which to study mineral modelling. Extensive laboratory analysis has been performed on a cored section through the Brent Group, in the Thistle Oil Field, to provide the appropriate data for this exercise.

4.1 Overview of the Brent Group.

The middle Jurassic (Aalenian-Bathonian) Brent Group has been intensively studied since the first well was drilled in 1971 in block 211/19 (Brenand, 1984). Since the early seventies the Brent Group has become the single largest oil producer in the UK, with over 25 separate fields covering an area over 6000 square km. Total reserves to date are in the order of 30 billion barrels equivalent Morton *et al.* (1992).

The Thistle Field lies in the general tectonic framework of the Viking Graben system (Rhys, 1974) and stratigraphic framework of the *Brent Province* (Bowen, 1975). The Brent Group has been described as a regressive-transgressive wedge (Brown *et al.*, 1987). It is thought to be part of an extensive Bajocian (173.5 Ma) to Bathonian (161.3 Ma) regressional phase that affected an area twice the size of Britain (Blanche and Whitaker, 1978). Many paleogeographical models for the Brent Group have been put forward to explain the sediment patterns. A number of workers, including Bowen, (1986), Zeigler (1982), Johnson & Stewart (1985), Graue *et al.* (1987); Falt *et al.* (1989) and Falt & Steel (1990) support the widely favoured opinion of Budding & Inglin (1981) that the Brent sequence is a northerly prograding offshore sandsheet - coastal barrier to delta top, wave dominated delta complex. Other models suggest different variations on a theme; Procter (1980), a northerly derived fan delta; Chauvin & Valachi (1980), a south-easterly derived fan delta; Eynon (1981) a

transgression interrupted south-easterly derived fan delta; Moiola *et al.* (1986) a fluvial dominated delta. Morton & Humphreys (1983), Leeder (1983), Richards *et al.* (1988) and Richards (1990), however, advocate a less unimodal source, with more complex sediment origins from surrounding basin margins and shelves.

Deegan & Scull (1977) recognised five major subdivisions of the Brent Group. These five subdivisions are summarised along with reservoir zones in Figure 4.1, in context of the northern area of the Brent Province. Thick sub-arenite to arkosic (micaceous) sandstones and thinner shales (with minor coal-beds of varying thickness) dominate the lithology. These sediments distinguish different environments including fluvial distributary channel sands; inter distributary and lagoonal fine sands, silt and shales; as well as shallow marine and coastal (sheet sand) deposits and delta front and slope sand deposits. Recent sediment provenance studies (Morton, 1985 & 1992), using garnet assemblages, identify three possible sediment sources; these include the Orkney-Shetland platform and two metamorphic terrains, namely, the Norwegian landmass & part of the Orkney-Shetland platform. Sandstone porosities range from 20-35% (average 25%), with permeability in localised intervals recorded up to twenty darcies (Bowen, 1975; Jones *et al.,* 1975). In some areas this porosity and permeability is suggested to be sustained regionally (Brennand and Siri, 1975).

4.1.1 Thistle Field: Introduction and structural setting of the reservoir

The Thistle Field is located 130 miles northeast of the Shetland Islands in the northern part of the Viking Graben, see Figure 4.2 A & B; sea depth is roughly 160m. The field was discovered in 1973 by a consortium of oil companies principally operated by the then BNOC Development (Hallett, 1981). The field covers an area of 3970 acres and originally had an estimated one billion barrels of oil in place with a recoverable 520 million barrels originating from the middle Jurassic *Brent Group* sandstones. A production platform was installed in 1976 and production commenced in 1978 from six injection wells (5 water, one water/gas). Total oil production in 1990 was in excess of 355 million barrels (C. Bajsaiowicz *pers. comm.* 1992). The original oil/water column (1981) extends some 240m, with the oil water contact at 2800m (9322 ft) below sea floor.

The Thistle Field comprises a major easterly dipping half graben fault block, bounded to the North, South and West by faults (see Figure 4.2 (D)). A *rollover* anticline is interpreted on the western margin (increasing thickness of upper Jurassic shales). Development of the reservoir units varies throughout the area due to growth faulting during sediment deposition (Hallett, 1981). Extensive faulting is interpreted within the field, having occurred incrementally throughout the Brent and later Kimmeridge times although the major phase of faulting occurred post late Jurassic deposition. The field is divided into three separate pressure areas by faulting which effectively halts fluid flow between these areas, (Figure 4.2c), and affects the net pay of the field. Where fully developed, the *reservoir units* are divided into four zones which are vertically separated by shale/siltstone permeability barriers (Hay, 1977; Hallett, 1981); these zones are summarised in Figure 4.1.

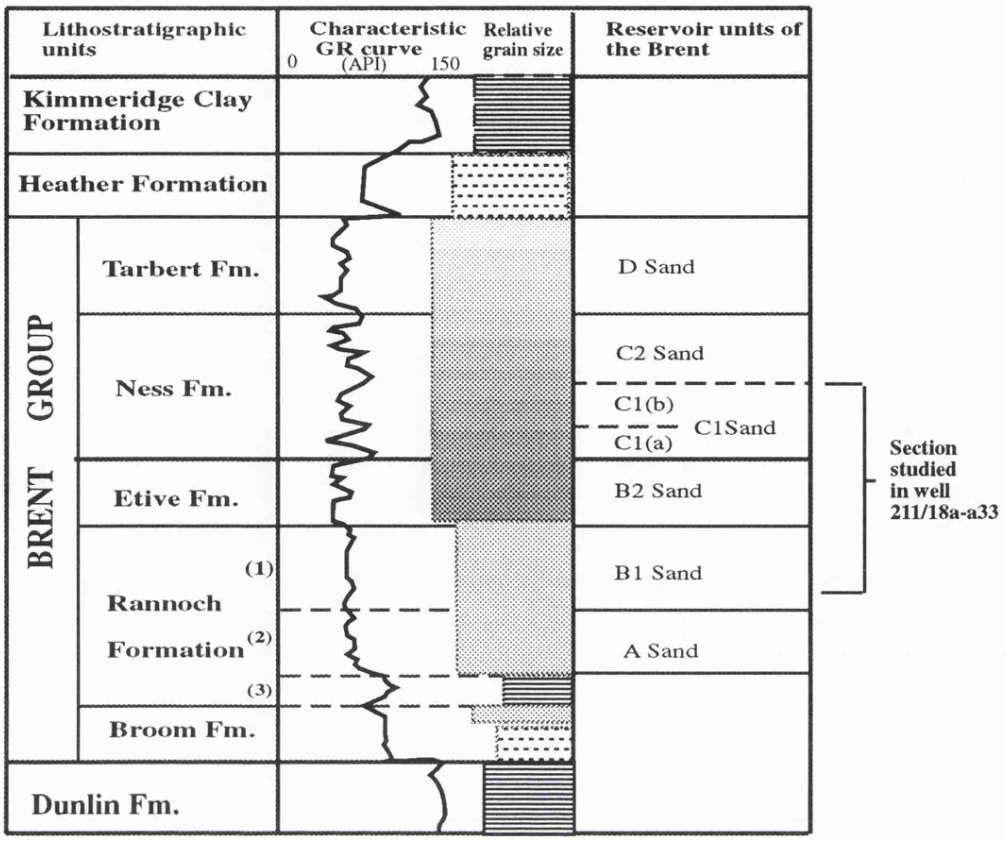

Key: Lithology and interpretation of each Brent Group formation

The lowermost *Broom Formation* a thin (<50m thick) poorly sorted argillaceous to arkosic sandstone with sheet like geometry, generally interpreted as a tidal flat sands & marine sand sheet (Budding and Inglin, 1981; Hay, 1978), although of possible fan-delta origin in areas, coeval with the Oseberg Formation .

The overlying *Rannoch Formation* is interpreted as a prograding delta front or shoreface (Johnson and Stewart, 1985, Budding and Inglin, 1981) comprising a very fine highly micaceous sandstone with 2-25% mica content, (Morton and Humphreys, 1985) coarsening upwards from its shaley base (Rannoch mudstone). It is dominated by flat bedding with few low angle cross beds (Pevararo and Russell, 1984) and contains a few localised diagenetic calcite doggers (Hay, 1978, Hallett, 1981, Pevararo and Russell, 1984).

The overlying *Etive Formation* has a variable interpretation from regressive bar (Hay, 1977;Brown et al 1987); tidal channel and distributary mouth bar (Davies and Watts, 1977); upper shore face beach and barrier/bar top sediments (Johnson and Stewart, 1985, Budding and Inglin, 1981); and distributary channel sands (Chauvin and Valachi, 1980). They consist of well sorted fine to medium grained subarkosic crossbedded sandstones very coarse in places becoming fine grained and more massive in the upper part. Thin mica beds and zircon concentrations have been identified (Pevararo and Russell,1984, Morton and Humphreys, 1985).

The *Ness Formation* is interpreted as a delta-plane, fluvial dominated environment with identifiable delta plain, tidal flat-lagoonal sediments and rare fluvial channel - splay and tidal sands (Budding and Inglin, 1981; Davies and Watts, 1977; Hay, 1978). The sediments of this formation consist of heterolithic very fine to coarse grained sub-arenite to sub-arkose sandstones and siltstones interbedded with thin coals and organic shales, often with pyrite and rootlets.

The uppermost *Tarbert Formation* sediments are suggestive of a returnto more marine conditions due to the end of the Bathonian regression, although some rootletted coals are locally present (Moiola, 1975, Brown et al., 1987). They consist of a dominantly very fine to medium grained often micaceous and burrowed sand sequence (Hodson, 1975) with few coarse sandstone intervals (Graue et, al., 1987) and few shale sequences (Albright *et al.,* 1980). Thickness is variable due to the erosion reworking and periods of non deposition (Stow and Jackson, 1986).

Figure 4.1 Subdivisions of the Brent Group and surrounding formations and placement of reservoir units in the Thistle Field.

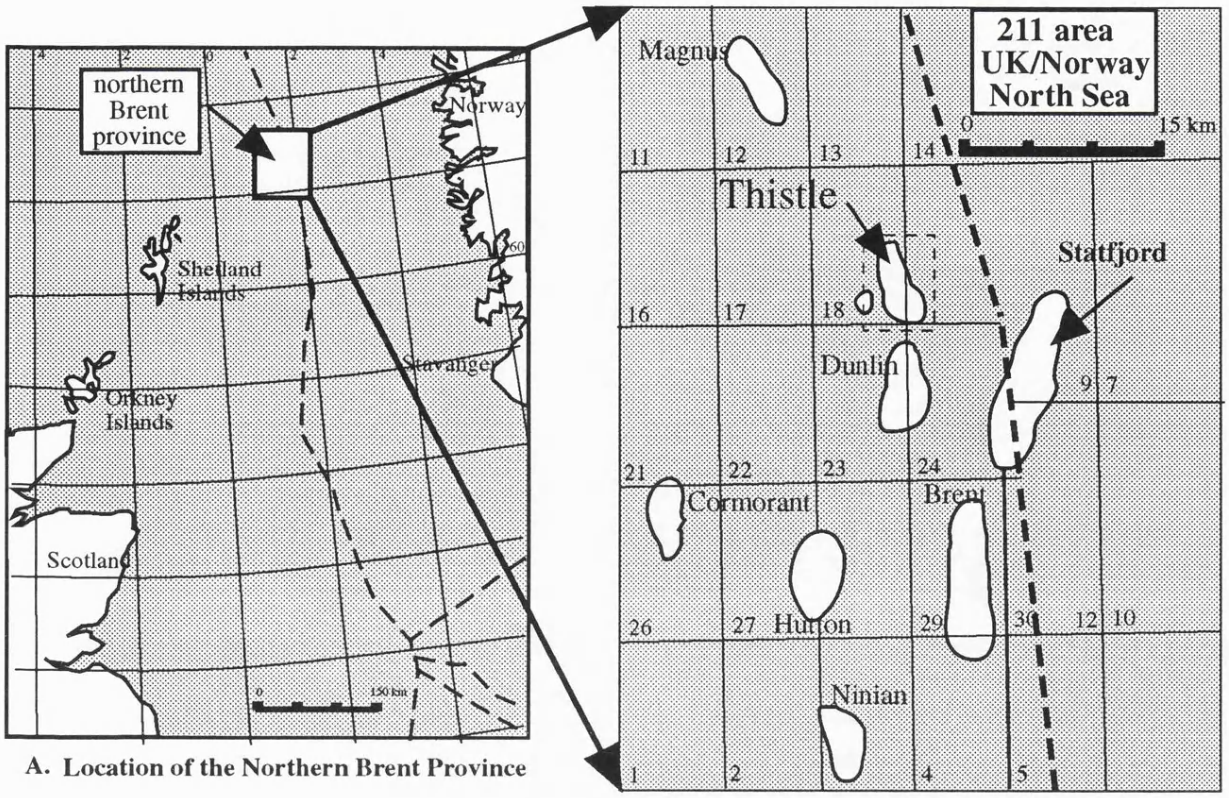

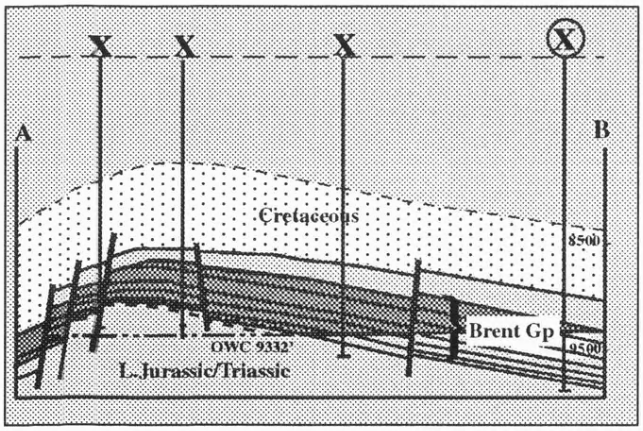

D. **Cross section of the Thistle Field, Northern North Sea (adapted from Hallett, 1981)**

- Injection well
- Producing wells
- Brent Sands
- Oil bearing section

Vertical exaggeration x2

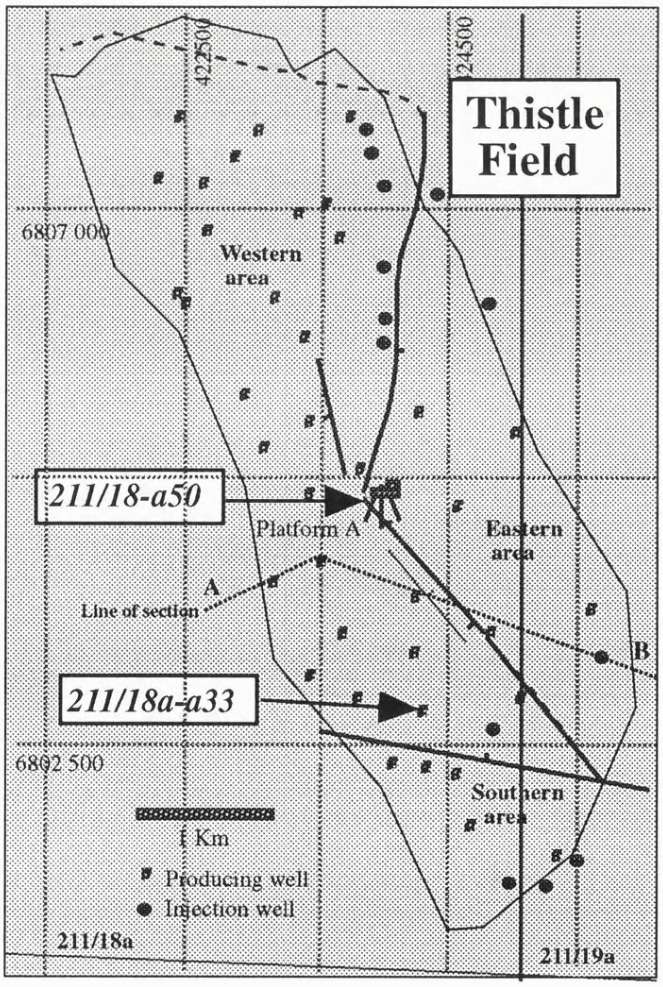

C.

Figure 4.2 Location of the Thistle holes 211/18a-a33 and a50 in the Thistle Field, North Sea, compiled with data courtesy of BP

4.1.3 Summary of the existing petrography of the Thistle field

Previous studies by Blanche & Whitaker (1978), Pevararo & Russell (1984) and Stow & Jackson (1986) (unpublished), of the petrography and mineralogy of the Thistle field are summarised in Table 4.1. These data are derived by thin section point counting. They serve to give an indication of the mineralogy present through the field. The values for quartz given by Pevararo & Russell tend to be lower than for the other authors while Stow & Jackson noted more feldspar and rock fragments. The amount of end-member feldspar in the reservoir sandstones is conflicting. Hallett (1981) suggests more sodic plagioclase, Pevararo and Russell (1984) equal proportions, while Humphreys & Lott (1990), and this study, suggest greater amounts of K-feldspar.

Table 4.1 Summary of the Thistle field sandstone mineralogy (Vol%). Summaries of point count data from different sources; Blanche & Whitaker (1978) and Stow & Jackson (1986) (range); BNOC 211/18a-a33 core report (Russell, 1982), Pevararo & Russell (1984).

	Blanche and Whitaker			Stow & Jackson	BNOC 211/18a-a33			Pevararo & Russell 1984			
	Mean	**Max**	**Min**	**range**	**Etive**	**Ran**	**Lr. Ness**	**Tar**	**Ness**	**Etive**	**Ran**
quartz	70	83	54	60-80	52-64	43-50	61	51	56	74	44
feldspar	2	4	0.1	10-25	4-12	6-15	7	10	12	14	15
mica	7	12.5	0.1	1-8	0-1	8-13	trace		8	1	19
clays	13	31	2	3-15	7-22	7-13	0-7	13	15	10	15
heavy minerals	4	14	0.4	0-2	trace	trace		8	2.5	1	2
others*	3	8	0.4	0-25	trace	trace	trace	1	4-5	1	3
cement (siderite)					0-7	0-2		1	-	-	-

* - incl. rock fragments; Tar = Tarbert Formation, Ran = Rannoch Formation

4.2 Characterisation of the Thistle 211/18a-a33 reservoir section

Well 211/18a-**a33** is currently a producing well. It is situated towards the south of the Thistle Field in the western pressure area (Figure 4.2). Production to date exceeds 4800 million standard barrels (MMStb).

Thirty-three metres of core (100 feet[1]) through part of the B & C reservoir sections, (Figure 4.3), has been extensively sampled. Core was *slab sampled*, along its axis, in 0.3m (1 foot) intervals, then crushed and homogenised. Each sample was treated as a bulk sample for geochemical analysis (XRF and carbon/sulphur analysis) and mineralogical analysis (XRD). Chip samples were preserved for the production of polished thin sections, for verification of mineralogy; for *electron microprobe* analysis of individual mineral grains; and for study under the scanning electron microscope (SEM). The homogenisation of each one-foot sample is a process that better approximates the volume measured by the geochemical logging tool in an attempt to reduce the effect of heterogeneity. Due to a reasonable amount of geological work having been undertaken in the Thistle Field, this study has aimed to collate and use existing data in combination with the generation of new data where none has previously existed. A review of parameters obtained for modelling follows.

[1] Imperial units are used here to define depth intervals, to remain consistent with original core and log data.

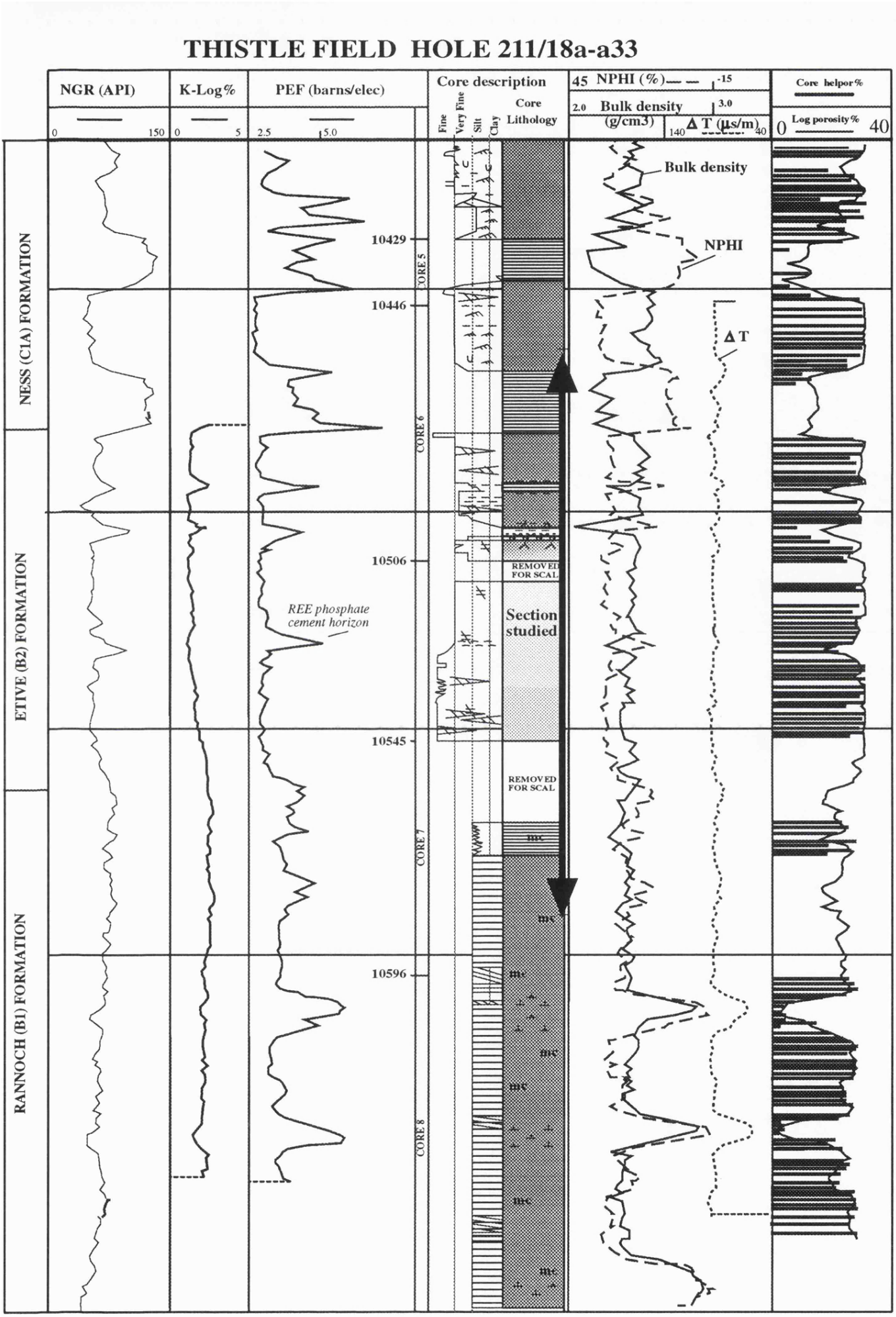

Figure 4.3 Composite plot of wireline and core data for the reservoir section studied in Thistle well 211/18a-a33. Depth in Feet. Compiled from data courtesy of BP and data from Humphreys and Lott (1990). NPHI - neutron porosity, NGT - natural gamma-ray log, K-log - spectral contribution from K to NGT log. PEF - photelectric factor, delta T -sonic travel time. Depth is not true vertical depth.

4.2.1 Mineralogy of the 211/18a-a33 section

Each homogenised 'bulk' sample was analysed by whole rock semi-quantitative X-ray diffraction. These results are summarised in Figure 4.4. and are tabulated in Appendix 3.0. Thin section point-counting, performed on twelve samples, and infra-red spectroscopy (MINERALOG), on six samples, were used to verify the mineralogy. A comparison of the advantages of MINERALOG with XRD is made by Harville and Hamish (1990) and between XRD and point-counting by Kaye *et al.* (1968). Details of analytical techniques are given in Appendix 2.0.

Quartz, K-feldspar (both orthoclase and microcline), albite, muscovite and biotite mica, volumetrically important authigenic kaolinite, and locally siderite, are the main mineral phases. Minor phases include organic material, pyrite, illite-smectite, chlorite, zircon and garnets. The main mineral phases identified are the product of diagenetic overprinting, and alteration of the primary detrital minerals. This is a result of sediment burial to depths of greater than 3000m (10,000 ft) (Blanche and Whitaker, 1978; Pevararo and Russell, 1984; Humphreys & Lott, 1990). No complete core was available for a study of the sedimentological/macroscopic features; these features are therefore summarised briefly here from the original BNOC geological report along with mineralogical features from this study. For the reservoir units in the interval these are summarised:

4.2.1.1 Upper Rannoch Formation (B1 unit) Core depth 10561'-10580'

This Rannoch section is reported to be a monotonous parallel laminated, oil stained, micaceous, very fine grained sandstone; see Plate 1 (*from this study*). It contains occasional moderate to low angle crossbeds and rare thin ripple marks with a slight coarsening in grain size upwards. Localised calcite-cemented intervals occur below the section studied.

Mineralogy

Semi-quantitative whole-rock XRD, and thin section point counting show this section to be dominated by quartz (40-58 wt%[1] , XRD data), K-feldspar (14-20%), albite feldspar (7-10.5%) and abundant mica (3-7%). Thin section estimates suggest slightly higher levels of mica (8-13.2 wt% muscovite in addition to 6-13% biotite); this is probably due to poor XRD calibration standards (and orientation effects) and a slight bias by thin section due to the generally larger grain size of micas. Kaolinite is the other abundant phase present (11-26%). Diagenetic siderite (1-2%) is seen under the SEM to grow small rhombs (Plate 4E). Trace amounts of garnet, zircon and rutile have been detected by microprobe and thin section analysis.

Texture

Minor pressure solution is seen at grain contacts with little quartz overgrowth. Quartz shows both monocrystalline and polycrystalline grains suggesting different sources, although both show undulose extinction suggestive of a derivation from a predominantly metamorphic or fold belt terrain (Hallett, 1981). Micas show a strong parallel orientation to bedding (see

[1] All percentage (%) values for elements/oxides/minerals refer to weight percent, except where stated.

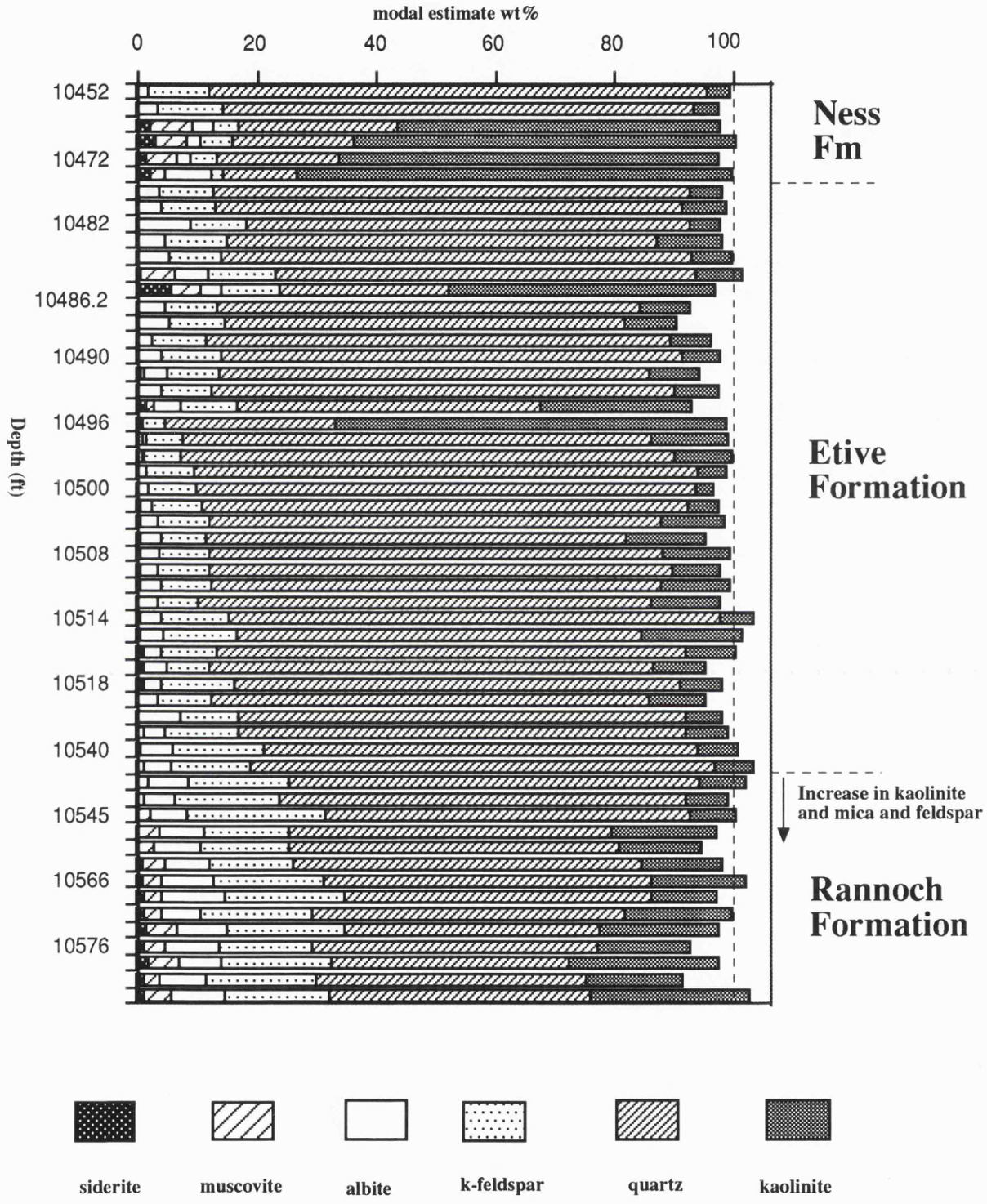

Figure 4.4 Mineral phases identified by whole-rock X-ray diffraction for core samples from Well 211/18a-a33.

Plate 1). Expansion and 'splaying' in micas is common due to diagenetic alteration of crystal ends. It is most prominent in biotite, where diagenetic siderite grows in pore spaces between grains (Plate 4 C) and along cleavage planes of rotting grains. This is best observed with back-scattered images from the microprobe, see Plates 5 A-C.

Factors affecting reservoir quality

Quartz overgrowths are developed to a minor extent and do not significantly effect porosity. A more important factor is the presence of bedding parallel 'platy' micas which act as an effective barrier to *vertical* permeability. Volumetrically important authigenic kaolinite is seen growing out into pore spaces from grain surfaces, although this is suggested only to exert a minor effect on porosity-permeability (Russell, 1982).

4.2.1.2 Etive Formation (B2 reservoir unit) Core interval 10475'-10546'

This is the most densely sampled interval of the current study. It is also the most important reservoir unit of the Brent Group reservoir, principally due to its consistent mineralogy and petrophysical character.

Core from the lower section is described as medium grained cross-bedded sandstone, (Plate 2), fining up to a fine sandstone in the upper section, where bedding becomes faint and massive. The sequence is interrupted by a 30 cm interval of organic mudstone (*viz.* 10486.2') and a mottled and rootletted, medium sandstone grading up into a 75 cm thick carbonaceous sandstone/coaliferous horizon (*viz.* 10495-96') with a mudstone interval directly above (*viz.* 10495-96'). Total carbon values for the carbonaceous horizons are in excess of 10%.

Mineralogy

XRD results suggest a reasonably pure sandstone succession consisting dominantly of quartz (61-84%), with less K-feldspar (5-23%) and albite (0-8%) than the Rannoch Formation. Micas do not appear in any great abundance (<1%) whilst kaolinite (3-17%) is the major clay phase. This is verified by orientated clay XRD analysis, (Figure 4.5). Authigenic kaolinite 'accordions' similar to the Rannoch unit are present in the cleaner sandstones. These are seen under the SEM to be filling pore spaces as well crystallised 'accordion booklet' structures and less crystallised vermicular structures, (Plate 4 A & B). This suggests it is authigenic (Blanche & Whitaker, 1978, Russell, 1982), and probably an alteration product of the leaching of K-feldspar (Plate 4D). Authigenic siderite and detrital rutile are also identified by XRD, garnet and zircon by thin section and microprobe (together approximately < 0.25 wt%). Minor pyrite is detected in samples surrounding the coaliferous layer (*viz.* 10491' and 10498-99'), see Plate 4E. Albite feldspar appears more altered than K-feldspar, often being partially or totally rotted. Microprobe analysis identifies K-feldspars with partially rotted/leached rims, that have altered to form kaolinite, although no significantly voluminous secondary porosity is present. K-feldspars may have been partially preserved, as elsewhere in the Brent Province, due to buffering of the pore waters with K by mica alteration (Bjorlykke & Brendsal, 1986). Quartz overgrowths are rare.

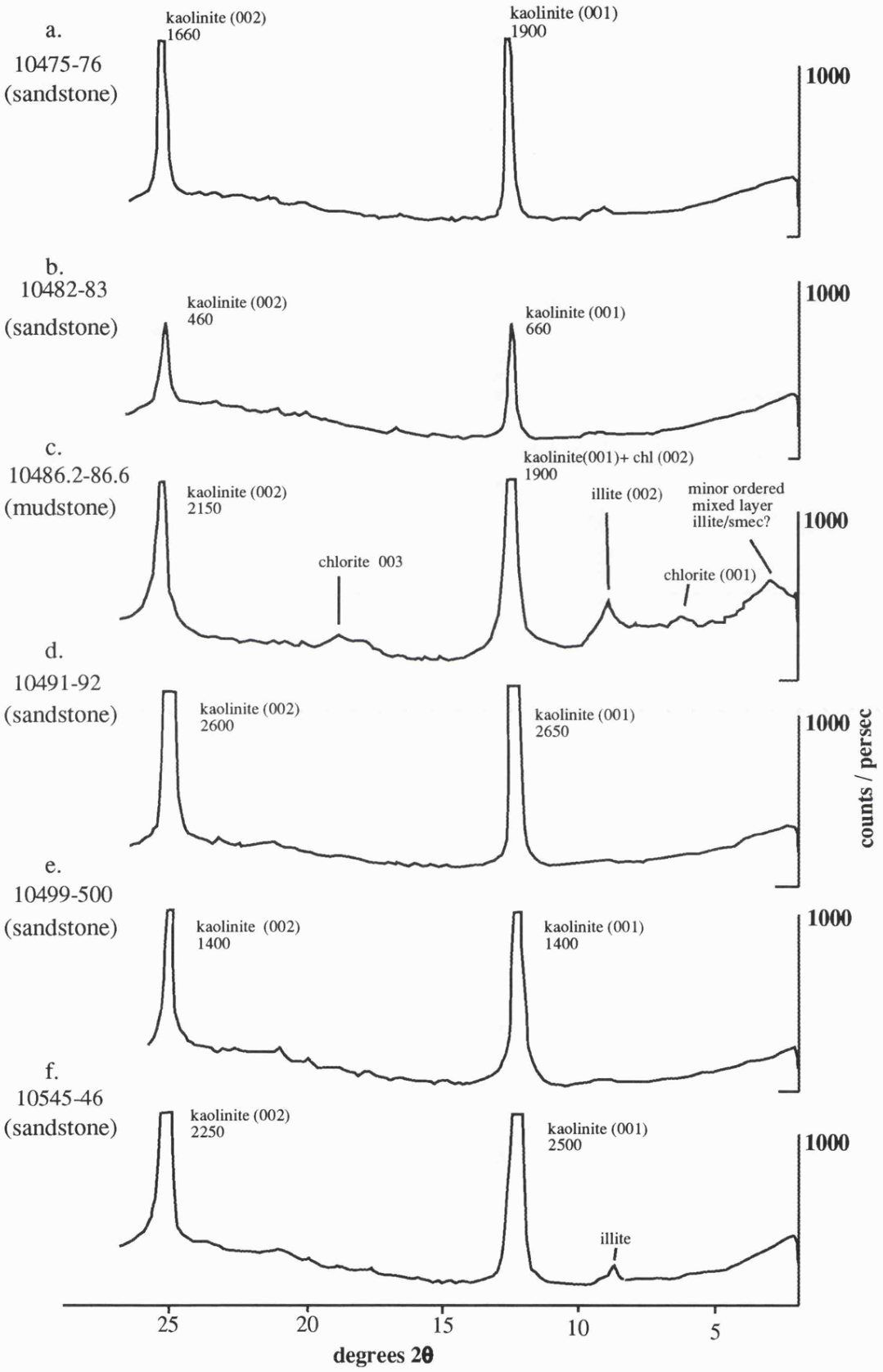

Figure 4.5 Glycolated XRD traces of <2μm clay fraction, Thistle 211/18a-a33 reservoir section (figures by peaks are intensity and reflection surfaces (in brackets)

Factors affecting reservoir quality

The Etive unit has no mica present to affect vertical permeability. It has a larger overall grain size and a net reduction in clay mineral proportions, all of which make the Etive a cleaner reservoir. Russell (1982) suggests the upper fine-grained unit of the Etive has more kaolinite resulting in a decreased permeability value; this is not observed in the current study. A restriction on vertical permeability comes from the shale intervals through the Etive section, although Russell (1982) reports that the carbonaceous/mudstone horizon does not extend to adjacent cored wells and is therefore not laterally persistent.

4.2.1.3 Lower Ness Formation (C1a reservoir unit) Core depth 10452'-10474'

The base of the Ness rests Formation conformably on the underlying Etive B2 unit. The first 75 cm consists of a silty shale passing rapidly into 4m of dark grey faintly laminated shales. These pass into a ripple laminated, burrowed, fine grained sandstone with frequent silty/mud drapes. Rippled sands comprise the rest of the Ness Formation studied, coarsening slightly upwards to include some medium grain sandstones (Plate 3).

Mineralogy

This appears the most heterogeneous unit of the interval. Only six samples were analysed, four from the basal mudstone, two from the overlying sandstone. The sandstone section above the shale sequence appears well sorted comprising a similar mineralogy to that of the Etive, locally with very clean sandstones, where quartz (80-83%), K-feldspar (10%), albite (1-3%) and kaolinite (4%) are the dominant phases. Trace amounts of detrital garnet and zircon have been identified by probe and thin section. Mica is rare.

Factors affecting reservoir quality

Locally mudstone drapes are reported in the upper sands which would affect net permeability. The two sandstone samples analysed (*viz.* 10452-54', 56-58') appear to be the purest of the whole section and interval *viz.* 10455' produces a helium porosity of 29.8%, a vertical permeability of 5310 mD and horizontal of 3790 mD. The shale interval between the underlying Etive provide the largest barrier to permeability. The reported heterogeneous nature of the formation suggests these localised pure sands (probable channel-splay sands) do not exist in great enough volume to make it as important as the Etive B2 reservoir unit.

4.2.3 Mineralogy of the mudstones in the upper Etive and Ness Formations

Five mudstone samples were analysed, four from the base mudstone of the Ness, one from the thin interval in the upper Etive (*viz.* 10486.2') sandstone unit.

A combination of techniques have been employed to characterise the mudstone lithologies seen in this Thistle section. These include whole-rock XRD, for the identification of the detrital phases; orientated and unorientated XRD of the <2μm fraction, for verification of the clay mineral species and SEM to verify mineral morphology. Whole-rock XRD

identifies eight mineral phases in the mudstone sequence. The dominant mineral is kaolinite (*tentative* estimates of between 64-73 wt%), with *detrital* quartz (20-26%), K-feldspar (4-5%), plagioclase (2-7%), and mica (2-7%); see Plate 6 A - B and Appendix 4.4. Detrital rutile (1-2.5%) and siderite (1-3%), as well as diagenetic pyrite, are also identified. Clay mineral phases identified by orientated XRD analysis are dominated by poorly crystalline, amorphous kaolinite (up to 80% of the clay fraction); see Plate 6 B-D. Authigenic illite is also observed (by SEM) to be growing as a replacement of the detrital mica in conjunction with authigenic kaolinite (Plate 6A). A mixed layer disordered illite/smectite (Plate 6F) and a chlorite phase are also identified but it is not possible to gain a reliable estimate of these phases except to suggest they occur as relatively minor clay phases, together forming less than 10% of the clay mineral fraction. Figure 4.6 indicates the *tentative* proportions of clay phases, using XRD relative peak intensities of the minor clays.

4.2.4 Geochemistry of the main mineral phases

In terms of mineral modelling, the variation in composition of the minerals through the section is an important requirement. A *wavelength dispersive* (WD) electron microprobe, was employed to analyse the composition of individual silicate mineral species. Up to fifty individual grains of each mineral were analysed. An *energy dispersive* electron microprobe (ED) system was used to analyse *beam sensitive* clays and mica minerals. A statistical summary of the major minerals is presented in Table 4.2. Analyses are presented in Appendix 4.3 and analytical details in Appendix 2.0. Variations in the major phases are listed below and summarised in Figure 4.7.

Feldspar - feldspar end-members K-feldspar and albite are reasonably pure, although K-feldspars shows a minor amount (*viz.* 1%) of Na substitution while albite shows a few excursions up to 3% CaO. One perthite analysis was recorded.

Kaolinite - analyses show very little substitution into their structure (mainly Fe and minor K) with Fe2O3 and K2O oxides to 0.7 wt% and 0.2 wt% respectively.

Muscovite - This phase shows the widest variability in composition. As no distinction can be made between the Fe species, Fe2+ and Fe3+ with probe analysis, all Fe is plotted here as FeO. The AKF[1] diagram in Figure 4.7 shows muscovites to be of a muscovite-phengitic composition. Between 1-7 wt% FeO[2] and 0.5-3.6 wt% MgO both substitute for Al2O3.

Biotite - Few grains of biotite were successfully analysed due to the intense alteration and diagenetic growth of siderite. Respectable analysis shows a fairly typical Fe-Mg composition (22% FeO and 9% MgO).

Siderite - Due to the fine-grained nature of siderite, analyses using the WD program were contaminated with Si and Al. Subsequent analysis using the ED system (although no CO3

---

1 Apices of the *Eskola's* AKF diagram are Al2O3, K2O and [FeO+MgO+MnO] in molecular proportions.
2 All Fe is quoted here as FeO for familiarity; it is however converted to Fe2O3 for modelling.

depth (ft)	Kaolinite 0% 100%	relative peak intensity only: illite 0 250	chlorite 0 250	illite/ smectite 0 250
10470-71	54%			trace
10471-72	64%		trace	trace
10472-73	64%		trace	trace
10473-74	73%			trace
10486.2	44%			

Figure 4.6 Summary of the <2um clay fraction of mudstone samples in the Thistle 211/18a-a33 section. Kaolinite figures are derived from bulk rock XRD of <2 um fraction and are expressed as wt% of the total rock. All other clay phases are simply intensities of basal peaks of each clay phase derived from orientated XRD traces (axis 0 - 250 c/sec). These are illustrated here for comparative purposes only, as no accurate estimates were possible.

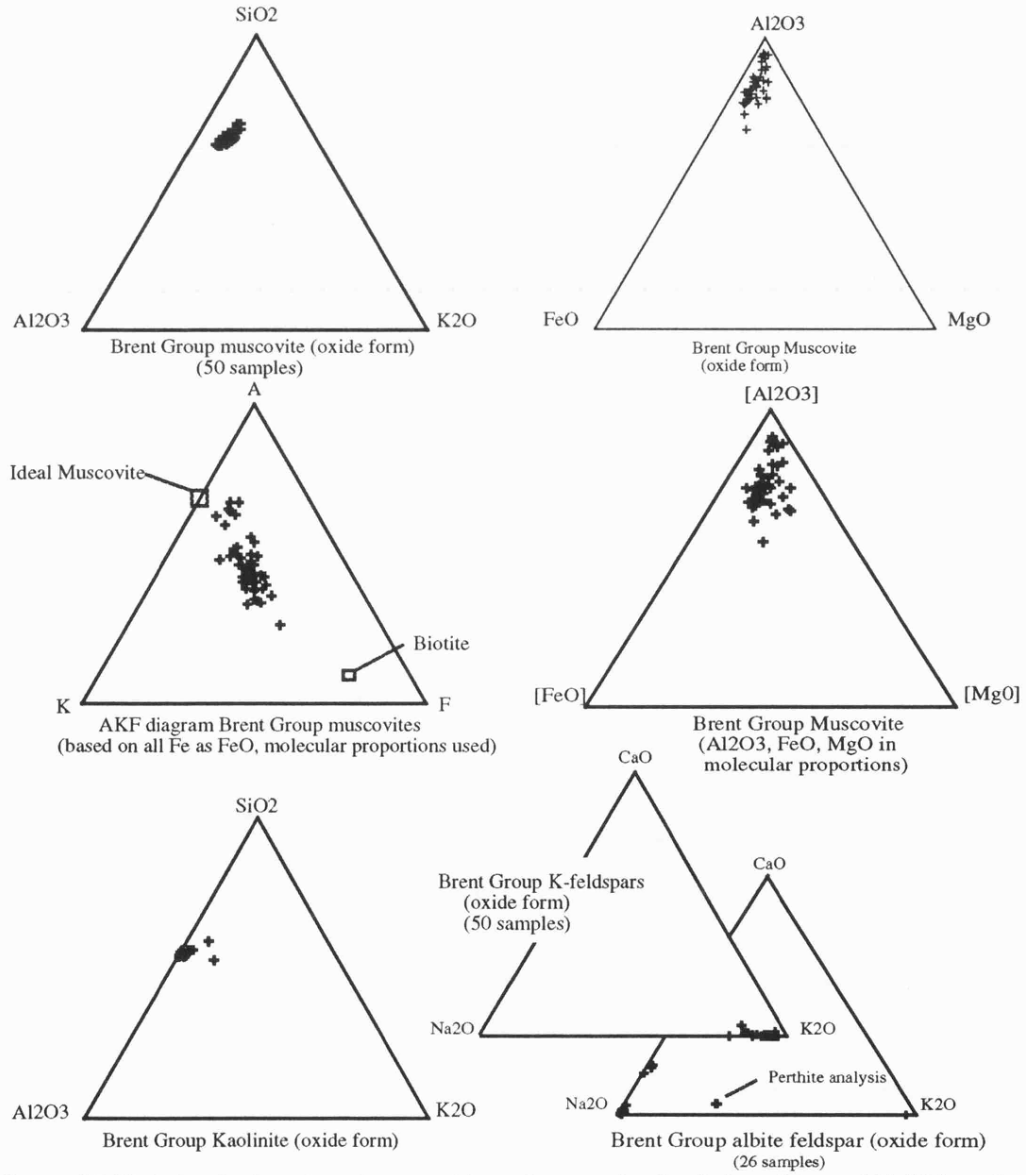

Figure 4.7 Variation in the mineral composition of muscovite, kaolinite, albite and K-feldspar based on microprobe analysis of separate mineral grains from Brent Group. All Fe quoted as FeO. Plotted either in molecular proportions or in oxide form, as stated.

Table 4.2 Summary statistics and cation proportions for individual minerals derived from microprobe analysis. Thistle hole 211/18a-a33.

n-- - Number of samples,
z - Number of zero values (not detected),
z+ - Number of Non zero entries

K-FELDSPAR ..no. samples.....31

Variable	n-	z	z+	mean	StdDev	Min	Max
SiO2	31	0	31	64.18	0.77	61.94	65.58
TiO2	31	4	27	0.0	0.00	0.00	0.0
Al2O3	31	0	31	18.23	0.22	17.83	18.79
Fe2O3	31	3	28	0.00	0.04	0.0	0.14
MnO	31	5	26	0.00	0.00	0.0	0.0
MgO	31	7	24	0.00	0.00	0.0	0.0
CaO	31	3	28	0.00	0.06	0.0	0.32
Na2O	31	1	30	1.02	0.59	0.0	3.10
K2O	31	0	31	15.52	0.84	13.21	16.77
total				99.088			
Si				2.993			
Ti				0.0			
Al				1.002			
Fe3+				0.001			
Ca				0.001			
Na				0.092			
K				0.923			
cations				5.013			
oxygens				8.0			

ALBITE..no. samples.....20

Variable	n-	z	z+	mean	StdDev	Min	Max
SiO2	20	0	20	68.14	1.54	64.92	70.75
TiO2	20	0	20	0.00	0.05	0.01	0.22
Al2O3	20	0	20	19.64	0.80	18.75	21.71
Fe2O3	20	0	20	0.08	0.06	0.01	0.22
MnO	20	0	20	0.00	0.00	0.00	0.00
MgO	20	1	19	0.00	0.00	0.00	0.00
CaO	20	0	20	0.55	0.86	0.02	2.70
Na2O	20	0	20	11.18	1.01	8.54	11.98
K2O	20	0	20	0.54	1.24	0.07	4.18
total				100.15			
Si				2.980			
Ti				0.001			
Al				10.012			
Fe3+				0.003			
Ca				0.026			
Na				0.948			
K				0.030			
cations				5.000			
oxygens				8.0			

KAOLINITE ...no. samples..... 27

Variable	n-	z	z+	mean	StdDev	Min	Max
SiO2	27	0	27	45.95	1.99	41.88	49.04
TiO2	27	20	7	0.20	0.66	0.00	3.39
Al2O3	27	0	27	36.38	1.90	30.92	39.70
Fe2O3	27	17	10	0.80	1.63	0.00	7.60
MgO	27	22	5	0.22	0.74	0.00	3.66
CaO	27	23	4	0.00	0.05	0.00	0.23
Na2O	27	22	5	0.06	0.15	0.00	0.55
K2O	27	11	16	0.23	0.34	0.00	1.39
total				83.87			
Si				4.075			
Ti				0.013			
Al				3.803			
Fe3+				0.052			
Mn				0.0			
Mg				0.028			
Ca				0.0			
Na				0.o			
K				0.026			
cations				7.997			
oxygens				14.0			

MUSCOVITE ..no. samples..... 29

Variable	n-	z	z+	mean	StdDev	Min	Max
SiO2	29	0	29	47.11	2.19	43.55	51.88
TiO2	29	2	27	0.74	0.35	0.00	1.26
Al2O3	29	0	29	29.68	2.85	24.48	35.78
Fe2O3	29	0	29	4.17	1.601	1.10	7.50
MgO	29	0	29	1.77	0.65	0.76	3.34
CaO	29	21	8	0.00	0.08	0.00	0.41
Na2O	29	17	12	0.35	0.61	0.00	2.77
K2O	29	0	29	10.32	1.08	7.94	11.63
total				93.79			
Si				3.197			
Ti				0.038			
Al				2.374			
Fe3+				0.213			
Mn				0.001			
Mg				0.179			
Ca				0.001			
Na				0.045			
K				0.893			
cations				6.941			
oxygens				11.0			

Table 4.2 *Cont.* Summary statistics and cation proportions for individual minerals derived from microprobe analysis. Thistle hole 211/18a-a33.

n-- - Number of samples,
z - Number of zero values (not detected),
z+ - Number of Non zero entries

BIOTITE MICA ..no. samples..... 4

Variable	n-	z	z+	mean	StdDev	Min	Max
SiO2	4	0	4	35.31	0.51	34.71	35.85
TiO2	4	0	4	3.45	0.28	3.22	3.82
Al2O3	4	0	4	16.09	0.08	15.99	16.16
Fe2O3	4	0	4	23.13	0.27	22.85	23.37
MnO	4	0	4	0.51	0.04	0.47	0.56
MgO	4	0	4	8.91	0.16	8.75	9.13
CaO	4	0	4	0.00	0.00	0.00	0.00
Na2O	4	0	4	0.14	0.01	10.13	0.16
K2O	4	0	4	9.01	0.26	8.61	9.16
total				94.29			
Si				2.59			
Ti				0.019			
Al				0.131			
Fe3+				1.277			
Mn				0.032			
Mg				0.973			
Ca				0			
Na				0.020			
K				0.843			
cations				7.317			
oxygens				11.0			

SIDERITE ..no. samples..... 3

Variable	n-	z	z+	mean	StdDev	Min	Max
SiO2	3	3	0	0.00	0.00	0.00	0.000
TiO2	3	3	0	0.00	0.00	0.00	0.000
Al2O3	3	3	0	0.00	0.00	0.00	0.000
FeO	3	0	3	49.18	5.41	44.35	55.02
MnO	3	1	2	0.30	0.28	0.00	0.546
MgO	3	0	3	5.21	2.96	2.09	7.990
CaO	3	0	3	5.28	1.67	3.37	6.430
Na2O	3	3	0	0.00	0.00	0.00	0.000
K2O	3	3	0	0.00	0.00	0.00	0.000
total				54.66			
Si				0.0			
Ti				0.0			
Al				0.0			
Fe2+				7.504			
Mn				0.046			
Mg				1.417			
Ca				1.032			
Na				0			
K				0			
cations				10			
oxygens				0			

QUARTZ no of samples 3

Variable	n-	z	z+	mean	StdDev	Min	Max
SiO2	3	0	3	98.68	0.28	98.38	98.92
TiO2	3	0	3	0.00	0.00	0.00	0.00
Al2O3	3	0	3	0.00	0.00	0.00	0.00
Fe2O3	3	0	3	0.00	0.00	0.00	0.00
MnO	3	0	3	0.00	0.00	0.00	0.00
MgO	3	0	3	0.10	0.16	0.00	0.28
CaO	3	0	3	0.21	0.35	0.00	0.61
Na2O	3	0	3	0.28	0.47	0.00	0.83
K2O	3	0	3	0.00	0.00	0.00	0.00
total				99.44			

CHLORITE no. of samples 3

Variable	n-	z	z+	mean	StdDev	Min	Max
SiO2	3	0	3	27.90	1.71	25.94	29.10
TiO2	3	0	3	1.25	1.03	0.06	1.85
Al2O3	3	0	3	18.90	2.53	17.43	21.83
Fe2O3	3	0	3	28.77	4.88	23.13	31.64
MnO	3	0	3	0.32	0.06	0.25	0.37
MgO	3	0	3	11.08	5.43	7.85	17.35
CaO	3	0	3	0.25	0.21	0.00	0.39
Na2O	3	0	3	0.22	0.09	0.12	0.28
K2O	3	0	3	0.45	0.35	0.05	0.71
total				86.28			
Si				5.995			
Ti				0.202			
Al				4.786			
Fe2+				4.650			
Mn				0.058			
Mg				3.555			
Ca				0.058			
Na				0.092			
K				0.123			
cations				19.518			
oxygens				28.0			

---

measurable) yield slight contamination from Si. This contamination was subtracted out and the analyses re-calculated. The composition of siderite is variable, ranging from 44 - 55 wt% FeO, with substitutions by MnO (0.7-0.5%), MgO (2-7%) and CaO (2.5-6 %).

An interesting point to note, although not in the remit of this study, is the composition of the slightly phengitic muscovite. This may reflect an origin from a low/medium grade metamorphic (possibly greenschist) terrain which, itself, will have implications for basin analysis and provenance studies.

4.2.5 Whole-rock geochemistry of the 211/18a-a33 section

The geochemical characterisation for this section was performed using XRF spectrometry for all major and selected minor elements. Figure 4.8(A) summarises the major element chemistry through the section. Total carbon and sulphur was independently determined using a Leco (carbon and sulphur) analyser. Elemental geochemistry for each sample is presented in Appendix 4.2, analytical details in Appendix 2.0. The only significant *minor* elements are Zr and Ba see Figure 4.8(B). Ba is present throughout the section, up to 5000 ppm (0.5 wt%) (mean 2500 ppm), probably reflecting the presence of baryte. Zr is only present in the Ness and upper Etive (mean 300 ppm) associated mainly with the mudstone/carbonaceous layers (up to 600 ppm) in the Etive and both muds and sands in the Ness. Zr reflects the presence of detrital zircons (ZrSiO4) identified also by the microprobe and SEM, (Plate 4C).

4.2.6 Diagenetic sequence in the 211/18a-a33 section

Petrographic observations from this study verify the overall Thistle Field diagenetic history documented by past workers including Blanche and Whitaker (1978), Hallett (1981), Russell (1982), Pevararo and Russell (1984), Bjorlykke and Brendsel (1986) and Humphreys and Lott (1990). Diagenesis is most evident in the Rannoch (B1) Formation and in localised patches through the coarser Etive. It is suggested that the formation of authigenic kaolinite was synchronous with the leaching of feldspar, and siderite with the alteration of micas (Blanche and Whitaker, 1978). Minor quartz overgrowths in the lower section may suggest a later phase of silica solution, probably from slight grain pressure solution after the main diagenetic event. Russell (1982) reports that further down in the Rannoch section calcite is seen to envelope kaolinite suggesting a later diagenetic event. Diagenesis is envisaged to pre-date the migration of oil into the reservoir, which would have effectively prevented any further diagenesis.

4.2.7 Wireline log interpretation of the 211/18a-a33 section

A conventional suite of wireline logs run in 211/18a-a33 are summarised in Figure 4.3 This combines a composite sedimentary log, core measurements and wireline log curves to enable full characterisation of the interval. The physical wireline log responses can be seen to respond to relative changes in mineralogy through the section.

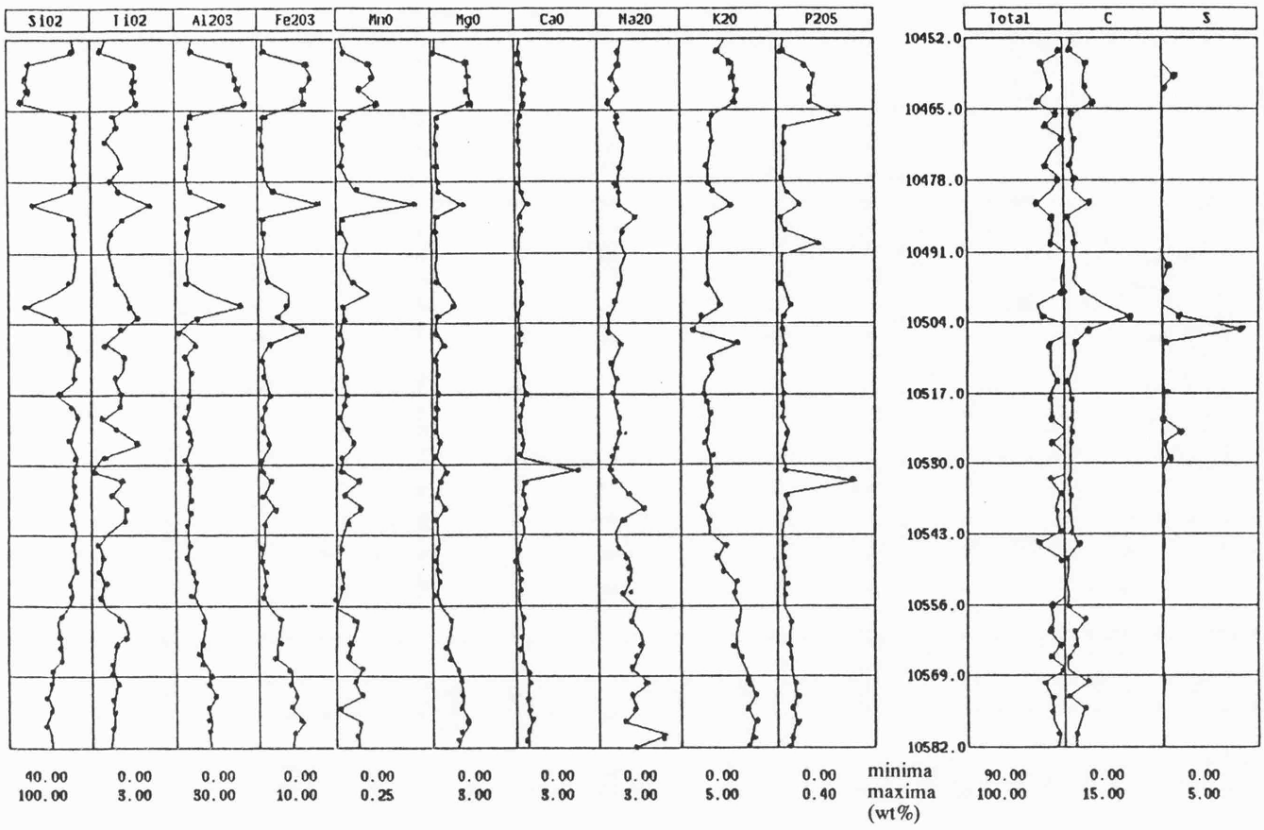

A.

B.

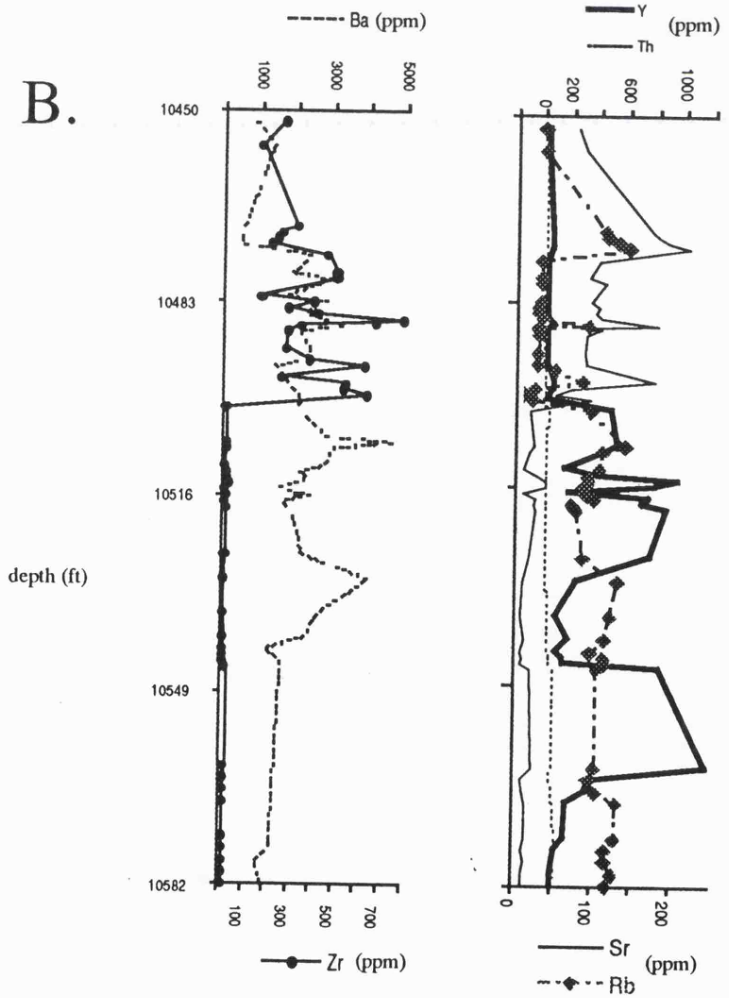

Figure 4.8 Summary of XRF data for the 211/18a-a33 section. (A), major element chemistry for the complete section (wt%) (LOI included in analysis), Carbon and sulphur performed on a Leco analyser. B,Zr, Ba, Y, Sr, Rb trace element signatures (in ppm). Note double Y axis, axis corresponds to labelled elements. Depth in feet.

4.2.7.1 Rannoch Formation

This Formation is known throughout the Brent Province to a give a high *natural gamma-ray signature* (Hodson *et al.*, 1976; Nyberg *et al.*, 1978; Suau and Spurlin, 1982; Pevararo and Russell, 1984) and is recorded through the Rannoch of this section. The presence of high natural radioactivity (GR curve) is primarily due to the high content of K bearing minerals, mica (muscovite, 8-13% and biotite, 6-13%) and K-feldspar (14-20%). Total gamma-ray curve is up to 25 API higher than in the Etive, showing up to 1.5% more potassium from the *spectral gamma* response (SG or K-Log curve). K-feldspar dominates the contribution due to a higher content of K within the mineral structure (refer to Section 3.8, and Figure 3.8). Excursions in the litho-density tool, *photoelectric absorption index curve* (PEF), are due to Fe in siderite. Humphreys and Lott (1990) attribute 80% of the PEF curve in this hole to the presence of siderite (FeCO3), the remaining 20% being attributed to background muscovite, biotite, and minor pyrite. The response to siderite is particularly well seen in thin layers bordering mudstones, (Figure 4.3). The *neutron porosity* and *density curves* are constant through the interval (28-30% porosity and 2.3 g/cm^3 respectively) suggesting no large variations in porosity and mineralogy. Three marked increases in the PEF curve do, however, occur lower in the Rannoch (not studied here). These are interpreted to be due to Fe-calcite cement horizons (*calcite doggers, see Chapter 6*). This is mirrored by a drop in GR (no K, U or Th) and neutron responses (less hydrogen), sonic *interval transit time* values (less porous, cement filled), an increase in density (calcite being denser than silica) typical of a Fe-carbonate lithology log response.

4.2.7.2 Etive Formation

A marked difference is seen in most physical logs from the Rannoch to Etive Formation due to the variation in mineralogy. The GR and K-log both fall to a more typical value for sub-arenite sandstone (<30 API GR units), attributable to the lack of mica and less feldspar, although K-feldspar is still reasonably abundant. Excursions in physical logs occur in the shale intervals; for example, the GR curve goes up to 75 API GR units. Only a slight increase in the K-log is seen suggesting the presence of Th and U at these intervals. A GR increase at one sandstone horizon (interval *viz.* 10530-10535 and to a lesser extent *viz.* 10550-55') up to 70 API units also shows no increase in the K-log. This is attributed to the increase in the Th, due to the presence of phosphatic cement enriched in rare earth elements (REE) (Humphreys and Lott, 1990). This excursion is also mirrored by the increase in the PEF log at this interval, as may be expected from heavier (REE) elements. Phosphates may also account for the increase in Th seen in Figure 4.8 at *viz.* 10550-55'. The neutron log tends to remain similar to the Rannoch Formation (28-30 % NPHI) suggesting no large change in porosity. The bulk-density log drops to a value of 2.15 g/cm^3 in the Etive, attributable to less dense minerals (less siderite, micas and pyrite). An increase in density does, however, occur at the shale and REE phosphate horizons, mirroring the PEF curve.

4.2.7.3 Ness Formation

The basal shales give classical mudstone responses from the physical logs; GR, neutron, density and PEF curves all showing an increase. PEF excursions mirror the siderite horizons in the mudstone. In contrast the clean sand above the mudstones shows a reversal of log responses with the lowest GR, PEF and density measurements of the section. The neutron log measurement is highest in these sands, attributable to the higher porosities observed by core helium porosity measurements.

4.3 Evaluation of transform models

Having extensively characterised the 211/18a-a33 section, it is now possible to use these data to evaluate transform models.

4.3.1 Evaluation strategy

Four different transform models have been evaluated here. These include the Euclidian Distance model, two *direct* Least Squares Error Minimisation models (Choleski and Gauss-Jordan) and the Linear Programming model. Individual sandstone samples have been evaluated for this exercise. Examples are used to illustrate a) the accuracy of each transform model in a clastic lithology; b) the variation in modal estimation due to different mineral compositions; and c) to further illustrate some of the problems, such as compositional colinearity, encountered during modelling of the synthetic data-set. Sandstone samples from the Etive Formation represent a less lithologically complex problem, and are used initially in the evaluation. Sandstones from the Rannoch Formation and mudstones from the Ness/Etive represent more complex lithologies and are modelled thereafter.

4.3.2 Model Parameterisation

XRF analyses for each sample form the *input response vector* for modelling. A full set of nine oxides; SiO2, TiO2, Al2O3, Fe2O3, MnO, MgO, CaO, Na2O, K2O, (wt%) have been used for this evaluation. P2O5, C and S have been left out of sandstone modelling due to their low abundance (<0.04 wt%). Other elements are not present in high enough concentrations to be 'usefully' included in the model. Principal *minor elements* are Zr, *viz.* < 0.25 wt% (assumed to be zircon), and Ba, *viz.* < 0.5% (assumed barite as no evidence of barium in feldspar). These concentrations, in terms of mineral modelling, are trivial and their inclusion would create unnecessary *noise* resulting from a sparse components matrix.

For the purpose of modelling, it has not been necessary to remove any *minor* mineral phases in a *'pre-processing step'*, suggested in Section 3.4.1. This is the strategy that could be implemented if the system is underdetermined, ie, if there are more minerals than oxides. Minor minerals such as barite or zircon, the two most abundant (in Wt %) minor minerals through this section, however, could be removed at this stage if deemed necessary.

The *components matrix* is constructed from the suite of minerals analysed by the micro-probe. Mineral analyses, shown in Table 4.2 , have been separated into *formation* or *hole* specific data-sets and the *mean* mineral composition for either data-set used in modelling. These are summarised in Appendix 4.1.

4.3.3 Results - modelling of sandstones

4.3.3.1 Model accuracy

Table 4.3 demonstrates the solution derived for two Etive sandstone samples by the different models; the Etive Formation representing a clean quartz-feldspathic sandstone mineralogy. Considering the accuracy of XRD is, at best, within +/- 5 wt% (Appendix 2.0), agreements with core mineralogy are excellent for both samples, lying within 3.5% of both the thin section and *MINERALOG* estimates. These results are comparable to the synthetic sandstones previously evaluated.

Figure 4.9 shows the close fit of model derived mineralogy to core XRD estimates for the five dominant mineral phases present over the complete Thistle section, using the Euclidian Distance model. Again, good core agreement suggests accurate modal estimates are possible. This supports conclusions from the previous modelling of synthetic rocks, that the prediction of a very accurate modal estimate is possible if the correct mineral assemblage is known.

Table 4.3. Estimation of mineral proportions by different mineral transform models. Thistle sandstone samples 10482 and 10485-86.

Column 1 XRD observed mineral proportions,
Column 2 MINERALOG observed mineral proportions.(M-log)
Columns 3 Euclidian Distance solution
Columns 4 Error Minimisation-Choleski direct solution
Columns 5 Linear Programming model.

Sample 10482-83	**XRD**	**Mlog**	**3**	**4**	**5**
kaolinite	5.38	5.0	7.22	6.48	4.48
K-feldspar	9.95	10.0	12.95	12.16	9.71
albite	8.80	7.0	6.64	6.38	7.41
quartz	74.38	72.0	73.19	73.82	74.05
SE	-	-	0.975	0.743	-
Mad	-	-	0.534	0.453	0.209
P%acc.					95.65
Sample 10485-86					
kaolinite	7.80	-	6.80	6.78	8.89
K-feldspar	11.38	-	11.50	11.48	11.46
albite	5.42	-	3.74	3.74	0.00
quartz	70.58	-	73.57	73.58	74.20
siderite	0.64	-	3.34	3.32	2.96
rutile	trace	-	1.05	1.05	1.01
SE	-	-	0.091	0.071	-
Mad	-	-	0.042	0.038	0.091
P%acc					98.52

In contrast, Table 4.4 shows a bad example. The Euclidian and Least Squares solutions, solved for using all the observed mineral phases for the sample (column 3) show negative mineral estimates for kaolinite and K-feldspar, the Euclidian model solving slightly less negatively (column 2). The estimate of muscovite from core in this sample is 0.5 wt%. If this is removed from the model, however, good estimates of mineralogy are obtained (column 1).

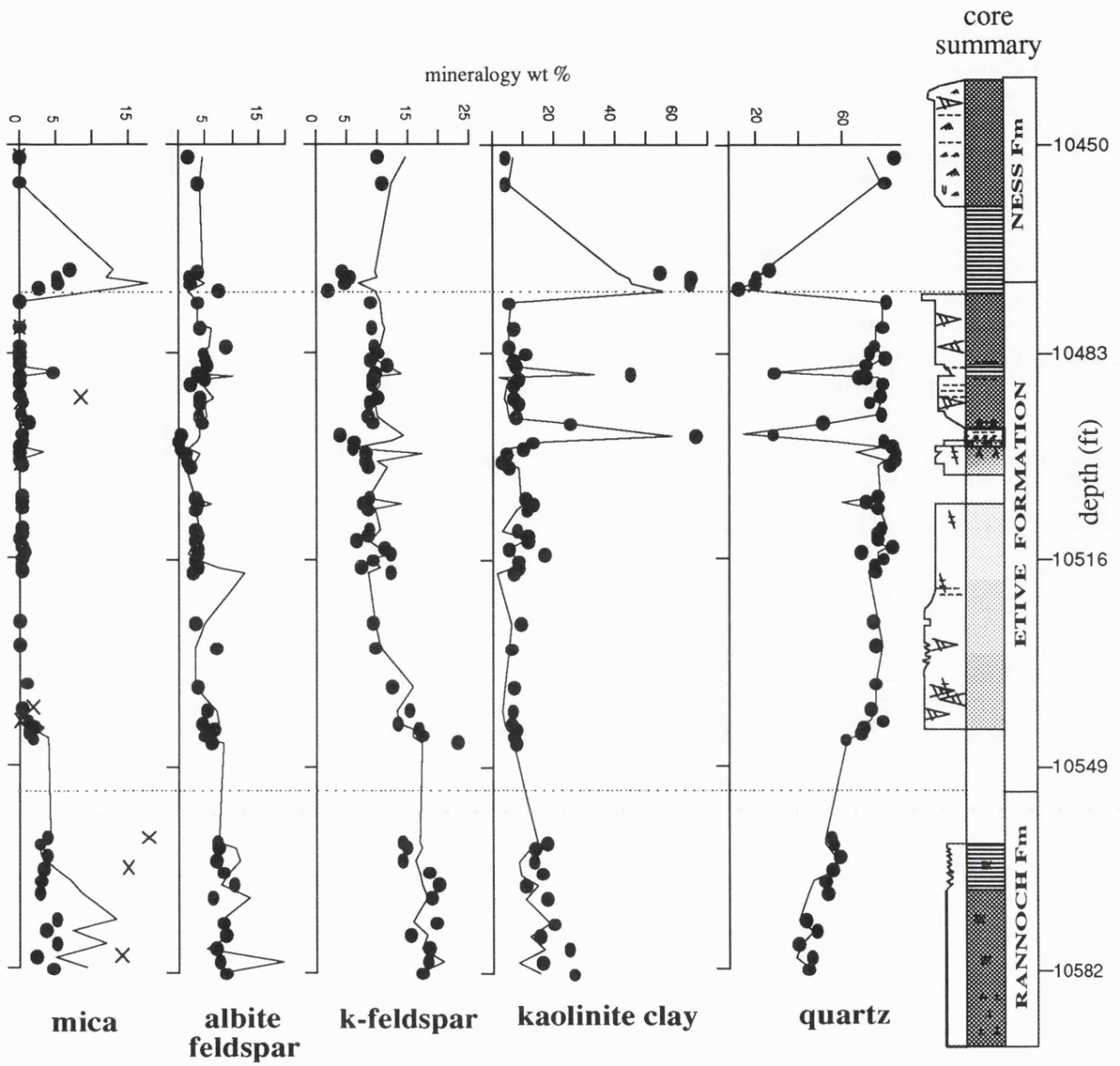

Figure 4.9 Comparison of mineralogy derived from the Euclidian Distance model (lines) and core XRD estimate (dots) over the Thistle 211/18a-a33 reservoir section. Thin section estimates are included in the mica plot (crosses).

Besides a difference in absolute estimates in columns 2 and 3 it is clear that both Euclidian and Least Squares models behave in a similar manner. Linear Programming (column 4), provides a positive result; but it is clear from the estimation of 30% muscovite that the solution is in error. The problem with muscovite is one of compositional colinearity.

Table 4.4 Estimation of mineral proportions by different mineral transform models. Thistle sandstone sample 10501-02.

Column 1 - Euclidian solution without mica, in the model
Columns 2 - 3 Euclidian Distance, Error Minimisation-Choleski direct solution.
Columns 4 - Linear Programming solutions with mica included.

	XRD	1 Euc/no mica	2 Euc	3 Lsq-Chol	4 LP
kaolinite	5.14	8.74	-4.51	-8.15	8.54
K-feldspar	8.32	12.38	-1.98	-5.73	10.89
albite	1.89	1.89	2.31	2.64	2.82
quartz	75.40	75.40	79.90	80.50	40.50
muscovite	0.4	-	23.18	30.33	30.33
rutile	trace	1.59	1.25	1.03	1.11
SE		0.374	0.374	0.606	0.606
Mad		0.177	0.177	0.344	0.344
P%acc					94.19

4.3.3.2 Compositional colinearity

The Rannoch Formation provides an excellent example of a compositionally colinear mineralogy[1] . Table 4.5 shows two samples from the section. Muscovite, K-feldspar, kaolinite and quartz all occur here together; these being essentially coplanar in the K2O-Al2O3-SiO2 system. Columns 1 and 3 indicate a solution *failure* resulting in large negatives and widely erroneous modal estimates. This is due to the inability of the model to solve for these four colinear minerals simultaneously. In contrast, columns 2 and 6 show very close estimates of mineralogy, when muscovite is excluded from the model. Similar results occur in sample 10574.

Table 4.5 Estimation of mineral proportions by different mineral transform models. Thistle-Rannoch Formation samples 10561, 10574. M-log - MINERALOG core estimates, note mica (muscovite & biotite) and illite is combined in brackets.

Column 1 + 3 Euclidian Model (Euc), all observed minerals solved for (including muscovite)
Column 2 + 6 Euclidian Model muscovite not included
Column 4 Error Minimisation model, (Lsq-Chol) all observed minerals solved for (including muscovite)
Column 5 Linear programming model (LP), all observed minerals solved for (including muscovite)

SAMPLE 10561

	XRD	1 Euc	2 Euc
kaolinite	15.64	39.82	13.26
K-feldspar	12.52	53.48	17.35
albite	7.03	5.36	7.58
quartz	48.09	41.92	50.73
biotite	8.41	16.14	10.01
muscovite	7.48	-57.77	-
rutile	trace	1.04	1.06
SE	0.064	0.407	
Mad	0.021	0.204	
P%acc		-	-

SAMPLE 10574

	XRD	M-log	3 Euc	4 Lsq-Chol	5 LP	6 Euc
kaolinite	18.89	13.0	48.33	48.73	21.89	19.65
K-feldspar	18.58	12.0	51.71	52.13	23.06	21.16
albite	7.98	10.0	5.02	5.01	7.37	7.30
quartz	40.81	44.0	29.11	28.98	37.86	37.86
biotite	7.57	(15.0)	20.62	20.80	3.73	10.23
Muscovite	4.92		-57.66	-58.30	0.00	-
siderite	1.25	2.0	2.65	2.64	5.77	3.8
SE	-	-	0.311	0.244	-	0.283
Mad	-	-	0.098	0.077	0.114	0.116
	-	-	-	-	99.67	-

[1] the term compositional colinearity is used here as a generic name, although the systems observed are infact coplanar.

Linear Programming shows reasonable estimates for some minerals, but fails to include any muscovite in the solution (column 5) and is therefore in error. Compositional colinearity is common throughout the rest of the Rannoch Formation.

4.3.3.3 Estimation of mineralogy with a reduced set of oxides.

It was demonstrated previously (Section 3.7.4) that a correct choice of oxides must be present to solve a mineral transform correctly. Two important elemental oxides not always recorded by the Geochemical Logging Tool are sodium and magnesium (See Chapter 2). An example is given here of how important these two oxides are in the solution of the Thistle mineralogy. Na is the dominant cation in albite (*viz.* 11 wt%); which, itself, is present through the Thistle section up to 15 wt%. Na is also found in muscovite, and to a small degree in K-feldspar and kaolinite. Mg is found chiefly in biotite (*viz.* 11 wt %), siderite (*viz.* 5 wt%) and muscovite (*viz.* 1.75 wt%) all of which are present throughout the section. It will be shown that these are clearly important '*descriptive*' oxides for most solutions through the section.

Table 4.6, sample (a) illustrates the effect that Na and Mg oxides have on a solution. Column 2 demonstrates the effect on modal estimates solved without MgO (and MnO). Here, there is a only a small change in mineral estimates indicating that MgO, in this example, is not critical for a reasonable solution. In contrast, column 3, solved without Na2O (and MnO), shows a drastic change in estimates. This is due principally to sodium rich albite feldspar in the sample (5.4 wt % in XRD). The minerals most affected are the minerals now constrained only by SiO2 and Al2O3. These are albite, quartz and kaolinite. The problem is one of colinear compositions as two oxides are present for the solution of three minerals. Without Na2O to constrain the estimation of albite the solution becomes unstable, resulting in negative values. Column 4 demonstrates the effect of neither MgO or Na2O being present; the result is clearly erroneous.

Table 4.6 The effect of using a reduced number of oxides on the estimation of modal mineralogy. Euclidian Distance model used in all solutions.

column 1 full set of 9 oxides modelled
column 2 no MgO modelled
column 3 no Na2O modelled
column 4 no Na2O and MgO modelled

a) Sample 10485-86, Etive Fm

	XRD	1	2	3	4
kaolinite	7.80	6.64	6.02	-40.48	-40.50
K-feldspar	11.38	10.90	11.94	6.71	6.71
albite	5.42	4.28	6.63	96.05	96.08
quartz	70.58	73.52	70.83	33.95	34.05
siderite	0.64	3.58	1.34	1.15	1.15
rutile	trace	1.07	3.25	2.55	2.55
SE		0.148	0.922	0.001	0.260
Mad		0.042	0.311	0.365	0.084

b) Sample 10580-82, Rannoch Fm

	XRD	1	2	3	4
kaolinite	13.97	9.29	9.99	-33.09	-45.73
K-feldspar	15.87	23.18	25.00	19.50	16.34
albite	6.82	19.23	20.82	89.14	105.49
quartz	39.74	37.49	35.91	7.58	0.63
biotite	11.84	3.72	-0.41	15.07	26.41
siderite	1.06	6.32	8.68	1.81	-3.11
SE		0.533	1.199	0.477	0.268
Mad		0.215	0.400	0.143	0.086

Table 4.6b, shows an example where MgO is critical for a solution. Biotite (column 2) shows a small negative (itself containing 9 wt% MgO). The instability of the solution apportions MgO incorrectly to siderite, and over-estimates siderite. The Fe2O3 here, originally in biotite is therefore being reallocated to siderite, resulting in an increase in siderite and a negative value for biotite. Na2O also has a large effect on the solution (for the same reason as sample 10485) producing negative estimates (column 3). Column 4 demonstrates how the lack of MgO and Na2O, together, further degrade the solution.

4.3.3.4 Effect of mineral composition on modal estimates

It was demonstrated in Section 3.8.1 that the choice of mineral composition may ultimately effect a solution. Table 4.7 shows a variety of solutions, obtained by the Euclidian model, where different mineral compositions are substituted into the *components matrix*. In this example, *mean* compositions specific to: a) the sample interval (*viz.* 10485-86'); b) the Formation; c) the complete Brent Group of the section; and d) a theoretical 'text book' composition were substituted and solved for (columns 1-4).

No real difference is seen in the estimation of modal mineralogy between *sample* (column 1), *formation* (column 2) and *hole* specific (column 3) compositions, with a 0.5 wt% difference at the most. The 'theoretical' composition, however, shows a discrepancy in the estimation of albite and kaolinite, yet a closer estimate of quartz. An increased Standard Error suggests, however, that the overall fit of theoretical chemistry is not as accurate as the localised Thistle compositions. Note: the XRD siderite estimate is below any reasonable detection limit and is meaningless here, except perhaps to suggest that siderite is present.

Table 4.7 The effect of a change in composition on the estimation of modal mineralogy. Euclidian Distance model used in all solutions. Thistle Sample 10485-86.

column 1 *Sample* specific composition used
column 2 *Formation* specific composition used
column 3 *Hole* (Brent Group)specific composition used
column 4 Theoretical compositions used
column 5 Theoretical quartz , siderite and rutile compositions used, others are *actual* (probe),compositions
column 6 + 7 Theoretical siderite and rutile compositions used respectively, others are *actual* compositions

		1	2	3	4	5	6	7
	XRD	**sample**	**formation**	**hole**	**theoretical**	**Th-q**	**Th-s**	**Th-r**
kaolinite	7.80	6.80	6.64	6.54	5.18	6.37	7.19	6.80
K-feldspar	11.38	11.50	10.90	11.03	11.54	12.63	11.96	11.50
albite	5.42	3.74	4.28	4.35	7.94	5.49	3.56	3.74
quartz	70.58	73.57	73.52	73.49	70.55	71.12	73.35	73.57
siderite	0.64	3.34	3.58	3.51	3.37	3.11	2.77	3.35
rutile	trace	1.05	1.07	1.08	1.41	1.29	1.18	1.05
SE		0.091	0.148	0.158	0.463	0.478	0.286	0.091

This demonstrates, as in the previous chapter, that for minerals with reasonably *fixed* compositions (all minerals in this example), consistent solutions may be expected. In fact the first three compositions are almost identical. In some instances the *formation specific* averages provide better compositions for modelling than *sample specific* compositions. This is understandable, as the mean composition of the *formation*, on a core scale, provides a statistically more meaningful composition than a single sample. *Formation specific* compositions are therefore used in the majority of subsequent modelling. This is quite

important in that it points to the way in which models could be used 'generally' within a formation following only a moderate amount of core/mineral input.

Column 5 illustrates a solution where a mix of *actual* compositions (for the minerals kaolinite, albite, K-feldspar), and *theoretical* compositions, (for the single fixed composition minerals; quartz, rutile and siderite) are used together. Columns 6 and 7 demonstrate how the modal estimates can vary with just the alteration of one of the compositions of the minor phases, rutile or siderite. This can have a marked effect on modal estimates.

Table 4.8 demonstrates the effect on a solution when different compositions of one mineral which has a *variable composition* are substituted. In this case, mica is only present in a small quantity. Compositions specific to the formation and to the section as a whole are used in addition to a set of theoretical compositions. An increasing discrepancy in mineral estimates, from former to latter, is clearly seen; the *formation specific* solution in fact being the only sensible answer without negative phase estimates. Column 4 shows an alternative solution where a slightly Fe-rich muscovite is substituted and whose solution is equally poor. In this example the *hole specific* composition is clearly too generalised a composition to use in the model (computed as a combination of all minerals from the Etive, Rannoch and Ness formations). It indicates that a reasonable level of detail, to a *formation* specific level at least, should be used when modelling minerals such as mica, whose change in composition may affect a solution drastically.

4.3.4 Modelling of mudstone samples

Ten mineral phases were identified in the two mudstone sequences from the section. They provide a different lithology to the sandstone examples and provide an example of a more mineralogically-complex problem.

Table 4.8 The effect of a change in mica composition on the estimation of modal mineralogy. Euclidian Distance model used in all solutions[1] . Thistle sample 10518.

column 1 Formation specific composition used
column 2 Hole (Brent Group) specific composition used
column 3 Theoretical compositions used
column 4. Fe rich muscovite used

	1	2	3	4
kaolinite	1.93	5.98	48.64	30.06
K-feldspar	8.12	13.96	58.67	60.33
albite	12.59	12.41	13.58	15.96
quartz	71.82	70.43	49.18	60.39
siderite	3.68	4.06	2.58	11.52
muscovite	1.32	-8.41	-73.91	-80.30
rutile	1.54	1.55	1.19	1.89
SE	0.699	0.667	0.286	0.325
Mad	0.286	0.276	0.083	0.100

It was not possible to obtain respectable microprobe analyses for *illite* from either of the sandstone or shale samples during this study. The estimation of such a fine grain phase by microprobe is difficult due to surrounding matrix contributions and in this sample set is compounded by the paucity of identifiable illite. More appropriate equipment (such as

[1] The Euclidian model is used arbitrarily here, Least Squares (direct solution) -models behave the same.

analytical transmission microscopy - ATEM) was not available for this study. Coupled with the problem that no published illite analyses from the Brent Group were found for use in modelling, a collection of 'global' illite analyses have been compiled to discern an *average value* to be used in modelling from Deer *et al.*, (1966); Weaver and Pollard, (1973); and G. Christidis *pers. comm.*, (1992). See Appendix 4.1. S. Burley *pers. comm.*, (1992) suggests that *authigenic* illites, such as observed in the Brent Group can have reasonably consistent compositions within a formation. Through necessity, this is assumed for modelling, although *detrital* illite compositions could remain a problem. (The problem of variable clay mineral compositions is addressed more fully in Chapter 5). Chlorite and mixed layer illite/smectite also occur in low concentrations although, again, it was also not possible to obtain analyses of these clay minerals by microprobe analysis.

The compositions of all *remaining* mineral phases have been kept consistent with sandstone compositions. The assumption here is that the small vertical thickness of the mudstone intervals (<0.3m) and lack of lateral continuity (Russell, 1982) suggest that the source area did not deviate strongly from that of the sandstones. It is conceivable, however, that the source area may have changed and compositions may therefore vary, especially with differences in diagenesis. Any minor change in composition of these relatively *fixed composition* phases should not affect the modelling to a great extent.

Initial attempts to model mudstones appeared problematical. An immediate problem is encountered when such a large number of mineral phases is present and the solution under-determined. Table 4.9 demonstrates different transform model solutions of three mudstones. The identification of illite and illite/smectite, in addition to detrital K-feldspar and muscovite, kaolinite and quartz further increase the problem of colinearity in the system K2O-Al2O3-SiO2 (Section 4.3.3.2). The presence of chlorite and illite/smectite, which both contain MgO and Fe2O3, in addition to siderite and biotite also tend to increase the degree of colinearity in the SiO2-MgO-Fe2O3 system. In these examples K-feldspar and plagioclase have been modelled as one phase (see *binary modelling strategy*, next chapter) to reduce the number of phases to be determined.

In column 1, Table 4.9 (a), chlorite is not modelled, so as to reduce the number of minerals. Columns 2-3 use the same assemblage of minerals (chlorite included this time) solved by Error Minimisation, Euclidian and Linear Programming models respectively. In all cases (columns 1-4) estimates are poor with kaolinite under-estimated by a factor of two and illite over-estimated by up to a factor of 5. Note that the illite estimation is only *tentative* and that there may possibly be another phase present, a trace amount of mixed-layer illite/smectite (refer to Section 4.2.3 and Figure 4.4).

In Table 4.9 (b), sample 10473-74', notice that two estimates of core mineralogy strongly contradict one another. This, itself makes any comparison with model derived mineralogy strongly subjective and indicates one of the largest problems encountered when evaluating mineral modelling in mudstone mineralogies. The Linear Programming solution in Table 4.9 (b), sample 10473-74', provides the most feasible result of the different models, (column 1 to

3) simply because no negatives are recorded. In fact it corresponds remarkably well with the MINERALOG mode. Compared to XRD; however, estimates of kaolinite are low by a factor of 2 and illite is over-estimated by up to a factor of five. Column 4 shows a Euclidian solution with illite left out and estimates are at least positive, although still in error. Sample 10486.2 also shows an erroneous solution.

Table 4.9 Modal estimates from two different shale intervals in the Thistle section demonstrating the poor solution by various mineral transform models.

Target - estimated mineral proportions, Mineral mnemonics: binary fsp- total feldspar (66% k-fsp-33% albite)., M-log - MINERALOG core estimate (NOTE. illite + muscovite are quoted TOGETHER as *illite* in Table b) Illite composition is that of a Fithian illite (average from Weaver and Pollard, 1973), chlorite- a MgO rich variety (Deer *et al.*, 1966). All other compositions are *specific* to the Thistle hole 211/18-a33.

Table a), **sample 10472-73**

column 1 Euclidian Distance solution (no chlorite)
column 2 Euclidian Distance solution (with chlorite)
column 3 Choleski direct solution (with chlorite)
column 4 Linear Programming solution (with chlorite)

	Target	1	2	3	4
quartz	20.00	12.94	15.69	15.70	15.78
binary fsp	6.00	5.95	13.36	13.38	13.09
Kaolinite	64.00	38.34	37.76	37.97	38.62
illite?	5.00?	29.87	21.87	21.79	22.72
muscovite	7.00	6.90	1.61	1.63	0.00
chlorite	trace	-	3.29	3.30	3.34
siderite	1.48	4.93	5.17	5.17	5.18
rutile	2.32	1.07	1.25	1.25	1.26
SE		-	0.015	0.010	-
Mad		-	0.004	0.004	0.019
P%acc					99.99

Table b)

column 1 Euclidian Distance solution (no chlorite)
column 2 Linear Programming solution (with chlorite)
column 3 Choleski direct solution (with chlorite)
column 4 Euclidian Distance solution(no illite)
column 5 Euclidian Distance solution

sample 10473-74

	Target	M-log	1	2	3	4
quartz	20.10	9.0	0.99	9.36	4.81	27.42
bin- fsp	10.50	2.0	5.03	5.23	7.91	23.24
Kaolinite	73.28	42.0	33.38	43.96	38.86	29.52
illite	5	40.0	76.56	26.25	47.79	-
muscovite	2.17	-	-20.00	6.84	-7.23	2.17
chlorite	1.00	6.0	-	-	2.45	4.85
siderite	2.10	1.0	2.78	5.07	3.92	10.49
rutile	2.16	n/a	1.28	1.30	1.38	2.30
SE	-	-	0.399	-	0.276	0.653
Mad	-	-	0.141	0.079	0.118	0.280
P%acc	-	-	-	95.31		-

sample 10486.2-8

	Target	M-log	5
quartz	28.57	21.0	18.60
bin-fsp	13.10	10.0	17.02
kaolinite	44.91	30.0	15.07
illite	5?	26.0	65.70
muscovite	5.00		-27.03
chlorite	trace	3.0	1.33
siderite	5.60	10.0	7.28
rutile	3.44	n/a	1.97
SE	-	-	0.572
Mad	-	-	0.250

This assemblage of minerals provides an example one of the most severe forms of compositional colinearity, the result being that the components matrix becomes ill-constrained, producing in erroneous modal estimates. The lack of very good quantitative mineral estimates of the clay phases has also hampered the evaluation. It may be, for instance, that the Linear Programming solution for sample 10473-74 (column 2) provides a closer estimate of modal mineralogy than the core estimates.

Summary of the problems with modelling the mudstone interval.

a) Severe compositional colinearity:

i)- illite-muscovite (mica) - K-feldspar - kaolinite phases (K_2O-Al_2O_3-SiO_2 system).

ii) -siderite-biotite-mixed layer illite (Fe_2O_3-MgO system).

b) Presence of a large number of mineral phases causing an *under-determined* system.

Ten mineral phases to be 'solved for' by 9 oxides.

c) Presence of clay and detrital phases which exhibit a high degree of ionic substitution and therefore compositional variation.

4.4 Synopsis and conclusions.

It is only possible to accurately evaluate mineral transform models on real sediments if extensive and careful analysis of all the variables in the problem are known and characterised. This has been attempted at the beginning of the chapter and the data preparation (parameterisation) for mineral modelling described. Mineralogy has also been related to the responses seen in wireline log data.

Subsequent mineral modelling results show that modal estimates that agree with core estimates are possible. Verification with core estimates can, however, be problematic; for example, where phases such as siderite and rutile are present at concentrations below their realistic detection limit by XRD, and cannot be compared directly with modal mineralogy (such as in Table 4.7). MINERALOG and thin-section estimates help to verify the existence of these phases.

Similar observations to Chapter 3 can be seen between models. Least Squares Error Minimisation models tend to solve in an identical fashion to the Euclidian Distance model in all examples, while Linear Programming produces different, often inferior solutions.

Compositional colinearity is a significant problem especially in the Rannoch Formation and mudstone lithologies. It must be recognised early in processing to avoid erroneous solutions and inaccurate estimates. Modelling of the Ness and Etive mudstone samples demonstrate one of the worst cases of colinearity possible. They also demonstrate how an inadequate set of oxides (under-determined system) will affect a solution. This should be considered *apriori.*

Different input mineral compositions also affect a solution. In general, the *sample specific*, *formation specific* and *hole specific* compositions show very similar estimates in modal mineralogy through the Thistle field if minerals with highly variable compositions are not present. For minerals that can vary in composition, such as muscovite, it is very important to get as close an estimate of the *actual* composition as possible; this is discussed in the next chapter. At the very least these compositions should be specific to a formation or single lithology scale.

In the light of the problems faced in the modelling of the synthetic and Thistle data sets, the next chapter looks at some of the strategies for overcoming these problems, drawing on examples from both data sets.

Chapter 5.

Strategies for overcoming the main problems faced by transform models

5.1 Introduction & Objectives

This chapter introduces and evaluates some *strategies* which attempt to overcome problems encountered by mineral transformation models, examples of which have been illustrated in the previous two chapters. Some of these strategies have been developed previously by Harvey *et al.* (1990) but lack a complete and extensive evaluation of their validity. These are therefore illustrated and evaluated using examples from the *synthetic rock* and *Thistle reservoir* data sets. Other strategies are introduced as new options and their usefulness evaluated on the same data set. At the end of the chapter, data from the Thistle 211/18a-a33 section provides a *case study* for the implementation and combination of some relevant strategies. This is in an attempt to produce, in a *single pass*, accurate mineral estimates that are unaffected by the inherent problems of mineral inversion. In the *case study*, strategies are deployed on three different transform models and the performance of each compared.

In summary, the main problems experienced by the various mineral transform models are:

-An incorrect choice of the mineral *assemblage.*

-The number of mineral phases *exceeds* the number of descriptive oxides available for modelling (the *under-determined* system).

-The compositional *colinearity* between three or more minerals, reducing rank of the matrix.

-An incorrect choice of the mineral *composition.*

5.2 Choice of mineral assemblage.

All mineral transform examples in the last two chapters have been performed on individual samples where the assemblage of minerals was known (from prior core knowledge) and could be modelled accordingly. Erroneous solutions will result if a single, *fixed*, assemblage were used to model a complete borehole interval, where substantially different lithologies and widely varying mineral assemblages might occur. This is an approach, however, that is used in *conventional log analysis,* where the components matrix is *inverted* once (commonly using an indirect inversion model, Section 3.3.1) and applied to all intervals (Doveton, 1986). None-the-less, for *mineral modelling* it is crucial that the correct mineral assemblage is chosen at *each* sample (depth) interval. If a wrong assemblage of minerals is chosen then the chemistry will be allocated to the wrong phases, resulting in erroneous mineral estimates.

5.2.1 Selected assemblage strategy

One strategy is to draw up a table of possible mineral assemblages, from local-field knowledge prior to modelling (Harvey *et al.*, 1990). This model in-turn solves for each of these assemblages. The mineral assemblage whose solution 'best fits' the given (observed) chemistry, shown by the lowest estimate of Standard Error, is selected as the most suitable mineral phase. Table 5.1 shows a summary 'output' for the six *synthetic* 'rocks' (using the *Error Minimisation* model). The six pre-selected assemblages are solved, in-turn, on each synthetic rock mixture, and the assemblage with the lowest Standard Error chosen. In this case we know the assemblages and can verify the results. The strategy both chooses the correct assemblage and the correct modal estimates. The results are in fact identical to the results from individual modelling in Chapter 3.

Table 5.1 Summary data for the selected phase assemblage strategy, performed on the synthetic data set Summary data includes the possible mineral assemblages chosen, the Standard Error estimates (SE) and the chosen assemblage for each sample.

Table of possible **mineral assemblages**

1	quartz + albite + kaolinite + K-feldspar	Equivalent to synthetic **Mix 1**
2	quartz + K-feldspar + calcite + dolomite + muscovite	Equivalent to synthetic **arenite**
3	quartz + albite + K-feldspar + dolomite + kaolinite + muscovite	Equivalent to synthetic **semi- pelite**
4	quartz + kaolinite + muscovite	Equivalent to synthetic **Mix 2**
5	quartz + K-feldspar + dolomite + kaolinite + muscovite	Equivalent to synthetic **pelite**
6	calcite + dolomite	Equivalent to synthetic **carbonate**

Assemblage chosen and Standard error estimate

Mix 1	SE 0.105	assemblage chosen	[1]
arenite	SE 0.243	assemblage chosen	[2]
semi-pelite	SE 0.303	assemblage chosen	[3]
Mix 2	SE 0.216	assemblage chosen	[4]
pelite	SE 0.286	assemblage chosen	[5]
carbonate	SE 0.001	assemblage chosen	[6]

It is often possible to obtain a detailed idea of mineral combinations from core or local knowledge. A computer program can then be used to collate all possible combinations of assemblages from such a list of minerals. These assemblages can be fed, then, into the model. An example of the use of this strategy is given in the *case study* later.

The Standard Error is used here as an appropriate measure for choosing the optimum assemblage. Care must be taken in interpretation as a negative, erroneous solution, may in fact produce the best fit (and lowest Standard Error), but it may not be 'geologically correct'. In fact a possible artefact in the use of Standard Error, is that phases not present in the mode are sometimes present with small, meaningless proportions (*viz.* <0.1wt%). This is not a severe problem and may be eliminated by not 'accepting' phases with proportions below an arbitrary figure (*viz.* 0.5-1 wt%). In general, however, it is observed through this study that the 'geologically correct' assemblage of minerals will often predict a Standard Error estimate far lower than any wrong combination, for a given degree of freedom. This provides some *validity* for the strategy which has become *(through this study)* a routine part of most borehole mineral models.

5.2.2 Reducing phase strategy

This is an alternative approach which has no formal or geological basis. This strategy can only be used with the Euclidian and Least Squares models where negative estimates may be produced. The model iteratively subtracts any negative phases present in a solution, one by one (taking the largest negative first), and re-running the model without that phase. This process is repeated until all negatives are absent. The assemblage with the lowest Standard Error is chosen then as the *correct* assemblage. Linear Programming models, in effect, do this automatically, by virtue of the non-negative constraint in place. In extreme cases, where no information is present to construct a set of assemblages to use in the previous strategy, this strategy may be considered. There is no 'geological' validity, however, for this approach and for this reason it is not considered further.

5.3 Making a solution over-determined

One problem faced when a large number of mineral phases are present is that the transform model becomes under-determined and a solution not possible. It is also important in Least Squares models to keep the number of mineral phases to a minimum, for statistical reasons as well as the *ill-conditioning* of the components matrix. The initial attempts at modelling the mudstone sequence of the Thistle demonstrated the effect a large number of mineral phases has on a solution (Section 4.3.4). Strategies may be implemented that reduce the number of minerals to be solved for, in effect, allowing the solution to work.

5.3.1 Binary iteration strategy

Certain minerals have compositions that vary between end-member phases, or can be treated as such in modelling. Such mineral groups in sediments include feldspars (plagioclase series, or K-feldspar series [albite-orthoclase]), muscovite (phengite-muscovite), chlorites, and Fe-Ti oxides (ilmenite-magnetite). In sedimentary systems where minerals are not necessarily in equilibrium, two such end members may often be found in an analysis. In such a situation by *iterating* between end-member compositions for the best fitting solution a suitable *binary phase* composition will be found that represents the two minerals. In samples which are under-determined such *binary phases* can be used to reduce mineral numbers.

This strategy inputs into the model all intermediate compositions (at specified increments) between each end-member. The Standard Error is used then as a suitable measure of fit to determine the optimum *binary* composition. Figure 5.1, purely for illustration, shows a 'map' of Standard Error values for such a model, shown at 5% intervals, for one gabbro sample containing two binary systems. The size of the square is proportional to the Standard Error estimate when that composition was input to the model. The smallest square is the composition chosen for inclusion in the model. In practice it is not necessary, however, to compute the whole map.

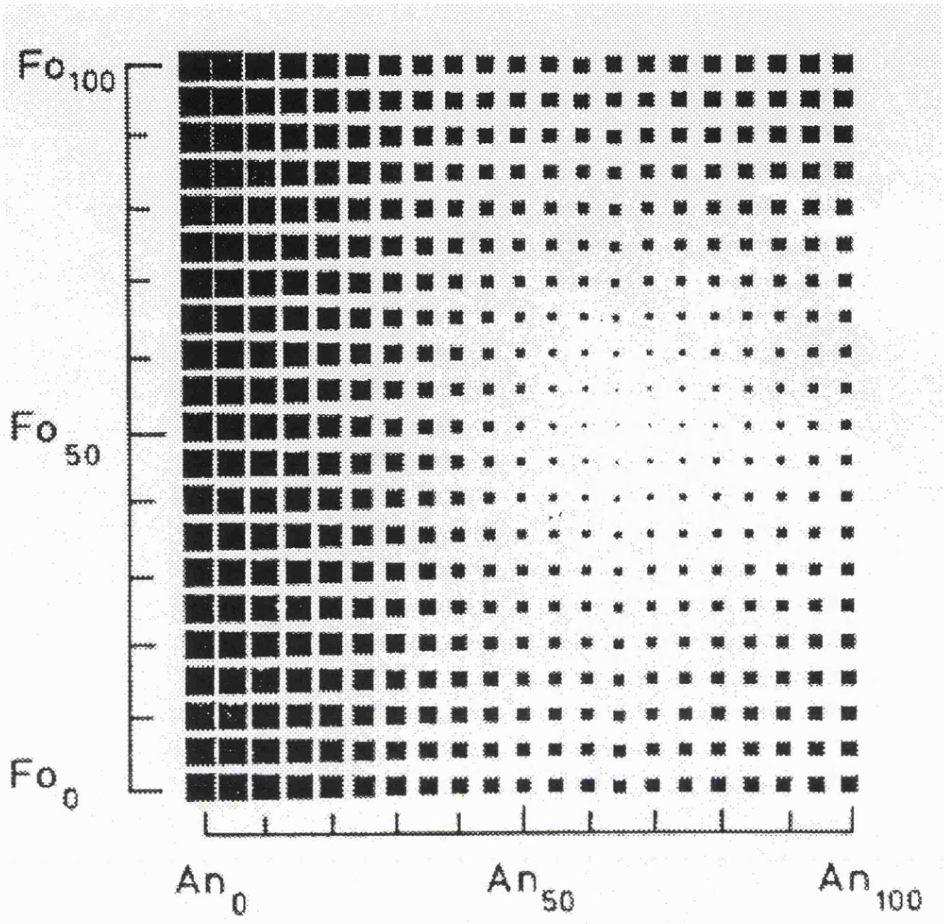

Figure 5.1 Diagrammatic estimation of the best fitting values for An% (Plagioclase) and Fo% (olivine) in a gabbro. An unweighted Least Squares model was used and the size of the square is proportional to the Standard Error for each model fitted. The optimum composition occurs at An % = 67.1, Fo = 48.8.(after Harvey et. al., 1990)

Table 5.2, sample (a) shows an example solution using the synthetic Mix 1. This is a four mineral rock, reduced here to three phases by the *binary iteration* of K-feldspar and albite feldspar. The final choice of composition, in terms of each end-member, is very close to the observed value (65% albite, 30% K-feldspar) and the estimates of modal mineralogy are in very good agreement. For the semi-pelite example (Table 5.2, sample b) the choice of end-member proportions is good (*approx.* 50:50) but because of the problem of colinearity in the sample the modal estimates appear slightly erroneous. The 'Thistle' sample (Table 5.2, sample (c)) also shows a good solution and demonstrates the general applicability of the strategy.

Table 5.2 Modal estimates from two Synthetic rocks and a sample from the Thistle section employing the *binary-iteration strategy*. Binary feldspar represents combined albite and K-feldspar. M-log - mineralog core estimates. Least Squares (Choleski) model used[1].

Column 1 Model with feldspars modelled separately
Column 2 Model with feldspars modelled as one *binary* phase

a. Mix 1		**1**	**2**
	XRD	**Full**	**Binary**
quartz	60.00	59.85	61.57
binary feldspar	30.00	30.28	29.54
Kaolinite	10.00	9.71	8.89
SE		0.246	0.325
Mad		0.120	0.147

b. Semi-pelite		**1**	**2**
	XRD	**Full**	**Binary**
quartz	40.00	38.08	37.81
binary feldspar	30.00	35.30	36.05
kaolinite	15.00	18.71	19.66
dolomite	5.00	4.86	4.88
muscovite	10.00	3.04	2.57
SE		0.35	0.217
Mad		0.146	0.075

Binary composition chosen	65% albite, 35% K-feldspar	45% albite, 55% K-feldspar
core feldspar ratios	66% albite, 33%K-feldspar	50% albite, 50% K-feldspar

c. Thistle sample 10482-83			**1**	**2**
	XRD	**M-log**	**Full**	**Binary**
kaolinite	5.38	5.00	6.84	4.85
binary feldspar	18.75	17.00	18.54	17.68
quartz	74.38	72.00	73.82	74.69
SE			0.743	0.246
Mad			0.453	0.251

binary composition chosen	50% albite, 50% K-feldspar
core ratios	50% albite, 50% K-feldspar

A *binary phase strategy* was employed for the Thistle model shown in Figure 4.9 (Chapter 4), where it was used to combine muscovite and biotite phases as a single *mica* phase. The modelling of binary phases has also worked well in igneous rocks such as for olivines (fosterite-fayalite) and pyroxenes (Harvey *et al.*, 1990).

A step further is to iterate between two such mineral series reducing further the number of minerals to be solved, as illustrated in Figure 5.1. Table 5.3 shows the solution of two Thistle samples modelled with albite and K-feldspar as one *binary phase*. Biotite and muscovite, for modelling purposes, at least, form a second *binary phase*; although they do not form solid solution series *sensu stricto*.

The solutions with all minerals modelled as separate phases (columns 1 and 3), show widely erroneous estimates due to compositional colinearity; the *binary* solution in both cases is far superior. It is not necessary, in general, to implement the binary strategy in the Thistle section, as the number of phases is not great enough to cause an under-determined

[1] The choice of mineral model used in examples in this chapter is arbitary, except where stated.

system. Its usefulness is therefore limited to the mudstone intervals, but as discussed next it can help considerably in alleviating compositional colinearity.

Table 5.3 Modal estimates from Thistle samples 10561 and 10574 using the *binary-iteration strategy*. XRD and MINERALOG values for binary phases are the sum of two independent minerals. Least Squares (Choleski) model used.

Column 1 feldspars modelled separately ("full")
Column 2 feldspars modelled as one *binary* phase ("binary")

a. Sample 10561		**1**	**2**
	XRD	**Full**	**binary**
kaolinite	15.64	39.82	10.47
binary feldspar	19.55	53.48	17.99
quartz	48.90	58.84	52.94
binary mica	15.89	-41.63	17.26
rutile	trace	1.04	1.06
SE		0.407	0.324
Mad		0.021	0.228
Compositions chosen by Standard Error mapping			
30% albite, 70% K-feldspar, (XRD feldspar 40%:60%)			
0% muscovite 100% biotite, (XRD 50%:50%)			

b. Sample 10574			**1**	**2**
	XRD	**M-Log**	**full**	**binary**
Kaolinite	16.42	13.0	48.73	16.42
binary feldspar	26.83	22.0	57.14	23.49
quartz	40.81	44.0	28.98	39.65
binary mica	12.49	15.0	-37.50	16.13
siderite	1.25	2.0	2.64	4.24
			0.244	0.236
			0.077	0.12
26% albite, 74% K-feldspar, (XRD ratio 42%:58%)				
0% muscovite 100% biotite, (XRD ratio 35%:60%)				

5.4 Strategies that overcome compositional colinearity

Certain strategies have been developed in an attempt to overcome the problem of *compositional colinearity* in mineral modelling.

5.4.1 Binary phase strategy

Section 5.3.1 demonstrated the usefulness of *binary* phases in reducing the number of mineral phases for solution. It was realised during this study that binary phases can also be used effectively to overcome compositional colinearity. Phases such as muscovite, are colinear with K-feldspar, kaolinite, illite and quartz in the Rannoch Formation. When treated as a binary phase (with biotite), however, muscovite is 'drawn off' the K2O-SiO2-Al2O3 compositional plane, with the effect of reducing colinearity. This accounts for the superior solutions in Table 5.3, using the binary phase strategy. The solution has become more constrained due to more chemistry being 'locked up' in the binary phases, alleviating colinearity (and reducing the ill-conditioning in the components matrix).

5.4.2 Iterative removal strategy

One strategy adopted by Herron and Herron (1990) in their *normative model* was to subtract a certain amount of the available chemistry from the analysis and allocate this to specific mineral phases before inversion of the remaining chemistry (see Section 3.4.1). The aim of allocating chemistry to minerals was to reduce the number of mineral phases for eventual solution. Such phases chosen for *apriori* subtraction were phases wholly or dominantly responsible for the presence of one particular oxide. Applied in a general sense a *normative* estimate is generated instead of a *modal* estimate, as the subtracted minerals may

not necessarily be present in the actual rock. This would be the case in the Thistle section studied here where pyrite and illite, which are present in Herrons model, are rare. The result would be an erroneously high prediction of these uncommon phases. It is possible to 'tailor' this so that any mineral is subtracted but it is impossible to program in a completely general way (refer to Chapter 3, Section 3.4.1).

If a local mineralogy is familiar so that an idea of the *range* in concentration of a phase that is likely to cause colinearity is known, a modified *subtractive approach* may be employed. This strategy involves subtracting a mineral phase that is likely to cause colinearity.

The composition of the mineral to be subtracted is firstly determined, and corresponding amounts of chemistry subtracted from the sample analysis in various increments up to a geologically realistic maximum concentration for that mineral. The transform model is performed on each remaining analysis, having been re-normalised to 100%. The analysis that has the lowest estimate of Standard Error is used to define the most likely modal mineralogy, in addition to identifying the most likely amount of subtracted mineral. The mineral estimates are then re-normalised to include the mineral originally subtracted.

For example, this was performed on the Thistle samples by subtracting muscovite mica, whose presence causes the colinearity seen in previous examples (Chapter 4). Muscovite is present in the Rannoch Formation, up to 13% although uncommon in the overlying Etive Formation (0-1 wt%). Figure 5.2A demonstrates the variation in modal estimates derived for a mica free Etive sample (10512-14). Muscovite was subtracted from the analysis in various increments up to 15% and the remaining chemistry modelled in a usual fashion. The optimum sample chosen here (the one with the lowest Standard Error (Figure 5.2 B), is the one with no muscovite. This is in agreement with core estimates of *viz.* <0.5% muscovite. Figure 5.2B illustrates the increase in estimates of Standard Error generated for solutions which have up to 10% muscovite subtracted before modelling. Erroneous negative modal estimates in fact occur for the models that include muscovite, see Figure 5.2C. Figure 5.3 shows a similar plot for a Rannoch sample, 10574. Erroneous results are present when muscovite is included in the model; good results occur (with the lowest Standard Error) with 4% muscovite subtracted. Again this is in good agreement with core estimates (*viz.* 5% XRD).

5.4.3 The Weighted Model - to enhance the mineral transform solution.

A further strategy to enhance a solution, especially if hampered by compositional colinearity, is to employ a *weighted model.* The weighted Least Squares model (Section 3.3.3) allows the input responses (contained in the input response vector) to be weighted in such a way that one or more oxides have a greater influence over the solution. The oxide with the greatest weighting therefore has greater influence over estimated mineral proportions. With geochemical logging data there is a considerable range in the accuracy and precision of

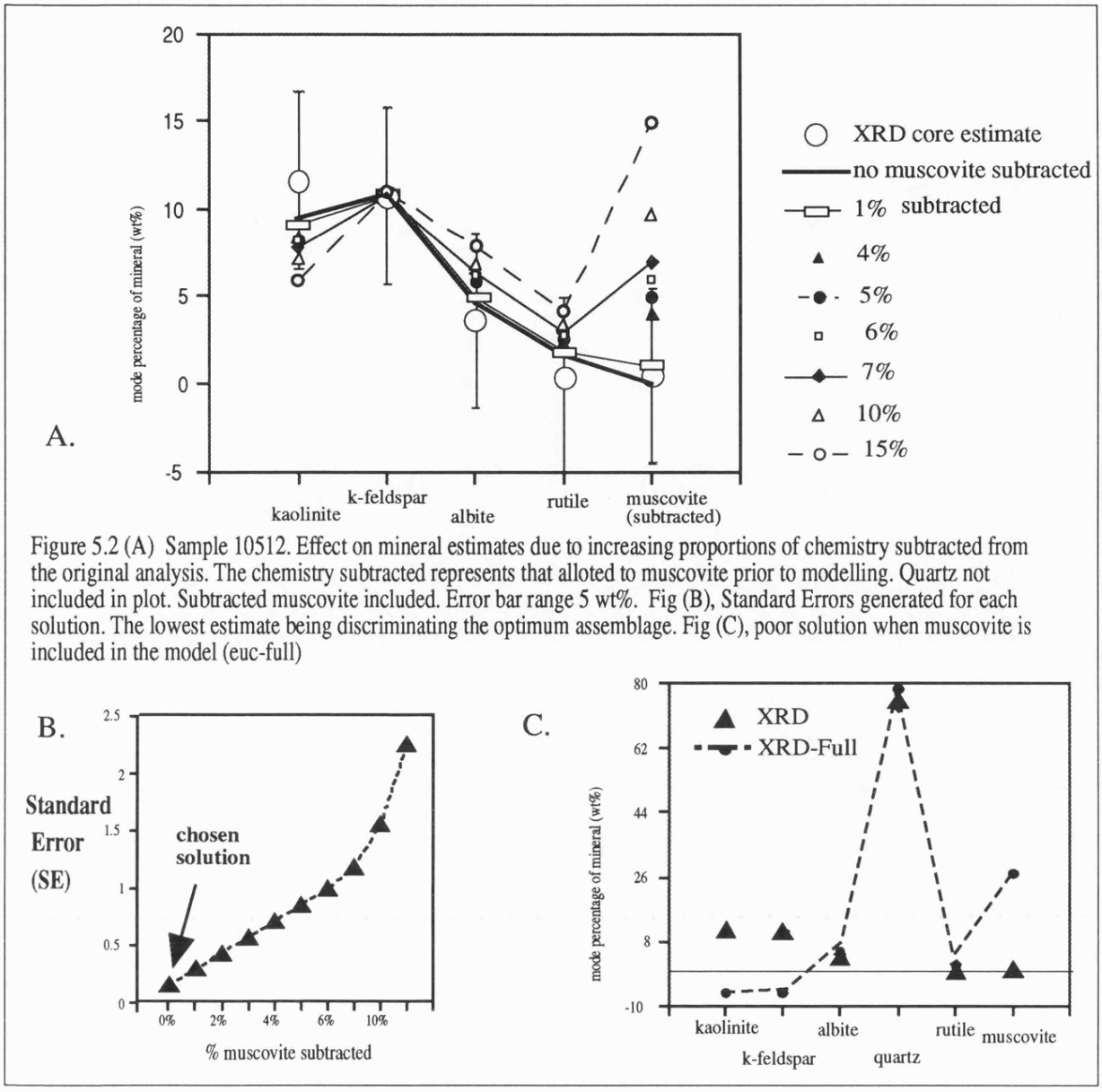

Figure 5.2 (A) Sample 10512. Effect on mineral estimates due to increasing proportions of chemistry subtracted from the original analysis. The chemistry subtracted represents that alloted to muscovite prior to modelling. Quartz not included in plot. Subtracted muscovite included. Error bar range 5 wt%. Fig (B), Standard Errors generated for each solution. The lowest estimate being discriminating the optimum assemblage. Fig (C), poor solution when muscovite is included in the model (euc-full)

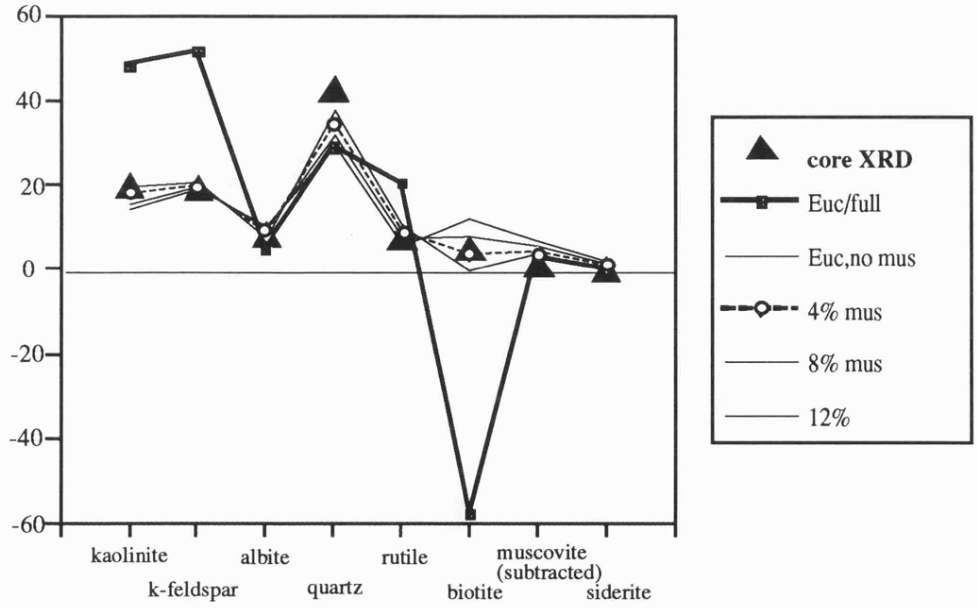

Figure 5.3 Sample 10574-76. Effect on mineral estimates with increasing proportions of muscovite (mus) subtracted from the analysis. 4% muscovite mica subtracted provides he best Standard Error estimate and also the closest solution (euc-full -model with muscovite included)

each of the measured elements. Such *weights* can be assigned to some arbitrary measurement of uncertainty in each input variable. Such weighting can allow, in the context of geochemical logging, elements to be weighted according to the size of these uncertainties. The reciprocal of the average uncertainty for each elemental measurement, is usually used for the GLT tool.

Weighting may also be used to *emphasise* certain oxides in a solution. The purpose of this being to constrain the solution in a way that the least dependence is given to the oxides that are colinear. Such an example of this is included in Table 5.4 where an extra parameter, $H2O^+$ [1], is included in the model, and is weighted strongly against other oxides. The solution is superior to the un-weighted solution.

5.4.4 Addition of 'physical' parameters to the mineral transform model

In a situation where severe compositional colinearity occurs, as in the Rannoch Formation, the addition of extra *physical parameters* into a solution can help 'alleviate' colinearity. In a similar way, addition of extra parameters may help in the 'under-determined' situation to produce an over-determined system. Parameters derived from other routine log measurements may be used for this (Herron, 1990; Wendlandt & Bhuyan, 1990; Van den Oord, 1990). These additional measurements are derived from conventional tools, where the tool response is primarily a function of the fluid fraction. Care must therefore be taken in using them in the context of mineral modelling. Some of these parameters are, however, more closely linked to the matrix rather than the fluid portion; for example, density, Photoelectric absorption, (Pe), and *bound water* $H2O^+$, and therefore may be considered valid as useful additional parameters.

Table 5.4 The use of a weighted model to improve the solution of synthetic *arenite.*

Column 1 Least squares inversion with $H2O^+$
Column 2 Weighted Least squares inversion with $H2O^+$ weighted 55:1 with oxides
Column 3 Weighted Least squares inversion with $H2O^+$ weighted 100:1 with oxides

Target	XRD	1	2	3
quartz	80.00	79.27	80.16	80.66
K-feldspar	5.00	7.85	5.58	4.27
muscovite	10.00	7.97	8.98	9.56
dolomite	2.50	2.62	3.12	3.41
calcite	2.50	2.27	2.27	2.27
SE		0.376	0.414	0.466
Mad		0.217	0.232	0.257

5.4.4.1 The use of bound water ($H2O^+$) as an additional parameter

Clay minerals such as the smectite or kaolinite, and the mica minerals, are *hydrous minerals* in that they contain varying amounts of chemically 'bound' water ($H2O^+$) within their atomic structure. In a situation where severe compositional colinearity occurs, as in the Rannoch Formation here, the addition of an accurate estimate of $H2O^+$ can effectively draw

[1] Modelling with $H2O^+$ is formally introduced in Section 5.4.4.1

kaolinite and muscovite, (which contain, on average, 13 wt% and 4.5 wt% $H2O^+$ respectively), from the colinear plane defined by the oxides common to them, namely SiO2-Al2O3-K2O. Values of $H2O^+$ for some common hydrous minerals are summarised in Table 5.5.

It is possible to gain an estimate of the 'bound water' in a formation from the epithermal neutron tool porosity and density porosity measurement (Ellis, 1986; Herron & Herron, 1990). The *difference* between the density porosity (a measure of the hydrogen in pore spaces, i.e. $H2O^-$ and pore water) and epithermal neutron porosity (a measure of total hydrogen, both $H2O^+$, $H2O^-$ and pore water), is ascribed to the amount of *bound water* contained in hydrous minerals. The difference, when converted to a dry weight percent is called *Wmin* (Herron & Herron, 1990). This tool derived estimate *Wmin* is investigated in Chapter 6.

An improvement in the estimate of the synthetic *pelite* and *semi-pelite* is seen in Table 5.6 where bound water ($H2O^+$) is included in the model. For this exercise an estimate of $H2O^+$ for the sample was calculated from the known proportion of kaolinite and muscovite in the sample, this being included in the model *input response vector.* Similarly, respective values of $H2O^+$ were ascribed to all minerals in the *components matrix,* namely zero for all minerals except the hydrous phases kaolinite and muscovite.

A clear improvement in estimates of both hydrous phases, compared with the *oxide only* solution, is seen the pelite and semi-pelite solutions (Column 2) modelled with $H2O^+$ in these well constrained examples. In the pelite solution the estimate of kaolinite has been improved to within 0.06% of the target value.

Table 5.5 Summary of some typical water contents ($H2O^+$ and/or $H2O^-$) in common hydrous minerals. ** figures in brackets are calculated uncertainties for that estimate.

	Edmunson (1979)		Hertzog & Herron (1990)	Deer *et* al., (1966)		Used in this study
	$H2O^+$	$H2O^-$	$H2O^{+}$ **	$H2O^+$	$H2O^-$	$H2O^+$
Muscovite mica	-	-	6.08 (0.04)	4.31	0.19	4.50
biotite mica	4.0	0.75	3.96 (1.10)	3.28	0.23	4.00
	1.89	0.60	-	-	-	-
Zeolite (Heulandite)	12.0	3.60	-	-	-	-
kaolinite	13.46	0.71	13.82 (0.08)	13.92	0.17	13.00
illite	6.49	2.92	7.21 (0.20)	5.98	2.86	6.92
chlorite (Mg -Fe rich)	11.09	0.51	12.93 (0.10)	11.45	1.80	11.65
Fe chlorite	-	-	12.60 (0.80)	11.07	0.51	-
montmorillonite	7.71	12.48	8.05 (0.10)	7.99	14.81	-
mixed layer aggregate	6.78	7.73	-			-

In the semi-pelite the kaolinite estimate is lowered by 3%, approaching the target. This is mirrored by an increase of 4% in muscovite and quartz 0.5%. All contribute to a better agreement with core estimates. $H2O^+$ helps to alleviate colinearity, especially in the semi-pelite solution, kaolinite and muscovite both contributing towards the mild compositional colinearity in the original solutions.

Improvements in kaolinite estimates for a *subset* of samples from the Thistle section can be seen in Figure 5.4 when modelled with (dotted line) and without an estimate of $H2O^+$.

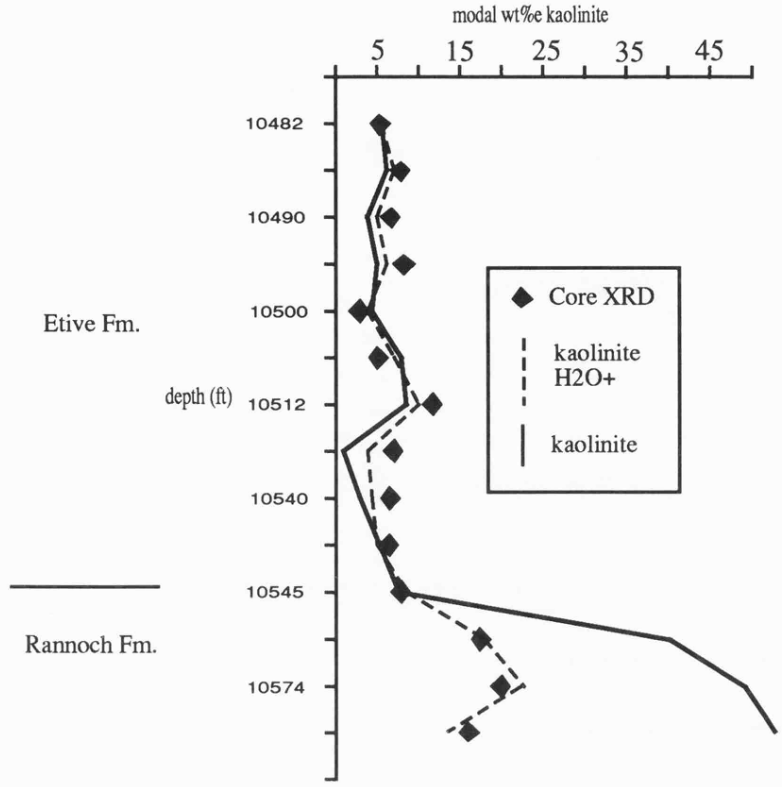

Figure 5.4 Comparison of two estimates of kaolinite modelled through the Thistle section, with and without H2O+ as an additional input variable. The solution modelled with H2O+ is much closer in agreement to core estimates.

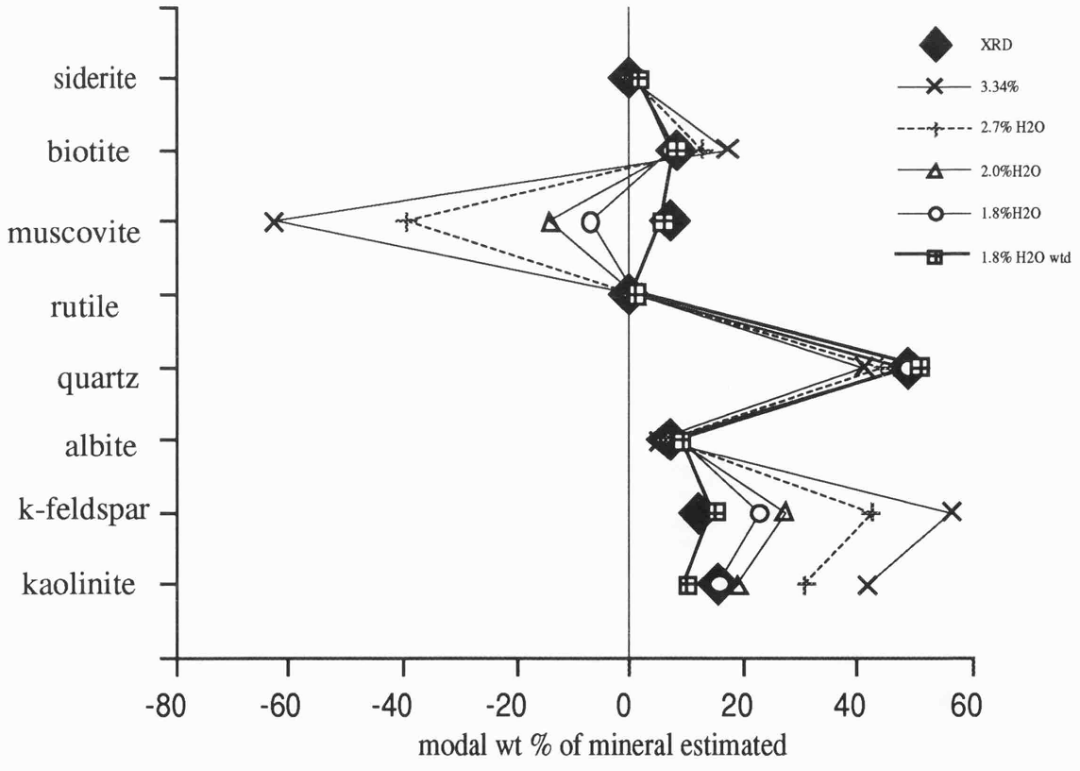

Figure 5.5 Thistle sample 10561. Modal estimates solved with variable amounts of water in the rock analysis. The weighted solution with 1.8% water gives the best fit.

Estimates of $H2O^+$ for these samples were calculated from the proportion of the hydrous phases found in core samples. Discrepancies in the *original* estimates occur in the lower samples, which are from the Rannoch Formation (*viz.* > 10545' depth), due to compositional colinearity effecting the solution.

Table 5.6 Estimated mineral proportions, 'modes' for two synthetic rocks with $H2O^+$ as an additional physical input parameter. (9 oxides used, Euclidian model), * improved hydrous estimates

Column 1 Least Squares inversion without $H2O^+$
Column 2 Least squares inversion with $H2O^+$

Pelite				**Semi Pelite**			
	Target	**1**	**2**		**Target**	**1**	**2**
kaolinite	15.00	13.42	14.93*	albite	15.00	14.83	15.98
quartz	20.00	20.54	20.02	kaolinite	15.00	18.71	15.87*
K-feldspar	15.00	14.38	15.80	quartz	40.00	38.08	38.56
muscovite	45.00	46.88	44.38*	K-feldspar	15.00	20.47	17.96
dolomite	5.00	4.78	4.84	muscovite	10.00	3.04	6.86*
				dolomite	5.00	4.86	4.71
SE		0.307	0.334	SE		0.350	0.389
Mad		0.143	0.164	Mad		0.146	0.166

Table 5.7 illustrates an example where the more complex Rannoch lithology has been modelled with bound water using both a weighted and un-weighted model. In the weighted model $H2O^+$ is heavily weighted in favour of the oxides (100:1) and therefore has a greater influence on the solution. Addition of water decreases the wild negatives previously observed (column 2+3) providing a closer agreement to core mineralogy in the case of the weighted model. $H2O^+$ has effectively constrained the solution by 'pulling' the hydrous phases, muscovite and kaolinite, off the compositional colinear plane, K2O-Al2O3-SiO2, shared with K-feldspar and quartz. Anhydrous phases such as rutile and albite, in this case, remain relatively constant throughout the solutions, indicating that addition of a hydrous phase does not effect them greatly.

Perhaps the main problem faced with this strategy is the acquisition of reliable estimates of $H2O^+$ in the laboratory and in the borehole environment. The $H2O^+$ values for this exercise were calculated from knowledge of the minerals and their proportions present.

Table 5.7 Improvement of the Rannoch sample 10561 solution by using $H2O^+$ as an additional input parameter.

Column 1 Euclidian solution (oxides only)
Column 2 Euclidian solution with $H2O^+$ added (no weighting) (1.8% $H2O^+$ in sample)
Column 3 Weighted Least Squares solution ($H2O^+$ weighted 100:1 with oxides)

	XRD	**1**	**2**	**3**
kaolinite	15.64	39.82	15.95	10.27
K-feldspar	12.52	53.48	23.01	15.24
albite	7.03	5.36	8.81	9.33
quartz	48.90	41.92	49.02	51.03
rutile	trace	1.04	1.16	1.15
muscovite	7.48	-57.7	-6.56	6.18
biotite	8.41	16.14	7.07	8.41
siderite	trace	1.04	1.53	1.85
SE		0.064	0.441	0.361
Mad		0.021	0.171	0.161

Figure 5.5 illustrates how a change of just 1.5% in the input $H2O^+$ estimate can make the difference between a geologically 'acceptable' mineral estimate and one that is totally

meaningless. An input $H2O^+$ value of 3.34 wt% results in a clearly erroneous mineralogy with kaolinite being over-estimated by 50% and a negative estimate of muscovite. Only the *weighted* solution with 1.8% $H2O^+$ produces a very close, acceptable, result.

In the case where this strategy may be applied in the logging scenario, such as the use of the 'Wmin' estimate of $H2O^+$, it is important to obtain at least as accurate an estimate of $H2O^+$ as that of the other oxide variables. This is considered further in Chapter 6. Care must also be taken because the amount of *bound water* in a particular mineral can vary like oxides. For example bound water in biotite can vary by 2-3%. As seen in Figure 5.5, this may have a severe effect on a solution.

5.4.4.2 Density as an extra parameter

It is also theoretically possible to add density as an *extra input parameter* to the mineral transform model in an attempt to further constrain a solution. Its implementation, from experience during this study, even using synthetic rocks where density for each mineral can be accurately calculated, however, remains sceptical. All minerals have reasonably specific densities, of which typical values for some more common ones are quoted in Table 5.8. Minerals with greater densities, such as siderite and rutile, may be more readily distinguished from *lighter* minerals if density is modelled with oxides.

Bulk density is a common physical measurement run routinely in most wells. From this, it is possible to gain an estimate of the *matrix density* (density of just the minerals present - without borehole fluids) by subtracting an estimate of porosity from bulk density. This matrix density estimate may be modelled with oxides as an input response with the appropriate assignment of mineral densities to each mineral phase in the *components matrix.*

Table 5.8 Commonly quoted mineral densities. For hydrous minerals that contain water as part of their atomic structure (hydroxyls) the density quoted is for a dry analysis, ie, analysis with only $H2O^+$ present, denoted (d).

Mineral	Edmunson (1979)	Ellis (1988)	Carmichael (1989)	Wendlandt (1990)	Used in this study
quartz	2.65	2.65	2.648	2.4	2.65
K-feldspar	2.55	2.57	2.570	2.52	2.57
Albite	2.62	2.61	2.620	-	2.62
muscovite mica(d)	2.83	2.84	2.831	-	2.83
biotite mica(d)	3.12	3.22	2.900	-	3.12
kaolinite(d)	2.44	2.62	2.594	2.61	2.61
illite (d)	2.65	2.78	2.660	2.8	2.80
chlorite (Mg rich)(d)	2.79	2.65	2.800	-	2.65
smectite(d)				2.7	2.7
pyrite	5.00	5.01	5.011	-	
rutile	4.25	4.23	4.245	-	4.25
siderite	3.94	3.96	3.944	-	3.94
dolomite	2.87	2.87	?	-	2.87
calcite	2.71	2.71	?	-	2.71

Table 5.9 illustrates the effect on modal estimates of three synthetic rock samples when density is included in a model. For modelling purposes mineral densities were calculated by multiplying the average mineral density for each mineral (from Table 5.8) by its mineral

proportion (wt %). Slight improvements (but not vast) are seen in the pelite and semi-pelite examples especially for weighted solutions. For the synthetic *arenite* sample (Table 5.9), the extra density parameter has no effect on the colinear discrepancy between K-feldspar and muscovite (column 2), although weighting of density heavily against all oxides, begins to improve the solution.

Table 5.9 Estimated mineral proportions, 'modes' for three synthetic rocks with density as an additional physical parameter, Least Squares model used (9 oxides, +/- density (g/cm^3)).

Column 1 Solution without density modelled
Column 2 Solution with density modelled
Column 3 Weighted solution with density added (100:1 weighting of density)

Pelite	Target	1	2
Kaolinite	15.00	13.42	14.38
Quartz	20.00	20.54	20.44
K-feldspar	15.00	14.38	14.64
Muscovite	45.00	46.88	46.55
dolomite	5.00	4.78	4.74
SE		0.307	0.330
Mad		0.143	0.149

Semi Pelite	Target	1	2	3
albite	15.00	14.83	14.84	16.13
kaolinite	15.00	18.71	18.66	13.60
quartz	40.00	38.08	38.08	39.77
K-feldspar	15.00	20.47	20.44	14.51
Muscovite	10.00	3.04	3.09	11.18
dolomite	5.00	4.86	4.89	4.80
SE		0.350	0.430	0.397
Mad		0.146	0.159	0.166

Arenite	Target	1	2	3
quartz	80.00	78.30	78.29	78.35
K-feldspar	5.00	10.35	10.37	10.19
muscovite	10.00	6.87	6.85	6.97
dolomite	2.50	2.07	2.07	2.08
calcite	2.50	2.27	2.27	2.27
SE		0.260	0.281	0.282
Mad		0.167	0.179	0.180

Two examples from the Thistle section, Etive and Rannoch (*viz.* 10540, 10580), do not show significant change in modal estimates between the straight oxide solution and one modelled with density (Table 5.10). Matrix density values for modelling have been calculated from the XRD mineralogy estimate. A less negative estimate is seen for the Rannoch sample (10580), when density is weighted, but worse when un-weighted. All solutions show unrealistic, negative, estimates and are clearly not acceptable. This sample is also hampered by compositional colinearity; the addition of density does not appear to resolve the problem, although it does cause a move towards a 'better' solution.

In general little improvement is seen in estimation of mineralogy when density is included. In theory, an extra density parameter may help in a solution in a way similar to the $H2O^+$ parameter. Even with a well constrained 'synthetic' data set it is hard to achieve any significantly improved results. This can be attributed to the fact that many of the common minerals have very small differences in mineral densities, such as seen in the two data sets here. The difference between the most dense mineral (dolomite) and the least dense (K-feldspar) phase is only 0.32g/cm^3. In contrast, with $H2O^+$, a difference of up to 13 wt% between minerals allows it to be a useful parameter. Only with a large weighting of density, in the best case, does a solution improve; however, any error in the density will also be magnified by the weighting.

Table 5.10 Estimated mineral proportions, 'modes' for two Thistle rocks with density as an additional physical parameter; Least Squares model. 9 oxides +/- density (g/cm^3).

Column 1 Solution with no density modelled
Column 2 Solution with density modelled
Column 3 Weighted Least Squares solution (density weighted 100:1 with oxides)

Sample 10540 (Etive Fm)					**Sample 10580 (Rannoch Fm)**				
	XRD	**1**	**2**	**3**		**XRD**	**1**	**2**	**3**
kaolinite	6.59	3.68	3.58	3.42	kaolinite	7.02	57.02	60.59	9.31
K-feldspar	15.11	13.74	13.79	13.41	K-feldspar	15.87	89.29	94.37	24.96
albite	5.40	7.38	7.46	7.27	albite	6.82	14.98	14.67	19.14
quartz	73.07	74.15	74.15	74.48	quartz	39.74	20.03	18.59	35.68
rutile	trace	1.04	1.03	0.91	rutile	trace	0.47	0.43	0.65
					muscovite	11.40	-113.86	-122.72	-9.24
					biotite	11.84	30.98	33.86	19.30
SE		0.662	0.593	0.447			0.257	0.219	0.625
Mad		0.340	0.308	0.259			0.063	0.076	0.333

We can not forget that the calculation of mineral densities based on core estimates in this exercise may have been in error. Any error in the core estimate would produce erroneous sample matrix densities in which to model. Such an uncertainty may totally 'mask' the subtle differences in density (*viz.* 0.3g/cm^3) between the different mineral species and may lead to incorrect modal estimates. This is pertinent to the *log environment*, as slight inaccuracies in tool measured porosity and/or a bulk density estimate would ultimately cause inaccuracies in mineral estimates, probably to much greater extent than observed in the examples here. Experience suggests that transform models are not sensitive enough to discriminate between such small values of change in a parameter, even if a heavy weighting is applied.

Mineral densities, like compositions, also vary (as a function of composition). For example, the density of the clay mineral smectite can vary between 2.1 and 2.7 g/cm^3 depending on ionic composition. Such a wide range of possible variation for an individual phase should be considered when modelling. However, if a lithology is dominated by heavy minerals, such as pyrite (5g/cm^3) or siderite (3.95g/cm^3) and possibly dolomite (2.87cm^3) then density may be useful in discriminating between these phases and much lighter quartz-feldspathic phases (*viz.* 2.60g/cm^3) common through the Thistle.

5.5 Variation in composition

Results from previous mineral modelling (Chapters 3+ 4) demonstrate that it is necessary to obtain a good idea of mineral composition, for any model to successfully estimate mineralogy. It is especially important for minerals, such as clay minerals, which have widely varying compositions, although variation is more likely to be restricted within a specific lithology or unit than throughout a complete hole. Knowledge of mineral composition and variation has, conventionally, come from a careful study of core material using microprobe or similar techniques. Even then, variation is still possible and may inevitably lead to an incorrect choice of composition in a model. An alternative is to apply a strategy that is directly sensitive to compositional variation.

5.5.1 Binary iteration strategy

The binary strategy is a strategy that can be employed to determine the composition of minerals with variable compositions within a solid-solution series. Examples of this strategy were shown in Section 5.3.1 and 5.4.1, where an optimum composition was sought by *binary iteration* between two end-member phases. This proved a feasible strategy for reducing the number of phases in a solution and as an aid in reducing compositional colinearity. In another sense the composition of certain phases is allowed to vary within constraining limits of the end-member compositions and as a result the solution is more flexible.

In a different context, if a reasonably constant proportion of the two end-members exist through a formation, a binary phase can be constructed without iteration, simply by 'mixing' the compositions in an appropriate quantity. This is used as a strategy to model muscovite and biotite mica in the case example later. Theoretically it can also be applied to any two minerals as long as the ratio between the two is known (and is realistic).

5.5.2 Stochastic modelling strategy

A modelling approach is introduced here that allows a mineral composition to vary within an implied multivariate normal distribution, as described by the mean and variance-covariance matrix of a *sample* of representative compositional analyses. In this way, compositionally *variable* minerals, such as mica or clay minerals, are allowed to fluctuate in composition within specified statistical limits. Such a *stochastic* approach provides a 'geologically' viable method for overcoming the need to accurately know compositions of highly variable mineral species at each depth interval.

Due to the *stochiometric* nature of minerals, some elements exert a certain amount of *interdependence* on one another; for example, when ionic substitution is present between cations of similar diameter. Low temperature metamorphic, Mg-Fe mica (phengite), is a good example of a mineral whose oxides are interdependent. With increasing metamorphism phengite will lose Mg^{2+} and Fe^{2+} in replacement for Al^{3+} in its octahedral sites, and the composition approaches that of an *ideal* muscovite. This trend is illustrated on the AKF diagram in Figure 4.7, Chapter 4. In effect, a negative correlation exists between Mg or Fe and Al. Preserving such a relationship between oxides in a mineral is crucial if the composition is to be allowed to vary in a geologically 'viable' way. This strategy allows such interdependence to be taken into account.

For any given lithological unit, the variation in a mineral composition may be characterised by its composition mean vector, and the variance-covariance matrix of oxide variables. Figure 5.6 (A) illustrates a surface plot defining the joint probability distribution of two independent *normal distributions* that could, for example, be two oxides that constitute a mineral. Each separate (marginal) normal distribution, itself, is described by the mean and variance where as the *joint distribution* is described by the covariance of the two variables

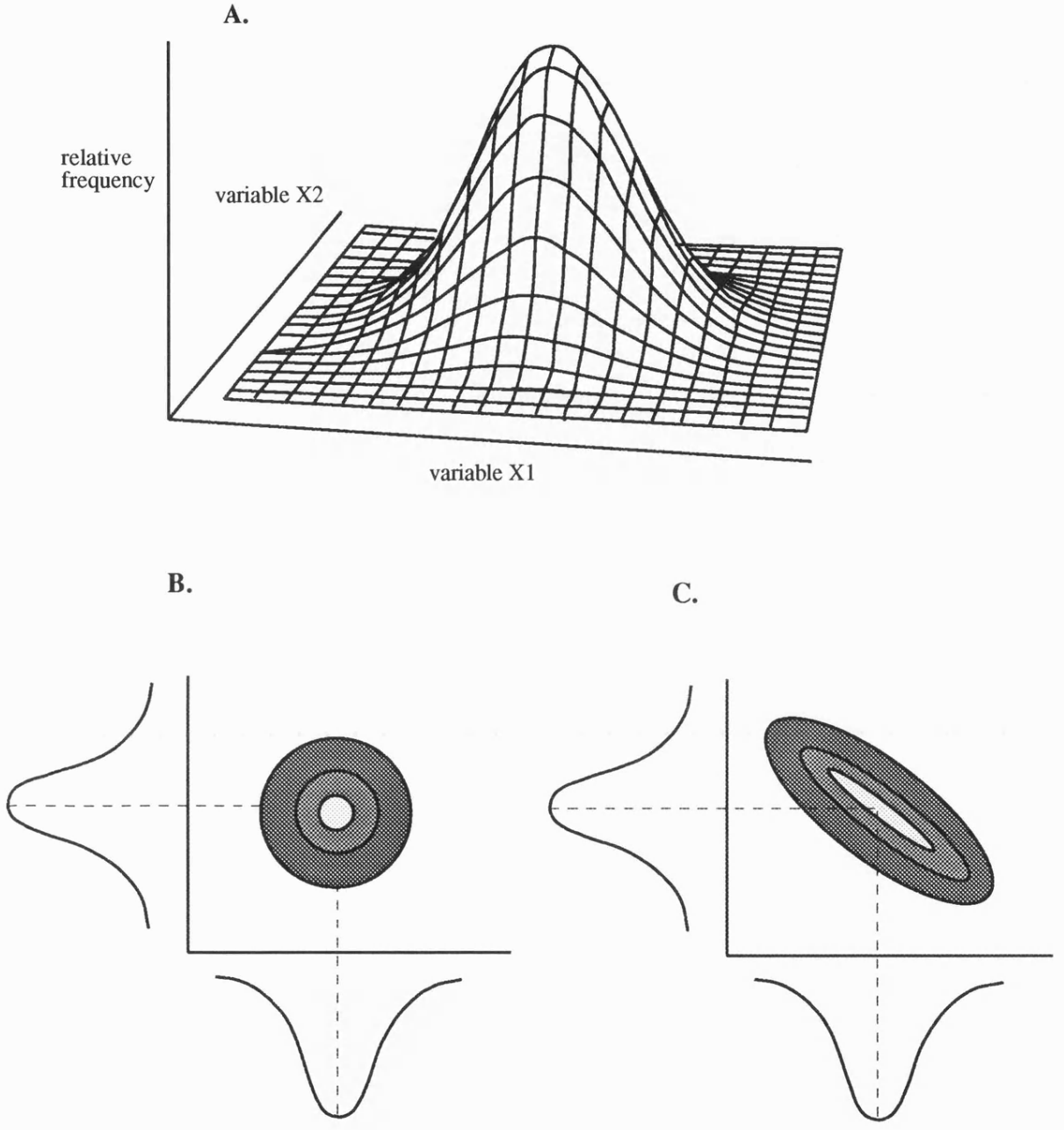

Figure 5.6. A) An illustrative example of the form of a joint probability distribution surface created by two independent normal distributions, such that may exist between two oxides that constitute a mineral (adapted from Davis, 1986).
B) Plan view plot illustrates a symmetrical nature (in this case) of the joint distribution around the common mean for two variables.
C) Plan view illustrating two independent normal distributions whose joint distribution surface has a strong negative correlation. The cigar shape illustrates the variation of the two variables about the joint mean, as described by the variance-covariance matrix.

(Davis, 1986). In Figures 5.6 (B & C), the *variance* describes the shape of the independent distributions while the *covariance* describes the orientation and the shape of the joint distribution, here a circle and cigar, with no correlation and a negative correlation respectively. When modelling a mineral with nine such major oxides a *hyper-space* of nine normal distributions is required. Although not an easy thing to illustrate, it is easily described mathematically by the variance-covariance matrix.

Such a set of compositional data can easily be acquired for a given lithology, unit or formation from core data; or more globally, from literature of that mineral species. The approach then is to allow samples, at random, to be picked from within the defined multivariate distribution using a Monte Carlo modelling technique. These samples are fitted in turn to the transform model employed, the best fitting solution being accepted and used as the most accurate mineral estimate. The criterion for this is the solution with the mineral composition that produces the *lowest* Standard Error and remains positive. Figure 5.7 is a flow chart which demonstrates this strategy. Subtleties of the model allow the number of repeated trials to be varied, of which, from experience, a minimum should be at least 1000; and a choice to repeat the same random sample pattern as previously used.

As an example, a sample of fifty phengitic micas from the Thistle section are used to demonstrate the distribution of a typical mineral that may be modelled stochastically because of its variable mineralogy. Figure. 5.8 shows the distributions of the five *dominant* oxides that make up muscovite-phengite. These serve, simply to illustrate that a unimodal, symmetrical distribution is a reasonable expression for each oxide. The mean, standard deviation and correlations matrix describing this data set are summarised in Table 5.11.

Table 5.11 Mean, standard deviation and linear correlations matrix for 50 muscovite micas from the hole 211/18a-a33, Thistle Field, Brent Group. NB Fe is quoted as Fe2O3 here to be consistent with modelling.

	SiO2	Al2O3	Fe2O3	MgO	CaO	Na2O	K2O
Mean	46.74	29.80	3.88	1.76	0.05	0.42	10.19
Std. Deviation	1.945	3.025	1.767	0.748	0.166	0.676	1.140
SiO2	1.0						
Al2O3	-0.298	1.0					
Fe2O3	-0.121	-0.774	1.0				
MgO	0.424	-0.645	0.281	1.0			
CaO	-0.167	0.134	0.011	-0.267	1.0		
Na2O	0.015	0.414	0.402	-0.328	-0.022	1.0	
K2O	0.218	0.196	0.483	0.424	-0.307	-0.4611	1.0

Figure 5.9 shows two *three dimensional* plots that illustrate the distribution of the important major components (K2O-SiO2-Al2O3 and Fe2O3-MgO-K2O). Plot **A** (K2O-SiO2-Al2O3) shows a tight cluster with little interdependence of variables, whereas Plot **B** (Fe2O3-MgO-K2O) shows a loose cluster which, as more closely observed in Figure 5.10, is strongly interdependent, manifested as negative correlations between Al and Mg, and Al and Fe. This is ascribed to the phengitic signature of these micas (refer to Section 4.2.4). Both relationships from plots A and B in Figure 5.9 are taken into consideration when modelling stochastically.

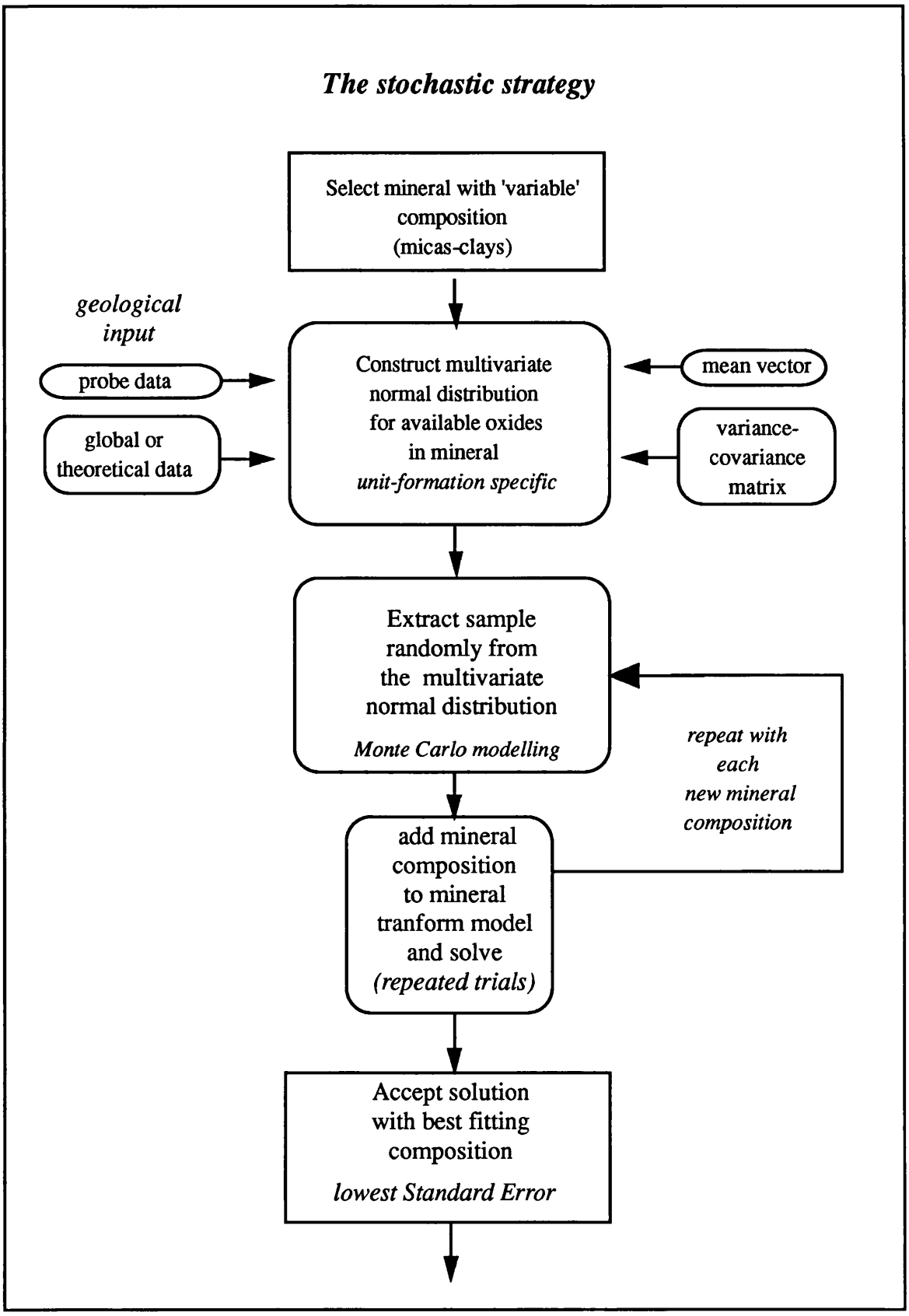

Figure 5.7 Diagrammatic flow chart illustrating the Stochastic modelling strategy

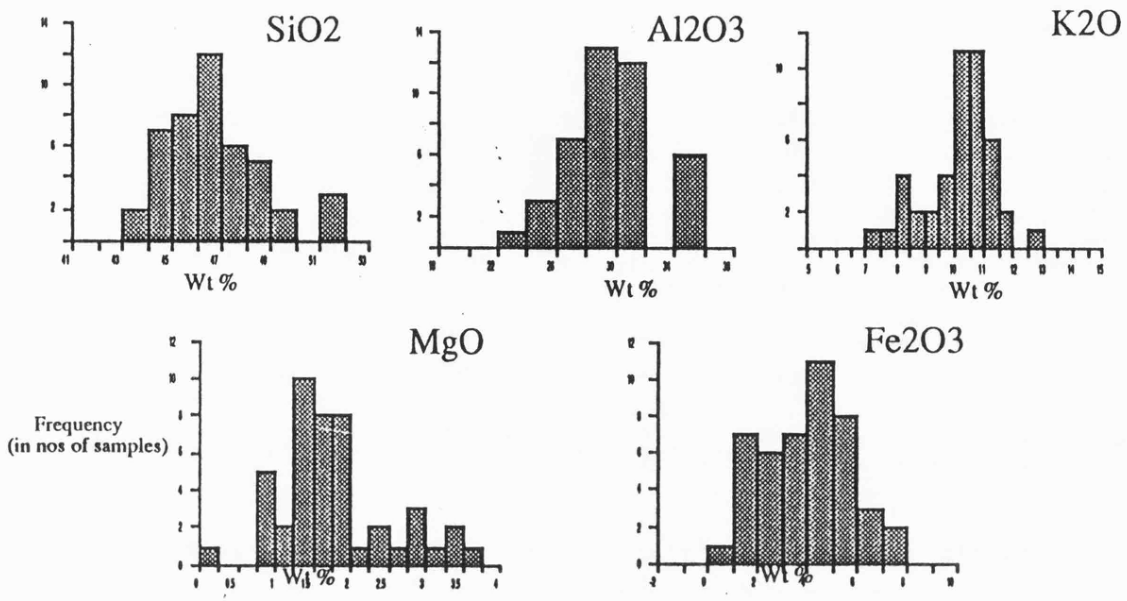

Figure 5.8 Histograms showing the symmetrical unimodal distribution of the major oxides in a sample of 50 phengitic muscovites from the Thistle Field, Brent Group.

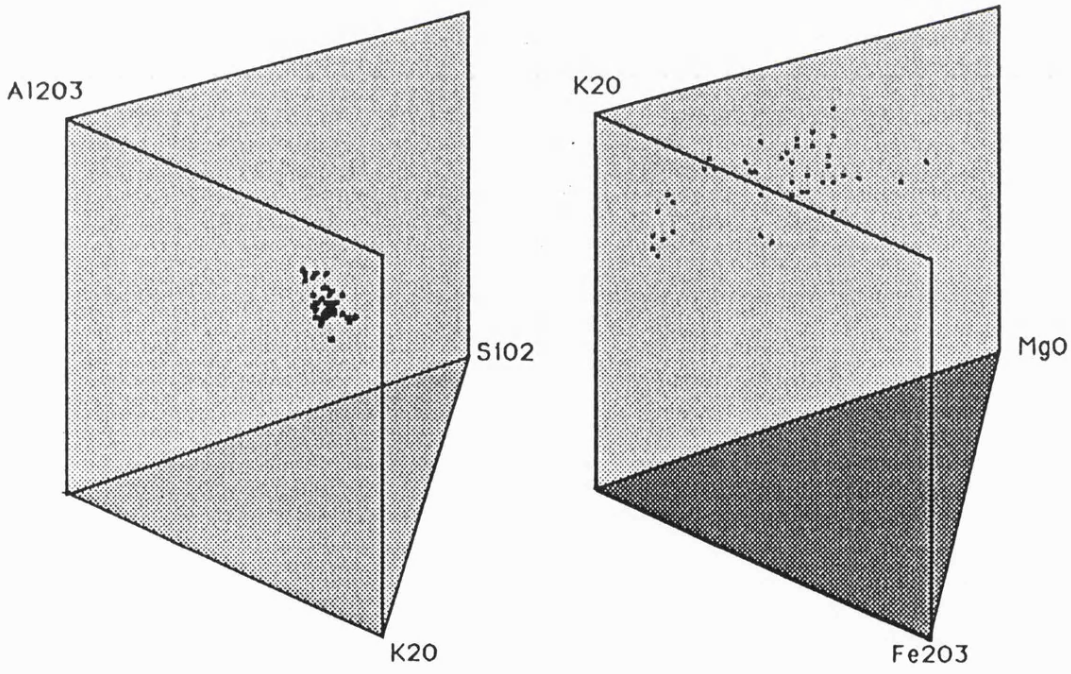

A. B.

Figure 5.9 3D representation of the inter-relationship of the dominant oxides in the Thistle muscovite sample set. The preservation of such relationships is important in stochastic modelling

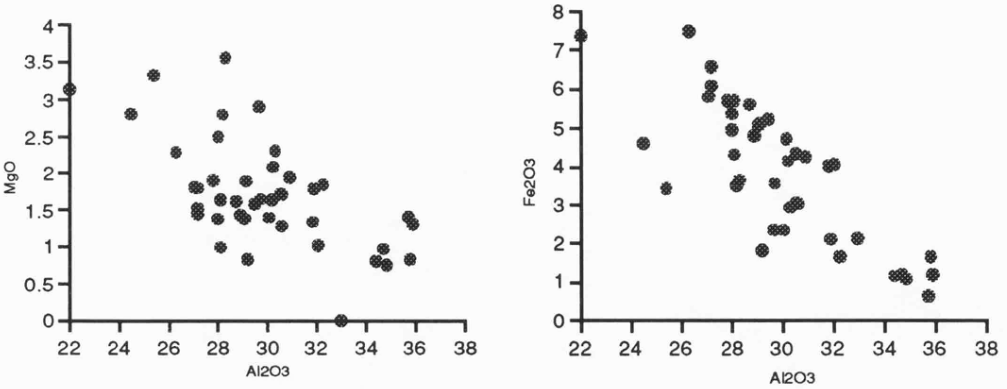

Figure 5.10 Cross plots of MgO and Fe2O3 versus Al2O3, showing the strong negative correlation that exists between these oxides due to replacement of octahedral Al 3+ by Mg 2+ and Fe 2+, in the slightly phengitic muscovites from the Brent Group. 50 analyses from microprobe data, wt %.

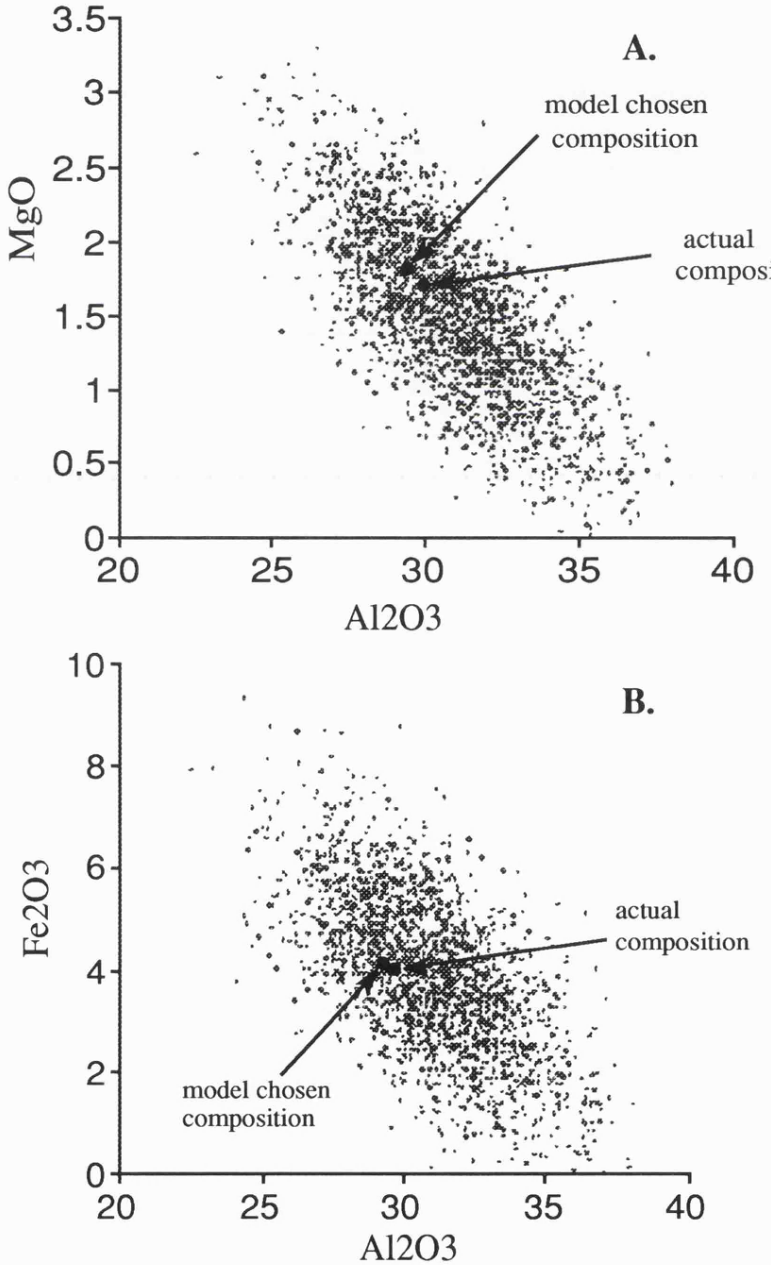

Figure 5.11 2000 muscovite compositions(wt %) generated by the *stochastic model* in terms of Al2O3 and MgO (Figure A) and Fe2O3 (Figure B) for the *mean-mus* sample. The actual composition and final composition chosen by the model are shown as black dots and indicate the close estimation of the true composition by the model. The distribution of random compositions closely follows that seen in Figure 5.10 for real muscovite compositions.

Five 'numerical' rocks ('greywackes'), each containing four minerals - albite, kaolinite, quartz and muscovite, serve here to illustrate the stochastic model. The only difference between these five rocks is the composition of muscovite. The first rock (called *mean-mus*) contains the mean muscovite composition of the sample of Brent muscovites whose normal distribution is given in Table 5.11. The other muscovites were chosen at random from within the sample-set Each rock was in turn modelled stochastically using the input variance-covariance data (Table 5.11) with 2000 repeated trials for each sample. Table 5.12 shows the predicted mineralogy and Standard Error for the model; and demonstrates respectable modal estimates for each sample. Also shown is the close similarity between the *model generated* and *actual*, muscovite composition used to make the rock.

Table 5.12 An example of the stochastic modelling strategy. Close solution of four theoretical 'greywackes'. Below, shows a comparison of the muscovite composition chosen by the model (ie, Mus-1) with the actual muscovite (ACTUAL) used to 'produce' the rock.

	quartz	albite	muscovite	kaolinite	Standard Error
Target mode	75.0	10.0	10.0	5.0	
mean-mus	75.14	9.69	11.67	3.50	0.008
mus-1	75.12	9.81	10.73	4.27	0.024
mus-2	75.40	10.16	10.10	4.33	0.008
mus-3	74.55	9.54	12.05	3.86	0.013
mus-4	75.10	9.80	10.74	4.41	0.014

Sample	SiO2	TiO2	Al2O3	Fe2O3	MgO	CaO	Na2O	K2O
mean-mus	47.08	0.70	30.93	3.70	1.38	0.02	0.66	9.02
ACTUAL	47.11	0.743	29.68	4.17	1.77	0.02	0.35	10.32
mus-1	51.25	0.68	26.76	2.80	3.16	0.00	0.30	10.88
ACTUAL	51.88	0.89	25.39	3.44	3.34	0.00	0.00	11.35
mus-2	47.10	0.39	32.23	3.01	1.78	0.03	0.56	10.60
ACTUAL	49.67	0.49	30.51	3.05	1.72	0.00	0.71	10.78
mus-3	50.49	0.94	30.89	3.82	1.46	0.04	1.18	9.57
ACTUAL	47.75	1.18	31.79	4.70	1.78	0.00	0.79	11.24
mus-4	45.70	0.82	27.74	4.70	1.65	0.05	0.23	9.11
ACTUAL	45.58	0.82	27.15	5.22	2.03	0.00	0.00	9.64

Mineral compositions used to produce rock samples

Rock	SiO2	TiO2	Al2O3	Fe2O3	MgO	CaO	Na2O	K2O
mean-mus	87.97	0.08	7.17	0.57	0.28	0.19	1.21	1.16
mus1	88.45	0.10	6.74	0.50	0.44	0.19	1.18	1.26
mus2	88.23	0.06	7.25	0.46	0.28	0.19	1.25	1.20
mus3	88.04	0.13	7.38	0.63	0.28	0.19	1.26	1.25
mus4	87.82	0.09	6.92	0.68	0.31	0.19	1.18	1.09
albite	65.81	0.02	21.33	0.11	0.05	1.86	9.82	0.67
kaolinite	47.62	0.06	37.94	0.65	0.01	0.03	0.71	0.86
quartz	100.00	0.01	0.00	0.0	0.0	0.0	0.0	0.0

Figure 5.11 illustrates all 2000 compositions generated by the model during the solution of the 'mean-mus' sample, in terms of Al2O3 and Fe2O3 (Figure A) and MgO (Figure B). The *actual* and *model generated* compositions are included to demonstrate the successful choice of a composition close to the real composition. The distribution (a negative correlation) generated by the model in both Figures, closely reflects (as expected) the realistic distribution shown in the real examples in Figure 5.10.

Increasing the number of repeated trials will inevitably result in a closer approach to the true composition, thus improving the correlation of the 'actual' and 'model generated' composition in Table 5.12. Restrictions on the number of trials are limited by computational time available. Other approaches, such as *pseudo-random walk* or *hill-climbing* algorithms, may be introduced to significantly reduce computational time (P. Harvey *pers. comm.*, 1992).

This example shows that the *stochastic* strategy can accurately predict mineralogy and accurately predict the change in composition of a variable, problematical, mineral. It is much harder with a real data set to illustrate such an example as the individual composition of, say, muscovite will never be known at each sample. The strategy has, however, been tested on the Rannoch Formation of the Thistle section with encouraging results. This is demonstrated in the following *case study*.

5.6 Combination of modelling strategies - a case study

A case study now demonstrates how a combination of strategies can be implemented to optimise the estimation of modal mineralogy in a *single pass*, such as would be expected when processing a borehole. Individual strategies, such as just described, can be selected and combined in an attempt to overcome the problems encountered by a specific lithology or formation. The strategies chosen here aim to alleviate problems both specific to modelling the Brent Group, such as compositional colinearity in the Rannoch Formation; and problems more generic to the borehole environment, such as the variation of mineral assemblages and lithology down-hole. Specific problems can often be identified from core or other evidence previous to modelling. A different strategy might therefore be employed for a different region or lithology.

In the following case study three mineral transform models were identically processed on the complete Thistle 211/18a-a33 section using the same combination of strategies. The Euclidian Distance model is primarily compared with core data to evaluate the closeness/accuracy of the modelling strategy. This model is then compared to the Least Squares Error Minimisation and Linear Programming models in order to evaluate the relative performance of each model.

5.6.1 Model Parameterisation

In previous examples from the Thistle section, nine oxides were employed for modelling, using XRF data from core. Nine oxides are modelled here, except MnO is not included as it does not occur in a great quantity, this being an attempt to reduce the sparseness of the components matrix. Sulphur, on the otherhand, is included as there is evidence of minor pyrite in a few samples. The other oxides modelled include SiO2, TiO2, Al2O3, Fe2O3, MgO, CaO, Na2O and K2O.

The *components matrix* is made up of the suite of *fixed composition* minerals used throughout the chapter, that represent the average compositions for the section. (ie, *hole specific* compositions).

5.6.2 Adopted strategies

Strategies chosen include the *selected assemblage* option. This allows the mineral assemblage to vary at each depth interval. Quartz, kaolinite and K-feldspar known to be ubiquitous, and rutile, to act as a 'mop' for any surplus TiO2, were used in all assemblages. The model was then set up with a selection of 9 mineral assemblages representing all possible combinations of minerals recognised from core analysis.

The second strategy adopted is the *binary phase strategy.* The presence of muscovite mica, in samples from the Rannoch, is known to cause compositional colinearity in the K2O-Al2O3-SiO2 plane. In this model, muscovite and biotite micas are treated as one *binary* 'mica' phase. This both reduces the number of minerals to be solved for, (making the system more determined) and also reduces colinearity. The 'mica' composition chosen for the hole is made up of 50% of each mica (named "a33mica"), in reasonable correspondence with core observations throughout the Rannoch.

5.6.3 Modelling results

5.6.3.1 Selected assemblages

The assemblages chosen by the *selected strategy* for each model are summarised in Table 5.13. Four out of the 9 available assemblages were chosen by all three models. These are the assemblages that include *all* phases, except two assemblages which do not have mica and/or pyrite. The remaining five assemblages represent subtle differences in the occurrence of minor phases - pyrite and siderite; whose presence may have not been correctly identified by core techniques.

Table 5.13 Selection of mineral assemblages identified from core (XRD) estimates. The last four columns summarise the assemblages picked by XRD and each model respectively. LP- Linear Programming, Euc- Euclidian, Em- Least Squares - Error Minimisation model.

Assemblage									core	model chosen		
	Kaolinite	Quartz	K-feldspar	albite	mica	siderite	Pyrite	rutile	XRD	LP	Euc	Em
1	*	*	*	*	*				13	-	-	-
2	*	*	*	*	*		*	*	2	-	-	-
3	*	*	*	*	*	*		*	4	10	11	9
4	*	*	*		*		*	*	1	-	-	-
5	*	*	*	*			*	*	1	-	-	-
6	*	*	*	*	*			*	17	-	-	-
7	*	*	*	*		*		*	1	28	9	4
8	*	*	*	*		*	*	*	0	0	24	28
9	*	*	*	*	*	*	*	*	0	18	13	16

The inclusion of mica in the assemblage for samples in the 'mica rich' Rannoch Formation and exclusion through the mica-free Ness and Etive intervals, in the Euclidian and Least Squares models, is in good agreement with core observations. In general, an acceptable

choice of assemblages is chosen. Some discrepancy in the Linear Programming model occurs where mica is included in some mica free intervals and a mica free assemblage is included in the mica rich Rannoch Formation.

5.6.3.2 Comparison of model and core derived mineralogy

Plots showing core versus log estimated mineralogy for each of the major phases for the Euclidian Distance model were illustrated in Figure 4.9 (Chapter 4) where a good correlation with core was seen. Cross-plots in Figure 5.12 compare mineral proportions estimated by the Euclidian Distance model and whole-rock XRD core estimates. Plots of the major minerals *quartz, K-feldspar* and *kaolinite clay* indicate a very good correlation mineralogy with core XRD data; with correlation coefficients of r = 0.901, 0.8, 0.813, respectively. The spread of all points being well within the uncertainty of the XRD technique. *Albite feldspar* (r = 0.560) and *'mica'* show reasonable correlations below concentrations of 10% and 5% respectively. Concentrations above that appear over-estimated by the model. Only 6 samples of albite are over-estimated, this may be due to XRD inaccuracies or to an excess of Na2O in the sample chemistry, perhaps due to an unidentified phase. It has already been noted that XRD under-estimates mica at high concentrations (10-20%); this is reflected by the apparent over-estimation of mica here. Verification with thin section point counting and MINERALOG, suggest the higher concentrations of mica determined by the model are similar (or slightly under-estimated) and are most probably more accurate than the XRD estimates.

The remaining three *minor* minerals *pyrite, siderite and rutile* are present at concentrations below the level of detection of the XRD technique. It is not possible to verify these *minor* minerals quantitatively although estimates are not unreasonable when verified with thin section and SEM observations. They therefore show rather meaningless plots except to demonstrate that no real quantitative comparison can be made for such 'minor' phases. Siderite estimates are not unreasonable considering the high proportion of biotite mica alteration and subsequent growth of siderite (see Plate 5). The cluster of points at very low concentrations on the X axis of all three minor minerals indicate that although the model has chosen the mineral, it is not identified by XRD. An increase in model siderite (and minor pyrite) estimates in the mudstone intervals, and through the Rannoch Formation, correspond well (qualitatively) to core observations.

In general the Euclidian model predicts mineralogy throughout the Thistle section very accurately for the *dominant* mineral phases (refer to Figure 4.9). The adopted strategy has accurately estimated the quartz-rich, kaolinite-poor, subarkose mineralogy of the Ness and Etive sandstones and the reduced quartz, kaolinite-mica-feldspar dominant mineralogy of the Rannoch Formation. The drop in quartz over the three mudstone horizons at the base of the Ness and in the upper Etive can also be seen mirrored by an increase in kaolinite, mica and siderite. No negative mineral phases are present and evidence of colinearity in the 'problematical' Rannoch Formation is minimal.

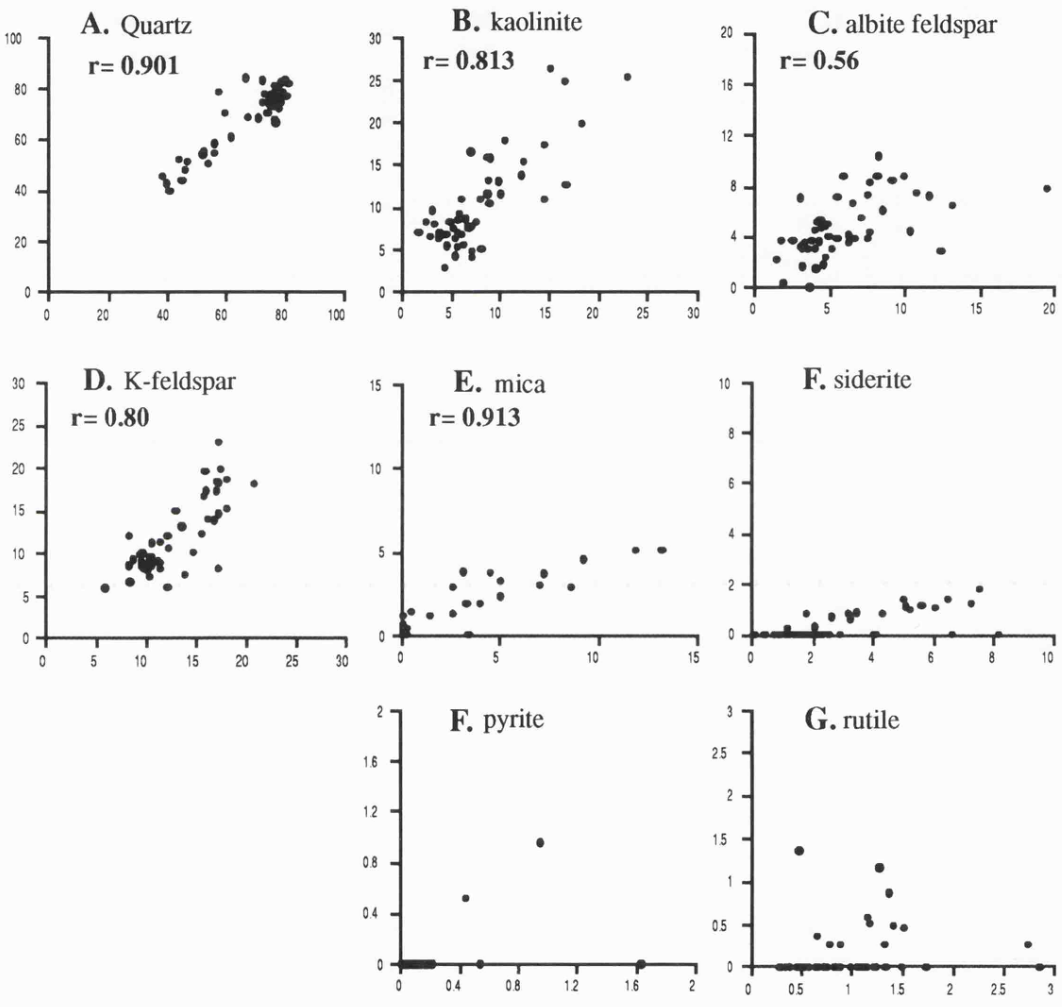

Figure 5.12 Comparison XY plots of Euclidian Distance model and XRD core mineralogy. X axis - mineralogy from the model, Y axis - core estimates.

As a contrast, Figure 5.13 shows a model processed for the same section where the mineral assemblage is fixed (for all depth intervals) and muscovite and biotite mica are modelled as separate phases. The model is heavily in error with large positive values (up to 350 wt%!) of kaolinite, K-feldspar, and biotite corresponding to large negative values of muscovite (down to -700 wt%). Compositional colinearity between muscovite-K-feldspar-kaolinite quartz causes the meaningless solutions in addition to the *fixed* mineral assemblage forcing the minerals, not present, to be solved for. The cross-plots for these minerals, Figure 5.14, show the effect of such an erroneous solution. A set of significant negative correlations are produced between muscovite estimates and all three minerals. This is a response to the system becoming unstable, so that when muscovite is violently negative the model compensates by estimating more, K-feldspar, kaolinite (and biotite) to balance the solution. This results in increased positive values for these minerals. Biotite is effected here as the muscovites contain reasonable amounts of Fe and Mg.

5.6.3.3 Comparison of different transform models

Table 5.14 summarises correlation coefficients for mineral estimates between the Euclidian model and the Least Squares, and Linear Programming models, respectively. Least Squares Error-minimisation and Euclidian Distance models predict almost identical mineral estimates (perfect correlations) consistent with previous observations in Chapter 3 and 4.

Table 5.14 Correlation coefficients of mineral phases predicted by Euclidian Distance model and Least Squares (first row) and Linear Programming (2nd row). Ksp = K-feldspar

Quartz	Ksp	albite	Kaolinite	Mica	Pyrite	Siderite	Rutile
1.0	0.999	1.0	1.0	0.999	0.976	0.995	0.999
0.998	0.885	0.903	0.995	0.682	0.959	0.794	0.845

Linear Programming shows less of a correlation with the Euclidian model. Modal estimates are compared in Figure 5.15 although correlation between models is best observed on the cross-plots in Figure 5.16. *Quartz* and *kaolinite* show near perfect correlations (Figure 5.16 plots A & B). *Albite* shows a consistent over-estimation of 3-5% by Linear Programming. *K-feldspar, siderite* and *rutile* all show good correlations except for slight deviations by a few samples, (notably less than 7% albite, and more than 5% siderite).

The most notable discrepancy is that of *mica* (plot D). Samples with high concentrations of mica have a reasonable correlation with the Euclidian model. At concentrations below 15% the majority of Linear Programming solutions do not identify mica even in the *mica rich* Rannoch Formation (points lying on the X axis). It is these samples from the Rannoch, that produce the scatter of points on the cross-plots for K-feldspar, albite and siderite.

5.6.4 Stochastic modelling of the Rannoch Formation.

As a final enhancement to the processing case study, muscovite was stochastically modelled on all samples from the Rannoch Formation. The same input parameters (Section

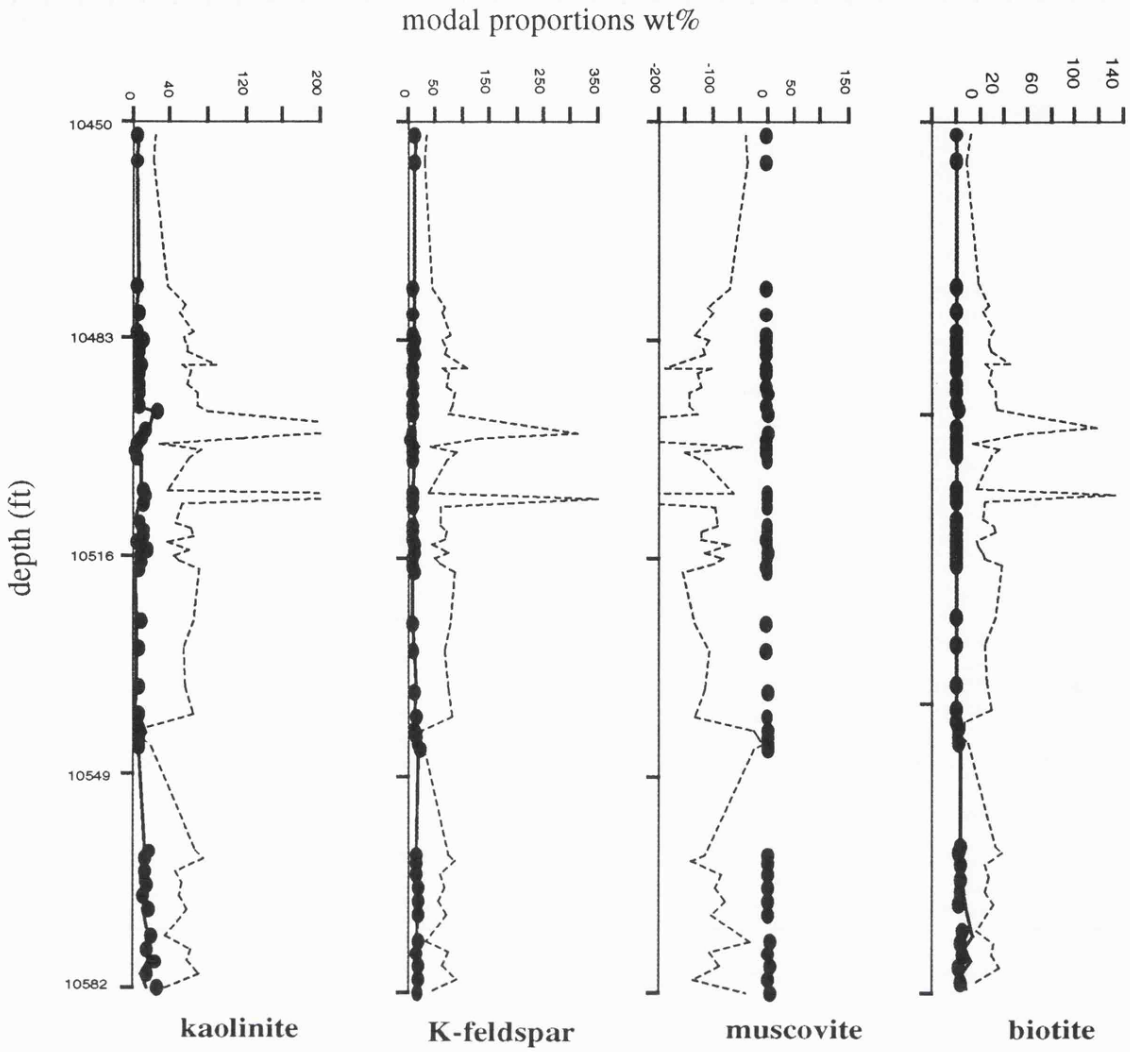

Figure 5.13 Comparison of 2 Euclidian Distance models, one using a binary mica composition (solid line), one modelling muscovite and biotite mica as separate phases (dotted line). Dots are XRD core estimates. This shows a good example of the effect of compositional colinearity on a solution. Depth in ft.

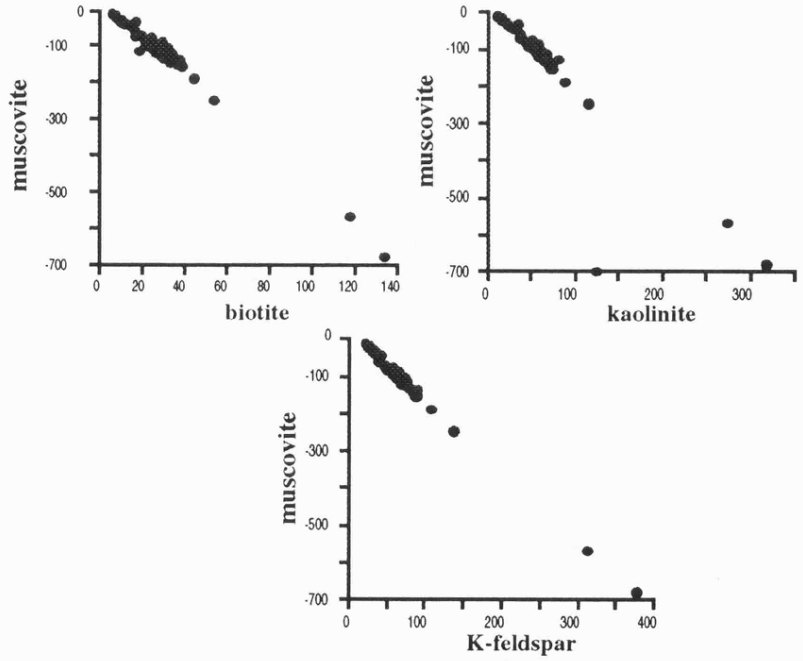

Figure 5.14 Crossplots of the colinear mineral phases kaolinite, K-feldspar (and biotite) plotted against muscovite. This demonstrates the stong negative correlation that exists with compositional colinearity. Muscovite on Y axis. Units in wt%.

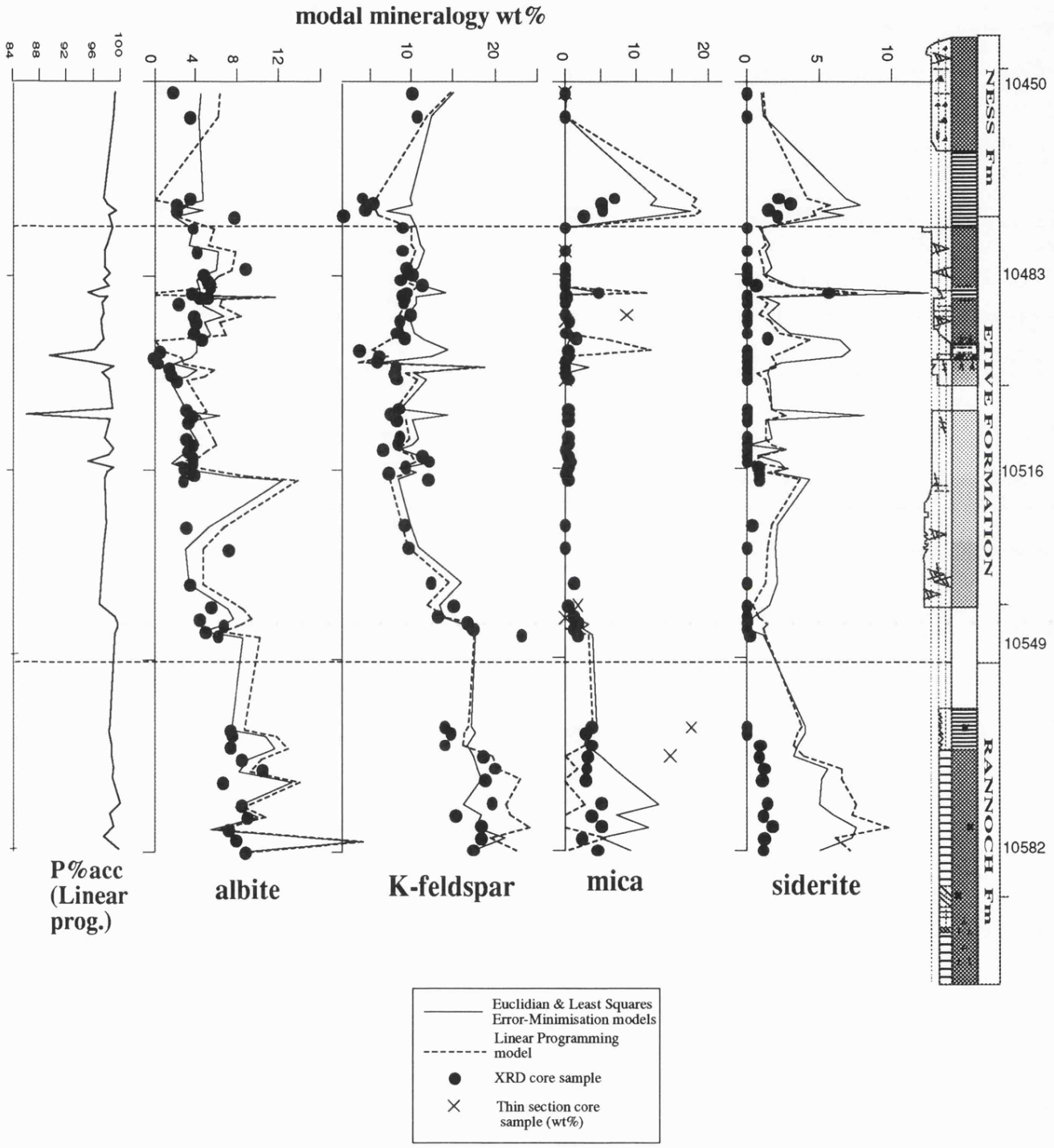

Figure 5.15 Comparison log plots of mineralogy from the Euclidian Distance and Linear Programming tranform models through the Thistle section. Dots indicate core XRD estimates. Crosses on the mica log indicate thin section estimates (where present). P%acc statistic also plotted to indicate inaccuracies in the Linear Programming model.Depth in ft.

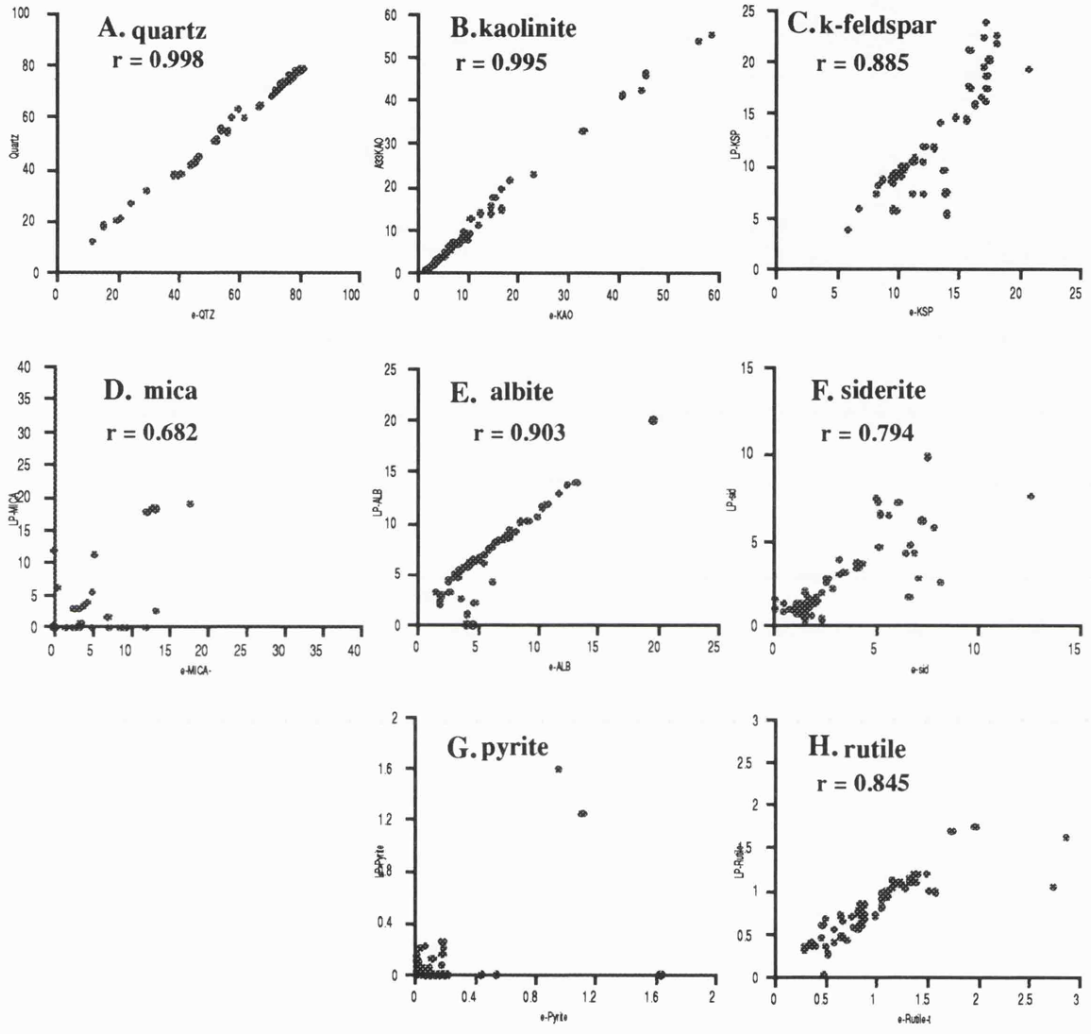

Figure 5.16 Cross-plots of mineral estimates derived from the Euclidian and Linear Programming models over the Thistle section. X axis - Euclidian model, Y axis - Linear Programming model. Units in wt%. .

5.6.3.1-2) and strategies were used in this model except that K-feldspar and albite feldspar were modelled as a *binary phase*, using equal proportions of both minerals. Muscovite and biotite micas were modelled as separate phases. Muscovite is chosen to be stochastically modelled, although biotite could alternatively be modelled, except that there is insufficient compositional data from this study to produce a meaningful sample. The mean and covariance-variance data in Table 5.12 was used to generate the relevant compositions in the model.

Results of the model show reasonable muscovite estimates of between 3-13 wt%, fairly typical for the formation, see Figure 5.17. Estimates of kaolinite appear closer to core estimates than the *first pass* estimates. Feldspar estimates are in close agreement over the section except for a spike (*viz.* 10578') in which the sample is clearly in error. This is probably a manifestation of compositional colinearity as it corresponds to a large increase in muscovite. Cross-plots in Figure 5.18 show the distribution of model generated muscovite compositions for all samples. Plots of Fe2O3-Al2O3 and MgO-Al2O3 (plots E & F) are in good agreement with the distributions seen in Figure 5.10 (actual mineral data). The model is reasonably successful in that it allows independent estimates of biotite and muscovite without the severe colinearity problems previously encountered. It is, of course, helped by having the two feldspars combined as a binary phase.

5.7 Synopsis and conclusions from the case study

This case study demonstrates how through careful choice and implementation of suitable strategies it is possible to effectively alleviate the problems that previously rendered a solution poor or meaningless.

Good correlations between mineral estimates from core and the Euclidian Distance and Least Squares-Error minimisation models are seen throughout the Thistle section, especially for the major minerals. This suggests that both models predict sensible, viable, mineralogy for the majority of the samples. A few excursions inevitably occur, such as at 10499 for K-feldspar, which could be due to inaccuracies in either element chemistry or the core estimates, or simply due to the inherent problems with the comparison of such different sample volumes. Once problematic *variable* minerals are recognised, stochastic modelling may then be employed to further enhance the solution. It is less easy to assess the prediction of the *minor* mineral phases simply because core mineralogy is not reliable. On qualitative grounds, the minor minerals (as verified by thin section, MINERALOG and SEM), are not unreasonable predictions for the mineralogy present.

Linear Programming predicts mineralogy in a similar fashion to the Euclidian and Least Squares models throughout the Ness and Etive intervals, except for a slight over-estimation of albite feldspar and minor spikes which correspond to intervals with poor solution (decreased P%acc, seen in Figure 5.15). In the Rannoch, however, erroneous solutions of muscovite, K-feldspar and siderite, occur frequently suggesting that the model has difficulties

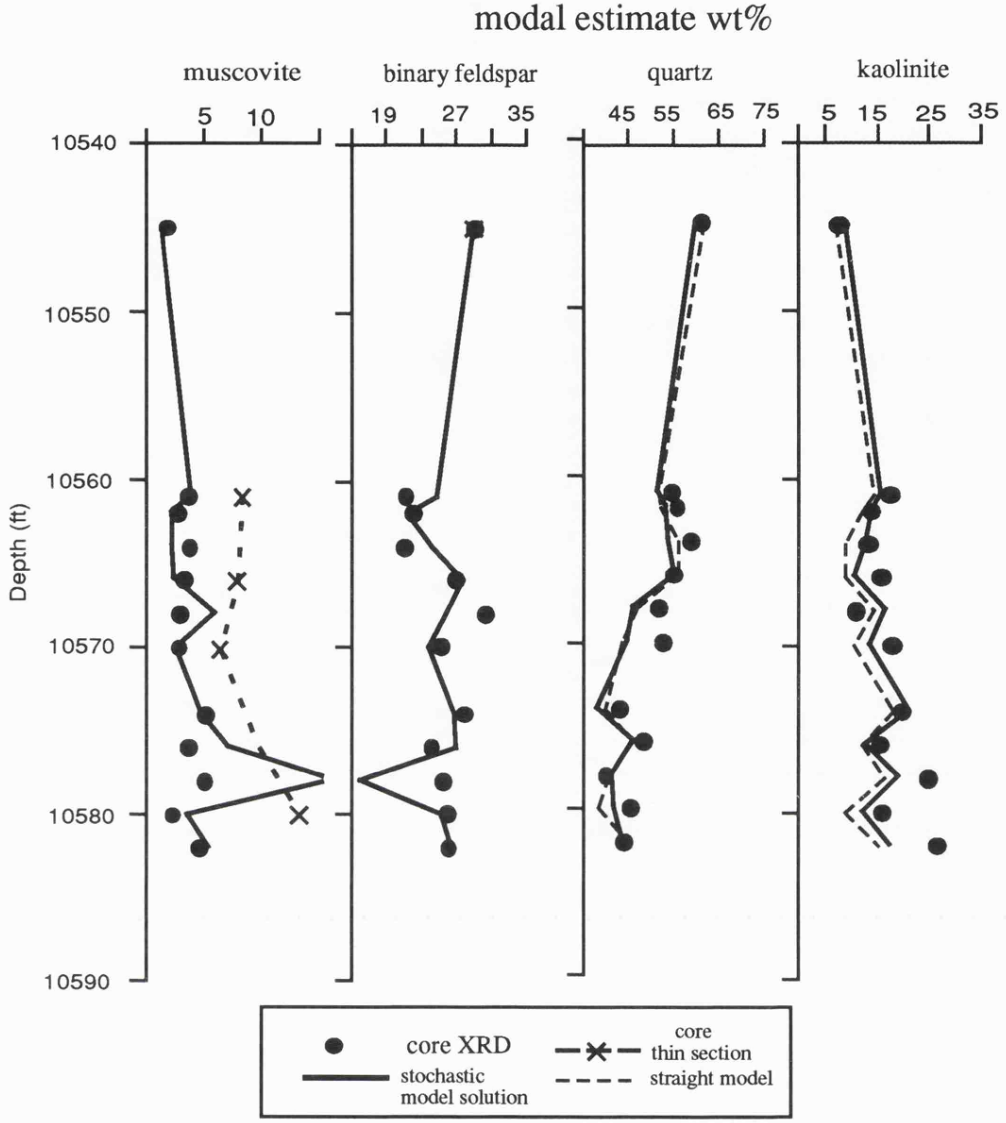

Figure 5.17 Core and *stochastic model* derived mineral estimates through the Rannoch Formation. Thin section point count data also included for muscovite (where present) estimates from first stage 'straight' processing (before stochastic modelling) also included for kaolinite and quartz. Kaolinite estimates in the stochastic model are in closer correspondance with core. Depth in feet.

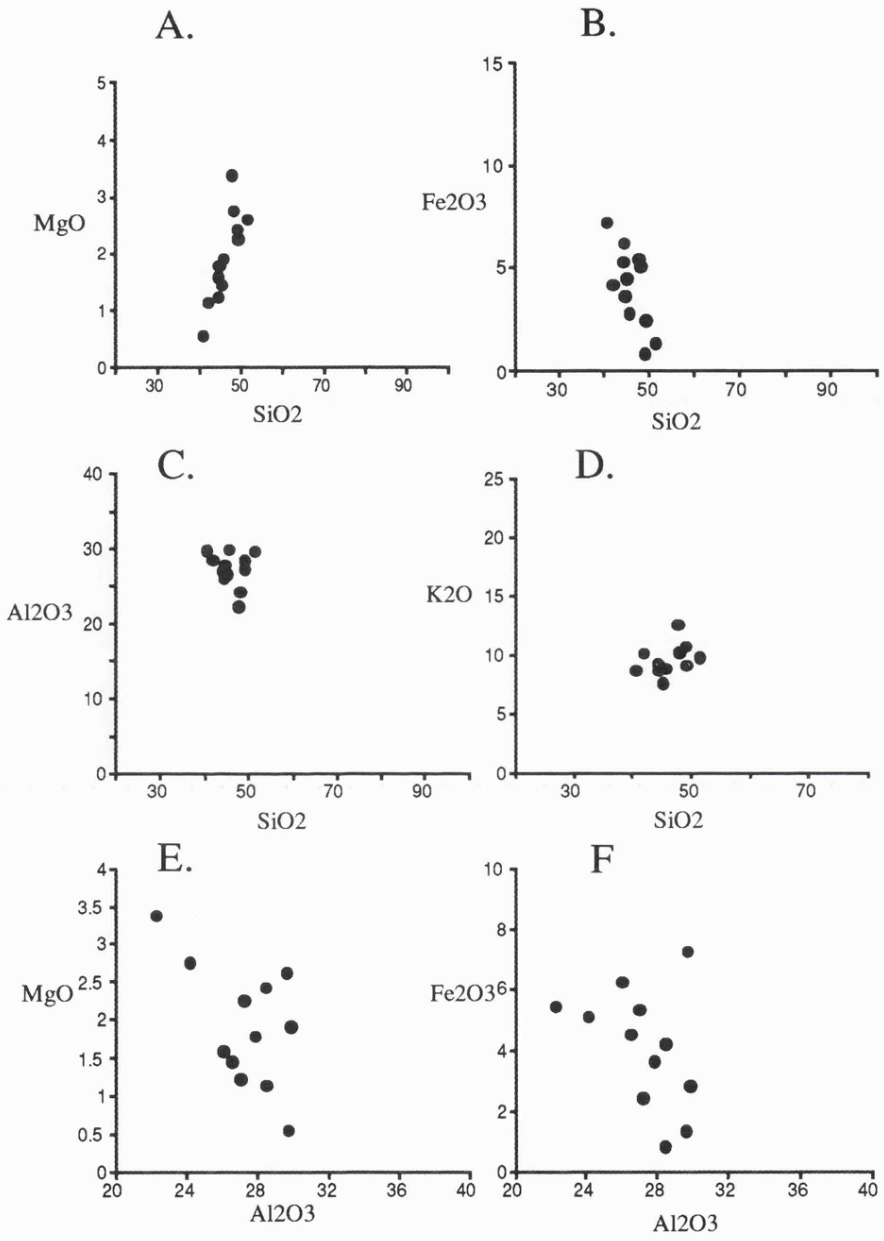

Figure 5.18 Cross plots illustrating the variation in composition of the chosen muscovites for each Rannoch Formation sample when modelled with the stochastic strategy. Units in wt%

solving for the mineralogy. The problem lies in the inability of the model to correctly partition K2O and Fe2O3 oxides between the three problematical phases *K-feldspar-mica-siderite* . This suggests that Linear Programming is more affected by colinearity than other models. This is discussed further in Chapter 6.

5.8 Synopsis and discussion of strategies

A desirable transform model and strategy should be capable of handling at least the number of phases present in a rock sample and yet be sensitive to the effects of compositional colinearity and variation in mineral composition. In part, this has been demonstrated possible by the implementation of modelling strategies described through this chapter. The possible mineral modelling routes are summarised in Figure 5.19

In terms of variable assemblages through a sequence, the *selected assemblage* strategy appears most appropriate. Standard Error, as used in this strategy, may not necessarily mean a geologically 'correct' answer, although experience has shown that the correct solution invariably derives the lowest estimate. The *reducing strategy* is not considered a valid option in the light of compositional colinearity, which may produce large negative estimates, for phases that do actually exist in a rock. With this strategy such phases would be erroneously subtracted before solution.

Reducing the number of mineral phases to make a system over-determined is a very important consideration for measurements from the GLT tool, where there are often fewer oxides than in a conventional laboratory analysis. The *binary strategy* is effective for reducing mineral numbers. It does rely, however, on an accurate knowledge of mineral phases prior to modelling, and on the mineral assemblage present. These are fundamental prerequisites to the whole modelling approach anyway. Both the *iterative* binary approach and the *'manual'* combination of two phases prove successful for estimating the feldspar series and the micas through the Thistle section. Use of this strategy does mean a reduction in the overall usefulness of a model, as the two phases are no longer independent estimates. This may be important for minerals such as clays which may need to be determined independently to estimate their effect on cation exchange capacity (CEC). For feldspars, however, are independent estimates necessary?

Compositional colinearity must be recognised early in processing. Strategies such as the *binary* or *iterative removal* strategy may then be employed. The *binary* strategy, which in effect 'pulls' a mineral phase off such a compositional plane, is very useful in alleviating colinearity. The *iterative removal* strategy offers a different approach in which to subtract problematic phases prior to solution. In the examples illustrated, muscovite was subtracted as an arbitrary choice, although any colinear phase can be subtracted. One drawback with the current strategy is that no variation in composition of the subtracted phase can be taken into consideration; for this reason muscovite may not be the most suitable phase to subtract here.

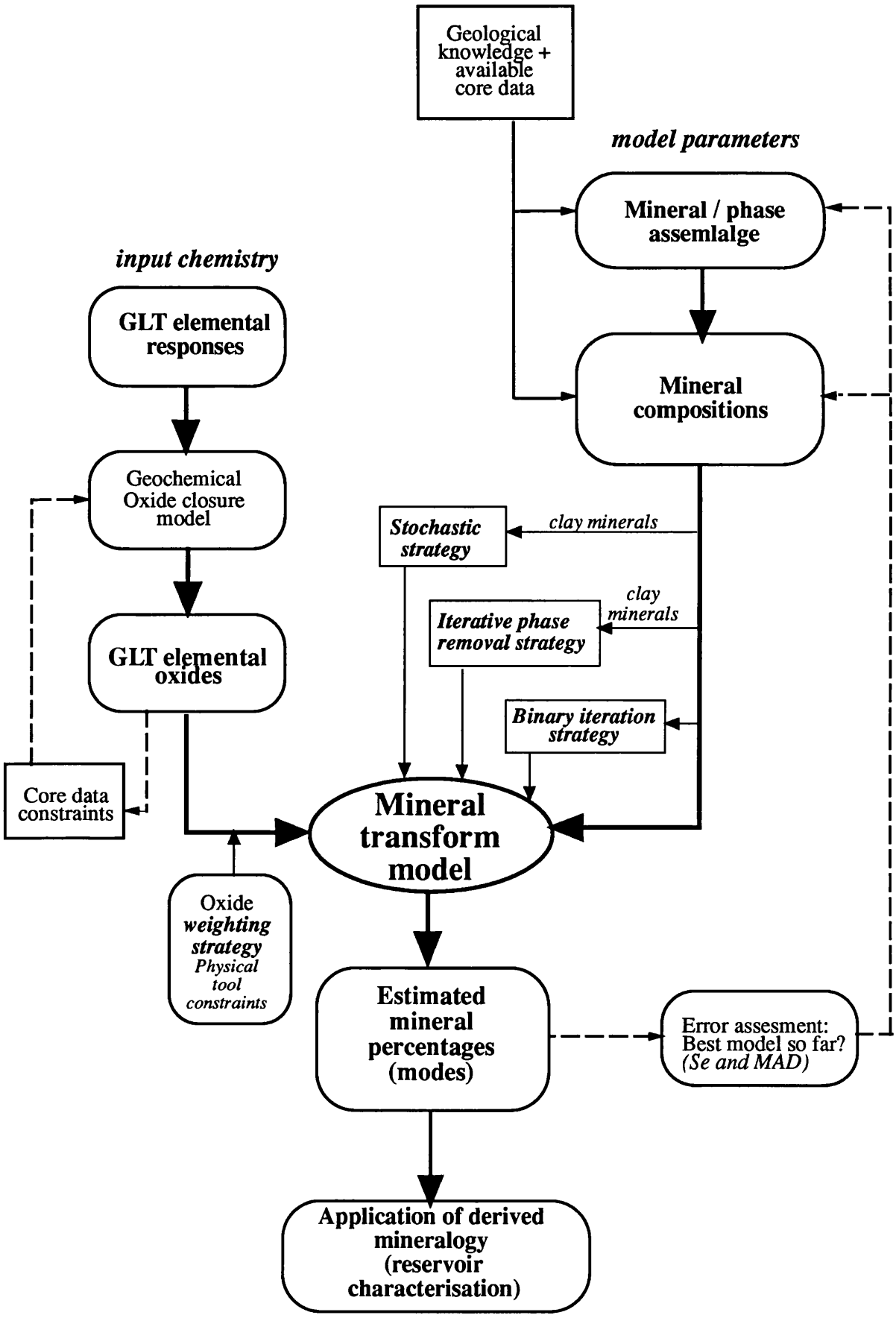

Figure 5. 19 Summary flow diagram of possible routes for mineral modelling of geochemical logging data as discussed in this chapter

The inclusion of *additional physical* parameters to a model, in the case of *bound water*, can significantly improve a model's solution if estimates are *at least* as accurate as the other input responses. Improved estimates of kaolinite, an important diagenetic (hydrous) phase through the Thistle section, occurred when $H2O^+$ was included. Additional parameters may also contribute towards the 'suppression' of compositional colinearity, again by pulling phases from the under-determined compositional plane. It is doubtful, however, that $H2O^+$ estimates from logging tools can provide accurate enough estimates to model; this is discussed in Chapter 6.

Modelling with density in quartz-feldspar lithologies, in which minerals exhibit similar densities, should be avoided. Such a variable introduces 'noise' to the solution and a sparsity to the *components matrix*. It may, however, be useful when a clear contrast in the density of minerals being modelled, is present.

The *weighted* Least Squares model provides an important method, especially for logging measurements, of allowing a solution to be weighted in favour of more accurate oxides. This method was successful in improving a solution when $H2O^+$ was weighted with respect to the oxides.

In terms of establishing *correct mineral compositions* for a model, the *binary* strategy can be useful for determining composition of reasonably fixed solid solution systems. *Stochastic modelling* provides an alternative approach, one that is geologically viable, and extremely important if an attempt is to be made to model minerals with highly variable compositions. The number of *trials* in composition the model can make is important. Sufficient trials should be made to satisfy the spread of the population; this should be no less than 1000 iterations per sample, although computational time, at present, is the restriction on the upper limit chosen. Different computational approaches may improve this. Drawbacks with the *current* algorithm include the restriction of this strategy to model one phase only, where quite often more than one phase may be present. The model may also be improved to account for bi-modal populations of compositional data; a property that could easily be expected in detrital sediments with more than one contributing source area. For such data, the establishment of *boundaries*, that restrict the compositions chosen by a model, could be implemented.

The majority of the models discussed above are shown to be effective in the relevant situations when modelled with laboratory-core data. These models and strategies remain now to be evaluated on real logging data where fewer oxides are present and where greater measurement errors exist.

Chapter 6.
Mineral transform modelling and evaluation of GLT data from the Thistle hole 211/18-A50(40).

6.1 Objectives

Until now, the evaluation of mineral transform techniques has involved using well constrained elemental data acquired in the laboratory. The primary aim of this chapter is to extend the evaluation study to the borehole environment, and demonstrate the capabilities and limitations of mineral modelling using log derived elemental measurements.

Geochemical Logging Tool (GLT) derived elemental measurements, acquired from a different section of reservoir in the Thistle Field, are used as input chemistry for the determination of mineral estimates. The *first section* of this chapter looks at the logging results from the GLT tool string and identifies areas of poor measurement quality. This involves a critical evaluation of the processing techniques and derived elemental estimates. This is important because the quality of measurement made from the GLT tool will influence the final mineral estimates by any transform model. The *second section* of the chapter presents the different attempts at mineral modelling these log data, using three previously introduced transform models. Each model is critically compared with core and with the other models in an attempt to further assess accuracy (and therefore usefulness), as well as associated problems of each model. Work in this chapter draws on the observations made throughout earlier chapters, and attempts to verify and extend those conclusions. Familiarity of the Brent Group mineralogy from Chapters 4 and 5 helps considerably with the interpretation of data from this hole.

A secondary aim of the chapter is to demonstrate the effect that mineralogy has on nuclear wireline logs, something which can only be attempted with a *good* prior knowledge of the formation being logged, as is the case here.

6.2 Introduction

It was fortunate for this study to be able to acquire logging data from the same field as the previous hole. Besides the acquisition of weight percent elemental concentrations from the GLT tool, more conventional nuclear, sonic and electric logs were obtained from hole 211/18-**a50(40).** Only nuclear logs, however, will be discussed here.

Hole 211/18-**a50(40)** lies 1.75 km due north of hole 211/18a-**a33** (see Figure 4.2) and consists of the same Brent Group sequence except that a major fault displaces the middle section of the Group. The missing sequence includes the *lower* and *mid* Ness, the *complete* Etive and the *upper* Rannoch formations. It is unfortunate, however, that no correlation can be made with hole 211/18a-**a33**, as it contains precisely those formations! Chapter 4 details the petrography of the Brent sequence, so only a brief summary of the *specific* sedimentological and petrographic features of the hole is given. This is summarised concisely in Figure 6.1.

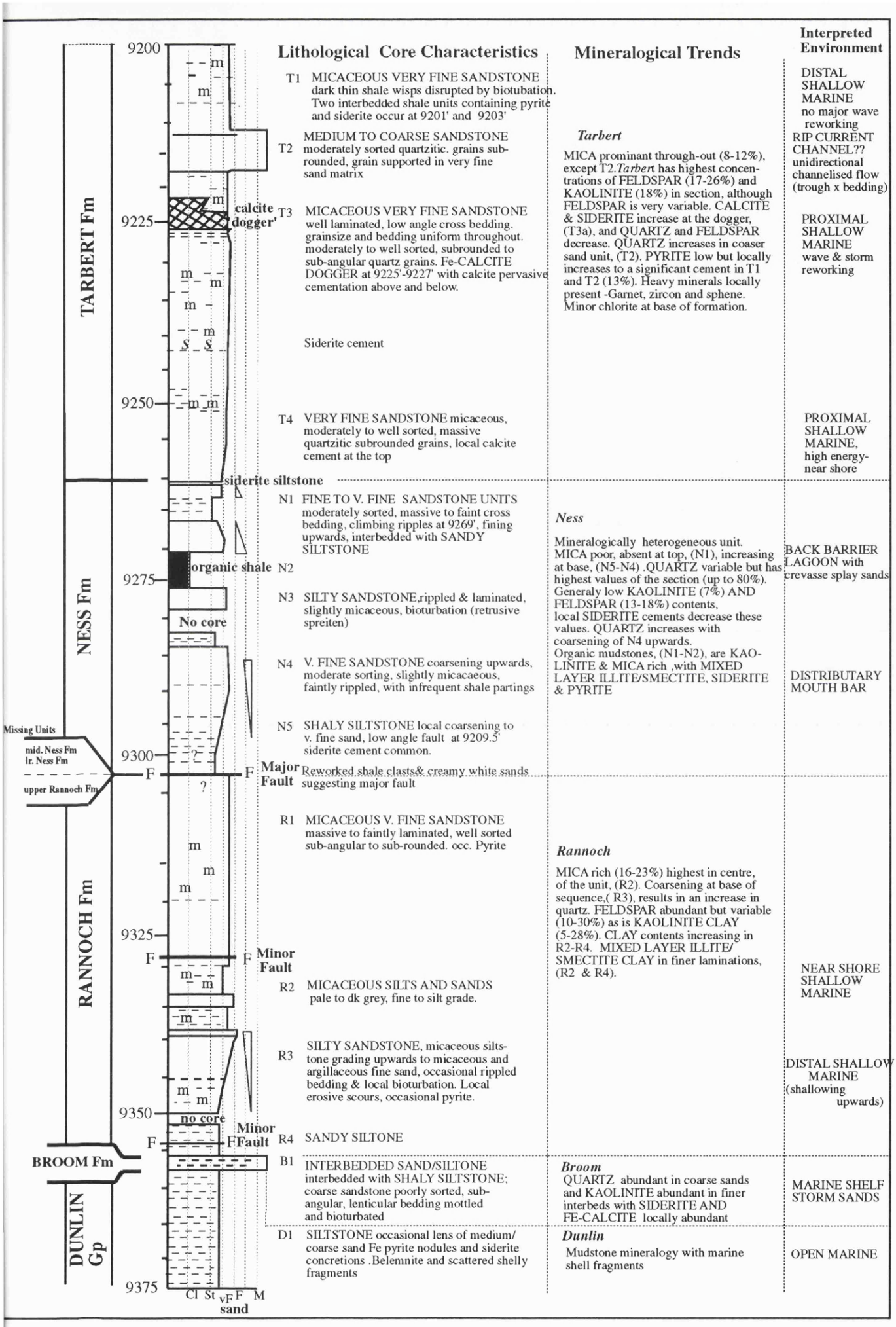

Figure 6.1 Sedimentological, lithological and mineralogical trends of the interval studied from Thistle well 211/18-a50. Depth in feet. (compiled from the original a50 core report)

6.3 Geology and lithological/petrological trends of the section

Each of the formations in the Brent Group section studied here contain essentially the same mineralogy. It is possible, however, to see changes in sandstone composition on three scales. These include broad compositional changes between formations (lithological units) as seen in the first hole; changes within formations as gradually increasing/decreasing trends, often by individual minerals; and thirdly, local changes between sample intervals, notably in minerals with low abundance such as siderite cements, pyrite and calcite.

Both semi-quantitative whole-rock XRD analysis (calibrated using standard mixtures and peak area/height measurements) and thin section data (300 points) were available for 39 samples, spaced at approximately 3' intervals; considered as being representative lithologies. These were analysed by Lomond Associates and documented in a report to Britoil (Russell, 1987). These *modal* estimates are subjectively compared later, as any discrepancies between the two will be critical in the evaluation of the mineral models. XRD totals have *not* been re-normalised to 100 except where they deviate greater than 5% from 100%. Thin section data was converted to dry wt% after subtracting porosity, so as to be compatible with XRD and modelling results; see Appendix 6.1. The average mineralogical composition of each formation is summarised in Table 6.1. A brief summary of the main petrographic trends is given here, primarily to familiarise the reader for later evaluation of the logging data and mineral modelling results.

Tarbert Formation

This consists of four distinct lithological units (T1-4, see Figure 6.1), composed dominantly of very fine micaceous, sub-arkosic sandstones. The main compositional variation takes place in the cements, micas and feldspars. A 1m *'calcite dogger'* in unit T3 (*viz.* 9223'-9226' core depth) causes a local increase in calcite and siderite and reduction in quartz (often to below 30%). Other localised siderite concentrations also occur. Mica is prominent throughout, but varies locally (from 4-38 wt%, [combined biotite and muscovite]) muscovite being slightly predominant over biotite (average 8%-XRD, 12.5% -Thin section). The highest feldspar values for the complete interval are found in this formation (average 26.5% XRD, 17.7% - thin section). A noticeable variation in feldspar occurs between samples, although not in any observable pattern. Pyrite is low in abundance except for local concentrations (up to 17% - XRD). Kaolinite is the dominant clay (average 18%), chlorite is identified at the base (<4%), and mixed layer illite/smectite between 9205' and 9211'.

Upper Ness Formation

This consists of a less micaceous, very fine to medium sandstone which coarsens upwards from silty-sand at the base of the unit. These sands are interbedded with thin organic rich mudstone/shales (considered terrestrial) in the upper half of the unit, notably between 9271-9274.5'. The *lower* and *mid Ness Formation* are considered absent due to major faulting. The highest quartz values are seen in this formation (average 65 wt%) although a drop below 30% occurs where siderite cement is present, i.e. 9246.6'. Mica is virtually absent in the upper half,

increasing in abundance at the base of the unit to 12.5% (average 3-4%). Feldspar (K-feldspar and albite) and kaolinite are both lower in abundance than the Tarbert, although a slight increase is seen in feldspar in the coarser units above 9271' (average-18% (XRD), 13%-thin section). Kaolinite is significantly lower than all other formations (average 7-10%) and pyrite is locally present up to 5%.

Table 6.1 Summary of minerals observed by XRD (wt %) and thin section point-counting (vol. %- 300 points) for each formation in hole 211/18-a50(40). Number of samples = 39. Max-maximum concentration, min- minimum concentration, std- Standard Deviation.

	XRD				Thin section			
Tarbert Fm.	**Mean**	**std**	**min**	**max**	**Mean**	**std**	**min**	**max**
quartz	42.6	16.70	15	80	43.3	15.24	11	63
kaolinite	18.5	16.70	5	35	16.8	7.28	4	30
total feldspar	26.5	5.56	10	35	17.7	3.07	11	23
mica	8	4.96	4	20	12.6	8.43	1	38
siderite	2.1	6.48	0	23	4.9	13.43	0	50
pyrite	0.9	4.04	0	17	2.56	3.87	0	13
calcite	1.42	4.32	0	15	2.13	6.29	0	26
Ness Fm								
quartz	64.3	16.8	36.5	80	69	13.47	45	79
kaolinite	7.8	6.54	0	27	10	10.35	0	27
total feldspar	18.8	3.94	15	24	13.7	3.12	8	16
mica	3	5.28	0	12	4	5.27	0	13
siderite	1.2	2.92	0	6	1.1	1.55	0	3
pyrite	1.88	2.06	0	5	1.5	2.0	0	4
calcite	0	0	0	0	0	0	0	0
Rannoch Fm								
quartz	40	6.45	14	75	45	13.70	19	69
kaolinite	19	6.45	5	30	13.7	7.07	5.3	25.5
total feldspar	22	7.89	10	36	10	1.27	8.3	12
mica	16	9.51	2	44	23	14.23	2	53
siderite	1.1	1.53	0	4.4	7.2	3.73	1	14
pyrite	0	0	0	0	0.5	0.57	0	1
calcite	0	0	0	0	0	0	0	0

Minor mineral phases (<2 wt %) (absolute estimates are speculative)

rutile Fe-dolomite illite illite/smectite

Rannoch Formation

This lies unconformably below the upper Ness Formation. It appears lithologically similar to the Tarbert, composed dominantly of a micaceous very fine sandstone in the top half. The bottom half consists of a coarsening upwards sequence from silt and silty-sandstone to argillaceous very fine sandstone. Mica here has the highest concentration of the section, increasing towards the centre of the formation (average 16% (XRD) 23% (- thin section)), biotite being slightly predominant over muscovite. A discrepancy in feldspar estimates occurs between thin section and XRD most notably in this unit; the average for XRD is 22% and thin section 12%, however, thin section is reported to under-estimate feldspar. Siderite cement is generally present, but variable (up to 14%). Quartz decreases towards the base of the formation particularly where mica and siderite content is higher. Kaolinite is significantly more abundant than in the Ness Formation (19% XRD, 13% - thin section) although similar to the Tarbert.

Broom Formation and *Dunlin Group*

The *Broom Formation* consists of dark grey shaly siltstone interbedded with poorly sorted very coarse sandstone (only one core XRD sample was collected). Quartz and kaolinite are most abundant with localised siderite cement. K-feldspar becomes more abundant towards the base, mica towards the top. Minor Fe-calcite is observed by thin section staining. The *Dunlin Group* lies conformably below the Brent sequence. This is a shale lithology representing the

fully marine environment before the onset of the Brent Group "regression". Only the very top part is present although no samples are available.

6.3.1 Comparison of core XRD data and thin section point count data

Due to the inherent problems with both thin-section point counting and whole-rock XRD, both methods of modal estimation are included in this study in order to establish as good an estimate of mineralogy as possible for the validation of wireline data and mineral models. Figure 6.2 shows the cross-plots of XRD and thin section estimates for the main minerals in the section. The thin section data has porosity removed to be compatible with XRD (and with modelling results). Agreements are reasonable; however a few discrepancies do occur:

a) A notable problem with thin section point counting (besides a rather low 'contractors' choice of 300 points for a very fine sandstone), was the suggestion by the contractor that quartz was over-estimated at the expense of feldspar. This was attributed to the problem of uneven staining in differentially weathered feldspar crystals. An empirical correction factor involving a decrease in quartz of 8% and an increase of 8% for feldspar (3% for albite, 5% for k-feldspar) was suggested by the contractor. The data presented here include this correction but compared to XRD estimates, feldspar is still under-estimated at higher values (plot d, Figure 6.2).

b) Conversely, mica is under-estimated by XRD relative to thin section (plot c) and this may be due to orientation effects or a poor calibration standard.

When compared, both techniques show significant correlations for both quartz and kaolinite, quartz being very high (correlation coefficient of r= 0.95). XRD-kaolinite is hampered slightly by preferred orientation effects and variable crystallinity between sandstone, siltstone and shale; a well crystalline standard (from a sandstone) was used. Thin section, on the other hand, only identifies crystalline, *matrix,* kaolinite. The less crystalline, *clayey* kaolinite was identified and 'lumped' with other clays. In general the 'low abundance' mineral phases, siderite, calcite and pyrite (plots e, f, g), show very poor correlations. This is inevitable with such different methods of mineral estimation and variable limits of detection.

6.4 Evaluation and interpretation of wireline data from hole 211/18-a50

6.4.1 Introduction

The borehole environment is often a very hostile place for *delicate* logging instruments. Tools will either fail to operate under *adverse* conditions, or more commonly, produce erroneous measurements. Such errors will normally either mask or totally exclude any changes in formation mineralogy and fluids. This section looks at the quality of elemental data recorded by the geochemical logging tool and demonstrates how bad hole conditions, as well as bad processing, will affect the final estimates. It aims to identify some of the pitfalls in the geochemical processing of GLT data, and show how reprocessing, with geological input, can increase the data quality.

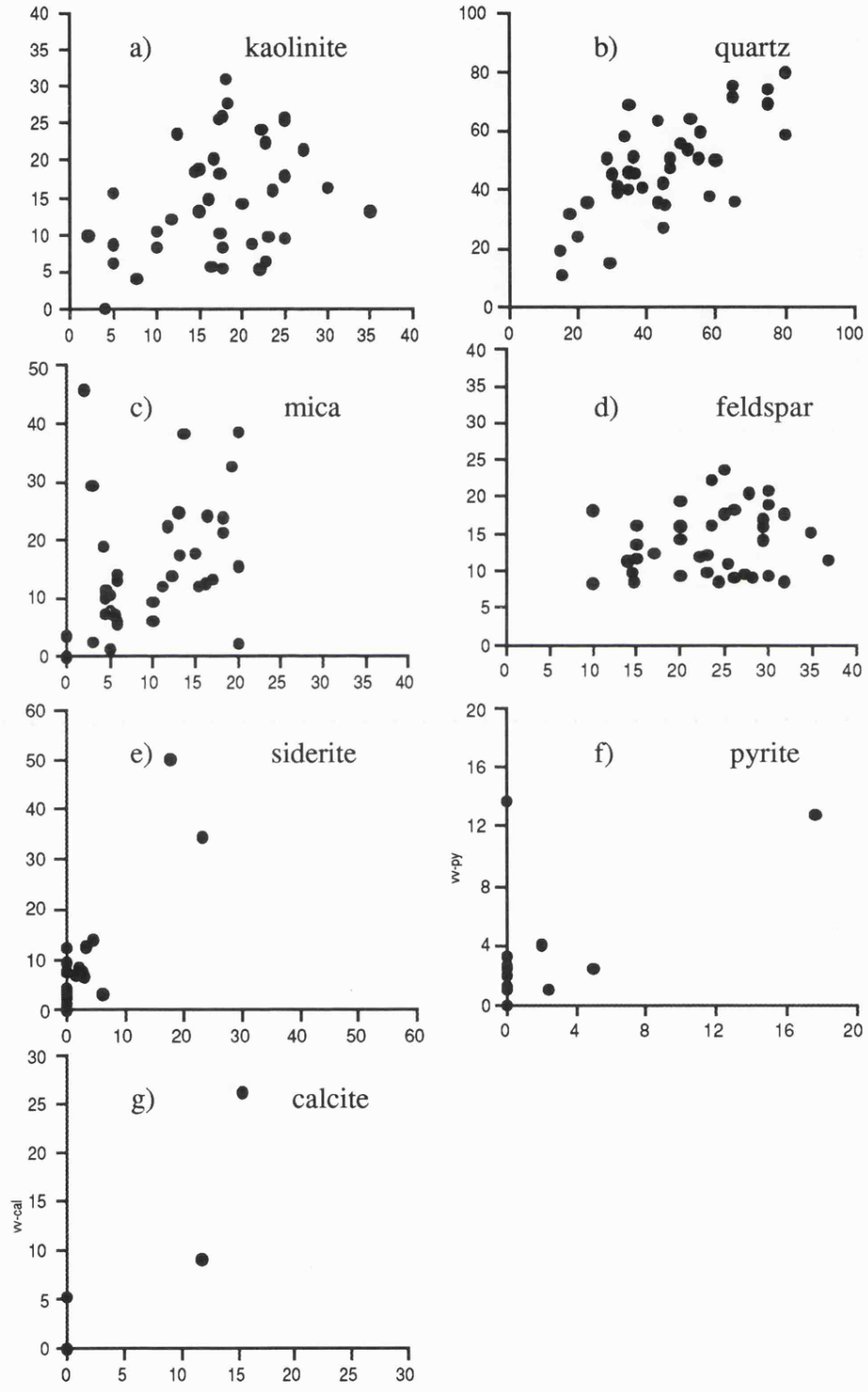

Figure 6.2. Cross-plot of core mineralogy (wt%) estimated by thin-section point counting (Y axis) and whole-rock X-ray diffraction (X axis) from hole 211/18-a50, Thistle Field.

From the GLT measurements in 211/18-a50 it is possible to estimate the elemental abundance of Si, Ti, Al, Fe, Ca, K, S, and Gd. The steps deployed to produce these estimates, and the errors involved, have been introduced in Chapter 2. A first *pass* attempt at processing the log data was performed in 1986 using early *prototype* processing routines, which were predecessors to the routines described in Chapter 2. Due to a number of discrepancies within this data, it was reprocessed in 1992 (by Schlumberger) on request of the author. Reprocessing provided logs of seemingly sufficient quality to allow mineral modelling of this data.

We shall now look at the discrepancies in the original log data (pass 1), attributed, firstly, to data acquisition problems and, secondly, to post-acquisition processing problems.

6.4.2 Data acquisition problems

Bad hole conditions, washouts and tool stand-off

The indication of bad borehole wall conditions can be clearly seen in Figure 6.3 on the caliper reading (DCAL). This shows an increase up to 30 cm from the standard hole diameter, primarily between intervals 9150'-9200' and as small spikes at *viz.* 9380', 9387', 9318', 9322'. This corresponds to the occurrence of shaly and sand/shale lithologies where drilling has caused *washouts*. The immediate effect can be seen by large excursions on the porosity (NPHI), the PEF (photoelectric factor) and bulk density (RHOB) nuclear logs. The effect of *washouts* is to increase the distance between the tool and the formation, and therefore volume of drilling fluid separating the two. The magnitude of the effect on logs is partially dependent on the drilling mud used. Washouts affect the tool measurements in various ways:

a) In the case of the *bulk density* log (RHOB), an increased volume of drilling fluid, in this case, decreases density, see Figure 6.3. This is attributed to an increase in H_2O, which is less dense (density, *viz.* $1 g/cm^3$). A lower density results in less *Compton Scatter* reactions occurring; which allows more gamma-rays to be returned to the detector. If barite (BaSO4) were present as a drilling fluid, because of its large density (due to the atomic weight of Ba), it would induce an increase in *Compton Scatter* reactions, with the effect of *increasing* density. Barite was not used as a weighting material, as is common; magnetite was used instead (M. Herron *pers. comm.*, 1992). The density tool only works well when forced against the borehole wall (effectively like a pad device). The dual sensors compensate for mudcake build-up but generally not for stand-off.

b) Magnetite, however, has a high *photoelectric absorption cross section* (*PEF*)(see Section 2.2.4) which is attributable to its Fe content. This is the cause of the increase in the *photoelectric factor* (PEF) over these *washed out* zones. PEF is required to calculate the Mg (+ Na) in processing (refer to Section 2.3.6). No attempt was therefore made at calculating Mg (+ Na) as the PEF is effected by the mud. It is also observed that Mg is not abundant through the section and any estimate is considered below any sensible detection limit for this calculation (Hertzog *et al.*, 1989), refer to Section 2.2.4.

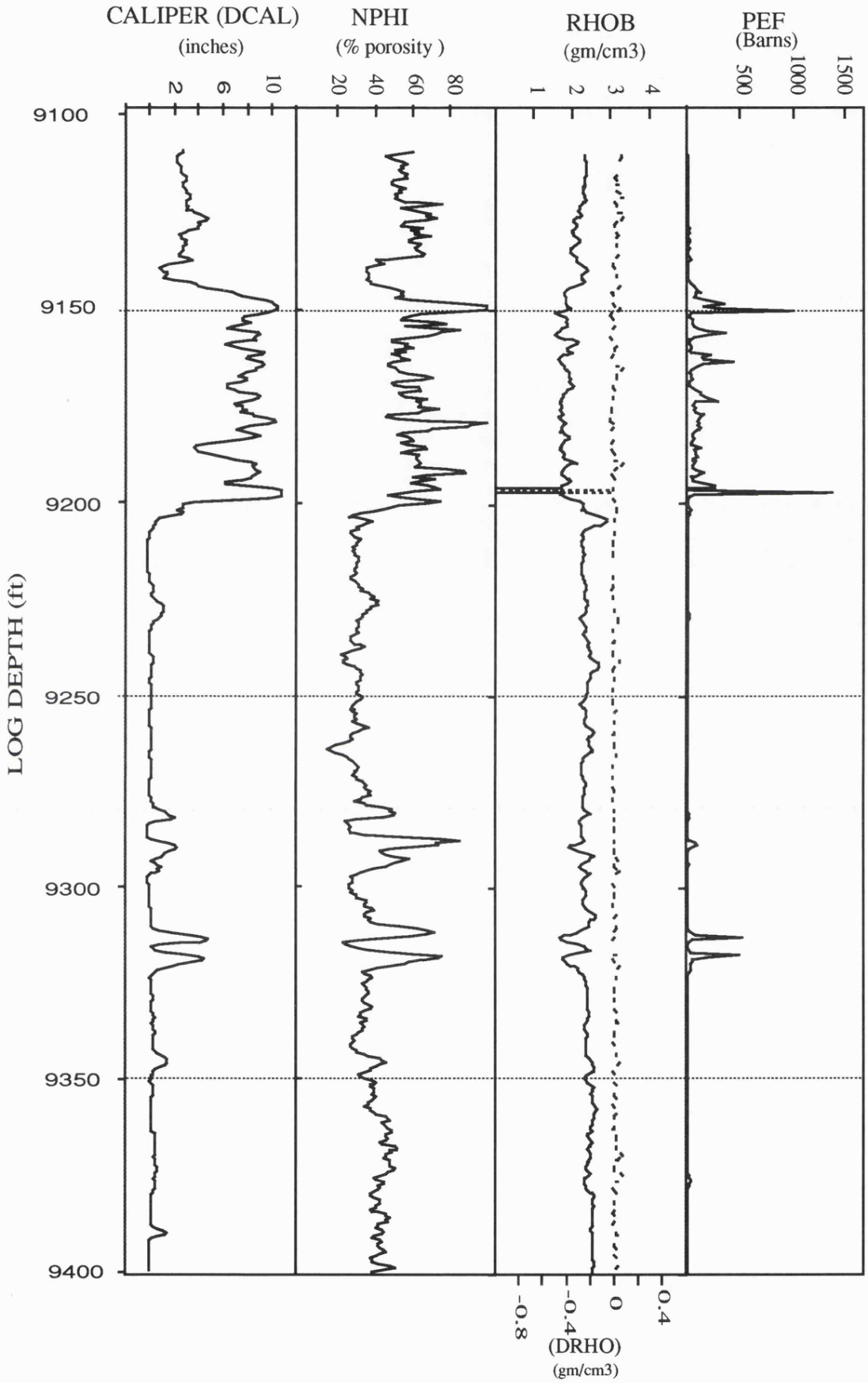

Figure 6.3 Log plots of Caliper (DCAL), Neutron porosity (NPHI), Density (RHOB) and Photoelectric factor (PEF) for the logged interval of hole 211/18-a50. DHRO is a correction applied to the density log measurement (dashed line). Note the extensive washout between 9150 - 9200 and similar washouts in localised intervals between 9275' - 9325'.

c) The use of magnetite, as with barite (as a drilling mud additive), in the situation of an extreme washout will also affect the *natural gamma-ray signal* that is measured by the NGT tool (see Section 2.2.1). Both of these mud additives will induce more Compton Scatter reactions through the borehole, reducing the count rate at the detector. The net effect is a reduction in the K, U, Th estimates. Estimates are relatively reduced through the interval 9150'-9200', but remain high due to the contribution of K, U, Th from the mudstone lithologies.

d) The effect of *washouts* on *neutron porosity* is to increase estimates over such intervals. This is a consequence of increased H in the drilling fluid (in H2O). H is an excellent neutron attenuator and has the effect of annihilating thermalised neutrons, reducing the neutron count at the detector; which increases the porosity estimate (see Section 2.1). The presence of Cl in saline drilling fluids will also affect neutrons at thermal energies (see Section 2.4). The neutron measurement may also be influenced by H^+ present in the shale lithology (in clay minerals) that dominates these washouts. Porosity increases to as much as 95% at *viz.* 9280'.

Effects from tool stand-off, as described here, can be corrected for by most tools, but here, extended washouts occur (> 25 cm) in radius, for intervals up to 16m (50') in vertical depth. Density and NGT tools commonly have a *depth of investigation* of less than 25 cm; any measured signal will therefore only be from the borehole and rendered useless. This was discussed in Chapter 2, where the effects on the GST tool were demonstrated in Figure 2.7. Unfortunately severe tool stand-off effects cannot be solved by enhanced processing. Effects are therefore present in the second pass (pass 2) processing and measurements from that particular interval deemed unreliable. All logs for *pass 1* are summarised in Appendix 5.0.

6.4.3 Poor post-acquisition geochemical processing.

This following section is by no means a *slur* on the techniques employed by Schlumberger; it is instead an exercise to demonstrate that careful processing of GLT data, and recognition of errors, is imperative if elemental estimates are to be acquired for mineral modelling.

For most measured elements, poor estimates were obtained from the first (*pass 1*) processing. This includes very low values for Fe (mean value *viz.* 0.010 wt%, standard deviation (Sd.) = 0.058 wt%), higher than expected values for Ca (mean 7.4 wt%, Sd. = 3.66 wt%) and S (mean 5.19 wt%, Sd. = 1.99 wt%). There is also a marked negative correlation between Si and Ca abundance, as shown in Figure 6.4. These are all the result of a) the input of wrong constants in the processing routines (such as drill fluid composition or *gain* and *offset* values), and b) to poor *spectral inversion.* Unfortunately, no details of the former were available and so cannot be commented on except to suggest it is a serious problem and one that probably accounts for the poor Fe concentration. The latter is, however, the cause of the inverse correlation of the Si and Ca, which inadvertently affect all other GST estimates.

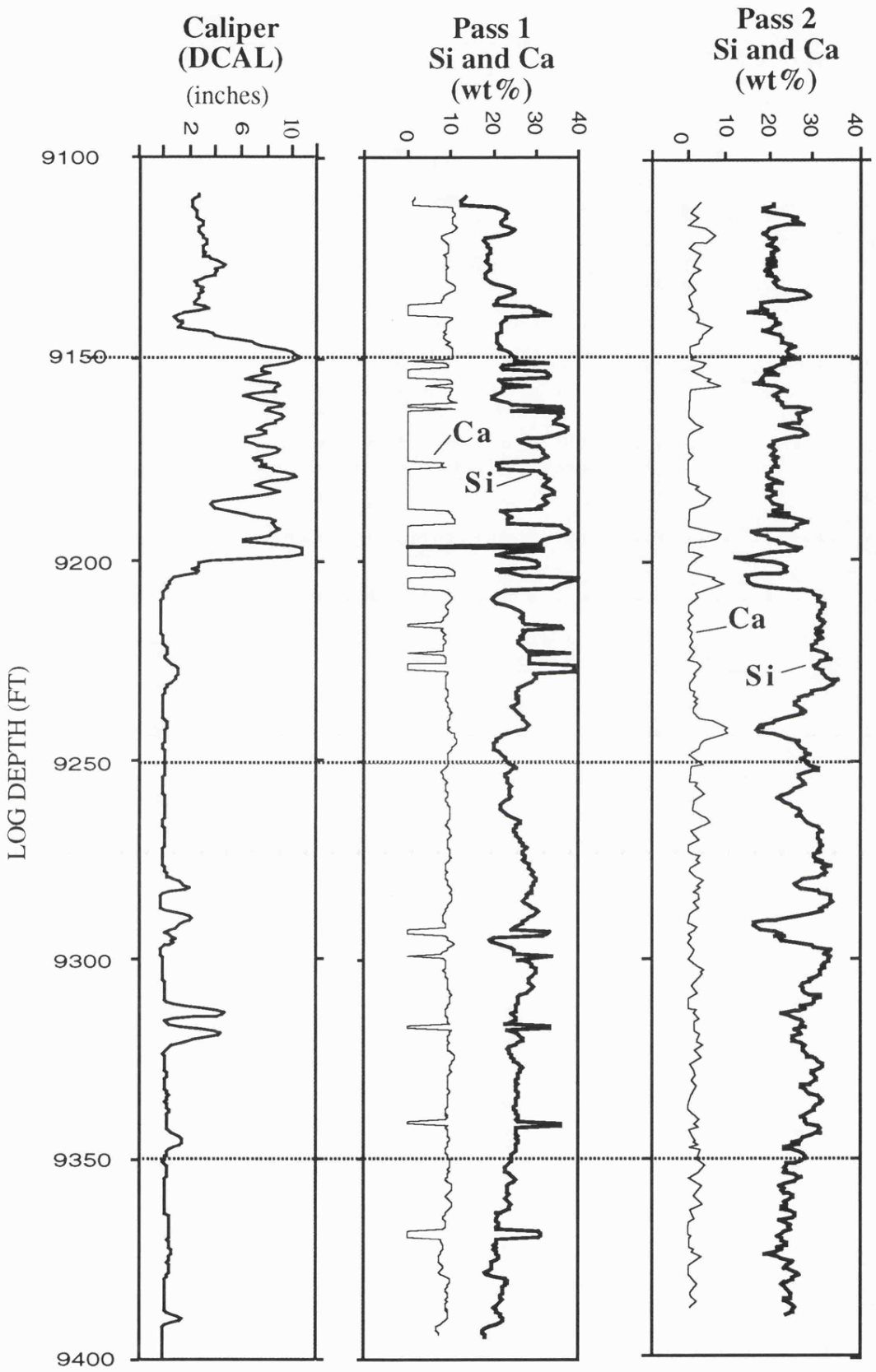

Figure 6.4 Estimates of the calculated Si and Ca (wt%) from the first and second pass processing of GLT data, well 211/18-a50. The difference between the first and second estimates is staggering. Bad spectral inversion is seen to cause the strong negative correlation between Si and Ca in the Pass 1 data; Ca is also over estimated. Inversion problems are greatest over the heavily washed out interval (9150' - 9200'). Si in bold. DCAL - caliper log. Depth in feet.

6.4.3.1 Spectral inversion and element re-partitioning

To explain this effect it is necessary to examine in more detail the method of resolving the spectrum into different elemental components to produce *elemental yields.*

The assumption when determining the relative contribution of an element from the total GST spectrum (refer to Section 2.2, and 2.3) is that the recorded spectrum (U) can be represented as a *linear* combination of a set of 'standards' or *basis spectra* of each element (Grau *et al.,* 1980); such that the spectrum (U) is given by:

$$U_n = \sum_i S_{ni} \cdot Y_i + \varepsilon_n \qquad (1)$$

Where n is the number of channels in the spectrum (normally 181). Y_i is the spectral yield coefficient which represents the number of counts in spectrum U which can be attributed to element i; and S_{ni}. is the standard spectra for element i, called a *linear estimator.* These standards (S_{ni}) are laboratory determined for each element. Two linear estimators, for the elements Si and H, are shown in Figure 6.5 (other elemental standards, in conventional spectral form, are shown in Figure 2.6). ε_n is an associated error for each elemental yield.

With the spectrum (U) known and spectral standards (S_{ni}) known, the determination of the relative elemental contributions (yields; ie, Y_i) from this spectrum can be performed by inversion. A weighted *Least Squares* inversion is used, as described in Chapter 3 (section 3.3.3), such that the best estimate of Y_i is the set which minimises the sum of the squares of the errors (ε_n) over all channels (n). Weighting the inversion takes into account any statistical uncertainties (precision) for each element in each channel. For a simple spectrum like H, the *linear estimator* is more or less just an image of the standard spectrum (like in Figure 2.6). However, for other elements, such as Si, it is more complicated, see Figure 6.5. Each *linear estimator* is positive in channels where its elements have spectral peaks and negative where other spectra have peaks. As these spectra overlap one-another, the negative parts of the linear estimators keep one elements counts from making a net registration as another element. Each linear estimator must be *orthogonal* (n-1) to the other standards. This forces a closure constraint on the calculated spectrum. A side effect of the induced closure is a forced correlation between some standards; for example, between Cl and Ca, and Ca and Si. Elemental yields are therefore not only determined by the counting statistics but also by these correlation statistics (ie, the extent the peaks either overlap or mutually interfere).

To illustrate an example; in the event of a high Cl yield, such as in a washout zone or with high porosity, the Cl spectra will dominate the spectrum. The effect of the massive interference spectra of Cl is to mask the *real* signature of the other spectra by forcing an increase (or decrease) in an elements yield which corresponds to its correlation with Cl. Cl has a strong negative correlation with Ca spectra. In such a case the Ca yield will be decreased. Because Ca and Si also have an inverse correlation; a decrease in Ca will force a increase in Si. In this situation the inversion becomes unstable and negative yields can occur. The net effect is to make the resolving of *true* elemental yields impossible. This probably occurs in the washout interval between 9150' and 9200'.

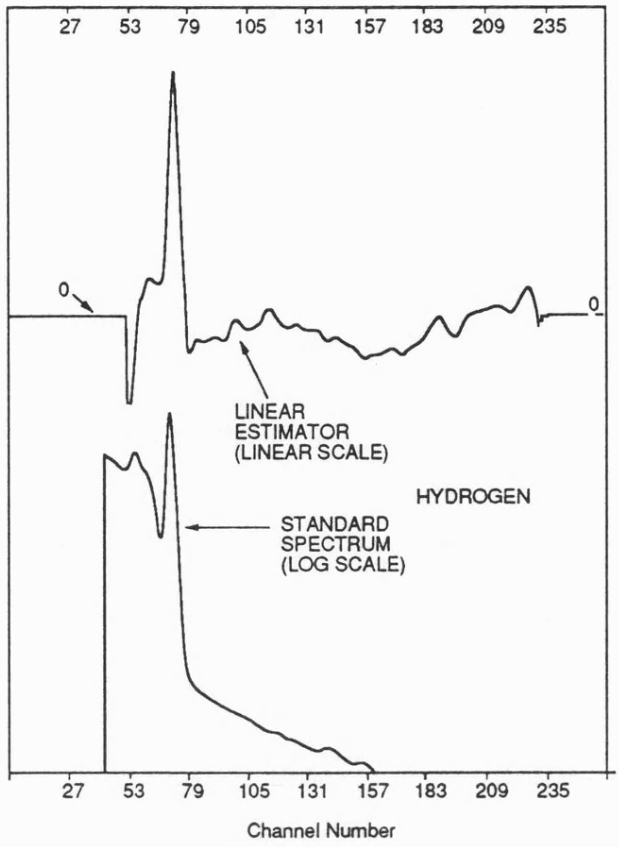

Linear estimator and standard spectrum for hydrogen

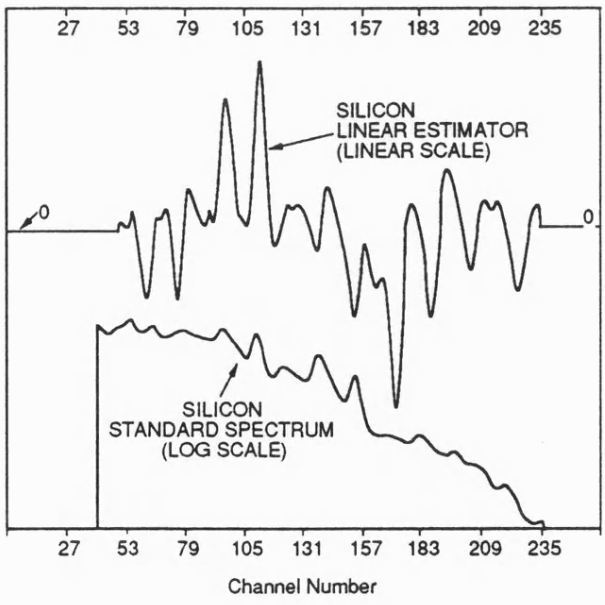

Linear estimator and standard spectrum for silicon

Figure 6.5 Linear estimator and standard spectrum for hydrogen and silicon. The linear estimator for each element is used in the spectral stripping inversion routine (GSTREC) to resolve the spectrum in to specific elemental yields.

Such a correlation between Si and Ca is present in the first pass processing of Figure 6.4, in the large washed-out interval (9159-9200') and in smaller intervals between 9200' and 9400'. A correlation is more likely to occur for Si and Ca than other elements as either element is typically the most abundant in a sandstone-carbonate lithology. The original processing here cut Ca off at zero although the inversion is likely to have caused negatives. This correlation will cause an effect on all the other elemental yields in a similar way to the Cl effect.

In Chapter 2 (Section 2.3.5) it was shown that spectral standards may be removed in the absence of an element, or alternatively new spectra added. This involves the re-partitioning of that spectral contribution between the remaining spectra for which proprietary *re-partitioning coefficients* are used. This is routinely done for K if there is any difference between the relatively poor GST measured spectrum and a *'back-calculated'* K spectrum derived from the NGT tool (which represents a better estimate of K). The Cl problem may therefore, in less severe situations, be partially resolved by re-partitioning small scale Cl changes in the Cl spectrum to the other spectra (Jarrard & Lyle, 1991)

The introduction of new spectral standards recently allows a more accurate inversion to be performed especially for the resolving of Ca and Gd (M. Herron, *pers. comm.* 1992). The new Cl standard more closely reflects the Cl signature from the borehole and less from the formation Cl. This reduces the effect on other elements which are more closely correlated to formation Cl and is especially a problem from older tools which had no boron sleeve fitted (J. Bristow, *pers. comm.* 1992). The effect is to reduce the correlation between Cl - Ca and Gd - Sm in particular.

Figure 6.6 demonstrates the improvement in the Fe, Ca and Si estimates in the second pass processing. This is due to enhanced spectral standards and improved input parameters. Pass 2 estimates of Si and Ca (see Figure 6.4) show no correlation with each other and probably represent contributions from the real spectrum. Unfortunately no elemental data were available to compare the accuracy and precision of these estimates. Calculated oxide percentages do, however, closely mirror the gross changes in lithology seen through the interval 9200 - 9400' as demonstrated in the next section.

6.5 Correlation of log derived element chemistry to mineralogical & geochemical trends.

Log derived elemental and physical measurements are now compared with the small scale mineralogical - lithological changes observed throughout the interval from *viz.* 9200' to 9390' (core depth). The aim of this is to illustrate the effect of both measurement resolution and lithology on GLT elemental measurements. The logs considered here include: the elemental oxides - K2O, SiO2, CaO, Al2O3, Fe2O3, TiO2; bulk density, Σ_{total}, natural gamma-ray (SGR), neutron porosity and caliper. These are illustrated in Figure 6.7 a & b. The geochemical measurements shown here are represented in their most common oxide form and the one used in later mineral modelling. With the exception of the neutron and bulk density measurements,

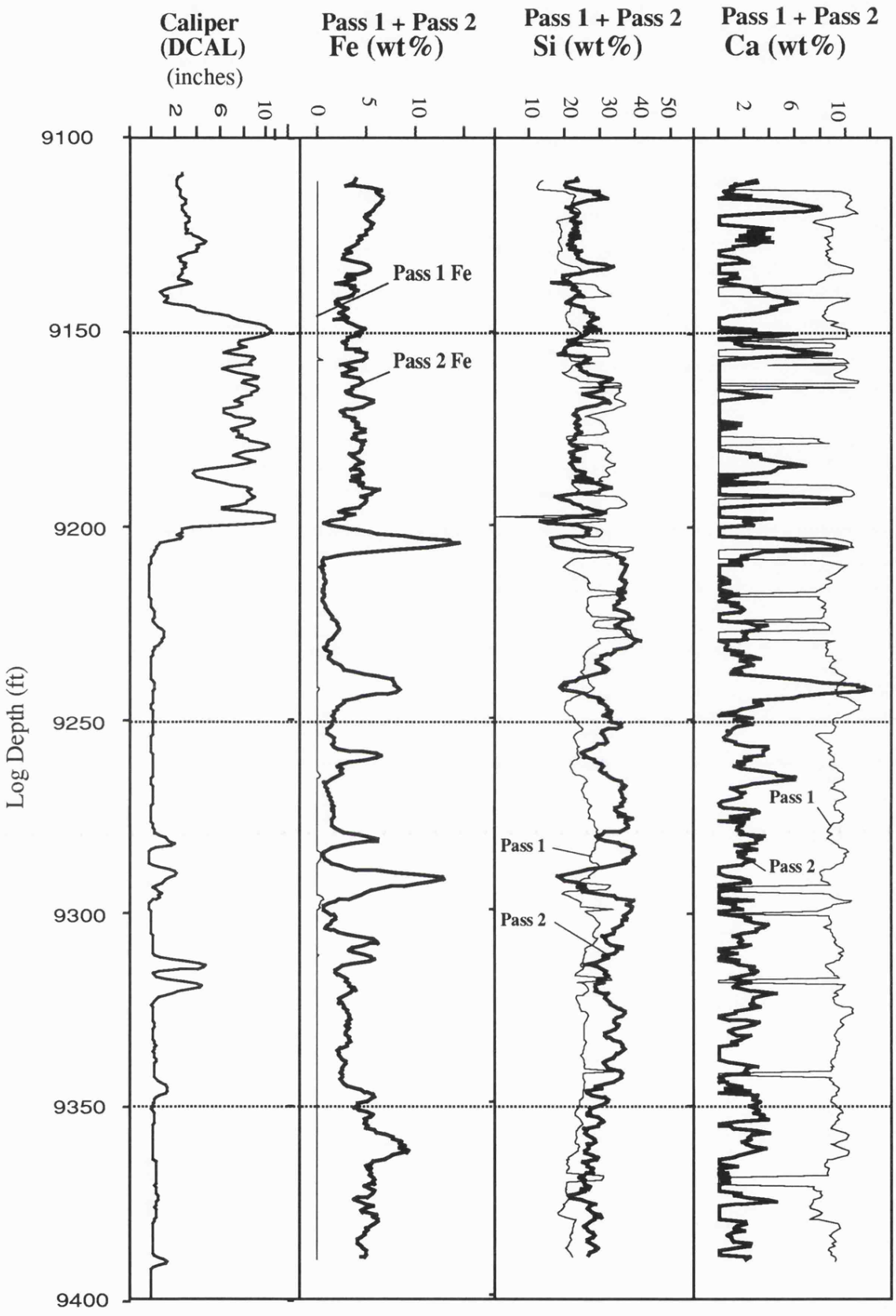

Figure 6.6 Estimates of calculated Fe, Si and Ca (wt%) from processing passes 1 and 2. Pass 2 (bold line) illustrates greatly improved estimates of all three elements, especially Fe and Ca. DCAL - caliper. Depth in feet.

all of the above logs respond primarily to the formation matrix and are therefore lithology dependent.

6.5.1 Tarbert

The most prominent log excursion in the Tarbert is caused by the calcite 'dogger' (*viz.* 9225'). Increases in CaO and Fe2O3 respond to the Fe-carbonate, mirrored by decreases in SiO2, natural gamma-ray (SGR), K2O, Al2O3 logs respectively; see Figure 6.7 a & b. Porosity (NPHI) also drops in response to the tightly cemented Fe-carbonate, while density increases in response to increased Fe in the carbonate. Refer to Chapter 3, Figures 3.8 and 3.9 for the extent that the common minerals in the Thistle Field, Brent Group, contribute to the oxide proportions - Al2O3, K2O, MgO and Fe2O3.

The upper T2, quartz rich, unit above the 'dogger', shows a high SiO2 excursion (78%) and porosity (NPHI) reflecting the medium to coarse sandstone. These mirror decreases in Al2O3 and K2O, CaO, Fe2O3 (see Figure 6.7b) relative to the surrounding (T1) lithology. The micaceous fine sandstone (T1) lithology that dominates most of the Tarbert reflects the overall increase in the K2O, Al2O3 and SGR signature, especially between 9225' and 9245'. Two siderite cement horizons through the Tarbert give high Fe2O3 and density spikes (*viz.* 9240' and 9260') and CSIG is also increased, while SiO2 is decreased. CSIG is a measure of the *total* thermal neutron absorption cross-section of the borehole and formation (Σ_{total}). Increases in CSIG are the direct response of Fe cement at 9240' (Fe having a large Σ); but at 9260', (a siderite-siltstone at the boundary of the Ness and Tarbert) increases in CSIG are due to the combined effect of increased borehole fluid Cl influence - induced by a washout (indicated by the caliper log), and also the effect of the Fe in the carbonate.

6.5.2 Ness

The Ness is hampered by a number of washout zones, shown by an increase in the caliper and CSIG. These washouts coincide with the finer grain mudstone - siltstone lithologies (N1, N2, N5 units) present throughout this *heterogeneous* unit. The most prominent mudstone/shale interval (N2 - *viz.* 9272' - 9276') shows classic *shale-mudstone* responses - including increased SGR, NPHI, CSIG as well as increased Al2O3 and K2O and Fe, which reflect the dominant kaolinite clay - mica mineralogy; while SiO2 and RHOB are decreased. Caution must be exercised in interpreting the *absolute* values obtained when large caliper increases occur, in view of the borehole effects referred to in Section 6.4.

The coarser sandstone units of the Ness show some interesting trends. The N4 unit, described as coarsening upwards, from 9295' to 9276', shows a gradual increase in SiO2 from 60 - 80%; with mirrored decreases in Al2O3 and K2O, SGR, Fe2O3. This clearly reflects the coarsening up trend caused primarily by an increase in quartz and decrease in mica and clay minerals. Localised siderite or pyrite horizons, however, cause the Fe2O3 log to deviate locally. The unit N1 (top Ness) shows a decreasing SiO2 trend reflecting a gradual fining

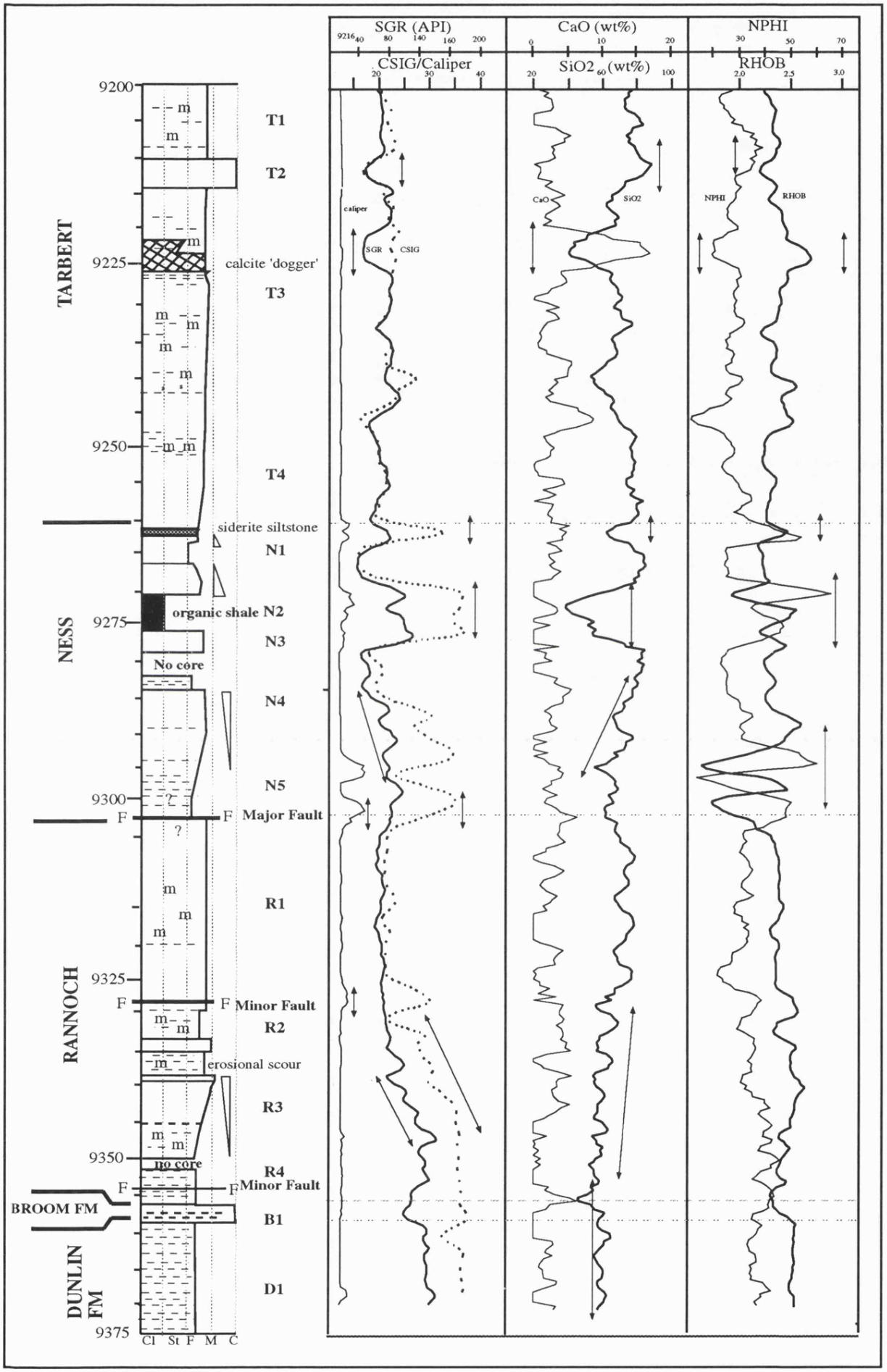

Figure 6.7 (a) Physical and chemical logs over the section 9200' to 9375', Thistle well 211/18-a50. Depth in Feet, (core depth). Arrows refer to trends mentioned in text.

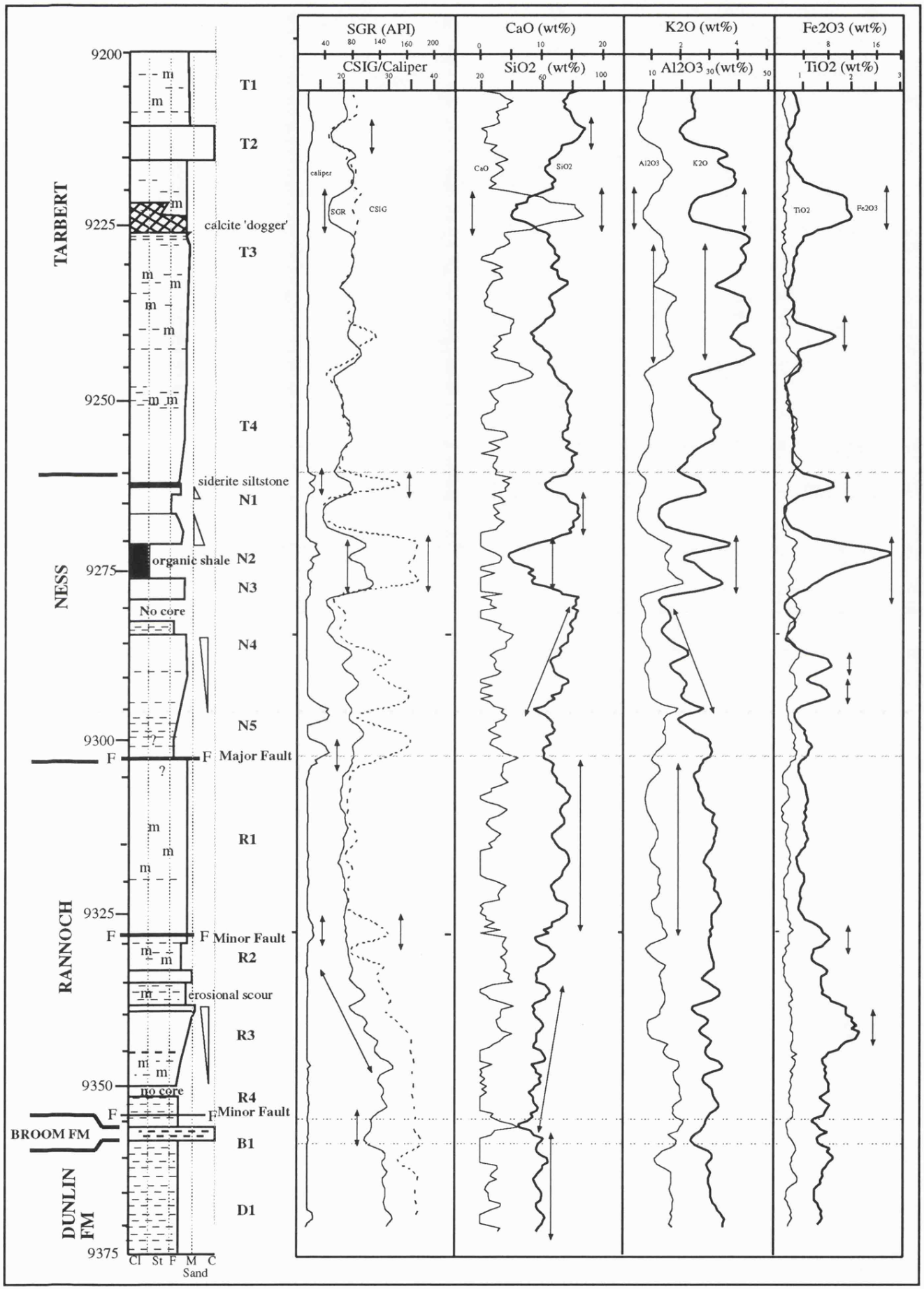

Figure 6.7 (b) Gamma-ray spectroscopy (GLT tool) determined oxide estimates (wt%) for the section studied in well 211/18-a50. Arrows refer to the trends mentioned in the text. Depth in feet (core depth). Caliper in inches. CSIG in capture units.

upwards, however, influences from other minerals tend to obscure this trend on the other log curves. The low Al2O3 and K2O signature in the N4 sandstone unit, relative to the sandstones in the Tarbert and Rannoch, reflect the lack of mica and kaolinite in this unit.

The base N5 unit has the worst caliper deviation (up to 40cm) and this correctly reflects the major fault between the Ness and the Rannoch that is implied from core data.

6.5.3 Rannoch

The top, R1, micaceous Rannoch unit shows a similar elemental signature to the Tarbert sandstones; notably a reasonable K2O and Al2O3 signature which reflects the feldspar, kaolinite and mica content. It shows very consistent values for most elements reflecting its homogeneity. The minor fault (*viz.* 9328.5'), between the R1 and R2 units, is recorded as a small caliper deviation (with an increase in CSIG). Another coarsening upwards sequence, unit R3, manifests as a decrease in K2O, Al2O3 and SGR and a small increase in SiO2 upwards. Pyrite causes an increase in Fe2O3 at the top of the R3 unit.

6.5.4 Broom and Dunlin Formations

The Broom Formation is not clearly resolved by any logs and this is probably an artefact of the mixed sand-silt character of this small (1m thick) interval. The Dunlin shows the highest SGR measurements (150 API units) and low SiO2, Fe2O3 and Al2O3 signatures characteristic of a return to a shale lithology.

6.6 Mineral modelling of GLT derived elemental data

Section 6.4 demonstrated the importance of assessing the validity of log derived elemental measurements before attempting any mineral modelling. The *Pass 2* elemental data are considered to be good enough, from assessment in section 6.5, to use for the mineral modelling. The exception to this is where washouts in the hole are large. For this reason only the interval *viz.* 9200' - 9375' (9217'-9390' log depth) was selected for modelling.

6.6.1 Model parameterisation

The *elemental data* available for this interval, converted to oxide form include: SiO2, TiO2, Al2O3, Fe2O3, CaO, K2O and S. No estimates of Na2O or MgO are possible from the tool in the hole, due to the poor PEF estimates effected by the Fe rich drilling mud (Section 6.5). Elemental measurements are tabulated in Appendix 6.2.

Collection of *mineral composition* data for this hole was beyond the scope of this study as no core was available. In the absence of such mineral data the compositions used in the earlier Thistle modelling, were employed. This choice is considered reasonable because of the similarity in the mineralogy and petrology of the two Thistle holes and the relatively short distance between them (1.75 Km). In any case, these mineral data probably represent the most

likely sort of data that would be available for a typical *field-wide* study. The major phases identified throughout the Brent Group here are very similar to those in the previous hole 211/18a-a33 although calcite and pyrite appear more common. These include quartz, K-feldspar, albite, muscovite, biotite, siderite, kaolinite. Some sandstones also contain negligible amounts of mixed illite/smectite, illite or chlorite which are too small to model independently.

6.6.2 Adopted strategies

It is clear that with the absence of MgO and Na2O oxides that a *reduced set* of oxides is present. The system to be solved is essentially under-determined with 7 oxides and 9 minerals. Without Na2O, albite (sodium) feldspar cannot be estimated. The strategy adopted to overcome this is to combine the two feldspar minerals into one '*binary phase*' in equal proportions, as suggested from core estimates (*binary phase option,* refer to Section 5.3). Similarly, muscovite mica and biotite mica are combined in to a single phase, 'mica'. Producing *binary phases* has the effect of reducing the minerals to be solved for by 2, making the *system* fully-determined. It was also shown that *binary phases* in fact help to reduce the effect of *compositional colinearity*, which occurs in the Rannoch and Tarbert Formations (refer to Section 5.4.1). Phases that are therefore available to model include quartz, *total-feldspar*, *total-mica*, kaolinite, siderite, calcite, pyrite, +/- rutile. Adopted mineral compositions are listed in Appendix 6.0

The *selected assemblage strategy* (Section 5.2) has been implemented to allow the mineral assemblage to vary at each sample interval. This has proved to be the preferable strategy in previous modelling (Section 5.6), in essence, allowing the best of a choice of assemblages to be chosen. The twelve assemblages of minerals identified from core observations are summarised in Table 6.2. These were the initial choice of assemblages input to the model. It was expected that the assemblages depicted by 39 core samples would not, however, satisfy the complete range of assemblages likely to be found in the 350 log measurements made.

Table 6.2. Different assemblages of minerals identified by XRD & thin section point counting core samples from the Thistle hole 211/18-a50 column. 'Euc' illustrates the number of times each assemblage was chosen by the Euclidian model. No. core samples = 39.
x - identified by XRD; **t** - identified by thin section; @ additional 'viable' assemblages included. Kao - kaolinite, Qtz - quartz, Fsp - total feldspar, sid - siderite.

Assemblage		Mica	Kao	Qtz	Fsp	Sid	Pyrite	calcite	Euc
1	x/t	*	*	*	*	*			0
2	x/t	*	*	*	*		*		11
3	x		*	*	*				0
4	x/t	*	*	*	*	*	*		33
5	x		*	*		*		*	0
6	x	*	*	*		*	*		11
7	x		*	*	*		*	*	49
8	x	*	*	*		*		*	8
9	x		*	*	*	*	*		23
10	t	*	*	*	*				0
11	t		*	*	*		*		0
1	@	*	*	*	*		*	*	58
2	@	*	*	*	*	*		*	5
3	@	*	*	*	*	*	*	*	151

6.6.2.1 Selection of the best assemblage: 'three pass attempt'

In Chapter 3 it was demonstrated that any solution with a correct (or perfect) mineral assemblage will produce a very low Standard Error as a result of a good fit between the observed and calculated chemistries. Similarly, this estimate of Standard Error was seen to deteriorate rapidly if a wrong assemblage were substituted. In view of this observation, a series of three *passes* were made before accepting a final assemblage to model. Starting with the selection of assemblages identified from core estimates, any assemblages that were not chosen by the model were withdrawn. Other possible, or sensible, combinations of minerals were substituted if a large Standard Error remained for a sample. The final criteria for selecting an assemblage being that the Standard Error, as a measure of geochemical fit, was less than one. Figure 6.8 demonstrates the reduction in Standard Error on each of the three passes. The third pass shows an excellent *average* Standard Error of 0.093 and 0.103 (for the Least Squares-Error Minimisation and Euclidian models respectively). Most assemblages chosen with good Standard Errors on the first pass in fact do not alter through the second and third passes. The strategy therefore has some validation in the discrimination of the optimum assemblage within just a few attempts.

6.6.3 Modelling with an alternative 'clay' composition

An additional pass was run with the same set of assemblages and compositions except that the pure kaolinite clay composition was exchanged for a composition, approximating to a mixture of kaolinite and the *minor* clay minerals identified from core (termed "a50-clay"). This composition represents the average concentrations for all clay phases identified in sandstone-silt lithologies by XRD. For modelling purposes this comprises of a mixture similar to previous 'binary *mixtures'* (refer to Section 5.5.1); including kaolinite (60 wt%), mixed layer illite/smectite (32 wt%), illite (3.5 wt%) and chlorite (5.7 wt%). Its implementation, as an alternative to kaolinite, is to demonstrate what a change in composition may make on *mineral estimates.*

6.6.4 Modelling with an additional estimate of bound water

An additional pass is also presented where an extra input parameter, *bound water,* is modelled with the oxide data. This is to evaluate its usefulness in constraining the estimation of minerals that contain 'bound' inter-layer or lattice water, which in this lithology is kaolinite and mica. An estimate of *bound water* (Wmin) is derived, here, from *epithermal* neutron and bulk density *porosity* measurements (refer to Section 5.4.4.1). Typical values of bound water are ascribed to the hydrous minerals, kaolinite (13%), 'a50 clay' (12.6%) and mica (4.2%), and correspondingly input in the *components matrix.*

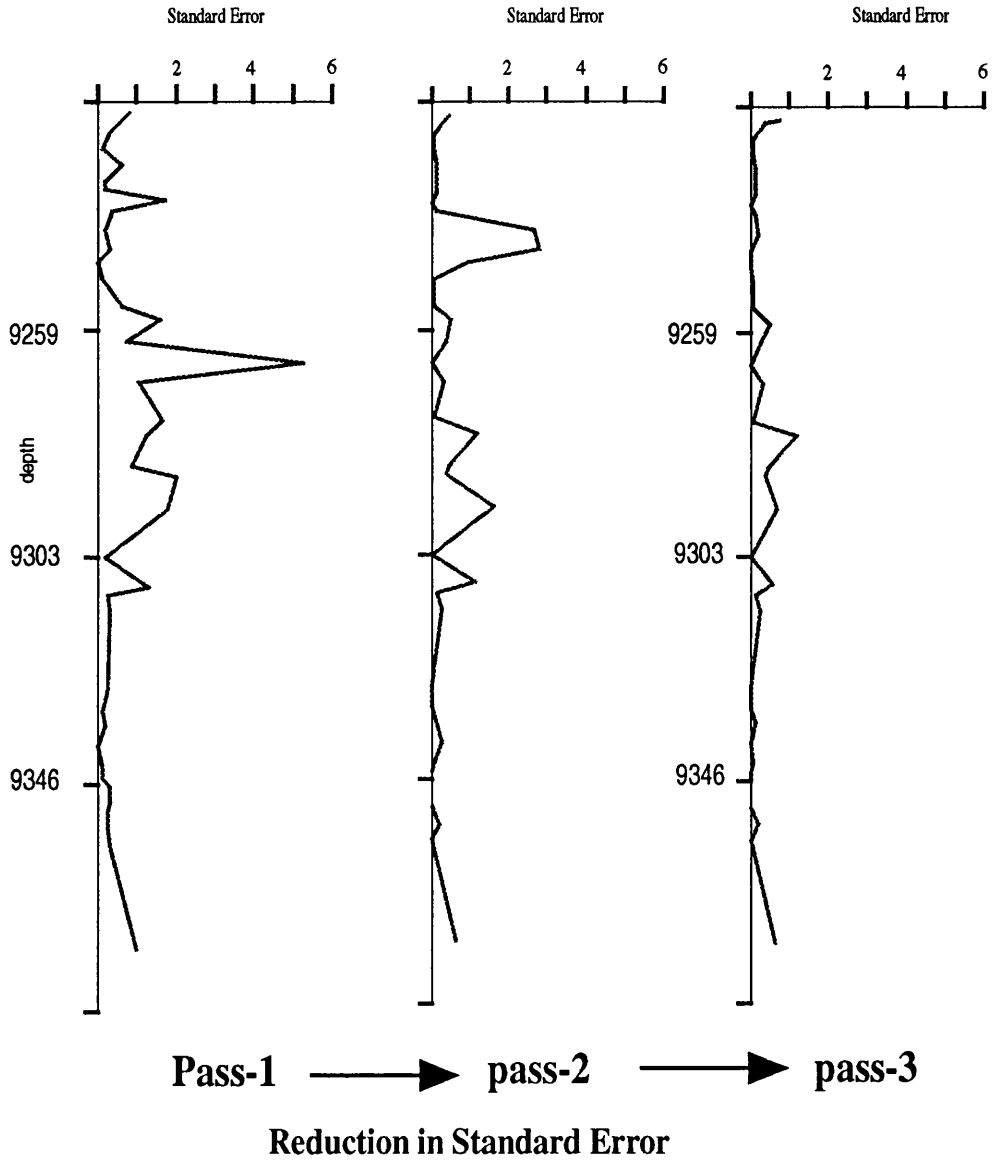

Figure 6.8. Log plots showing the reduction in Standard Error on each modelling pass of the Thistle 211/18-a50 data. Standard Error is significantly reduced in the third pass and represents the assemblage chosen in the final solution. Depth in feet.

6.7 Modelling results

6.7.1 Comparison of model and core derived mineralogy

Figure 6.9 shows cross-plots of core mineralogy and estimates from the Euclidian and Linear Programming models for the four major mineral phases present through the section. Discrepancies in estimates between core techniques have been discussed (Section 6.3.1) and it is imperative that these are considered in any comparison with modelled mineralogy. In terms of *sample volume differences*, problems of *heterogeneity*, core *sampling bias* and an XRD absolute error of within +/-5 wt% (at best), any comparison with core is only semi-quantitative. Sample size/volume differences are especially a problem here because unlike the earlier Thistle 'a33' data set, XRD samples were not taken from homogenised strip samples of core.

6.7.1.1 Cross-plot comparisons

Quartz in Figure 6.9 (plots A & E), follows a linear trend that is satisfactory for both models, as is *mica* by Euclidian model (plot B). The points lying on the mica Y axis (plot B & F), indicate that mica is not selected by the model even-though up to 20% has been identified by core. This remains a problem and is worse in the Linear Programming model (plot F). Mica, at higher concentrations, is over-estimated by thin section compared to both models. This is probably an error related to the thin section technique that does not necessarily suggest the numerical model is at fault. For the Euclidian model *kaolinite* has a scattered distribution (plot D), although slightly better for Linear Programming (plot H). *Feldspar* estimates tend to be slightly over-estimated by both models above 25% (plot C & G), especially by four erroneously high predictions of >50% feldspar. Linear Programming fails to choose a number of assemblages which include feldspar, although it is identified in core up to 30% (plot G). Feldspar is perhaps the least accurate major mineral phase predicted by the model and this is probably due to the colinearity of the potassium rich minerals and core measurement discrepancies mentioned in Section 6.3.1.

In general, the correlation with core is far from good, although reasonable *qualitative* similarities and trends recognised in core can be seen in mineralogy derived from both models. Another way to compare estimates, in light of the afore-mentioned discrepancies, is by comparison of the mean values of mineralogy calculated from each formation; see Table 6.3. It can be seen that model estimates for the major minerals quartz-feldspar-kaolinite-mica are (surprisingly) close to values from the core analysis (within 5%). Deviations occur in the Tarbert, where the kaolinite clay phase is under-estimated and feldspar over-estimated.

6.7.1.2 Comparison of mineralogical trends in model and core data.

Mineralogical features and trends from core studies were summarised in Figure 6.1 and Section 6.3. In Figure 6.10, core-model *log* plots illustrate the general *mineralogical trends* that are 'predicted' by the Euclidian Distance model. The alternative "a50 clay" pass (refer to Section 6.6.3) is also included. Estimates from both passes do in fact follow most of the mineralogical

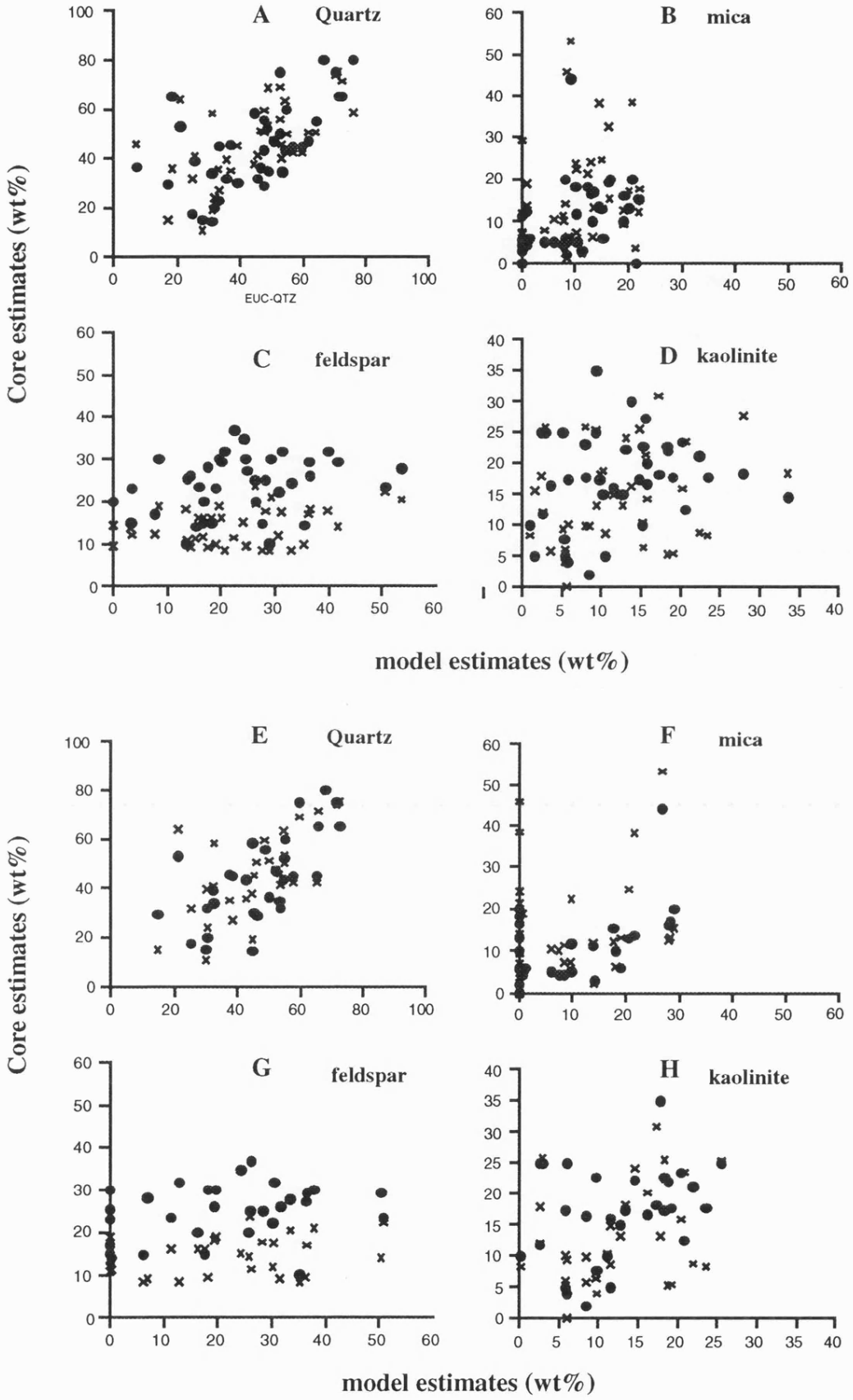

Figure 6.9. Cross-plots of core and model derived estimates of mineralogy, hole 211/18-a50. Plots A-D Euclidian Distance model, E-H Linear Programming model. Dots represent XRD estimates, crosses - thin section estimates. Estimates in wt%. Y axis core mineralogy; X axis model mineralogy.

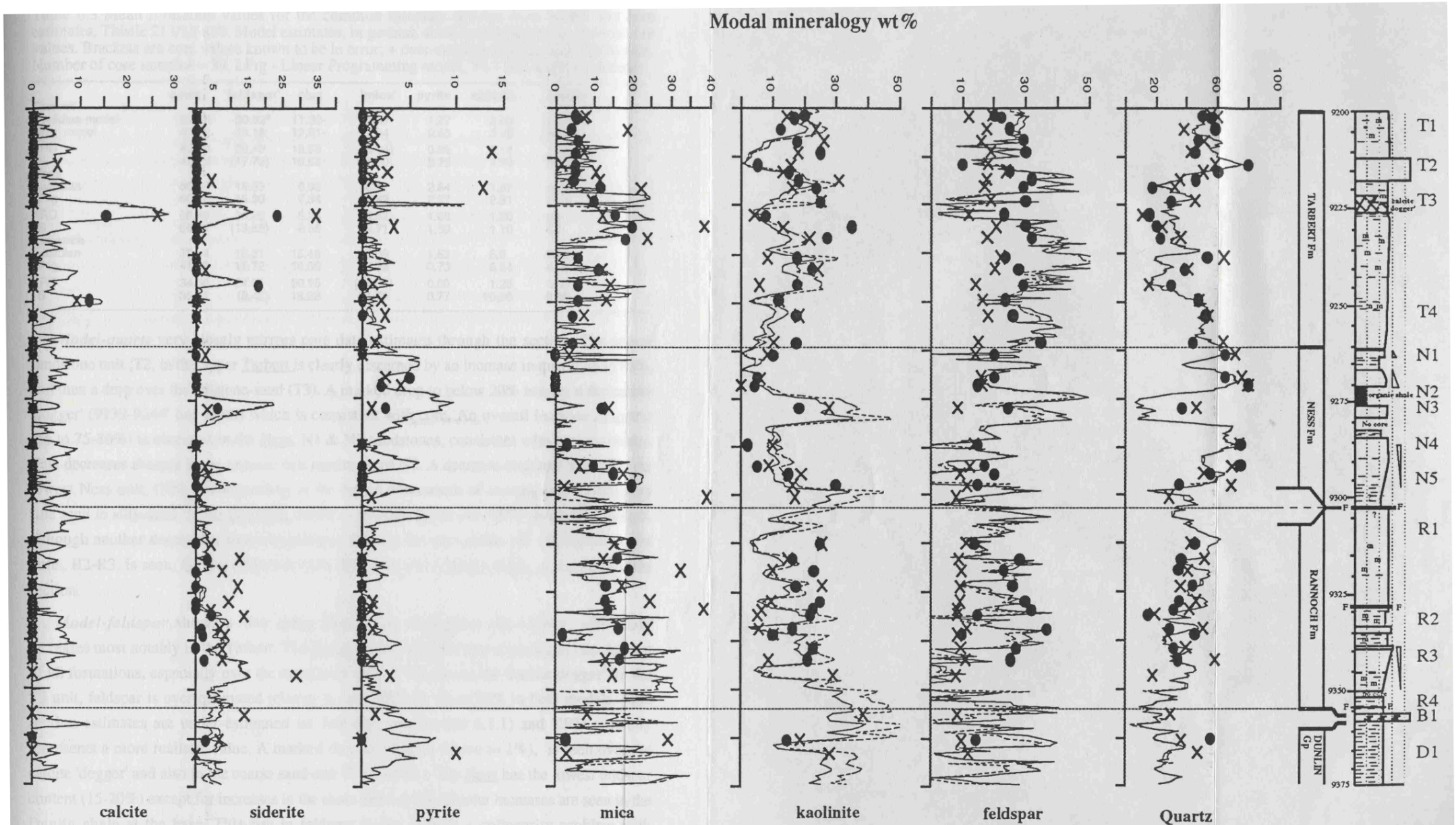

Figure 6.10

Figure 6.10. Log plots comparing the wt% mineralogy derived from the Euclidian model, with two different clay compositions input; Thistle hole 211/18-a50. Solid line - kaolinte composition modelled; dashed line - "a50 clay" composition modelled, see text. Core mineralogy represented by dots (XRD estimates), and crosses (thin section estimates). Depth in feet.

trends observed through the section by core techniques. Differences between the two passes lie mainly in the estimation of kaolinite and mica. The most prominent features/trends and comments on their correlation with core are now summarised.

Table 6.3 Mean formation values for the common minerals derived from model and core estimates, Thistle 211/18-a50. Model estimates, in general, show a close approximation to core values. Brackets are core values known to be in error; + over-estimated value; under-estimated. Number of core samples = 39. LPrg - Linear Programming model, TS - thin section estimates.

	quartz	'feldspar'	clay	'mica'	pyrite	siderite	calcite
Tarbert							
Euclidian model	41.20	30.62*	11.32-	7.47	1.27	2.08	5.63
LPrg model	41.72	26.18	13.91-	7.34	0.63	3.55	6.32
XRD	42.69	26.46	18.55	(8.04)	0.92	2.14	1.42
TS	43.26	(17.72)	16.83	12.50	2.25	4.90	2.13
Ness							
Euclidian	60.05	16.83	6.98	6.47	2.84	1.67	4.39
LPrg	60.98	15.30	7.34	6.42	2.27	2.21	4.74
XRD	65.49	20.25	8.34	(4.62)	1.88	1.20	0.0
TS	69.07	(13.86)	8.85	5.71	1.50	1.10	0.0
Rannoch							
Euclidian	39.54	19.31	15.48	15.09	1.53	5.3	3.29
LPrg	41.26	16.72	16.05	13.89	0.73	6.84	4.29
XRD	34.56	24.31	20.15	(17.53)	0.00	1.25	0.00
TS	38.31	(9.42)	16.28	24.75	0.77	10.56	0.00

Model-quartz very closely mirrors core data estimates through the section. The coarse sandstone unit ,T2, in the upper Tarbert is clearly discerned by an increase in quartz up to 80%, and then a drop over the siltstone-sand (T3). A marked drop to below 20% is seen at the calcite 'dogger' (9239-9244' log depth) which is consistent with core. An overall increase in quartz (up to 75-80%) is observed in the Ness, N1 & N3 sandstones, consistent with core estimates. This decreases sharply in the organic rich mudstone of N2. A decrease in quartz is seen in the lowest Ness unit, (N5), corresponding to the fining downwards of the sequence, from very fine sand to silty-sand. In the Rannoch, quartz is less prominent (40-55%) and more constant, although another decreasing trend downwards through the silty-sands and silts of the lower units, R2-R3, is seen. Quartz drops very low throughout the Dunlin shale, at the base of the section.

Model-feldspar shows a very spiky distribution throughout the section, with sharp increases most notably in the Tarbert. The Tarbert feldspar prediction is (correctly) the highest of all formations, especially over the basal units (T3 & T4), below the 'calcite dogger'. In the T3 unit, feldspar is over-estimated relative to core XRD by up to 20% in both models. Thin section estimates are under-estimated for feldspar (see Section 6.3.1) and XRD probably represents a more realistic value. A marked drop in feldspar (down to 1%), is seen over the calcite 'dogger' and also in the coarse sand unit T2 (13-20%). The Ness has the lowest feldspar content (15-20%) except for increases in the shale interval N2. Similar increases are seen in the Dunlin shale at the base. This rise in feldspar in the shale is a colinearity problem with modelling shales and is discussed later. Over the Rannoch feldspar values tend to rise again, although variable, but fairly consistent with core XRD.

Model-kaolinite is variable through all formations, typically the lowest in the Ness Formation, except for a large increase over shale interval, N2. Kaolinite, in the Tarbert, drops

over the coarser T2 sand unit and at the calcite dogger as seen in the core. The mean formation feldspar of 11-13% is 5-8% lower than core estimates and could therefore be under-estimated. The *a50-clay model* estimate (dashed line) tends to model kaolinite slightly higher, resulting in a better comparison with core XRD. The Rannoch has similar values to the Tarbert, although a notable increase is seen towards the base of the formation in correspondence with the increase in silt between R3 and R4. Kaolinite (correctly) rises in the Dunlin Group in response to the change to a shale lithology.

Model-mica has perhaps the spikiest appearance of the major minerals. The Tarbert has a moderate mica concentration, which increases either side of the calcite 'dogger', and a marked decrease over coarser T2 unit. The Ness is mica poor, except for an increase at the base, (N5 silt) and is consistent with core observations for this unit. Conversely, the Rannoch has the highest concentration of mica, again exhibiting very similar values to core XRD (and some thin section).

Model-pyrite, *siderite* and *calcite* tend to mirror the more local changes in lithology within the section. Siderite and calcite are abundant in the calcite 'dogger', together accounting for up to 50% of the sample. *Model-siderite* appears as localised 'spikes' through the Tarbert and Ness. These represent localised siderite cements, a feature consistent with core observations. The 15 cm interval of 'siderite-siltstone' at the base of the Tarbert (Sections 6.3 & 6.5) is not, however, identified by the modelling. Siderite increases in the Rannoch (up to 15%) with a downward increasing trend that mirrors the fining of the R3 to R4 units at the base. The Broom and Dunlin Group both have concentrations locally up to 20%. *Model-pyrite* has a *background* presence through the section of 1-2%, notably increasing at the calcite 'dogger' (up to 12%) and in the Ness shale-siltstone lithologies (5%) as well as the Dunlin shale (5%). *Model-calcite* has a similar *background* presence (3-6%) which appears inconsistent with core, which indicates little through the section except over the 'dogger'. This may reflect the inability of the petrographic techniques to determine calcite at such detection levels, or may still be an artefact of GLT processing.

Table 6.4 Mean formation values for each mineral, derived from two Euclidian models. Pass 1 has a clay phase of just kaolinite; Pass 2 has a clay phase composed of a mixture of kaolinite, illite, mixed layer illite/smectite and chlorite denoted 'a50 clay'. The main differences are in estimates of clay and mica. * greatest deviation in estimates between passes.

	quartz	'feldspar'	clay	'mica'	pyrite	siderite	calcite
Tarbert							
Pass 1 ('kaolinite')	41.2	30.62*	11.32*	7.47	1.27	2.08	5.63
Pass 2 ('a50 clay)	40.73	28.87*	15.17*	6.39	1.67	1.22	5.51
Ness							
Pass 1	60.05	16.83	6.98*	6.47	2.84	1.67	4.39
Pass 2	59.52	16.55	9.00*	5.57	2.80	1.47	4.32
Rannoch							
Pass 1	39.54	19.31*	15.48*	15.09	1.53	5.3	3.29
Pass 2	39.23	15.84*	20.46*	14.95	1.52	4.42	3.24

6.7.1.3 Alternative "a50 Clay" Model

Only slightly different modal estimates are obtained when the kaolinite clay is exchanged for a clay mineral mixture ('a50 clay', Section 6.6.3). The main differences are a lower *feldspar*

estimate and an increased *'clay'* estimate. Comparison of formation averaged mineral estimates from each model, see Table 6.4 and Figure 6.10, illustrate this. In general, the greater the kaolinite originally predicted, the greater the increase seen in the prediction of clay in second model.

6.7.2 Comparison of transform models

6.7.2.1 Least Squares & Euclidian Distance models

Throughout the entire section these two models behave in an almost identical fashion. Table 6.5 summaries the correlation coefficients between minerals derived from both models; effectively illustrating their closeness in solution. For all except 10 of the 350 sample intervals both models predict the same assemblage of minerals and mineral estimates. With the ten samples that do differ, the difference is only negligible; for example, for interval 9244'(log depth) the difference between assemblages is in the additional selection of pyrite by the Least Squares model (lowering the standard error by 0.0077!). The amount of pyrite calculated is negligible (0.03 wt%), as is the difference between mineral estimates of all other phases. The identical behaviour of these models was also observed in previous modelling exercises (Chapters 3, 4, 5). The results from Euclidian Distance model in the remainder of this chapter are also applicable to Least Squares, Error Minimisation models.

Table 6.5 Correlation coefficients between mineral phases predicted by Euclidian Distance model and Least Squares (first row) and Linear Programming (second row).

	quartz	'feldspar'	clay	'mica'	pyrite	siderite	calcite	rutile
Least Squares	0.999	0.982	1.0	0.979	0.994	0.996	0.999	0.984
Linear prog'ng	0.506	0.316	0.824	0.375	0.609	0.773	0.992	-

6.7.2.2 Euclidian Distance and Linear Programming models

Correlation coefficients in Table 6.5 suggest that there is a marked difference between Linear Programming and the Euclidian/Least Squares models. A number of solutions from the Linear Programming model appear to have a very low amount of chemistry accounted for in their solutions (P%acc of between 22% - 96%). The consequence of such a poor fit are erroneous estimates of mineralogy, including negative mineral proportions (*by definition, an impossibility with Linear Programming*).

For the remainder of the evaluation, samples with low "fits" have been removed to enable a comparison of the models to be completed. The remainder of the samples are compared to the Euclidian model in Figure 6.11 and cross-plots are shown Figure 6.12. It is apparent that estimates of quartz, kaolinite, & calcite appear very similar for both models. Discrepancies are indicated in Figure 6.11. Mica and feldspar have a number of samples that trace a 1:1 correlation, but also have a number of samples that are scattered, see Figure 6.12. A large number of samples lie on the X-axis for both minerals (the same is for the Y-axis but not so severe). This indicates the Linear Programming model has chosen an assemblage without these

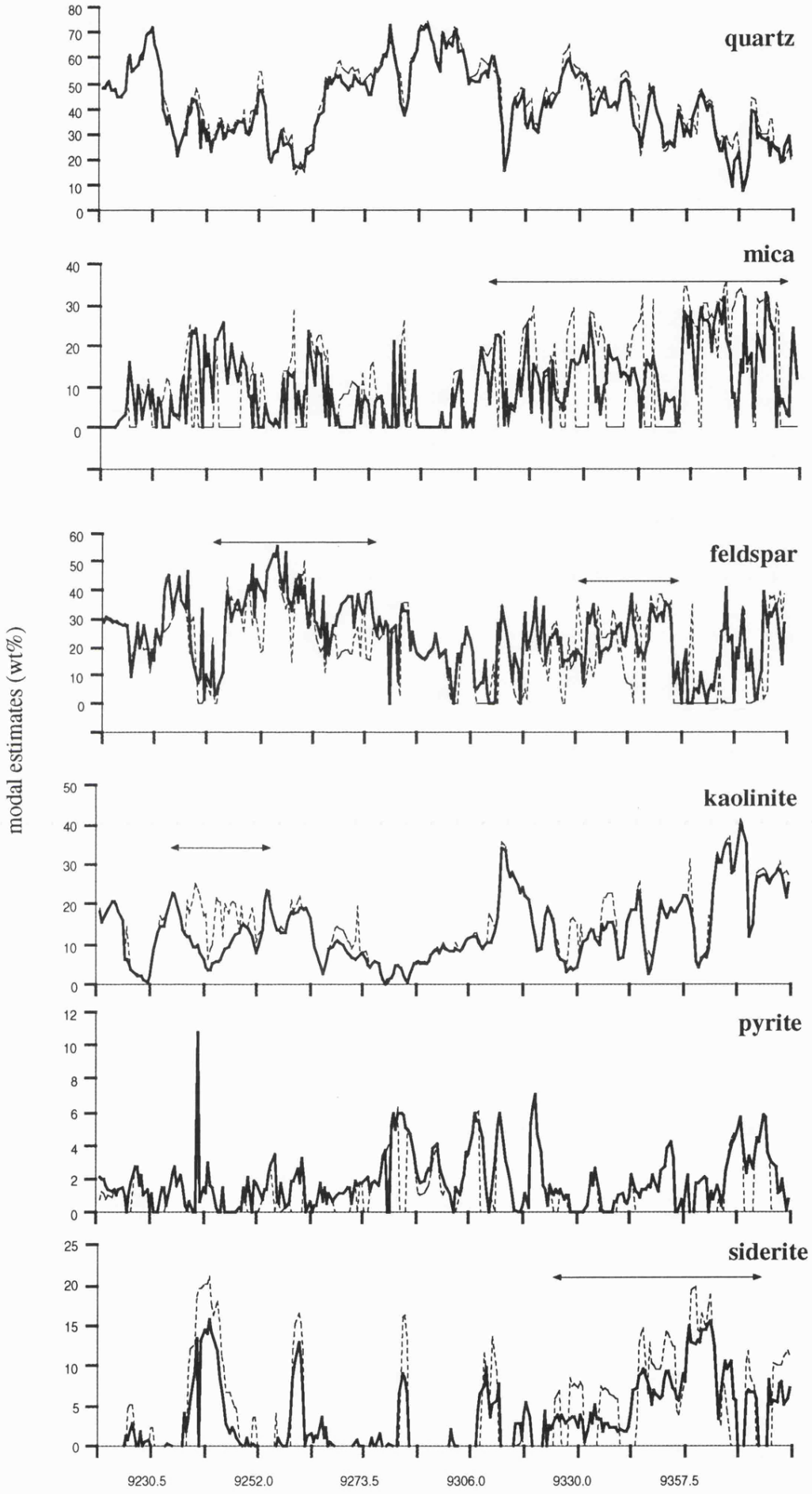

Figure 6.11 Comparison of mineral estimates (wt%) from different mineral transform models over the Thistle 211/18-a50 section. Arrowed lines refer to the main intervals where Linear Programming estimates differ from other models. Depth in feet. Dotted line - Linear Programming model. Solid line - Euclidian Distance model (& Least Squares model)

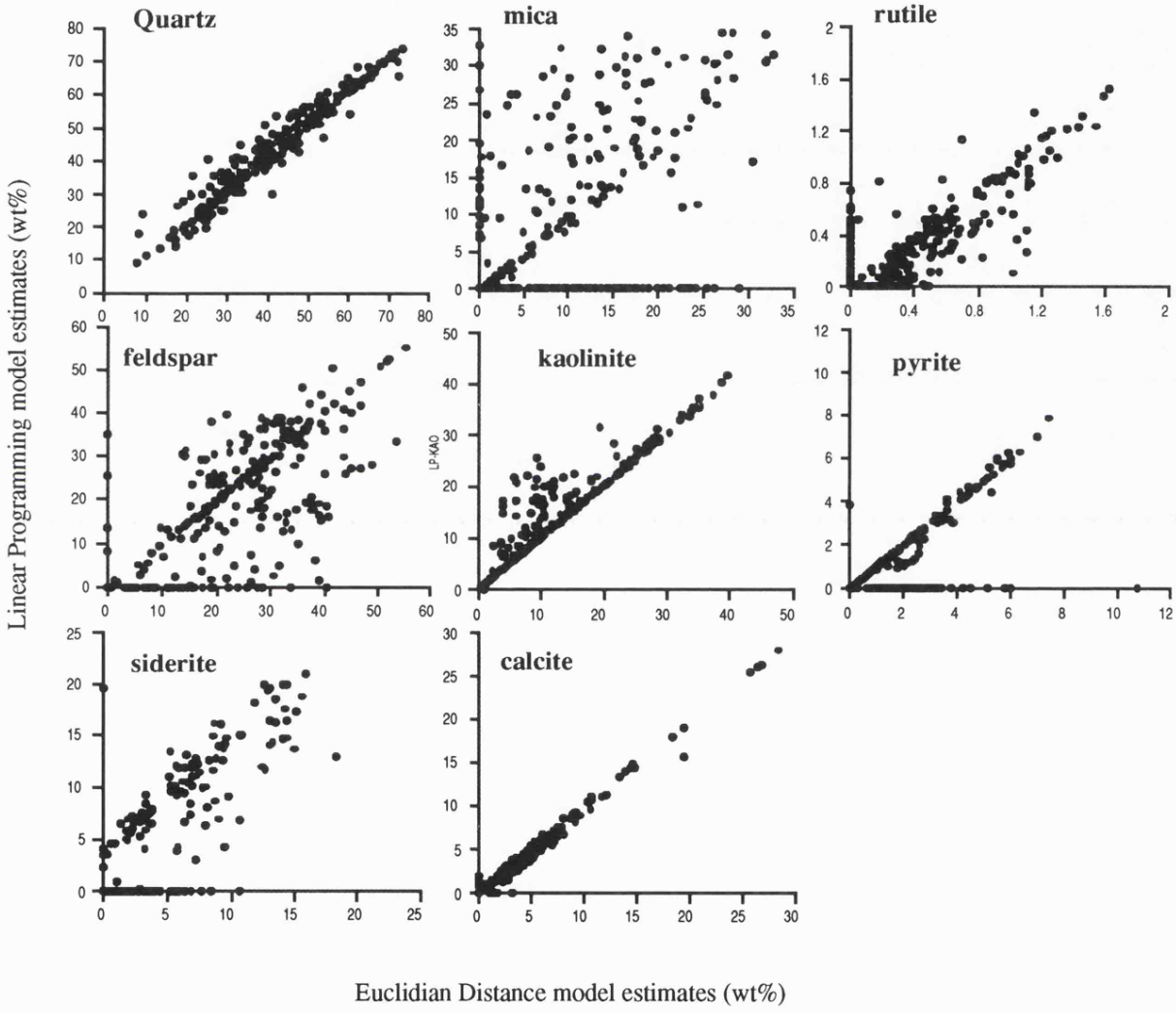

Figure 6.12 Cross-plots comparing mineralogy derived from the Euclidian and Linear Programming models (wt%). Feldspar and mica show the greatest variation between models, see text. Linear Programming model Y - axis, Euclidian Distance model - X axis.

minerals (although chosen by the Euclidian/Least Squares models). A sub-set of samples appears to over-estimate mica and under-estimate feldspar in the Linear Programming model, relative to Euclidian estimates. These two phases are *colinear* and the observations here reflect the way in which each model handles this colinearity.

This can be more easily observed in the cross-plot of feldspar and mica by the Linear Programming model, Figure 6.13 (A). It is apparent that there is a strong negative correlation between these two phases (r= -0.6) and that in a great number of cases, points lie on the X or Y axis (Figure 6.13 plot A), suggesting that where feldspar is chosen by the model, mica is not and vice-versa. This is not so evident in the Euclidian model, except a few (probably real cases) see plot D. It is apparent that a similar negative correlation exists between siderite and mica, and siderite - pyrite (plots B & C). Again this is not so evident for the Euclidian model (plots E & F). The conclusion is that Linear Programming has difficulty allowing certain phases to be modelled together at certain horizons, namely, feldspar with mica, siderite with mica and siderite with pyrite. This, in effect, is a problem of handling compositional colinearity by the Linear Programming model.

This is verified by earlier cross-plots of core and model mineralogy (see Figure 6.9 plots E-H). A large number of points lie on the Y-axis for both mica and feldspar (plots F & G), indicating that the model has not predicted these phases. As a result, mica and feldspar have a much more patchy distribution on the log-plot in Figure 6.11 (a result of the strong negative correlations), especially in the bottom half of the section. On this plot siderite is therefore present when pyrite is not. In general, Linear Programming (although having similar estimates of few phases), shows a less superior solution than that of the Least Squares and Euclidian models.

6.7.3 Results of modelling with bound water ($H2O^+$)

Figure 6.14 shows the *pass* that was modelled with the inclusion of an estimate of the 'bound water' ($H2O^+$) as an additional *input* parameter ('wet' model). Plot A shows the relationship of the bound water (Wmin) estimate (derived from logging tool epithermal porosity and density porosities), to the estimate of kaolinite from the 'wet' model. A significant correlation is seen between the two curves, as may be expected, because kaolinite is the dominant *hydrous* phase. Plot B, however, shows curves of the amount of Wmin used in the 'wet' model solution, and the amount of *actual* Wmin available. It is clear from this plot that not all of the available $H2O^+$ (Wmin) is used in the solution of mineralogy. This results in high Standard Error values for samples especially in the kaolinite rich silty-shaly mineralogies (Standard Error is also included in plot B). Plots C to F demonstrate how the addition of Wmin to the model alters the estimation of K-feldspar, kaolinite and mica considerably. Quartz remains reasonably consistent in both models (plot C) .

The effect of the Wmin parameter is demonstrated by a sample from the Ness mudstone/shale interval (core depths *viz.* 9271.5' - 9276'). This sample consists of a mudstone

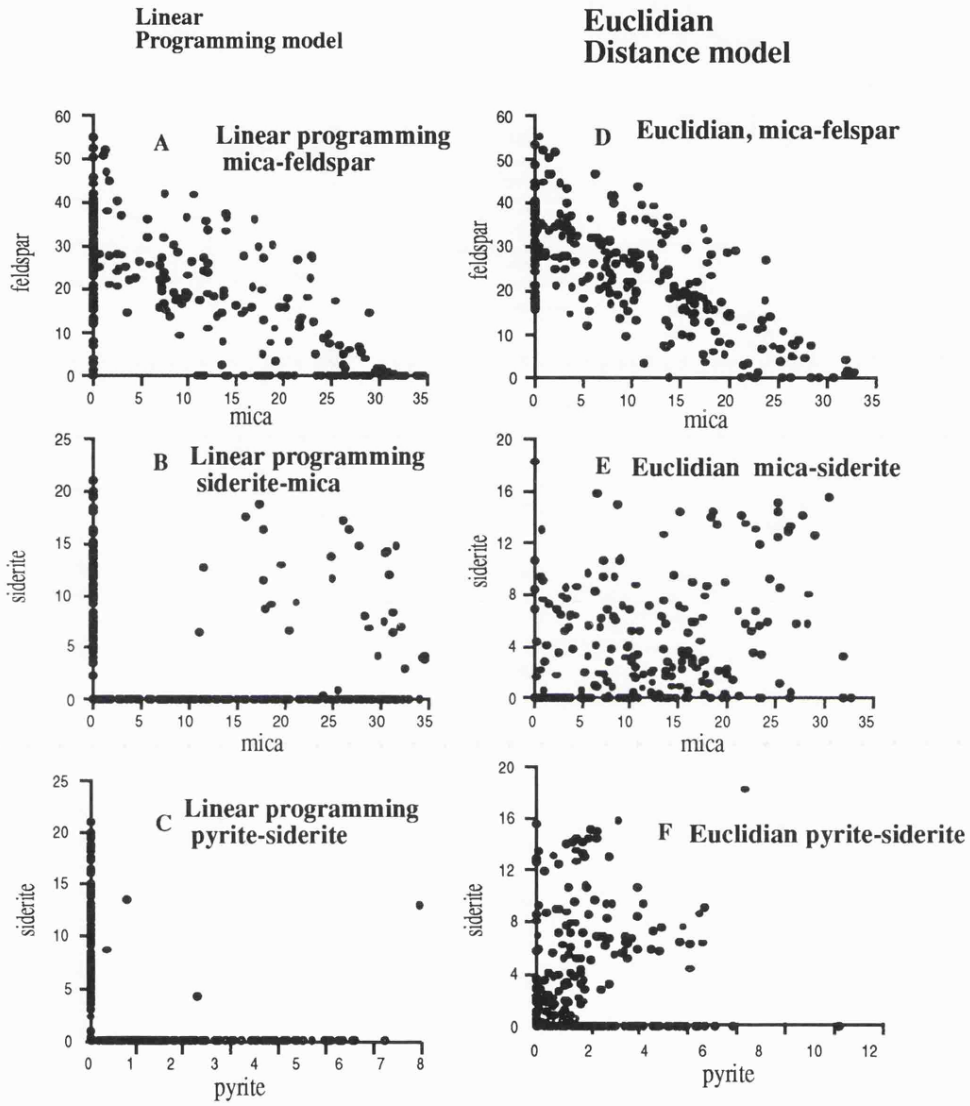

Figure 6.13. Cross-plots of mica and K-feldspar, siderite and mica, siderite and pyrite illustrating the strong negative correlation that exists between these minerals for the Linear Programming (plots A - C) and less strongly in the Euclidian model (plots D - F). See text. estimates in wt%.

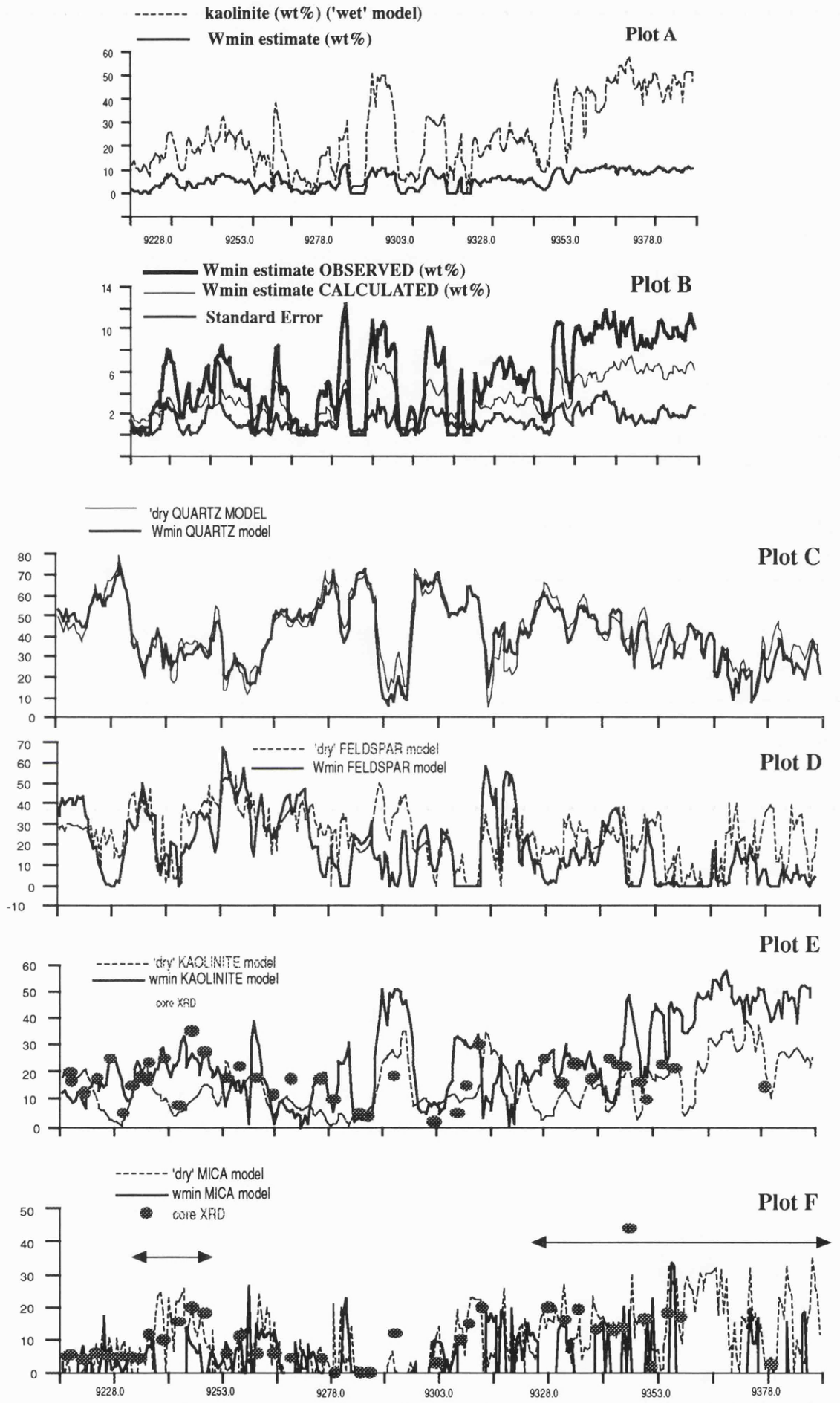

Figure 6.14 **Plot A** - log plot showing the correlation of the log derived estimate of Wmin and the model estimated kaolinte, (wt%). **Plot B** - the observed Wmin estimate compared to the proportion of Wmin used in the model. Clearly, not all the available Wmin is used in the model. **Plots C - F** show the estimated mineralogy from the 'wet' model (where Wmin is included in modelling) and the 'dry' model. In general the 'wet' model under-estimates, or fails to estimate mica and over-estimates kaolinite. Depth in feet. Arrows in plot F indicate areas of poor correlation between data sets.

lithology dominated by kaolinite and mica, both minerals that contain 'bound water'. Table 6.6 illustrates four solutions for sample interval 9277'. Estimates of core mineralogy are strictly qualitative as no successful calibration of phases (for XRD quantification) was reported possible in the mudstones.

From Table 6.6 it can be seen that the closest estimate to the shale lithology is achieved by the solution modelled *without* Wmin (column 2). The solution modelled with the Wmin estimate (column 3) clearly shows an over-estimation of clay and under-estimation of mica. A noticeable discrepancy between the calculated $H2O^+$ and observed $H2O^+$ (Wmin), and similarly for K2O, suggest the model is behaving as a response to the $H2O^+$ variable introduced. An excess of $H2O^+$ makes the model predict more of the *clay* phases, and less of the *mica* phase. The under-estimation of mica results in less K2O being used in the solution, resulting in the K2O discrepancy between calculated and observed estimates.

Table 6.6. Estimation of mineral proportions by a Least Squares model with and without *bound water* added (top section). Below, calculated chemistry for each solution. Thistle 21/18-a50, shale interval 9277'.

Column 1 Qualitative best estimate of shale whole rock composition, based on bulk and oriented XRD
Column 2 Solution with no water (Wmin) included in solution
Column 3 Solution with Wmin estimate included (9.4% $H2O^+$)
Column 4 Solution with half Wmin estimate (4% $H2O^+$)
Column 5 Chemistry calculated from core estimates of mineralogy (back-calculation)
Column 6 Weighted model, $H2O^+$ weighted 10:1 against oxides.

SE -standard error of the chemical fit, **Mad** -mean (absolute) difference of the residuals. 7 oxides used : SiO2, TiO2, Al2O3, Fe2O3, CaO, K2O, S and $H2O^+$, where stated. 'A50 clay' comprises 60% kaolinite, 30% low illite/smectite, 6% Fe-chlorite, 4% illite. n/a - not applicable

Sample 9277'

	1 (XRD)	2	3	4	5	6
total clays	45	38.16	53.75	32.36	n/a	78.28
mica	15	21.52	4.28	27.18	n/a	-24.16
siderite	5-10	10.63	13.59	8.60	n/a	18.20
Quartz	15	15.50	15.05	15.52	n/a	14.75
calcite	5	5.60	4.83	5.84	n/a	3.27
pyrite	5	8.10	8.15	8.09	n/a	8.27
SE		1.076	1.974	0.986	n/a	3.516
Mad		0.507	0.965	0.459	n/a	1.020
SiO2	41.90	42.39	42.27	41.96	42.47	41.97
TiO2	0.92	0.54	0.21	0.64	0.41	0.99
Al2O3	16.12	16.82	17.73	16.31	17.14	18.86
Fe2O3	14.63	15.44	15.24	14.91	15.70	14.75
CaO	3.03	3.90	3.68	3.90	3.55	3.16
K2O	2.48	2.69	1.27	3.14	2.17	-1.10
S	4.48	4.29	4.32	4.29	5.30	4.38
H_2O^+(Wmin)	**9.44**	-	**6.95**	**5.23**	**6.31**	**8.84**

This is verified in column 4, which shows the solution if half of the log derived Wmin $H2O^+$ were present in the sample. Here the mica estimate is increased at the expense of the clay. All other phases remain constant in each solution except siderite (and mica), which varies as a direct result of changes in Fe (due to mica estimates). Further validation that the Wmin estimate for the sample interval is too large, comes from the back-calculation of an estimate of mineral composition derived from core mineralogy estimates (column 5).

Column 5 suggests that around 6.3 $H2O^+$ would be produced from such a mineralogy, while column 6 demonstrates the result if the $H2O^+$ estimate is *weighted* heavier in solution

(10:1) with all other variables. In this process of *forcing* a solution, so that all the Wmin estimate is used, the model is thrown in to error, infact causing negatives for mica (resulting in a deficit of K2O in column 6).

These results suggest that the values of Wmin for this sample interval, as for the majority of the section, are over-estimated. This manifests throughout the reservoir section, especially in the Rannoch, Broom and Dunlin lithologies (9353'-9390') as an over-estimation of kaolinite (plot E, Figure 6.14, and an under-estimation of mica and k-feldspar (Plots D and F).

6.8 Synopsis and discussion

Having discussed the potential acquisition and processing problems that might account for the discrepant data from first pass processing of the GLT data, the second pass processing illustrates the staggering difference in the quality of data that can be acquired through careful processing. A check on elemental log quality must, therefore, always be made prior to any subsequent application of such data.

It is encouraging that almost all of the GLT derived elemental trends observed through this reservoir section, both within and between formations, can be explained by the variations in mineralogy - lithology, often just by one mineral species. This suggests (in the absence of core elemental data with which to compare results), the GLT data from this hole, in a relative sense at least, is reasonably accurate and informative. This is encouraging for the application of GLT derived elemental data in mineral modelling. The rhetoric presented in Chapter 1 that log derived *elemental responses* are much more sensitive to subtle changes in matrix lithology than conventional nuclear tool logs originally used to discriminate lithology (bulk density and neutron porosity), is further substantiated through this careful study.

The ability of the Euclidian Distance and Least Squares (Error-Minimisation) models to predict the mineralogical features and trends throughout the 211/18-a50 interval is again encouraging. This is especially so in view of the fact that two oxides, (MgO and Na2O) were unavailable. The *strategies* adopted allow all the major mineral phases to be predicted, and alleviate the majority of the effects of colinearity, previously found when modelling the Rannoch Formation. The micas (biotite and muscovite) and the feldspars (K-feldspar and albite), however, cannot be interpreted separately without Na2O and MgO.

Sample size differences (mainly its effect on heterogeneity) between core and log data, as well as *sample bias* remain the two largest problems in the validation of the accuracy of log derived mineralogy. Discrepancies between the two sets of core data (Figure 6.2) were also identified. In consideration of these problems, correlation between core and model estimates of the *dominant* minerals is fair (except quartz which is significant) and at least point to where a model is, relatively, in error. Mica *trends* are well predicted throughout the section as are the quartz rich, slightly coarser units of the Tarbert T2 and Ness formation. The calcite 'dogger' is very well characterised by the models, as are the fining-up sequences which manifest as decreases in quartz/feldspar and increases in kaolinite/mica/siderite. There is a slight problem,

however, with the over-estimation of feldspar in the lower Tarbert. This may be due to the *fixed* binary composition of feldspar, (50% k-feldspar & 50% albite). One feldspar may in fact dominate over part of the section, which would put the fixed binary composition at error. It may therefore be a better strategy to allow the feldspar composition to vary, at each sample, either between both end-members; or alternatively *stochastically*. A small over-estimation of *background* calcite by all models relative to core observations (*viz.* 3-4 wt%) may still be an artefact of geochemical processing but is most probably due to the finite level of detection of calcite by the core techniques.

The exchange of a kaolinite for a composition that encompasses minor clays as well as kaolinite (the 'a50 clay' model) demonstrates the effect a change in composition of one mineral phase has on the estimation of modal mineralogy. In this model a slight improvement in feldspar and kaolinite clay estimates increases their overall correlation with core estimates. Both passes are illustrated in a final plot that combines all modelled mineral phases, in Figure 6.15. A sedimentological/lithological log is included for comparison with core sedimentology.

The addition of extra physical parameters to the components matrix, while allowing a model to be more fully-determined, can seriously effect the *modal mineralogy* if inaccurate. The addition of a log derived estimate of Wmin fails to enhance the solution through the reservoir section. This reiterates that caution must be taken, especially with logging tool estimates, if additional parameters such as *bound water*, are included in a transform model. The inaccuracy of the *Wmin* estimate (although a separate problem), is most probably due to the implicit assumption in its calculation, that the matrix density, used in the density porosity calculation, is 2.65 g/cm^2. With a considerable siderite and mica presence through this interval, with core matrix densities up to 2.71 g/cm^2 not uncommon, this would be clearly in error. This assumption may well affect the calculation of Wmin parameter especially in shales and siderite rich silts where Wmin is highest.

While Euclidian and Least Squares models behave identically, and in an acceptable fashion, Linear Programming shows inconsistancies in its ability to accurately estimate modal mineralogy. This ranges from determining a correct solution, similar to the other models, (such as in the lower Tarbert and Ness intervals), to failure to solve for a sample (samples with a low percentage fit, P%acc). A common problem is its mis-identification of a phase, such as mica, resulting in an erroneous prediction of mineralogy (which can go unnoticed). This observation was also made in Chapter 5. Computational differences with Linear Programming lie in the way the model partitions oxides between phases that are partly or fully colinear. In the worst case, Linear Programming fails to partition an oxide between two or three phases if colinearity is severe. Instead, all (or most) of the oxide is assigned to one phase. This results in the mis-identification of a mineral phase, over-estimation of another phase and the negative correlations seen in the processing of this hole.

The problem which caused the low estimates of accounted chemistry (P%acc) and negative mineral estimates in the Linear Programming model (Section 6.7.2.2) was later found to be a fault with the program , which was affected by very small oxide values, such as S and

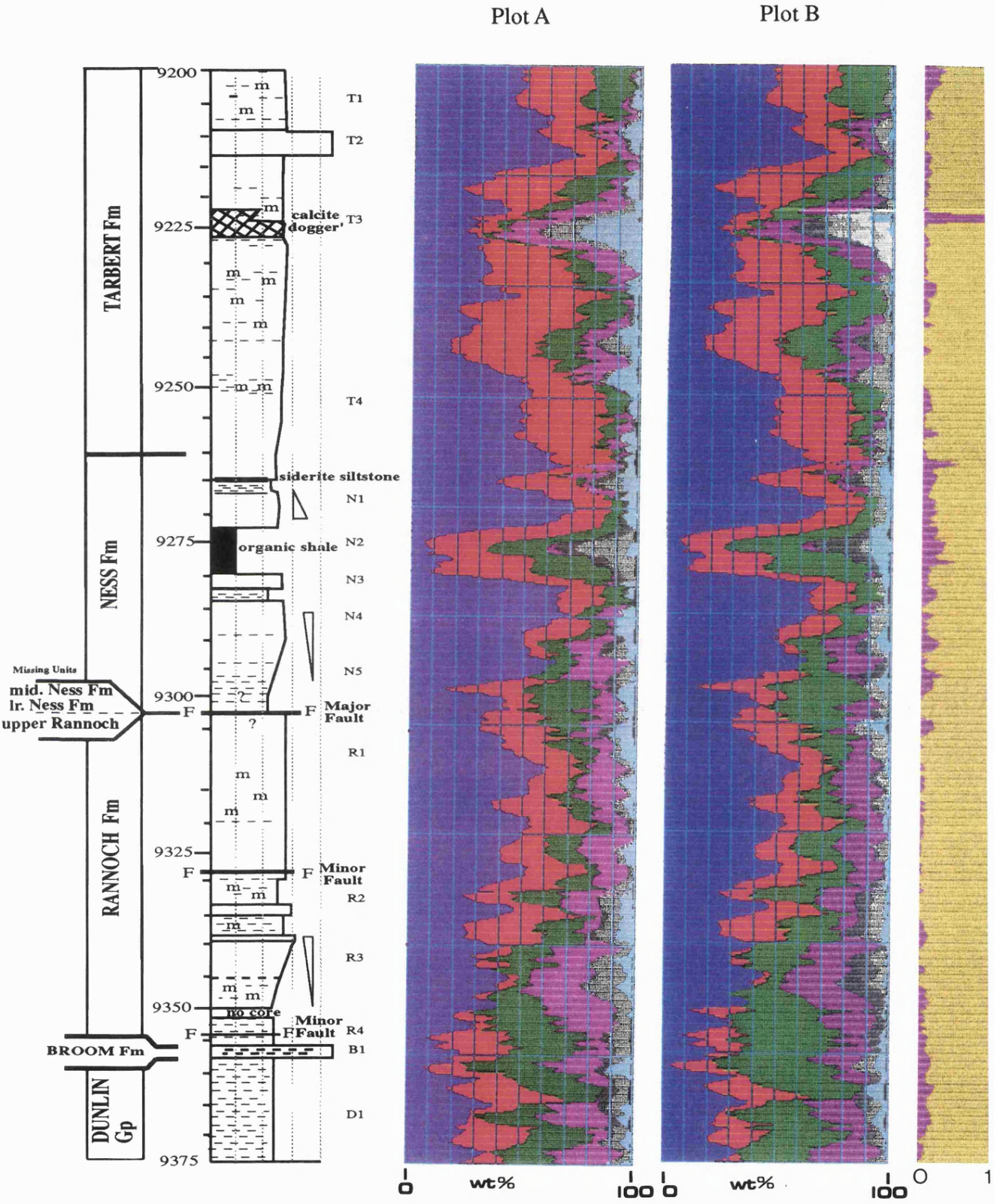

Figure 6.15 Lithological log of the A50 section studied, with predicted mineralogy estimated from the Euclidian Distance model. Plot A clay phase modelled with a 'kaolinite' composition. Plot B the clay phase modelled with the "a50 clay composition, see text. Error log is the Standard Error.
Key: Dark blue- Quartz, red- feldspar, green- kaolinite, purple - mica, dark grey- pyrite, light grey- siderite, light blue- calcite, black- rutile

TiO2, in the input composition matrix. This makes no effect to the conclusions above as these samples were not used in the evaluation.

Throughout this exercise it has become apparent that two factors may compromise estimates of mineralogy that are derived from log data.

The first is a problem that inhibits the quantitative estimation of small, localised, changes in mineralogy from logs - namely, the resolving power and averaging effects of GLT log measurements. Local changes in minerals, such as siderite cement, pyrite and calcite are *indicated* on elemental logs. Due, however, to the *vertical resolution* (0.5-1m), the *volume of investigation* of the GLT tool of $1m^3$, and the *seven point averaging* applied to data in processing (see Section 2.3.5), the elemental response of a thin horizon will be averaged over 6 sample intervals that lie directly above and below the sample. The result is a '*smearing* 'of the elemental data over those sample intervals. An example is seen at the base of the Tarbert over a 15cm siderite *rich* silt horizon (*viz.* 9260' core depth, see Figure 6.7(b)). The Fe2O3 curve predominantly from siderite is averaged over 1m. This is also most notable at the boundaries of the 'calcite dogger' and over the Ness shale/mudstone interval.

The fact that a point sample (from the point the sample was taken) is not analysed is a considerable problem for mineral inversion. In effect, it will *dilute* the actual response of two contrasting lithologies if a boundary is present (*bed boundary effect*), or if a small localised interval is present. In contrast, in a homogeneous medium, such averaging may well provide a more representative estimate of composition than the traditional, small, core plug sample. This will bear great consequences on the applicability of mineral data in the estimation of accurate, representative, petrophysical parameters.

The second factor is the magnitude of the effect that *relative errors* (precision), in GLT tool estimates, will have on mineral modelling. This can be demonstrated by a simple simulation using the *synthetic rock mixtures* introduced in Chapter 3. Implementing the estimates of tool measurement uncertainties (precision) from Grau *et al.* (1989) (see Chapter Two, Section 2.5.1) the effect of relative error on the modelled mineral estimates for four of the synthetic rocks introduced in Chapter 3, has been be calculated. These are tabulated in Table 6.7. Estimated modes and compositions used in calculations, are quoted in Appendix 6.3. In these simulations the composition of the *input* synthetic rock composition was firstly increased, then decreased by the quoted values of precision for each element. In this sense they represent a worst-case scenario. Mineral models were then performed on these data.

For these four rocks (chosen because their compositions span the range of most clastic sediments), the variation in the prediction of most minerals due just to relative error can be as much as 12 wt %. Precision can therefore be a major source of error in mineral modelling.

Table 6.7. The amount of variation possible in mineral estimates as a result of extremes in quoted relative error (precision) of GLT measurements (wt %).Four synthetic rocks

	quartz	kaolinite	K-feldspar	muscovite	dolomite	albite
Mix 1	12%	4%	6%	-	-	4%
Mix 2	0.2%	11%	-	10%	-	-
Arenite	5%	3%	11%	8%	6%	-
Pelite	7%	6%	13%	8%	4%	_
Range	0 - 12 w%	3 - 11 t%	6 - 11%	8 - 10%	4 - 6%	4%

In holes of reasonable quality, where good data acquisition is possible and lithological units are greater than the intrinsic resolution of the GLT tool (*viz.* 1m), *quantitative* mineral estimates can be expected, provided a correct model and strategy is employed. These mineral estimates may then be used to accurately predict additional petrophysical parameters such as grain density, CEC or enhanced estimates of porosity. Although mineralogical features and trends are well characterised it is doubtful, however, that the data from areas near bed boundaries (at least 1m) of the 211/18-a50 reservoir section are of sufficient resolution and therefore quality to allow an accurate estimation of such mineral data.

Chapter 7
The application of GLT derived mineralogical data

7.1 Introduction

It was stated in Chapter One that there are numerous potential applications for information gained from *geochemical* logging tools. Herron (1987) categorised these into *direct, indirect* and *inferred* applications. *Direct applications* make use of the raw elemental data acquired from the GLT, and include such applications as lithological classification, hydrocarbon detection and mineral estimation. *Indirect applications* use the latter (mineralogical data), produced by mineral transform models, to estimate certain parameters that relate more to mineralogy than element chemistry; examples are grain density, porosity, cation exchange capacity (CEC), and thermal conductivity. *Inferred applications*, on the other hand, integrate mineralogical data (from the GLT) with existing geological knowledge to infer geological processes and conditions. They include, for example, the estimation of depositional environment, grain size analysis and hydrocarbon viscosity. A summary of these different applications is presented in Table 7.1. At present there is very little *direct* work documented on this subject and plenty of scope for future workers.

This chapter focuses, as an example, on investigating two different types of *indirect* application. Both are relevant to sedimentary reservoir characterisation and are pertinent to this study. *Indirect applications* form an important category in reservoir characterisation because of the direct relationship between mineralogy and *petrophysical* or *sedimentological* parameters.

The first aim of the chapter is to ascertain if modelled mineralogy can be used as a correlative tool for identifying and mapping *sand units* horizontally between exploration holes in the same reservoir/field. In contrast, the second aim is to assess if mineralogy (modelled from the GLT derived elemental chemistry) can be successfully used to calculate the petrophysical parameters matrix (grain) density and porosity.

7.2 Cross-hole correlation of mineralogical data.

7.2.1 Introduction

Mineralogy can, theoretically, provide an enhanced 'tool' for the correlation of lithological units between exploration holes, especially when compared to *conventional* correlation tools such as gamma-ray and neutron-density logs. The task sometimes becomes difficult with conventional techniques when a formation undergoes spatial sedimentological variations that can effect porosity, fluid content and composition, all of which can obscure correlation. Minerals are the fundamental 'building blocks' which affect the textural and geochemical features recorded. As mineralogy responds primarily to these *compositional* changes and not to *fluid* changes (like the neutron and density logs), it is less affected by fluid-porosity variations. Greater confidence in correlation should result from using mineralogy, since it is more geologically *meaningful* and subjective. For example, conventional gamma-ray curves, often

Category	Application	Derivation	Knowing:	Comments/uses
Direct	Geochemial analysis by grouping elemental trends: a)Mudrock facies analysis. b) sand-shale litho-classification.	Statistical analysis and cross plots	GLT derived concs of: Fe, S, U. GLT derived Si, Ca, Al, Fe.	Prior knowledge by Calibration with core is required.
	Inter-well correlation	simultaneously cross correlating well chemistry	GLT derived mineral or element oxide abundances.	
	Hydrocarbon detection	Inelastic detection of C and O spectra	measure ratio of C/O	Independent of salinity
	Determination of formation mineralogy	Mineral transform calculations		See this study.
Indirect	Source rock evaluation	Subtracting inorganic C, (GLT derived $Caco_3$) from organic C	Formation O_2, C bearing elements in formation	
	Clay volume determination V_{cl}	Sum of all GLT derived clay mineral species	Clay mineralogy from GLT.	Potentially more accurate than GR and SP tools
	CEC estimation	Differentiating clay mineral species	Clay mineral species Theoretical CEC of each species.	Helps correct resistivity readings.
	Formation grain density determination	Difference between bulk and grain density	Fluid, bulk density and miner-alogy. Mineral densities	Relies on fixed (averaged) mineral densities
	Porosity determination	Subtraction of grain density from bulk density	GLT derived grain density. Bulk density from density tool	
	Determination of formation neutron capture cross section (Σ)	mineral Σ & mineral concentration	GLT derived mineral modes & typical mineral Σ	Useful for inferred applications
	Inter-well correlation	cross correlation of mineralogy	Formation mineralogy or geochemistry	Useful in basin analysis & pet-roleum exploration
	Formation thermal conductivity	Mineral volume & thermal conductivity values	GLT derived mineral estimates. Typical thermal conductivities of mineral species.	Allows a continuous measure of a form-ations heat cond-uctance.
Inferred applications	Depositional environment (marine / freshwater)	Elemental oxide and mineral abundances	Clay mineral comp-osition(illite-marine and kaolinite- F/W)	
	Diagenesis	Mineral compostion variations & trends	Mineralogy	Important to know for estimation of permeability
	Intrinsic permeability	Substitution of min-eral parameters into the Kozeny-Carman, porosity dependent relationship	'Enhanced' porosity, mineralogy and grain density from the GLT.	VERY TENTATIVE!! restricted to homo-geneous lithologies
Enhance-ment of other logs	Enhanced estimate of Archies of 'n' exponent (resistivity S_W determination	Improved estimate of invasion resitivities (Roxo & Sxo)	Σ Formation CEC & grain density fro m the GLT	Allows a real, not empirically derived, 'n' to be calculated
Enhance-ment of other logs	Enhanced estimate of Q_V for formation resistivity - R_O determination	Estimation of Qv from CEC, matrix density and porosity	Formation CEC, matrix density and porosity	
	Formation heat flow estimation	Thermal conductivity x temp. gradient	GLT derived formation conductivity. Log meas-ured thermal gradient.	Allows continuous heat flow to be calculated.

Table 7.1 Summary of the different 'literature quoted' applications for elemental data derived from the geochemical logging tool.

used for inter-well correlation, have been known in the Brent Group of Rannoch and Tarbert formations to be indistinguishable between sands and mudstones because of the high potassium content in the sandstones (due to feldspar & mica). This is so that inter-well correlation is often impossible (Sau and Spurlin, 1982). A mineralogy log, on the other hand, would distinguish lithologies immediately, allowing a confident correlation.

This study makes use of core data from two holes, 33/12-**b26** and 33/12-**b41**, from the Norwegian Statfjord Field. This lies approximately 25 km South-East of the previously studied Thistle Field, North Sea (see Figure 7.1). Two 30m reservoir sections from these holes have been selected in this study. These have been confidently correlated previously by lithologic/wireline log data and by core elemental data across the 3 km separating the holes (Stow and Jackson, 1986 *unpublished*). Mineralogy is modelled here using elemental estimates from core and after validation with core data, the success of the cross-hole correlation is investigated.

7.2.2 Previous correlation of sections by lithology and elemental geochemistry

Both reservoir sections lie directly above the mid-Brent Shale in the lower part of the Ness Formation. Each section consists of four vertically stacked *subarkosic* sandstone packets (3 of a *meso-scale*; Stow and Jackson, 1986), separated by organic rich mudstones, thin coals and rootletted siltstones. These are all interpreted as deposits of a *cyclic* delta environment. Section **b26** consists essentially of three well defined and continuous, sandstone packets (units 1, 3, 4) and one slightly less continuous, heterogeneous, silt/sand packet (unit 2). In Section **b41** this unit is more continuous and better defined. On the basis of lithology and sedimentology, each individual sand-packet and intervening mud/coal - silt horizon can be correlated between sections. The textural similarities, as well as the trends in major element geochemistry, form the basis of the correlation between sections. These are summarised in Figure 7.2.

Natural gamma-ray/density/neutron wireline logs have also correlated these units. The sandstone units show a density/neutron negative separation and low GR response, characteristic of clean sandstones. The coaliferous mudstones show a high gamma-ray response (from organic mudstones), a low density (due to coals), and high neutron porosity log (due to combined shale and coal).

7.2.3 Data acquisition

The Statfjord Field consists of the same lithological formations and sediment petrography, as the Thistle Field. A summary of the mineral species from both sections is shown in Table 7.2.

XRF data from core-plugs, taken at 30 cm intervals throughout the four sandstone packets from both intervals, are used as the input elemental data. Core mineralogy was measured by whole-rock XRD for the purpose of validating the modelling results. Samples include 13 core trim samples from the b26 section and 15 from of the b41 section. These were regarded as

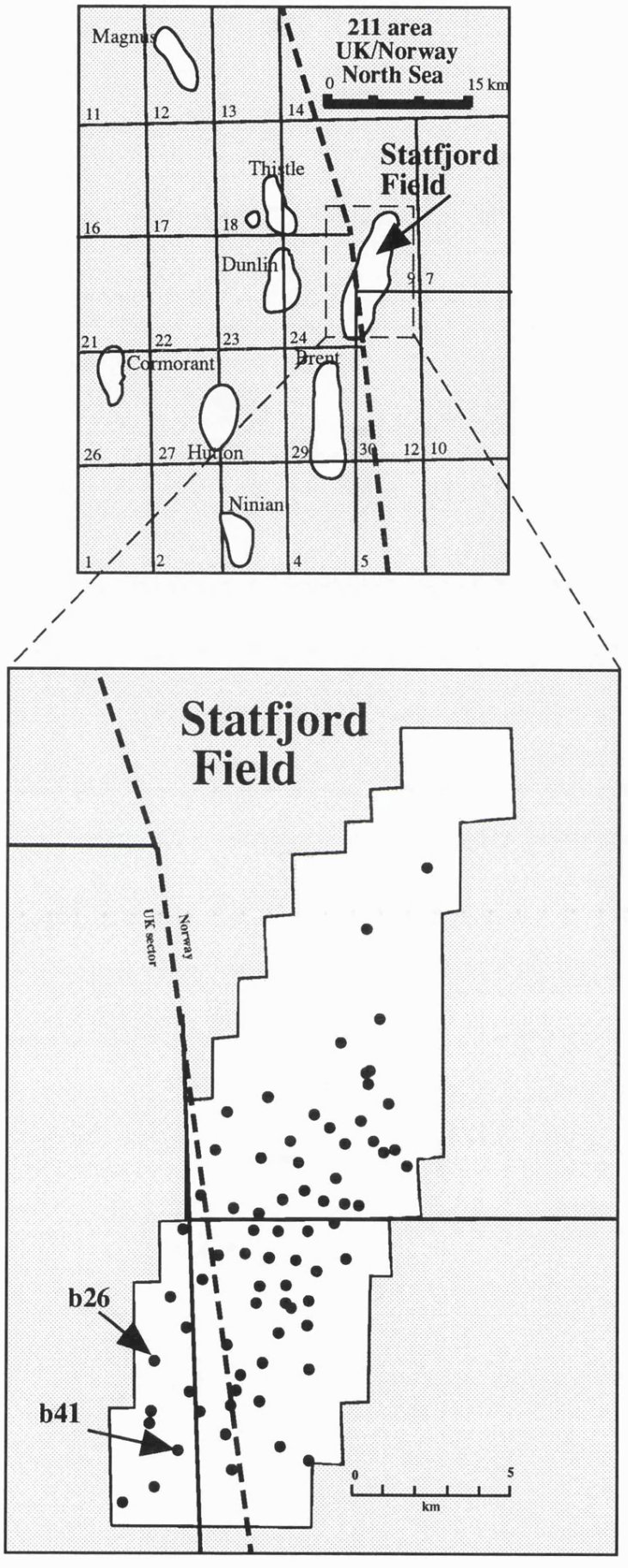

Figure 7.1 Location of the Statfjord Field in the northern North Sea, Brent Province and the location of holes - 33/12-b26 and 41

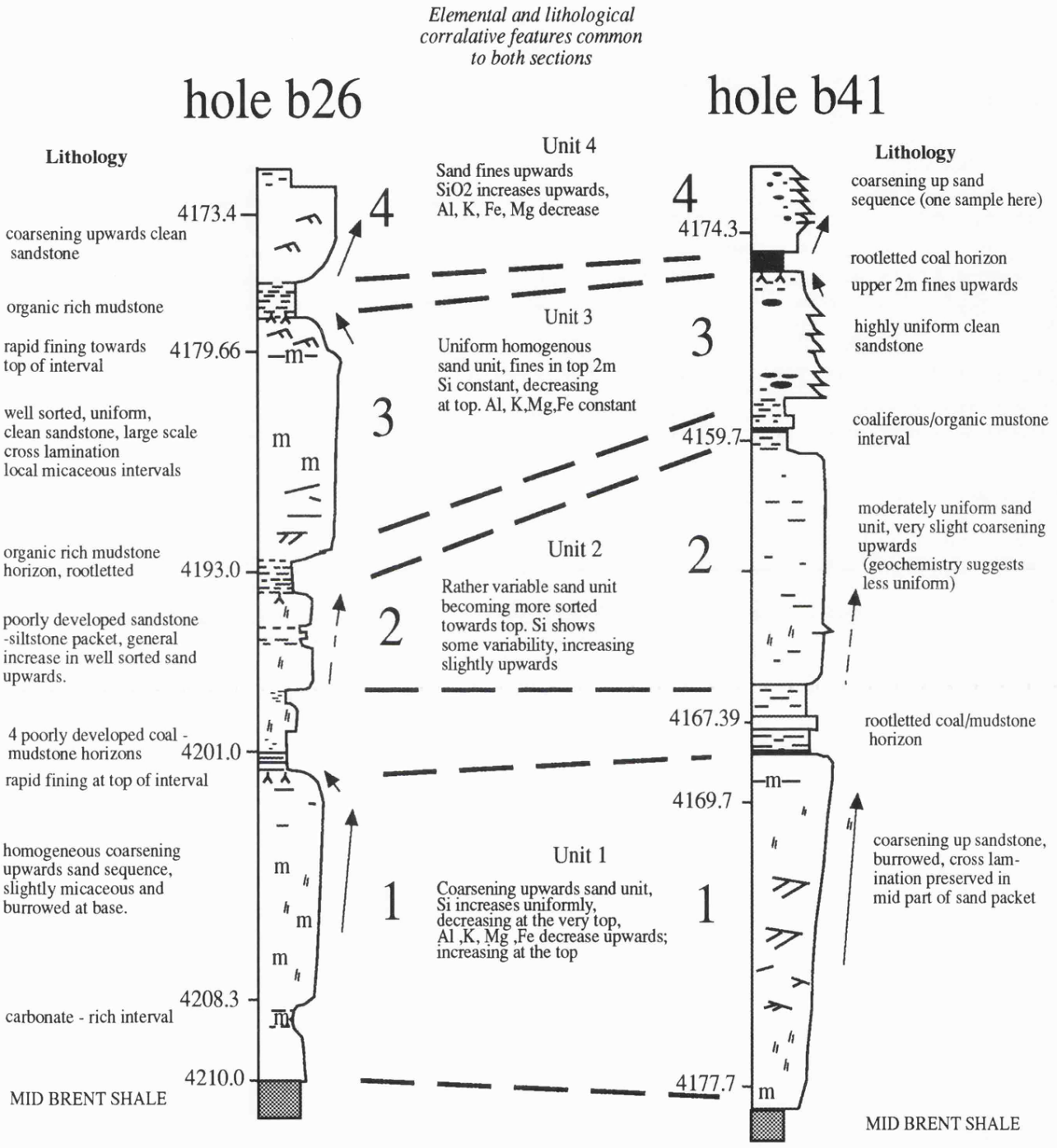

Figure 7.2 Summary of lithological and geochemical features that can be correlated between holes 33/12 -b26 and b41, lower Ness Formation, Brent Group, Statfjord Field. Depth in feet.

representative of each of the 4 sand units and intervening siltstone horizons. XRD sample preparation, operating conditions and interpretation methods are equivalent to those employed for the Thistle section (Chapter 4, Appendix 2.0) . XRD analyses are listed in Appendix 7.1,. XRF data is proprietary.

Table 7.2 Summary of minerals observed in sandstones of the Statfjord b26 and b41 sections by XRD (wt %). Number of samples = 39

	Mean	std	min	max
quartz	65.18	18.48	21.91	87.81
kaolinite	12.76	11.03	2.37	42.83
K-feldspar	11.58	3.39	6.34	17.50
albite	6.19	2.36	2.40	12.01
mica	3.09	4.48	0	22.00
siderite	2.05	4.24	0	22.18

Minor mineral phases (<2 wt %) (absolute estimates are speculative)

pyrite	calcite
rutile	dolomite

7.2.4 Mineral transformation - model parameterisation and strategy

The Euclidian Distance model was used for this exercise. Laboratory determined *elemental input data* were modelled with seven oxides (replicating the elements available from the GLT tool). *Input compositions* consist of average values of microprobe-analyses derived from both the Thistle and Statfjord fields. 'Mica' was modelled as a *binary* composition of 50 wt% muscovite and 50 wt% biotite, consistent with thin section estimates. This was chosen primarily both to reduce the compositional colinearity (See Section 5.4) and the number of phases to model. A '*selected assemblage*' strategy (Section 5.2.1) was implemented to allow mineral assemblages to vary with depth. Minerals identified by XRD (and verified by thin section) make up the selection of minerals available in the model. Rutile and siderite are, however, kept in all assemblages as 'mops' for Fe and Ti respectively.

7.2.5 Verification of modelled mineralogy

Cross-plots in Figure 7.3 compare the mineral proportions estimated by the model and XRD whole-rock estimates for both sections. Model estimates of the four major mineral phases quartz, K-feldspar, albite and kaolinite have a significant correlation with XRD estimates for both sections (Figure 7.3). An excellent correlation is seen for quartz (correlation coefficients of r=0.91, 0.97 for b26 and b41 intervals respectively) and for kaolinite in both sections (r=0.91, 0.97). A slightly less significant correlation is seen for the K-feldspar (r= 0.64, 0.88) and albite plagioclase (r= 0.57, 0.88). *Model* albite is slightly over-estimated (up to 3%) relative to XRD estimate, as is kaolinite in just the b26 section (up to 5%). *Model* K-feldspar is, in contrast, over-estimated (up to 4%). Bearing in mind that XRD estimated concentrations generally have an absolute accuracy of within 5 wt%, the comparisons for these mineral phases are surprisingly good. Minor discrepancies occur mainly in the interval between sand units (ie, low quartz intervals)

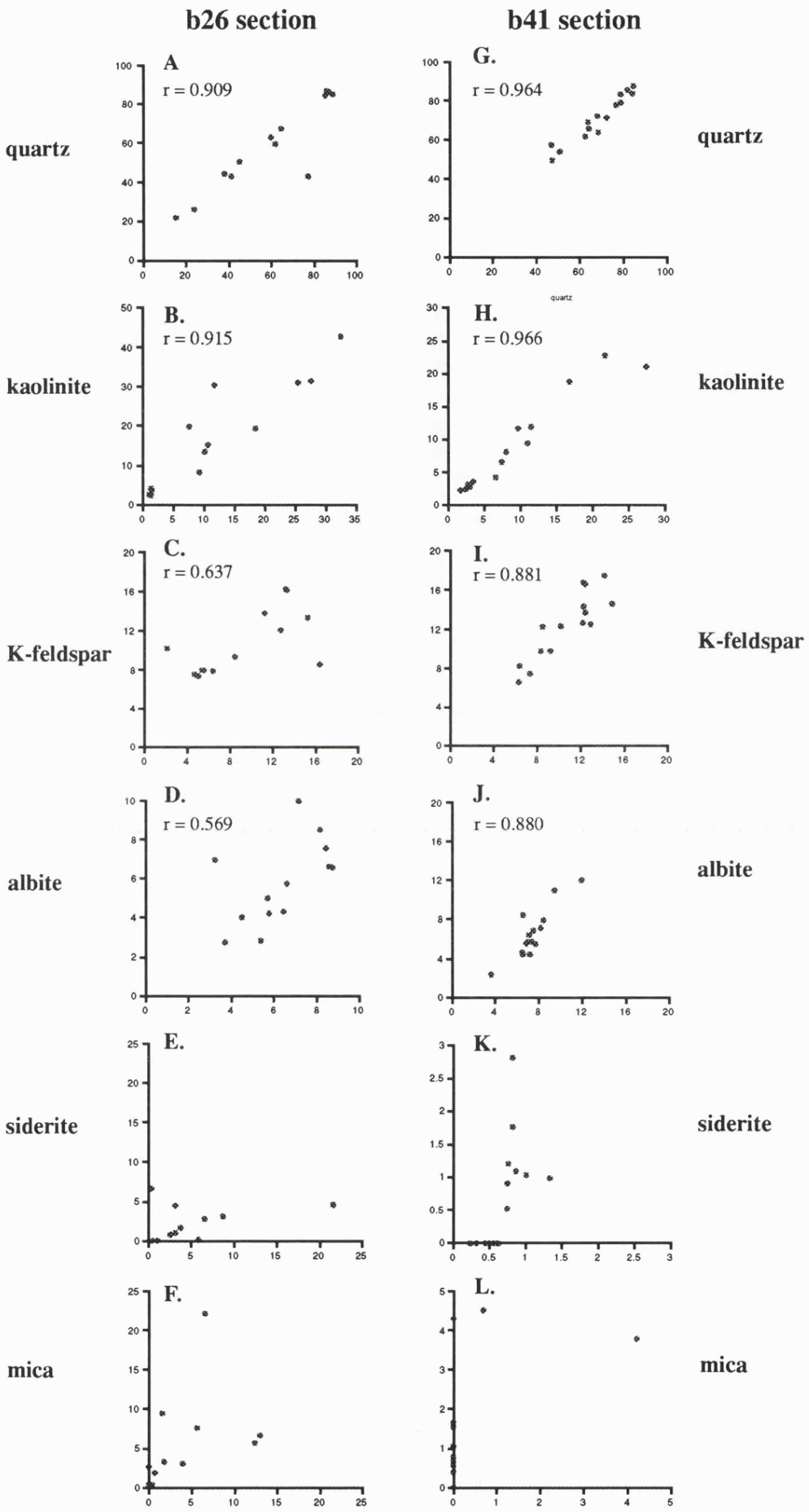

Figure 7.3 Cross-plots of model derived (wt%) mineral estimates (X axis) and core XRD estimates (Y axis); Statfjord holes 33/12-b26 and b41. r - denotes correlation coefficent.

Siderite is defined by two poorly defined clusters of points in Figure 7.3 (plots E & K). The first cluster lies around the 1:1 line and represents reasonable correlation between *modelled* and core estimates (most notable in b41). The second cluster lies on the X axis around 0.5% and relates to where siderite has been included in the solution to 'mop' up excess Fe2O3 and is not observed by core estimates. This low level (*viz.* 0.5 wt%) is below any sensible detection limit for XRD and may well be real. Two discrepancies in Section b26, occur at 4201.0' and 4208.3' where siderite is over-estimated by 15-16% It is possible that XRD is in error here but more probable that the model is in error due to there being an excess of Fe2O3 at this horizon. An excess of Fe may be due to another mineral phase not identified and therefore not included in the model.

Mica shows a scattered distribution in Figure 7.3 with some model estimates over-estimated (up to 8%) or under-estimated (by up to 10%). Low levels of mica through the section, under-estimated values of mica by the XRD technique (refer to Chapter 4 & 6) and possible compositional colinearity all contribute to this discrepancy in estimates. However, it only affects a few samples and as negative solutions are not present and as it does not adversely affect the estimation of other mineral phases it is not considered a serious problem in the overall solution.

In general, these results suggest strongly that the model is predicting the correct mineral proportions for the *major* mineral phases (an excellent overall Standard Error estimate for the model of < 0.170). Due to the low concentration levels of the minor minerals, validation of these phases is difficult.

7.2.6 Comparison of modelled mineralogy with lithological and elemental data

A composite summary relating core lithology, elemental trends and model derived mineralogy is presented for each section in Figures 7.4 and 7.5. These demonstrate that the model derived mineralogy relates very closely to textural and lithological observations, as well as spatial trends in elemental chemistry. Trends such as an increase in Si and a *mirrored* decrease of Al, K, Mg, Fe and Na content, are representative of an increase in quartz and a decrease in kaolinite, feldspar and/or mica minerals. This, in turn, manifests *texturally* as an increase in grain size. The rapid fining in grain size, for example, at the top of both units 1 and 3, in both sections, corresponds to a decrease of Si and increase an increase in Al, K, Mg, Fe and Na. This is in response to an increase in clay (kaolinite) and feldspar concentration. In general, a very good comparison of model mineralogy with existing observations is seen through both sections.

7.2.7 Cross-hole correlation of derived mineralogy

Figure 7.6 summarises the correlation in derived mineralogy cross-hole. Subtle changes, in mineralogy can be correlated between sections. Correlative observations for each unit can be summarised as follows:

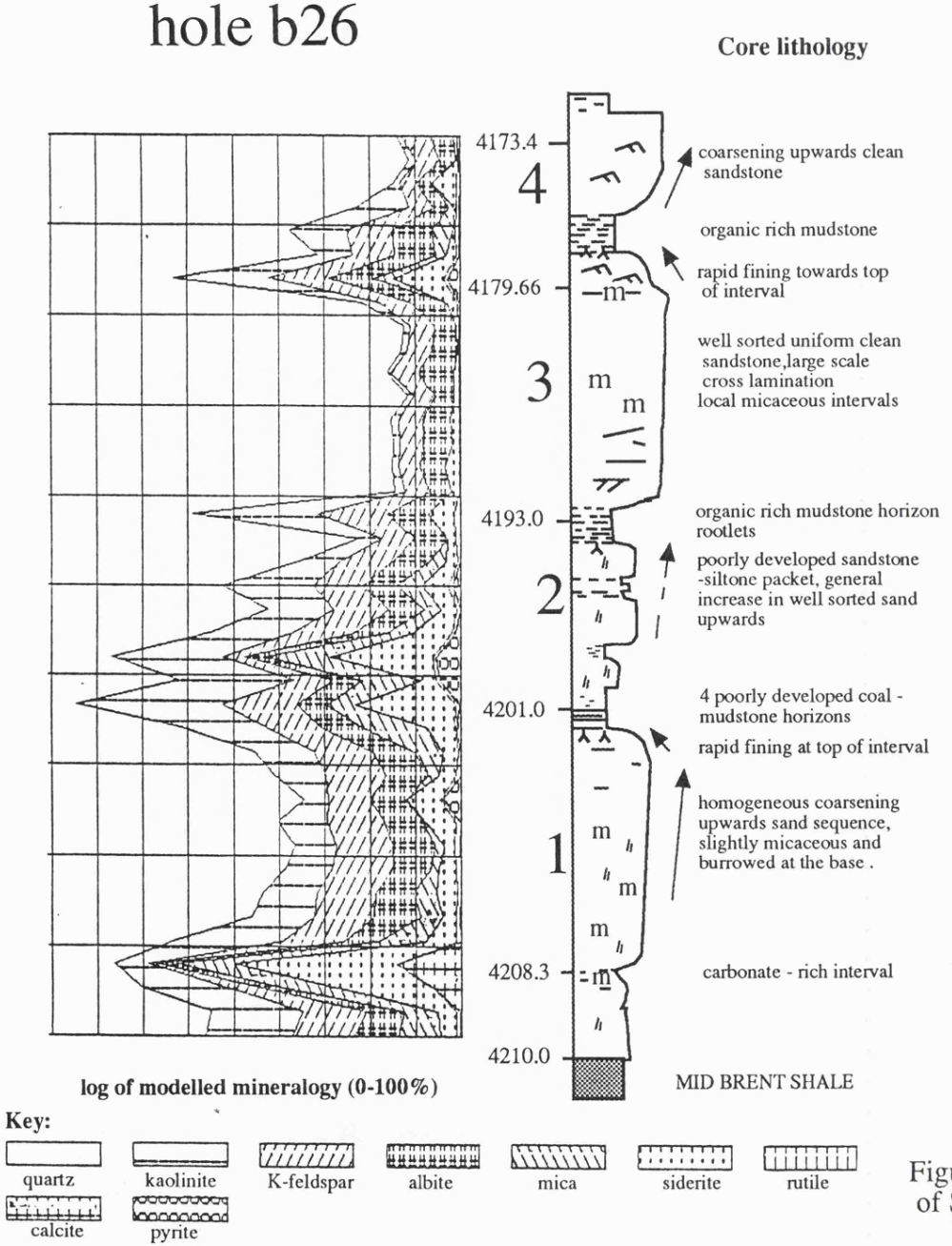

Lithology-elemental trends	Mineralogy trends estimated from mineral inversion model (verified by XRD)
Unit 4	
Sand fines upwards Si increases upwards, Al,K,Fe,Mg decrease	Subarkose, quartz increases upwards (77 > 88%), kaolinite decreases (11 > 2%), constant K-feldspar (5-6%) and albite (3-5%), variable siderite (0-5%)
Unit 3	
Uniform homogenous sand unit, fines in top 2m Si constant, decreasing at top. Al, K,Mg,Fe constant	Subarkose, very uniform clean mineralogy except upper 2m, quartz (85%), kaolinite (1-2%), k-feldspar (5%), albite (6%) siderite (1.5%)
Unit 2	
Rather variable sand unit becoming better sorted towards top. Si shows some variability, increasing erratically upwards with a decrease in Al,Fe,K and Mg	Subarkose; quartz increases erratically upwards (45% > 77%), kaolinite decreases (18 >5%) as does K-feldspar (13 >7%), albite remains constant (7%) as does mica (3-5%), decreasing at very top.
Unit 1	
Coarsening upwards sand unit, Si increases uniformly, decreasing at the very top, Al,K,Mg,Fe decrease upwards increasing at the top	Subarkose-arkose, quartz increases upwards (43- 64%), decreasing at very top; kaolinite decreases upwards (20% > 5%), with mica (10% > 0%). Both increase again at very top mirroring the decrease in quartz. Albite and k-feldspar remain constant. Muddy carbonate interval at 4208.3 - calcite 9%, siderite 35%, mica 12%

Figure 7.4 Summary of the lithological, elemental and mineralogical trends of Statfjord b26 section. Depth in feet, minerals in wt%.

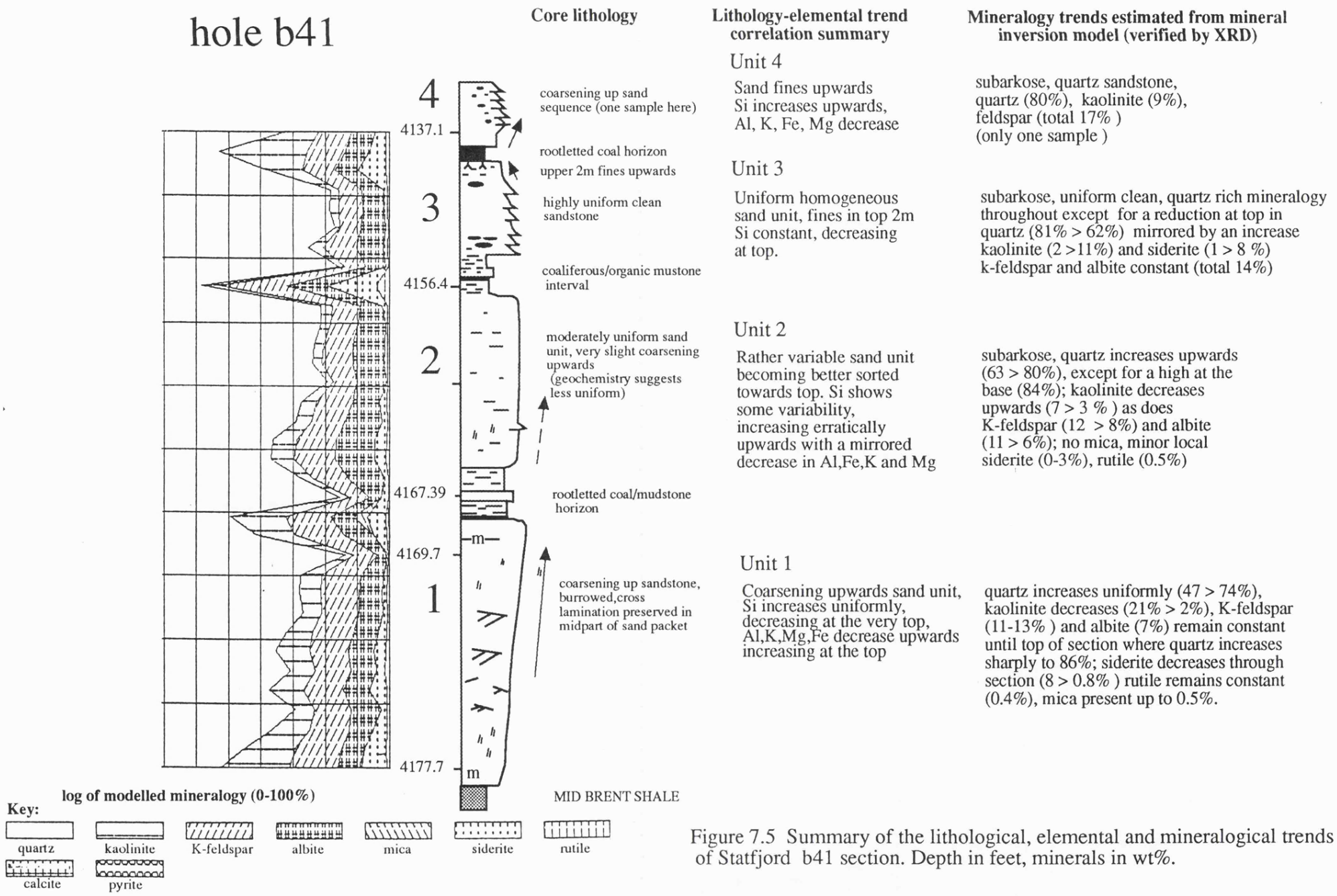

Figure 7.5 Summary of the lithological, elemental and mineralogical trends of Statfjord b41 section. Depth in feet, minerals in wt%.

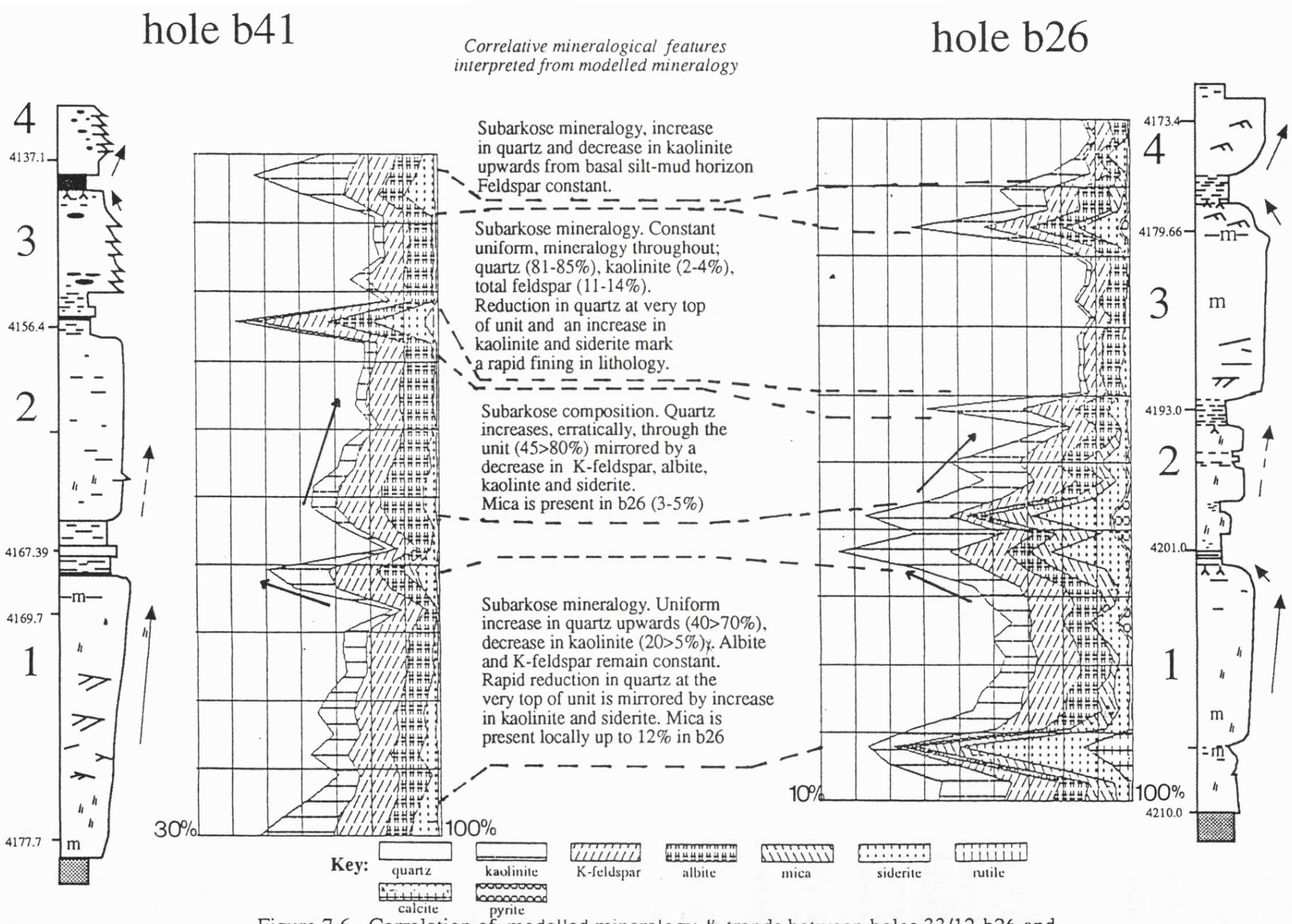

Figure 7.6 Correlation of modelled mineralogy & trends between holes 33/12-b26 and b41, Statfjord Field. Depth in Feet, minerals in wt%.

For **unit one** an increase in quartz from 45% to 70% is mirrored by a decrease in kaolinite in both sections; feldspar in both remains constant. At the top of both units quartz drops quickly and kaolinite increases. Mica is present in both sections although more prolific in b26, up to 10% (possibly mirroring a slight sediment source supply change across the 3 km distance between wells, or a change in hydraulic conditions).

The **second unit** shares a slightly heterogeneous mineralogy, b41 appearing more sandy. This is probably the least well correlated unit in the section. This could be due to a sub-facies change between wells explaining a slight change in sand-silt ratios. A general trend of increasing quartz, and decreasing kaolinite is, however, observed upwards. Section b26 has a minor amount of mica (3%), b41 has none. A slightly higher value of kaolinite in section b26 may be an artefact of the presence of mica in the section and its subsequent degradation to kaolinite; this was observed in the Rannoch Formation of the Thistle Field (Section 4.2).

Unit three shows a very homogeneous mineralogy of 81-85 wt% quartz, 2-4% kaolinite, 11-14% feldspar in both sections and the correlation is perhaps best of all units. A rapid fining and reduction in quartz is observed at the very top of the unit in both sections.

Unit four can only be tentatively correlated for trends because only one sample is present for the b41 section; however, the mineralogy of the sample from b41 is in good agreement with b26.

In general, the prediction of mineralogy is excellent throughout both sections, although the minor mineral phases prove slightly harder to validate due to the detection limits of the XRD technique. It is apparent that this *modelled mineralogy* (although not implementing GLT derived elemental data) can be well correlated between sections, and that this correlation does correctly follow the previous correlative trends. It may therefore be an important tool for correlation in the future.

7.3 Estimation of petrophysical parameters

One of the essential parameters required in petrophysical formation evaluation is the *porosity*, or the 'fraction of the total volume of a sample that is occupied by pore spaces'. It is most often acquired from either neutron, resitivity or density log measurements.

The density tool measures the *bulk density* of a formation. This is a combination of the density of both the mineral and fluid fractions of the rock and is directly related to the porosity if the average *matrix density* (grain density) and fluid density are known, such that:

$$\rho_b = \phi.\rho_{fl} + (1-\phi).\rho_{ma} \qquad (..1)$$

Where ρ_b is the bulk density, ρ_{ma} is the matrix density and ρ_{fl} the fluid density (usually set at $1.1 g/cm^3$, although changed depending salinity) and ϕ is porosity. In practice, the average matrix density is rarely known and so is set to a constant value, typically a value of $2.65 g/cm^3$ for sandstone and $2.7 g/cm^3$ for limestone. Alternatively it may be estimated from a combination of PEF and ρ_b (Schlumberger, 1989).

Log derived estimates of porosity (ϕ) from the bulk density tool can then be calculated using a relationship derived from Eqn. 1 such that:

$$\phi = \frac{\rho_{ma} - \rho_b}{\rho_{ma} - \rho_{fl}} \qquad (..2)$$

7.3.1 Matrix density

In conventional log analysis without the facility of expensive core calibrations or customised interpretation models, a constant matrix density value is often used in the calculation of porosity (using Eqn. 2). Considering that the density of a sandstone matrix will vary with mineralogy, improved estimates of porosity may be acquired if a more exact matrix density can be determined. It is theoretically possible to estimate the average *matrix density* from the mineralogical estimates derived from the GLT tool, by the simple relationship shown in Eqn. 3. This can then be used to produce an *enhanced* estimate of porosity.

$$\rho_{ma} = \frac{1}{\sum \frac{M_j}{p_j}} \qquad (..3)$$

where ρ_j is the matrix density of the mineral j and M the weight % proportion of the mineral. Standard values for grain densities are quoted in Table 5.8, Section 5.5.4.

Matrix density has been calculated, using Eqn. 3 from the mineralogical data derived from Thistle 211/18a-**a33** interval in Chapter 5, (refer to Section 5.6) These estimates are compared to *core measured* estimates of matrix density in Figure 7.7 (A & B). A good correlation is observed over the section between matrix density estimates, suggesting that a reasonably accurate matrix density can be estimated (in this example to approximately +/- 0.05 g/cm^3). The slight systematic error noticeable in plot A is due to a rounding of the core derived estimates. The largest discrepancies of 0.06 g/cm^3 occur for the most dense matrix densities. This may be due to the inherent sample size differences that may effect the heterogeneity of each sample.

It is not surprising that a reasonable correlation exists with core because laboratory elemental data was used and the subsequent mineral modelling well constrained (refer to Chapter 4). Figure 7.8 shows the matrix density estimated from *modelled mineralogy* acquired using GLT derived elemental data from hole 211/18-**a50** (data from Chapter 6). Excepting the circled area, correlation of estimates is again very good. From plot B, Figure 7.8, it is clear that the good correlation exists down to *viz.* 9340' with only small systematic discrepancies of < 0.02 g/cm^3 between *viz.* 9200' - 9340". The two larger discrepancies in calculated estimates, at 9280' and 9308', are due to localised siderite rich intervals and probably represent a sampling discrepancy. Below 9340' a larger overall discrepancy occurs in estimates, up to 0.2 g/cm^3 (circled in plot A). These coincide with the presence of silty-sands and muds at the base of the Rannoch through to the Dunlin Formation.

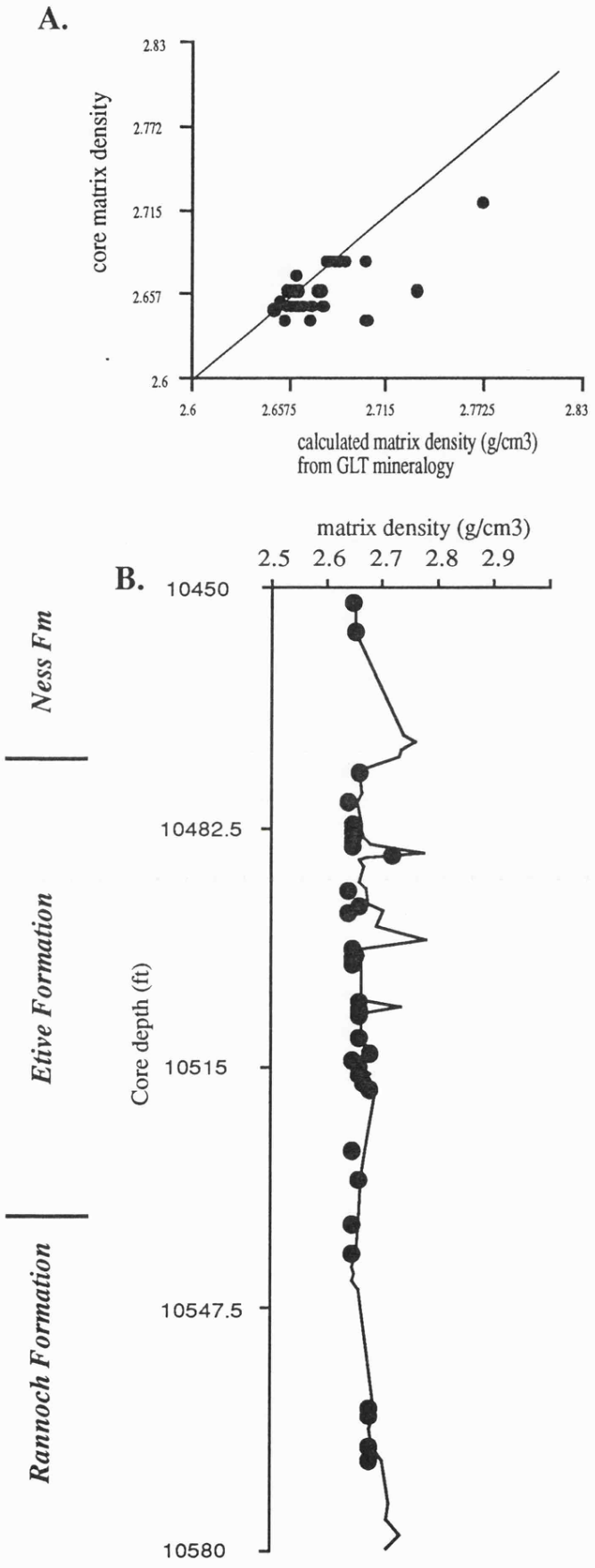

Figure 7.7 Log plot of calculated matrix density (line) and core estimated grain density (dots). Thistle 211/18a-a33 section, samples 10452 - 10580'

One interesting observation from Figure 7.8, plot A is the spread in density values (*viz.* 2.58 - 3.0 g/cm^3). Conventional estimates of porosity, calculated from one *assumed* value of matrix density (*usually* 2.65 g/cm^3) would clearly produce porosity values in error for the majority of samples in this section. This is also noted by Moss (1992).

7.3.2 Porosity

Estimates of porosity have been calculated, using Eqn. 2, for the 211/18-**a50** section. These estimates were calculated using *matrix density* derived in Section 7.3.1 from modelled mineralogy, the log derived bulk density estimate ρ_b; and the assumption of a fluid density (ρ_{fl}) of 1.1 g/cm^3. These estimates of porosity are compared in Figure 7.9 to core derived estimates of porosity (helium porosity); see plot A. In general, there is a good correlation of both porosities, although some core estimates are under-estimated (circled in plot A). These represent the calculated porosity values below depth *viz.* 9340' and are the effect of the poor matrix estimates seen in Figure 7.8.

Plot B, Figure 7.9 shows a comparison of core helium porosity with a porosity estimate derived from the density tool. The correlation with core is poor in comparison to plot A; this is emphasised in plot C. Estimates below 9340' are widely in error; and this may point to the density tool measurement being adversely affected through this interval. A corresponding increase in CSIG at this point, (refer to Section 6.5) also indicates possible environmental effects.

Independent *model derived* estimates of matrix density produce, in this example, a more accurate porosity estimate than the conventional log estimates. This is particularly encouraging as the mineralogy is derived directly from the GLT tool.

7.4 Synopsis and discussion

A continuous log of the mineralogy is potentially valuable on its own for creating a *geological model* (almost in *real-time*) in which reservoir characterisation can be based on in the absence of (or to *enhance*) core measurements. This may be a particularly valuable in formation evaluation stages for the characterisation of clay minerals.

The potential for *derived mineralogy* to be used as a correlative tool between holes is also made quite clear from Section 7.2. Inter-well correlation is made much more subjective when mineralogy is used, as all minerals responsible for producing the trends on conventional curves are fully identified. This should therefore allow greater confidence in the placement of correlative markers between wells. The power of mineralogy as a correlative tool remains to be investigated using real GLT data where the problems of tool precision and volume of investigation, mentioned in Chapter 6, (Section 6.8) may compromise the accuracy of mineral estimates and their usefulness as a correlative tool.

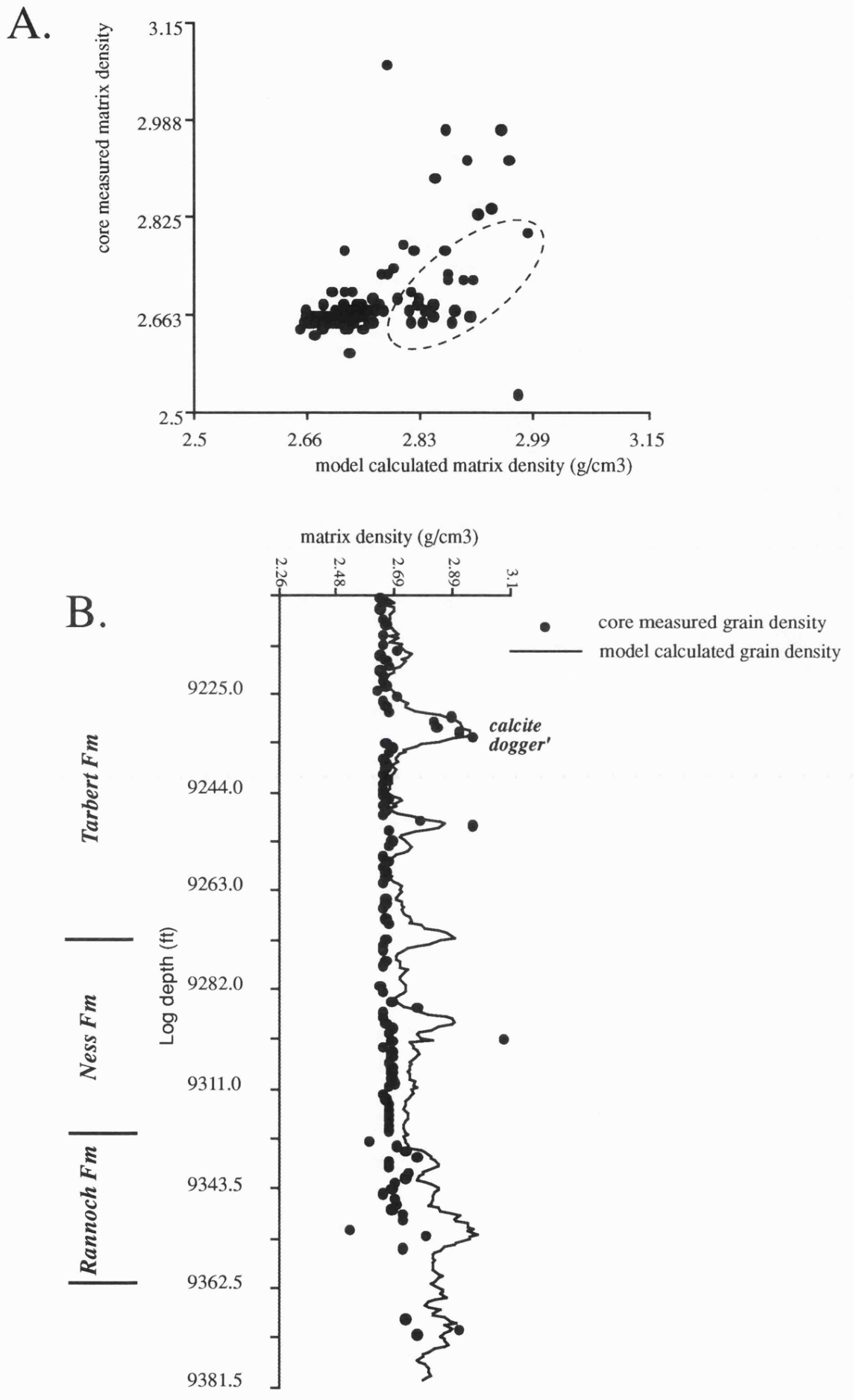

Figure 7.8 Comparison of grain density calculated from the model estimated mineralogy and core measured grain density, Thistle hole 211/18-a50. Circled area in plot A indicates the discrepant samples below depth 9340' in plot B, See Text.

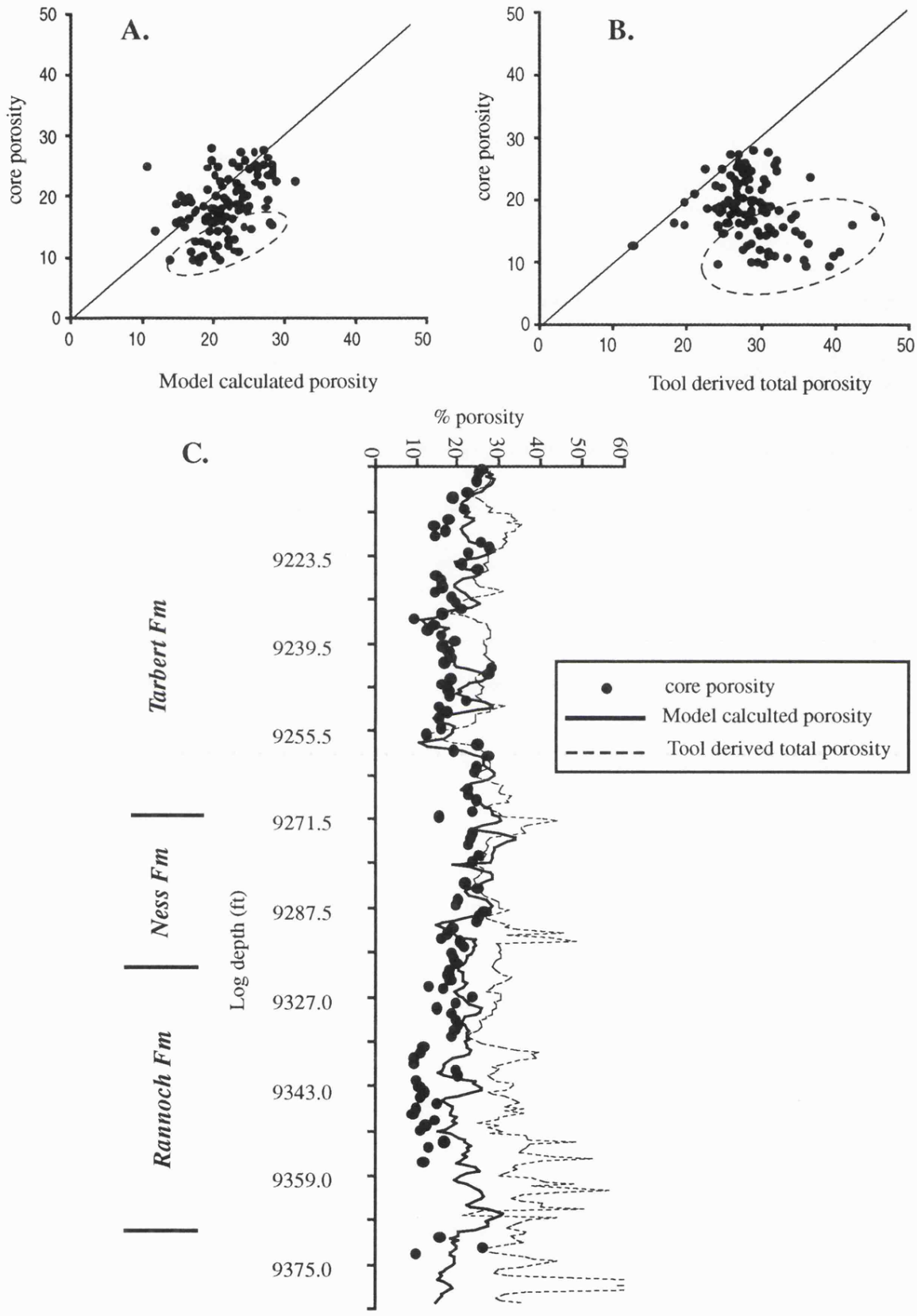

Figure 7.9 Comparison of core helium porosity with a porosity derived from *mineralogy calculated* matrix density estimates; and a porosity estimate from the density tool. A better correlation exists between the 'enhanced' estimates from mineral modelling (plot A) than with conventional logging tool derived porosity (plot B.). Plot C comparison of both estimates through the Thistle section. A good correlation with core is seen down to 9340' by the *model derived* porosity. The discrepancy that exists below 9300' is probably due to the discepancy in grain density estimates, affected by the silt-siderite lithology. These data are circled in Plots A & B. Values for mineral densities are quoted in Chapter 5.

As a second *indirect* application, the calculation of *porosity* and *matrix density* in the Thistle 211/18-a50 section appears very encouraging. This is especially so for the upper part of the studied section (*viz.* 9216' - 9340) where estimates of both *parameters* are in very good agreement with core and in the case of porosity, appear superior to those values estimated by conventional log-based petrophysical methods. The discrepancies below 9340' may be due to a) sampling problems (in measurement of helium porosity in silty sands), b) sample size differences, c) errors in the bulk density estimate at this interval, d) incorrect mineral estimates from the modelled mineralogy.

Most samples over thick and consistent lithological units (most samples above 9340') have accurate estimates of matrix density. Discrepancies occur, however, at the boundary between two contrasting lithologies. The averaging of mineral estimates (the *bed boundary effect),* as an artefact of GLT processing (refer to Section 6.8), has a clear effect on estimates of matrix density in more localised horizons through the section. For example, the increase in *calculated matrix density* up to 2.9 g/cm^3, at the 'calcite dogger', is verified by core measurements, see Figure 7.8. Core measurements on the boundary indicate a sharp drop, to more typical sandstone densities (*viz.* 2.65 g/cm^3) as illustrated in Figure 7.10. The *model calculated* matrix density values for sandstone samples surrounding the 'dogger' on the boundary, however, show a smooth drop in calculated matrix density, over 1-2m, before a more typical sandstone density is recorded. This smooth drop in density values is a good example of the *bed boundary effect* indirectly produced from GLT derived chemistry which has been passed through into the mineralogy. This, in turn, affects the calculation of matrix density and will therefore ultimately affect porosity. The effect of a 0.2 g/cm^3 error (increase) in estimation of matrix density at 9244', for example, is to double the porosity estimate.

Enhanced estimates of both grain density and porosity appear possible, over good intervals, using GLT derived data. This will hold true as long as the mineralogy model is correct and the interval is reasonably homogeneous. It is not unreasonable to expect that estimates may, in fact, be superior to the core measured values by the nature of the sample volume measured. Great care must be taken in interpreting these derived parameters over bed boundaries and in thin bedded, heterogeneous units as these *bed boundary effects* may seriously affect estimates.

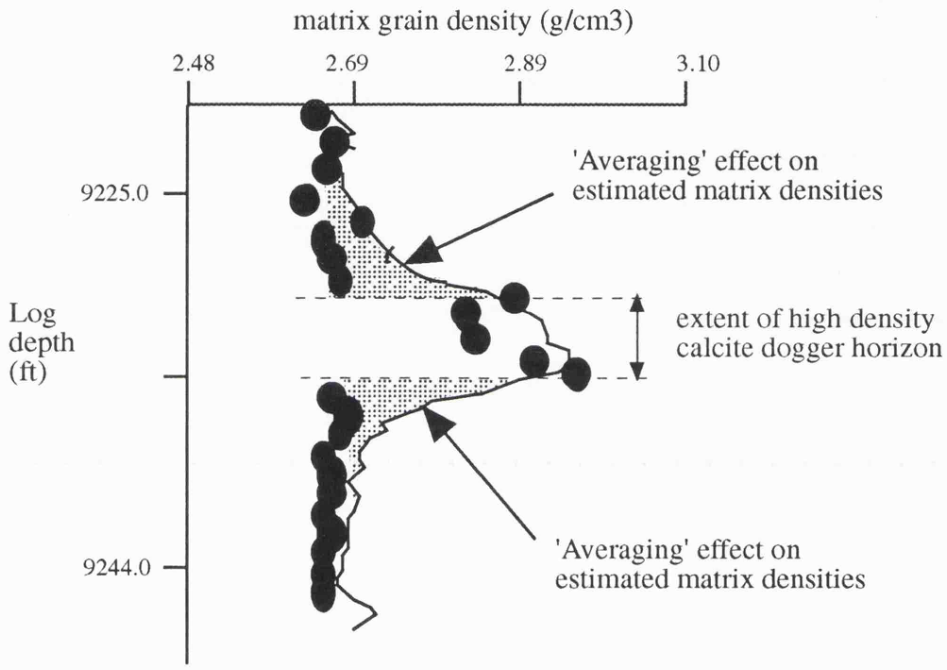

Figure 7.10 Close-up log showing averaged estimates of matrix density on the boundary of the 'calcite dogger', caused by the *bed boundary effect*. Thistle 211/18-a50 section. Shaded area represents the difference between *averaged* log (black line) and *actual* core matrix density estimates (dots). The worst affected estimates are nearest the 'calcite dogger' boundary. Estimates of porosity calculated from these 'averaged' data are in error over this interval.

Chapter 8.
Conclusions

It is at this point that we can now consider the questions posed in Chapter 1. These were....

Can we produce meaningful mineralogy from a chemical analysis?

Can this be attempted successfully on data from a borehole environment?

Can a mineralogy derived from nuclear log measurements be relied on to use in subsequent applications?

8.1 Can a meaningful, accurate modal mineralogy be derived from a chemical analysis?

Apart from its application to the borehole environment, *mineral transformation* itself can be considered as a purely geological problem. This is the situation to which the first question is addressed.

A desirable mineral transform model should be capable of handling at least the number of phases present in the rock sample yet be sensitive to the effects of compositional colinearity, and variation in mineral composition. It has been demonstrated that it is possible to obtain accurate mineral modes from numerically and synthetically produced data using *all* the models considered. Accurate modelling is also demonstrated to be possible in a real reservoir scenario, as seen in the Brent Group, but it is important to have an idea of the range in variation of mineral *assemblages* as well the *compositional variation* of any mica or clay mineral species. Strategies that reduce these problems are shown to be successful, with help from localised core input.

Compositional colinearity, as seen in the Rannoch Formation, is a serious potential source of error and must be recognised early in any routine processing. Strategies which 'pull' mineral phases from such colinear planes help to alleviate this problem.

The *stochastic strategy*, although in its infancy, provides, potentially, the greatest recent advancement in mineral modelling. It allows a means of overcoming the problem of compositional variation within an individual mineral species without having to accurately know a composition *apriori* at each depth interval. Its success will be limited, however, by the data available to form the appropriate statistical distribution.

Shale - mudstone lithologies represent the worst case scenario for *transform models* and in general they prove impossible to model successfully because of a) the *under-determined system* produced by the large number of detrital and authigenic phases present; b) the *compositional colinearity* often present between three or more phases; and c) the large *variation in composition* of the clay species. Further studies, in the future, on the relationship between geochemistry and the individual clay minerals (especially involving the elements

Gd, Sm and Th, U, Mn and V) may allow minor elements to be modelled successfully along with existing elements, enabling a solution to become more constrained.

The addition of *extra physical parameters* in the case of *bound water* ($H2O^+$) may also improve a solution, but only if estimates are at least as accurate as the other input responses. Modelling with *density* in quartz-feldspar rich lithologies should be avoided as this introduces 'noise' to the solution and produces a sparse components matrix. It may, however, be useful when a clear contrast in density between minerals being modelled is present.

In terms of the effectiveness of each transform model, the Euclidian Distance and Least Squares - Error Minimisation (*direct solution*) models appear very similar in behaviour and in their determination of modal mineralogy. However interpretation of *residual* unused chemistry remains perhaps more meaningful for the Euclidian model in terms of a failure in mineralogy. Linear Programming appears as proficient in simple lithologies but it is generally inferior in cases of acute compositional colinearity and should be avoided. Least Squares *indirect solution* methods should also be avoided as they defy the basic assumptions for mineral modelling. Conclusions more specific to each model have already been discussed in Chapters 3, 4 and 6.

At present there is no direct measure that can validate the *accuracy* of a solution, apart from cross-checking with core data, which on a regular basis would prove expensive and impractical. Although the two former techniques may produce negatives, in the authors view this can be regarded as a helpful indication that something is in error in the model and in this sense provides a means of rejecting a poor solution. It is hoped a 'feel' for the use of *Standard Error*, in the case of Euclidian Distance and Least Squares models, and *P%acc* in the case of the Linear Programming model, has been achieved throughout this study. They both serve as useful indicators of error in terms of the 'geochemical fit' of a solution (but cannot tell us directly about the validity of a solution).

8.2 Can a mineralogy be derived successfully from the borehole environment?

It has been necessary to look at the physics of the Geochemical Logging Tool to understand the way in which errors in *data acquisition* and subsequent *processing* may affect the final elemental measurements that form the *input responses* for mineral modelling. It is shown that any error will be passed through to subsequent modelled mineralogy and ultimately through to applications that involve the *derived mineralogy* (or element chemistry). From the tool physics discussed in Chapter 2 and processing in Chapter 6 it is seen that it is imperative to have good idea of the quality of the GLT data. This can be assessed visually from the caliper log and *Normalisation Factor* log.

One of the largest problems with evaluating the accuracy of GLT derived *mineralogical* data is the difference in sample volume that exists between core and the geochemical measurements. This would not pose a problem if the two were homogeneous. Inevitable

differences in the homogeneity between core and log samples (particularly due to the size differences) must be considered when comparing data sets. This problem can be reduced by careful, representative, core sample selection and treatment.

Consideration must also be given to the substantial *uncertainties* (accuracy and precision) associated with existing core techniques. In the absence of a better method, these techniques at least provide a means of validating derived mineralogy. Poor *lower limits of detection* of existing core petrographic/mineralogical techniques are also found to inhibit any effective semi-quantitative comparison of the less abundant mineral phases. Careful depth matching of core and log data must also play a considerable role in the success of any correlation of data sets.

Establishment of *accuracy* and *precision* of the tool *elemental* measurements could not, unfortunately, be included in the remit of this study because no core data were available (although it has been addressed by a number of other authors, as seen in Chapter 2). Tool derived elemental chemistry does, however, correlate surprisingly well with the sedimentological and mineralogical features seen through the a50 reservoir section. Careful comparison of mineralogical trends helps to substantiate the link between nuclear logging measurements and mineralogy.

The *bed boundary or 'smoothing' effect* coupled with the *vertical resolution* of the tool measurement are a problem in thin-bedded and heterogeneous intervals and do lead to a compromise in estimates of *derived mineralogy* over such zones. This is a serious problem with the GLT derived data, and use of mineralogy over such horizons should be avoided.

Tool precision may also affect the estimation of mineralogy considerably, and in a worst case-scenario it is shown that mineral estimates may vary by up to 12 wt%. This is again potentially a serious problem. Observation, during processing, of the calculated elemental uncertainties (derived using the *Normalisation factor,* Grau *et al.,* 1989, refer to Section 2.5.1), help to indicate where elemental measurements are poor and subsequent derived mineralogy likely to be in error.

In conclusion, GLT data may derive reasonably accurate estimates of bulk mineralogy, if a) borehole conditions are known to be good; b) the horizon that is being logged is reasonably homogeneous and substantiates a thickness greater than the intrinsic vertical resolution of the tool (and is free of the possible *bed boundary effect*); and c) the specific problems pertaining to mineral inversion mentioned in Section 8.1 are alleviated by appropriate strategies (introduced in Chapter 5). It is likely, for instance, that the modelled mineralogy in the larger units through the a50 section (*viz.* Units T1, T3 and R1) are representative estimates of the actual modal mineralogy present. The lack of the availability of Na2O3 and MgO (as seen in the a50 section) currently remains a large disadvantage with the current GLT tool set-up especially for the more complex lithologies where extra oxides are crucial. As for the identification of minor phases or rare element specific phases, however, its use remains highly sceptical.

8.3 Can a mineralogy derived from the nuclear log measurements be relied on to use in subsequent applications?

Reliability can only be placed on parameters subsequently derived from mineral transform models if accurate *chemical modes* are performed. This is shown to be possible with well constrained laboratory data and in certain situations (as just discussed) with mineralogy derived from the GLT tool data.

The use of the derived mineralogy in *inter-well correlation* is encouraging but it remains to be seen whether some of the more subtle mineralogical trends can be correlated using GLT derived measurements. The mineralogical trends observed in derived mineralogy, and accurately verified by core, in the 211/18-a50 section suggest that this is feasible. Again, care in interpretation over bed boundaries must be taken.

Estimation of matrix density and of subsequently derived porosity in the 211/18-a50 section indicate that a) it is possible to use mineralogy to predict (or enhance) petrophysical parameters where *bed boundary effects* are not present. b) they may produce a more reliable estimate in terms of the sample volume measured, than a conventional side-wall core measurement. Log data, at least, provide a continuous estimate of such important parameters which can be used to characterise a formation in the absence of core.

8.4 Recommendations for future work

Tool related.

1) Further advancement in the physics of gamma-ray detection in the extremes of the borehole environment will lead to improved counting statistics and through enhanced spectral de-convolution the ability to measure less *detectable* elements. This has already proved possible for the measurement of Na, Mg, Mn and V by delayed activation using cryogenic detectors (Schweitzer & Peterson, 1992). These detectors provide infinitely better counting statistics than conventional NaI crystals and should lead to radically improved elemental estimates. Greater, information and more accurate estimates from improved detectors will lead to the availability of more *input responses*, resulting in a better constrained mineral model.

2) Further work could be directed at reducing the *bed boundary effect* currently present between two contrasting lithologies. One way of overcoming the *bed boundary effect* may be to use other *high resolution* logs, (such as the FMS, Formation Micro Scanner) to identify the location of individual bed boundaries coupled with advancements in tool response de-convolution. The normal 7 point averaging applied to GLT data could then be truncated exactly at the boundary with the result of reducing the *'averaging'* effect. In this way more reliable mineral predictions may be obtained over such intervals.

Mineral modelling related

1) In terms of mineral modelling, the *stochastic model* has great potential for over coming the need to accurately estimate compositions of highly variable mineral species at every depth interval. Further work could be undertaken in allowing the model to account for bi-modal populations of data and secondly developing a technique to model more than one phase stochastically. Further work could be undertaken in terms of establishing a large, representative data-base of compositional data that may be implemented in the stochastic modelling strategy. This could be implemented on different scales; for example, a single lithological *unit* or *Formation specific* scale or on a *Group specific* scale. Illite analyses from the Brent Group, for instance, would have helped in the modelling performed in this study.

2) With knowledge of mineral modelling in the borehole environment from this current study future work may be directed towards non-linear systems seen in conventional geophysics, where all measurement uncertainties may be formally accounted for. This would have to take on the formulation of a complete set of new algorithms which attempt to model when one or more of the assumptions set out in Chapter 3 (Section 3.2) become violated.

3) Finally, further work could be undertaken in further quantifying the effect that GLT uncertainties (precision) have on modelled mineralogy. This would need to take the form of a formal Monte Carlo algorithm that was designed to vary each oxide independently, at random, in a stochastic model. Results would then ameliorate the *worst case scenario* presented in Chapter 6.

****

PLATES 1 - 6

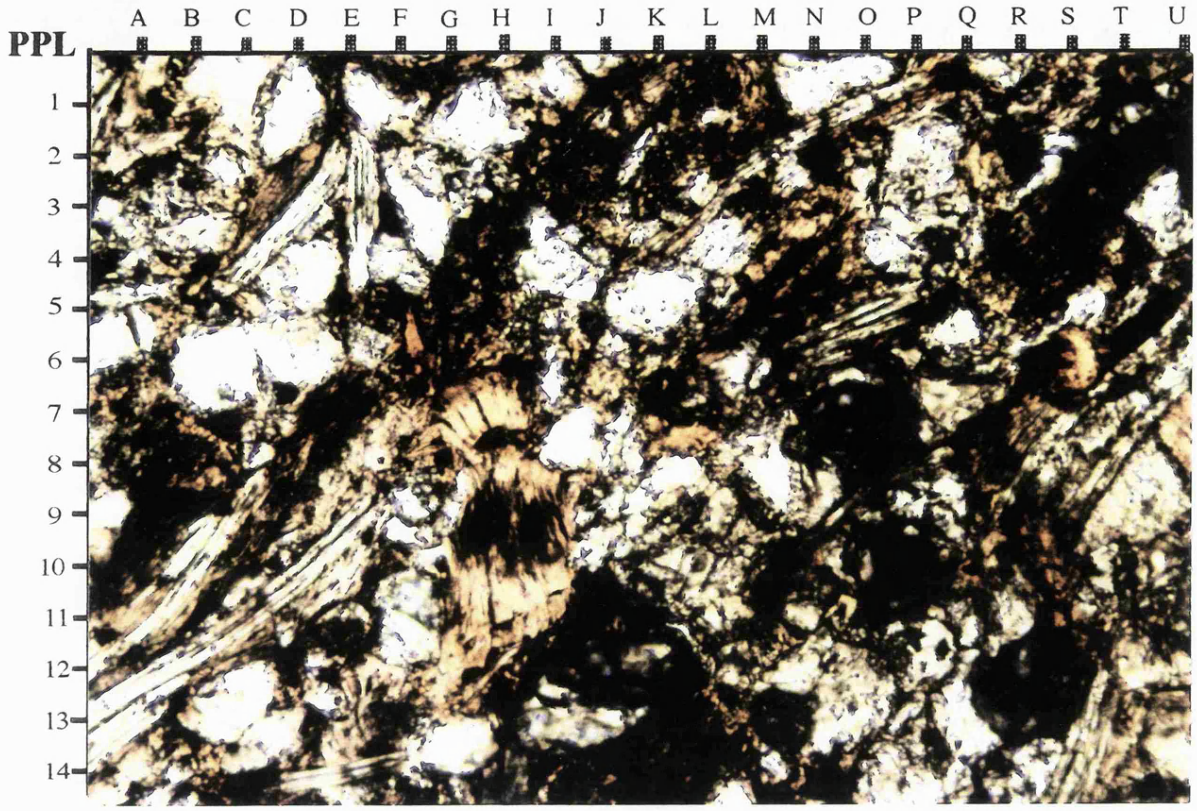

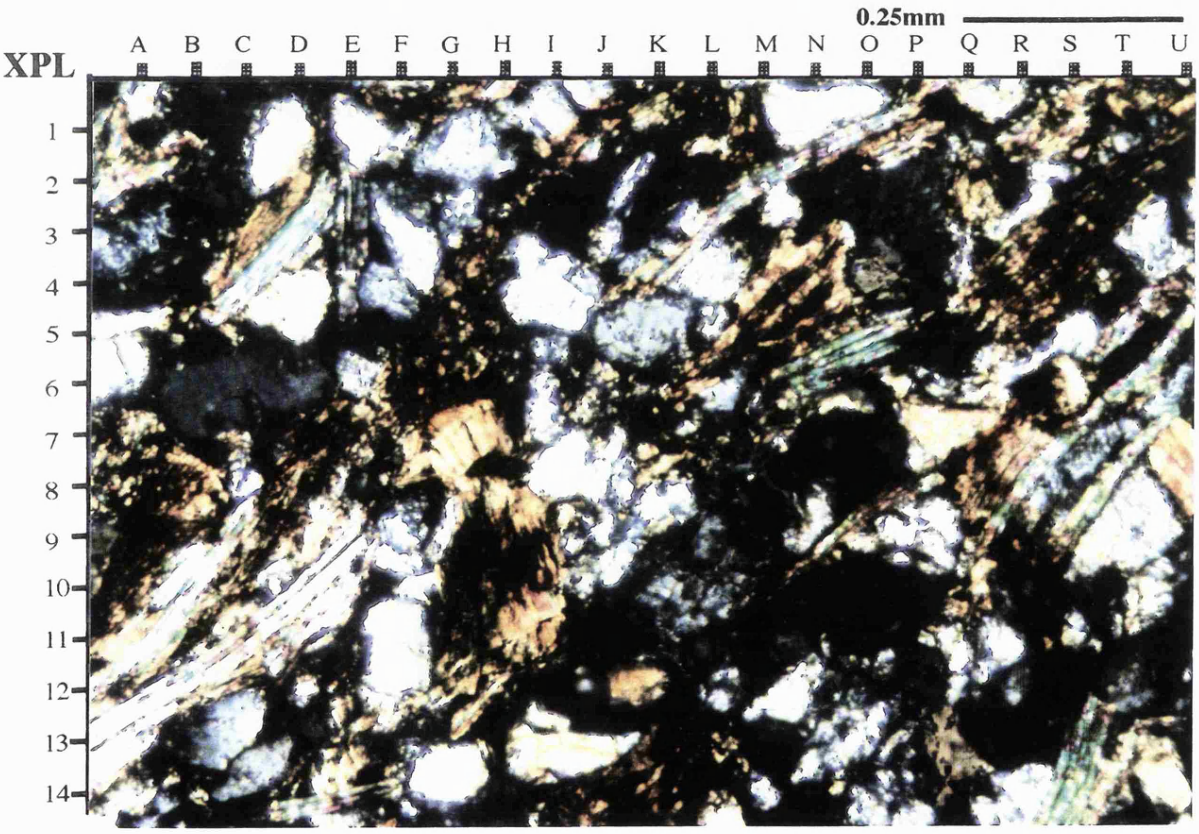

Sample 10580-82 Rannoch Formation, hole 211/18a-a33 (Scale x 200)

Moderately-well sorted, fine grain sandstone with subhedral-rounded grains. Porosity is moderate-poor. Composition is dominated by detrital, strained, subhedral quartz grains (K4-5,C13, N,1) and platy micas. Pale brown/green biotite (H7-11,R7,B8) and clear muscovite (A13,D3,O5) are present in equal proportions. Biotite is strongly altered, replacement amorphous kaolinite and siderite forming at grain ends and along cleavages (G4-6,A8). Detrital albite and K-feldspar with moderate to high alteration (P3,) are subordinate. Kaolinite is the dominant poor filling clay mineral(A7).Trace opaques and heavy minerals.

PLATE 1

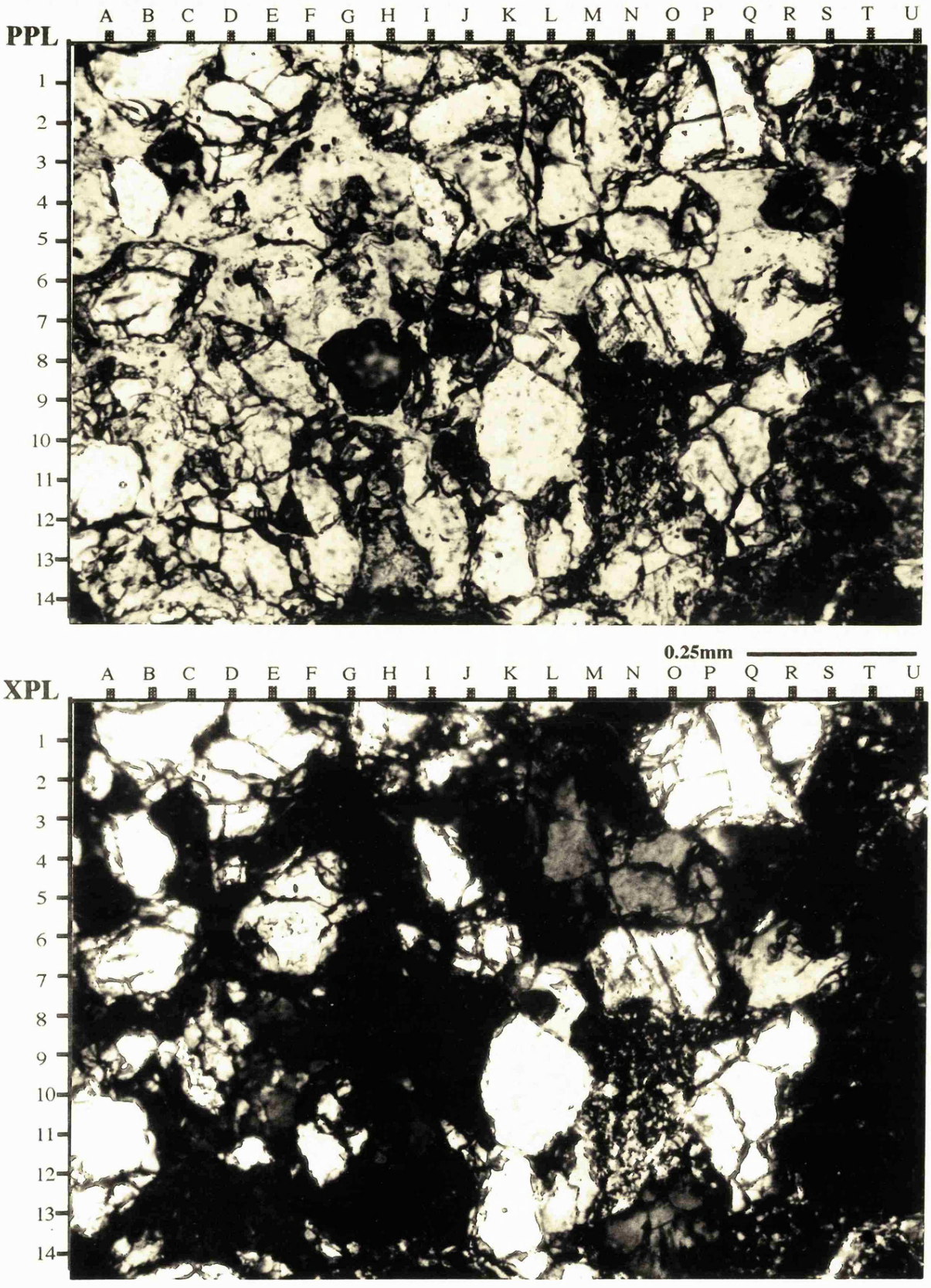

Sample 10540 Etive formation, hole 211/18a-a33 (Scale x 200)

Moderately sorted, fine grain sandstone with subhedral-rounded grains. Porosity is moderate, picked out by pale green, low relief mounting cement in a, (R5). Composition is dominated by detrital, strained, quartz grains (D10-11, O5, A11). Detrital albite, K-feldspar with moderate to high alteration (O7). Kaolinite is patchy as a grain coating - pore filling cement (O9-12). Mica is rare or absent.

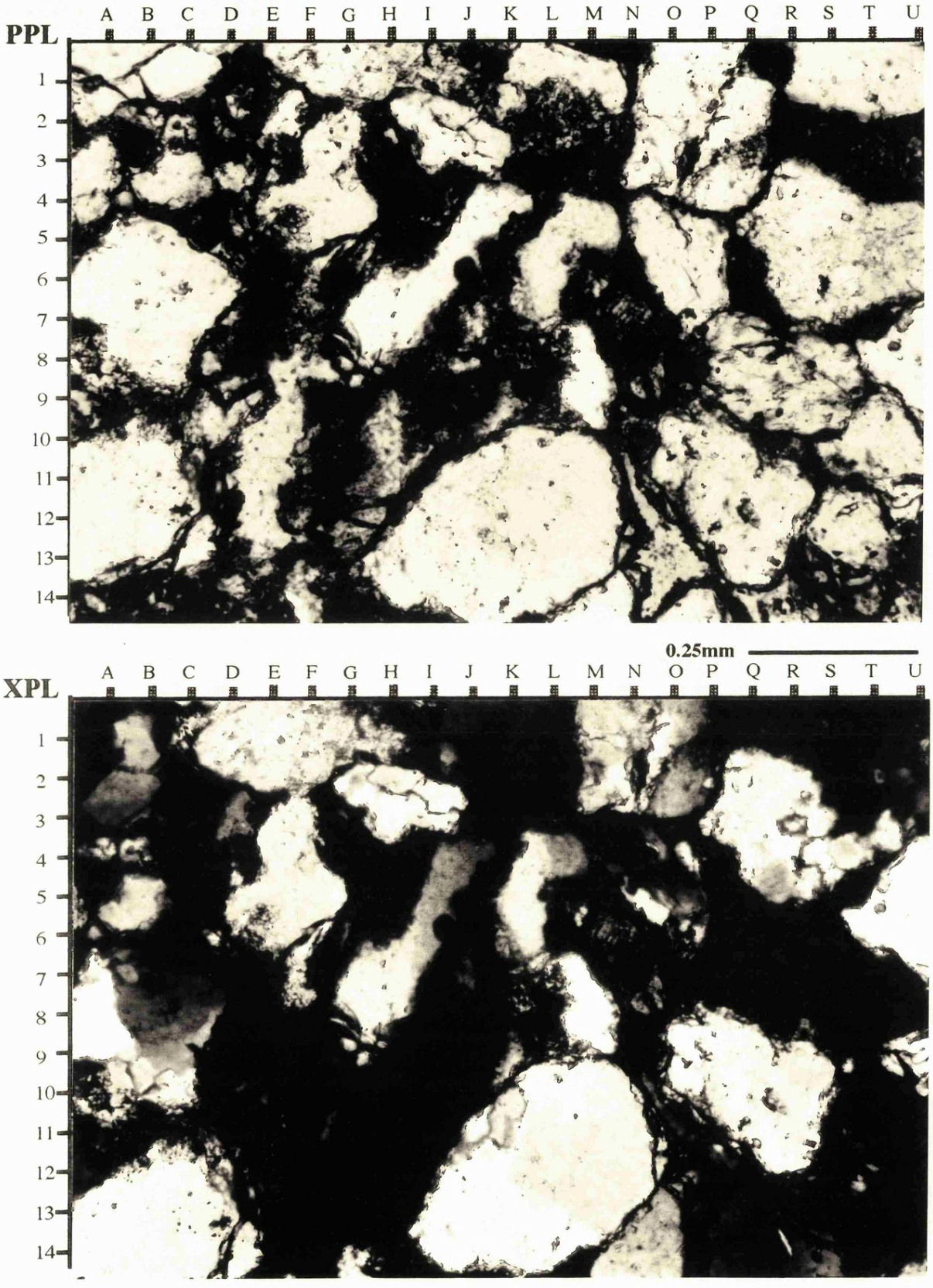

Sample 10452 Ness formation, hole 211/18a-a33 (scale x200)

Moderately sorted, fine-medium grain quartz rich sandstone with subhedral-rounded grains. Porosity is moderate to good, picked out by pale green, low relief, mounting cement (O14,H11,E11). Pore space is locally filled with clay (T3, M3). Composition is dominated by detrital, variously strained, quartz grains (K10-13, B6-7,S5). Subordinate detrital albite and K-feldspar with moderate to high alteration (Q8). Trace opaques (including organic matter) and zircon grains (N6). Kaolinite is dominant pore filling and replacement clay mineral.

Description of plate 4.

SEM micro-photographs from the Etive and Rannoch formations
of Thistle well 211/18a-a33

A. Sample 10499, Etive Formation.
Well formed kaolinite 'accordion' booklets (vermicules) and less well formed amorphous kaolinite on the surface of a striated quartz grain. Scale bar 10μm.

B. Sample 10499, Etive Formation.
Enlargement of kaolinite 'accordion' booklet in a background of amorphous kaolinite. Scale bar 5μm.

C. Sample 10584, Rannoch Formation.
Centre grain possibly an Fe-carbonate (siderite, *Fe-rich* EDX spectrum). Bottom centre, a leeched K-feldspar grain. Bottom left a detrital zircon grain (Zr spectrum). Centre top, detrital quartz grains. Scale bar 10 μm

D. Sample 10584, Rannoch Formation,
Leeched K-feldspar grain, corroded along cleavage planes, kaolinite in background. Scale bar 50 μm.

E. Sample 10499, Etive Formation,
Well formed accordion kaolinite crystals just below centre with small scattered cubic pyrite grains. Background of amorphous or poorly formed kaolinite and detrital mica flakes. Centre left, rhombohedral siderite grain. Scale bar 5 μm.

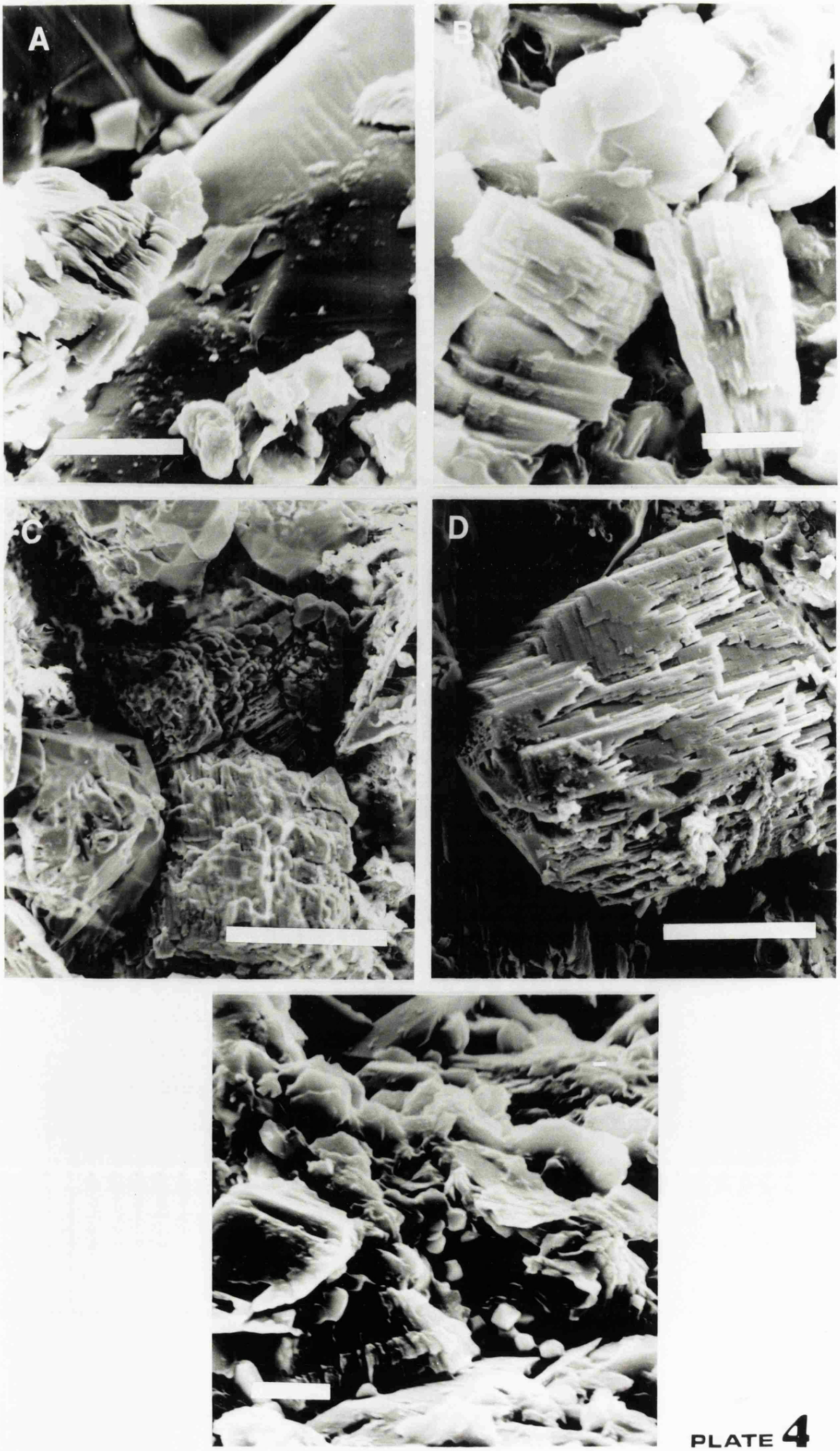

PLATE 4

Description of plate 5.

Electron microprobe photo-micrographs of micas in the Rannoch Formation of Thistle well 211/18a-a33

A. Sample 10561, Rannoch Formation.

Prominent light crystal is a detrital biotite mica, displaying very clear cleavage and 'splaying' at the bottom left end. Light grains 'wedged' along mica cleavage planes are authigenic siderite, forming at the expense of biotite. Minor clays also line some of the cleavage planes. The crystals to the top left of the biotite are quartz and albite feldspar. Scale bar 50 μm

B. Sample 10561, Rannoch Formation.

Heavily altered biotite grain (centre) showing heavy a growth of small siderite grains along cleavage planes. The clear crystals either side of the biotite are quartz grains. The elongated crystal at centre left is a muscovite mica with a 'splayed' end. The splaying is partially altered to kaolinite (slightly dull colour). Amorphous kaolinite forms between grains to the right of the 'splayed end' and between grains in the bottom right corner. Scale bar 50 μm.

C. Sample 10561, Rannoch Formation.

Close-up of an altered biotite crystal showing the displacesive habit of a siderite grain. Siderite is replacing biotite primarily along the cleavage planes. Scale bar 10 μm.

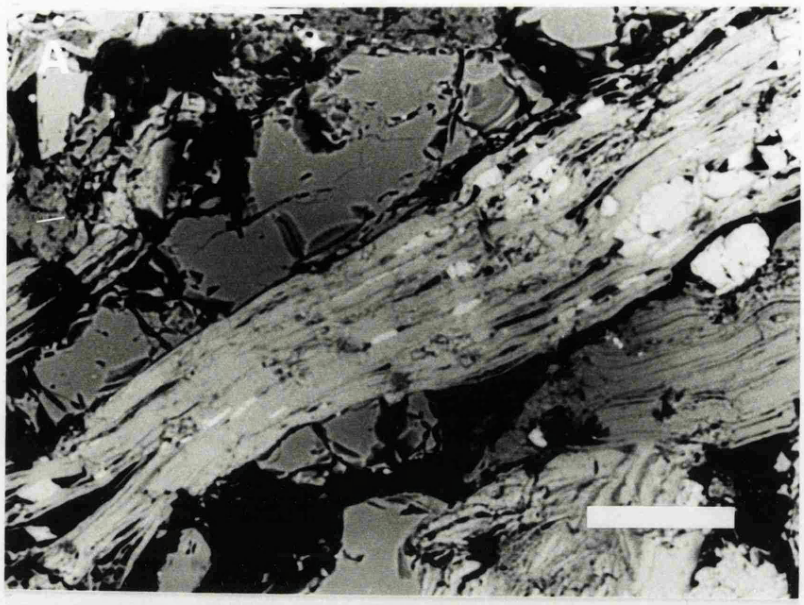

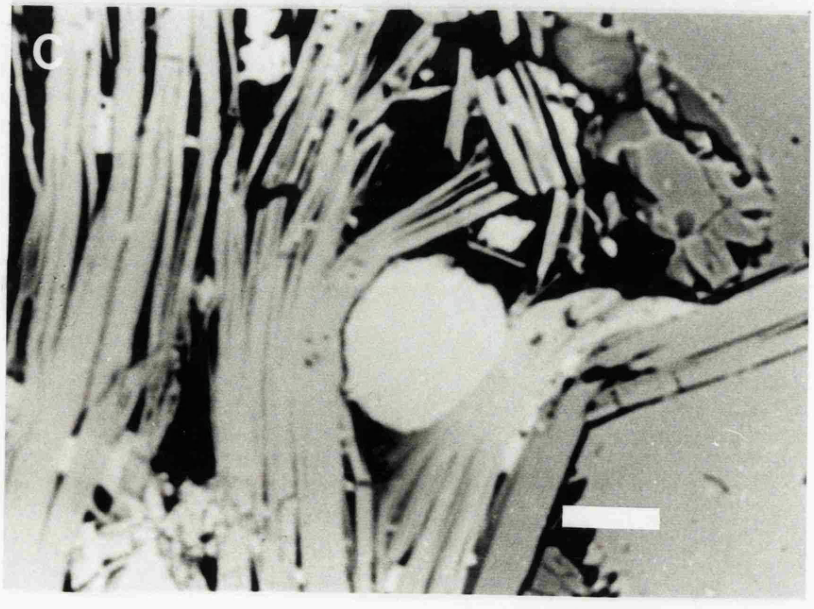

PLATE 5

Description of plate 6.

SEM micro-photographs of the mudstone lithology from the Ness and Etive formations of Thistle well 211/18a-a33

A. Sample 10470-71, Ness Formation.

Detrital mica grain, bottom and centre left, clear of authigenic illite/smectite clays except in far bottom left corner where it partially obscure and infills between splayed cleavage. Bottom right and top right, amorphous kaolinite. Scale bar 2 μm.

B. Sample 10470-71, Ness Formation.

Detrital grains of K-feldspar, bottom left corner; rutile, just left of centre (light grain) and two detrital mica flakes, top right quarter. Background composed partially of detrital mica and amorphous kaolinite. Scale bar 3 μm.

C and D. Sample 10471-72, Ness Formation.

Amorphous and massive kaolinite. Scale bar 3μm.

E. Sample 10471-72, Ness Formation.

Amorphous and massive kaolinite background with small authigenic siderite crystals, centre. Scale bar 10 μm.

F. Sample 10486.2 - 86.7, Etive Formation.

Poorly defined illite-smectite phase showing partially curly 'boxwork' texture. Far bottom right and far top left, amorphous kaolinite. Scale bar 2 μm.

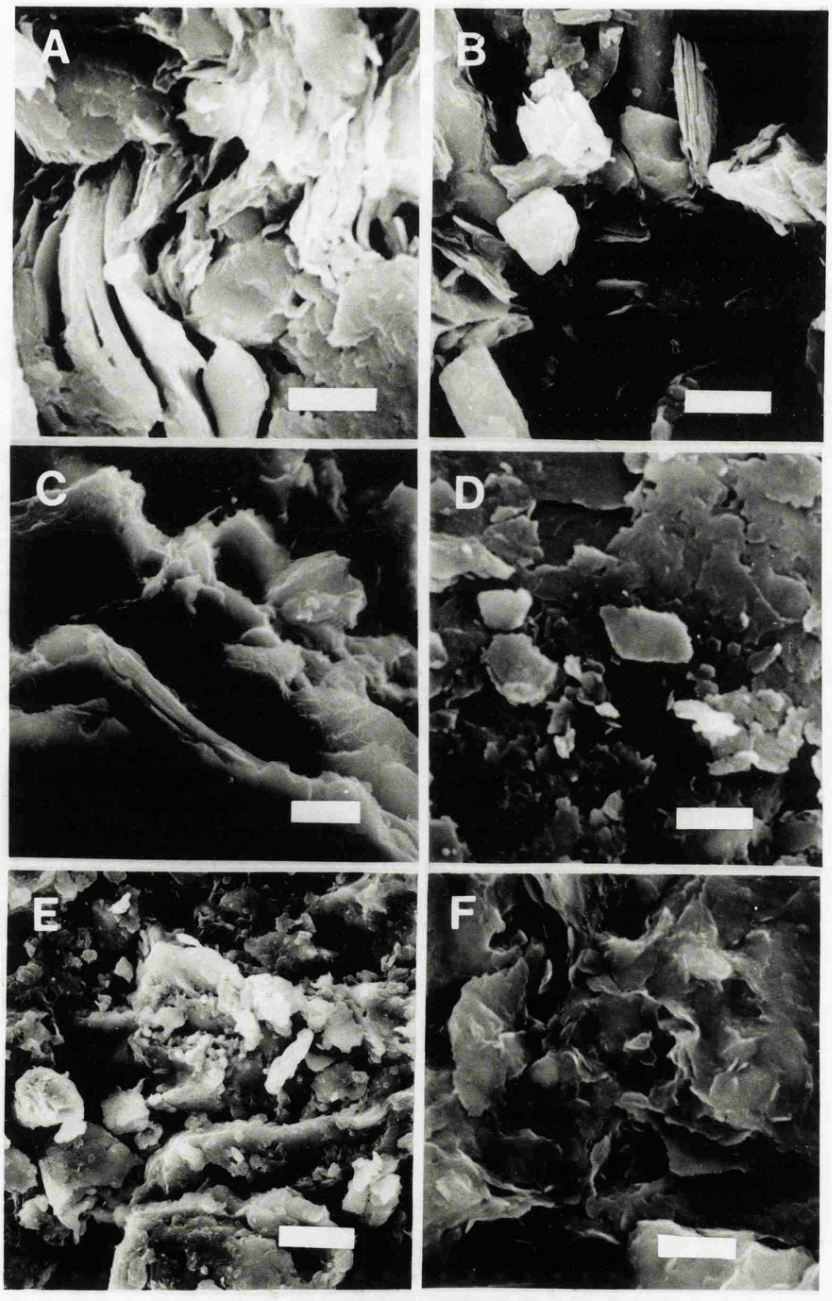

PLATE 6

APPENDICES

Appendix AA.

Logging tool acronyms used in this thesis

GLT	Geochemical Logging Tool[1]
NGT	Natural Gamma-ray Spectroscopy Tool[1]
AACT	Aluminium Activation Clay Tool[1]
GST	Gamma-ray Spectroscopy Tool[1]
LDT	Lithodensity Tool[1]
CNG-T	Compensated Neutron Tool[1]
AMS	Auxillary Measurement Sonde[1]
SDT	Digital Sonic Tool[1]
CALI	Caliper tool
DITE	Dual Induction Tool[1]
FMS	Formation Micro Scanner[1]

Additional acronyms used

Pe	Photoelectric effect
PEF	Photoelectric factor (from LDT)
CSIG	Total capture sigma measurement
RHOB	Bulk Density (from LDT)
NPHI	neutron porosity

---

[1] Trade Mark of Schlumberger

Appendix one

Composition of different minerals used in synthetic modelling; composition of each synthetic rock; composition of different muscovites used in modelling

	Quartz	Albite	Kaolinite	K-feldspar	Muscovite	Dolomite	calcite
SiO2	99.07	65.81	47.63	64.33	45.78	0	0
Al2O3	0.23	21.33	37.95	19.04	34.21	0	0
TiO2	0.01	0.02	0.06	0.01	0.24	0	0
Fe2O3	0.15	0.11	0.65	0.11	3.04	0	0
MgO	0.13	0.05	0.01	0.01	0.69	21.34	0.04
CaO	0.00	1.86	0.03	0.04	0.00	31.27	55.92
Na2O	0.21	9.82	0.72	2.49	1.01	0	0
K2O	0.02	0.67	0.86	13.16	10.24	0	0
MnO	0.00	0.00	0.01	0.01	0.12	0	0
P2O5	0.01	0.03	0.11	0.48	0.22	0	0
S	0.01	0.00	0.00	0.00	0.00	0	0
Total	99.84	99.7	88.03	99.68	95.55	52.61	55.98

XRF analyses of synthetic rock mixtures

	Mix 1	Arenite	Semi-pelite	Mix2	Pelite	Carbonate
SiO2	83.54	87.22	70.90	62.84	57.40	0
Al2O3	9.83	4.30	0.03	25.41	23.85	0
TiO2	0.02	0.12	15.22	0.10	0.13	0
Fe2O3	0.14	0.50	0.40	0.99	1.62	0
MgO	0.06	0.51	1.05	0.18	1.30	15.66
CaO	0.41	1.45	1.95	0.07	1.58	38.52
Na2O	2.28	0.92	2.07	0.04	0.80	0
K2O	1.57	1.90	3.27	2.90	6.81	0
MnO	0.00	0.00	0.0	0.00	0.07	0
P2O5	0.71	0.03	0.10	0.06	0.10	0
S	0.00	0.00	0.00	0.00	0.00	0
Total	98.56	96.96	94.99	92.61	93.66	54.17

Composition of muscovites used in Figure 3.6

	theo-retical	ideal	1	2	3	4	5
SiO2	45.25	47.08	45.87	46.01	47.11	48.42	48.54
TiO2	0.00	0.20	0.00	0.00	0.74	0.87	0.66
Al2O3	38.40	30.81	38.69	35.64	29.68	27.16	21.99
Fe2O3	0.00	3.08	0.00	0.01	4.17	7.47	9.37
MnO	0.00	0.00	0.00	0.00	0.01	0.00	0.00
MgO	0.00	1.71	0.10	0.00	1.77	0.00	3.09
CaO	0.00	0.35	0.00	1.12	0.19	0.00	0.35
Na2O	0.00	0.75	0.64	1.89	0.34	0.35	0.75
K2O	11.82	10.11	10.08	8.19	10.32	11.23	11.27

Appendix 2.0 Analytical techniques

X-ray diffraction analysis

Sample preparation

Two types of samples have been prepared for quantitative analysis, a) unorientated bulk powders (5μm) for analysis of the matrix minerals; b) <2μm orientated samples for the analysis and quantification of clay minerals.

Unorientated clay traces

Unorientated bulk powder samples (5μm) were made of all samples being studied, including the synthetic rocks, Thistle and Statfjord cores. A microniser was employed for the reduction of powders to the optimum size of 5 μm for X-ray diffraction. Unorientated mounts were prepared by packing powders into a holder, as described by Moore & Reynolds, 1989. Traces were run using Ni filtered CuKα monochromatic radiation generated at 40kV, 30mA, scanning at 1 degree per minute using a Phillips 1729 X-ray generator and Phillips 1710 diffractometer control unit.

Orientated clay traces

Oriented <2μm clay aggregates were prepared by pipette extraction (Folk, 1974), subsequently centrifuged for five minutes and then dropped on to glass slides (Moore & Reynolds, 1989). Analysis was performed under the same conditions as the unorientated samples. Two runs were made for most samples, a) after air drying at room temperature, b). after glycolation for 12 hours. This was performed to verify the clay species present. Results and peak traces are presented in appendix 4.4 and Figure 4.5.

Two unorientated bulk samples of pipette separated 2μm clay aggregates were also analysed for the identification and semi-quantification of the mineral phases from the mudstone intervals (10472-73,10486.2) in the Thistle well, see Appendix 4.4.

Whole rock data- quantification of mineral proportions.

The abundance of non clay *mineral* species, kaolinite and mica has been interpreted from the height of the strongest undisturbed diffraction peak for each mineral. Identified unorientated peaks are those suggested by Schultz (1964). If more than one good peak was present, an average of all peak heights for the mineral was taken for quantification. The peak, its 100% intensity on an external standard and mineral mass absorption coefficient are summarised in Table A1.

Quantitative/semi-quantitative analysis was performed using the *mass absorption coefficient* of the sample calculated from the XRF chemical compositional data, the 100% peak heights of the pure standard of each expected mineral (an external standard) and the *mass absorption coefficient* of each mineral phase, (Brinley and Brown, 1980). These were used to derive mineral percentages present such that:

$$\mathbf{Ip} \;/\; \mathbf{Ip_0} \;=\; [\mu / \mu o]\;\; \mathbf{wp} \qquad (1..)$$

where **Ip** is the peak height from the mineral in the sample, $\mathbf{Ip_0}$ is the 100% external standard peak height, μ is the mass absorption coefficient of the mineral phase; μo is the mass absorption coefficient of the sample and **wp** the weight percent of the mineral.

By not using an internal standard, a diluting effect on diffracted intensities is avoided as is the interference of reflections from the internal standard and the seven or so mineral species.This method is seldom used because of the reluctance to measureμo (Brinley and Brown, 1980), which is not a problem in this study.

A check on the accuracy of this technique by analysis of the *synthetic data set* (with mineral proportions known) suggest an average absolute error of +/- 3 -3.5 wt% for the estimation of mineral phases. Mica is worse up to 8 wt%. It is expected that due to crystallinity and lack of good internal standards for the Brent formations that the errors may be greater (*cf.*+/- 5%)

Kaolinite peak intensity and crystallinity

A calibration curve was constructed using five different mixes of the two minerals quartz and kaolinite, which are the dominant minerals in all *sandstones* analysed. The curve suggests an over-estimation of kaolinite at higher concentrations (due to the orientation effects of

kaolinite). This is the opposite to the kaolinite quantified in silt-mudstones of the Brent Group and is probably due to the low crystallinity of the kaolinite in this formation. SEM suggests the crystallinity of kaolinite in the purer sandstones is of a high order. From the calibration curve, sediments with less than 10% kaolinite (sandstones) were treated as having kaolinite with *good crystallinity* and the external standard intensities can be applied to these in quantification. Samples with greater than 10% kaolinite (silts-mudstones) have been quantified using an internal standard separated by pipette extraction from the whole-rock mudstone samples. Unorientated XRD traces are shown for this <2um extraction in Appendix 4.4. Subtraction of the *minor phases* (micro-quartz, feldspar, siderite) and subsequent scaling of the kaolinite intensity to 100% gives a reasonable internal standard for analysis of the mudstone rocks of the well 211/18a-a33.

Table A1. Peak heights used and 100% external standard intensities used for XRD analysis, calculated from minerals used to make up the *synthetic data set.*

mineral	Identification peak (2 Theta)	External standard 100% intensity c/sec	mineral mass absorption coefficient
Kaolinite (sandstones)	12.35	1850	39.9
	24.9	2070	
Kaolinite (silt/muds)	12.35	1250	39.9
	24.9	1200	
Quartz	36.5	1020	36.4
	39.45	1020	
	40.3	580	
	50.1	1920	
	59.9	1300	
K-feldspar	25.6	1360	50.6
	27.5	2350	
	41.8	300	
Plagioclase (albite)	22.1	1300	34.3
	27.9	7100	
Dolomite	30.9	11250	48.8
Calcite	29.43	6200	73.4
Mica (muscovite/illite)	8.8	4450	43.9
	17.8	1305	
Siderite	32.0 (31.7-32.0)	3330	151.5
Rutile(TiO2)	25.3	4650	125.5
	48.1	1100	
Pyrite	33.07	1870	190.9
	37.1	1000	
	56.3	2200	
chlorite	6.24		29.4

Oriented clay fraction XRD

Six Oriented slides with the clay fraction (2μm) were run under the similar analytical conditions to determine the clay phases present throughout the Thistle section. Semi-quantification of the area of basal reflections was performed as described by Biscaye (1965), on the assumption that all basal reflections were made solely by clay minerals. Appropriate multiplication factors were applied to the basal peak areas (2 x 002 kaolinite peak, 4 x 001 kaolinite peak) and the approximate wt% derived from the ratios of peak areas to the summed peak area. This technique was only crudely attempted on the mudstone sample 10486.2 as there is the probable identification of poorly ordered illite/smectite with a broad 2.8 - 3.0 degree peak and a small shoulder peak on the high angle side of the 002 illite peak (9.3A). Figure 4.5 shows the XRD traces from the analysis of the six samples.

Appendix 2.0 (cont.) ***analytical techniques***

XRF spectrometry analysis.

Method

All Thistle samples were fly pressed and crushed to 50μm in a tungsten carbide swing mill for the period of one minute, thoroughly cleaned between samples, to avoid cross-contamination. Powders where then dried for 12 hours at 150c to remove most of the oil residue from the samples.

A 5-10 gram fraction was then ignited at 1000c for three hours to remove volatile and hydrous fractions and *loss on ignition* determined. One gram of ignited powder was then made into a 46mm fused disc consisting of a mix of 80:20 lithium metaborate and lithium tetraborate flux (similar to *Johnson Mathey Spectroflux* JM100B). Fused beads were then analysed for the major elements on an ARL8420+ XRF spectrometer using a 3K Rhodium anode X-ray tube at 50kV 50mA. Processing was performed on an IBM using ARL386 Phase 1 software. Analytical details are given in Table A2.

The remaining powder was used to make 46mm pressed powder pellets for selected trace element analysis. This was performed on a Phillips 1400 XRF spectrometer with either a 3K Rh or W anode X-ray tube, operated at 80kV 30mA. The trace elements Nb, Zr, Y, Sr, Rb, Th, Ga, Zn, and Ni were analysed with the Rh tube; V, Cr, (Co?), Cu, Ba, La, Ce, and Nd using the W anode. Analytical details are given in Table A2. Full details of the equipment, operating and processing conditions for both instruments are given by Tarney *et., al.,* 1991 and Pickering *et., al.,* 1993.

In order to control the quality of the output data, both internal monitor samples (m) and international standards (s) were run within each batch of samples (u). Monitors allow the performance and instrumental drift of the machine to be monitored (precision) while comparison of standards to their reference compositions allows an indication of accuracy. Accuracy, precision are detailed in Table A2.

Problematic mudstone totals

The more pelitic lithologies in the Thistle hole were observed to contain a lot of organic material, (plant debris) and most of the results for the mudstone samples yield poor major element (fusion bead) totals, averaging 97%. Consistent repeat analysis (between two and five re-makes) suggest that it is not a sample preparation error.

Other reasons for a low *total* have been investigated. These include:

a) improper ignition of the sample, yielding low totals. This was overcome by re-weighing the sample before casting and adding the weight of material (for sample 10486.2-86.6 this was a weight loss of 0.6% and for 10496-97 a weight loss of 0.7%) the weight loss was not sufficient to lower the totals by 3%.

b) The high organic content could have been the problem where improper ignition failed drive off all carbon in the mudstone; the carbon turning to graphite and staying fixed to the clay molecule only to be ignited, forming CO2 at the higher temperature of 1100c on bead production. Carbon-sulphur analysis (Leco analyser) of the original un-ignited powder, ignited powder and a lack of carbon in the fused beads suggests that the carbon is not the source of error (For example, 0.0828 wt% carbon in the analysed bead for sample 10472-73).

c) Similarly sulphur in the sample is not a problem, i.e., the formation of unresolvable anhydrite (CaSO4), due to the break down of carbonate material producing free lime (CaO) and CO2. The free lime reacts with any free S to produce anhydrite. Siderite is known to be the only carbonate present in the section but carbon-sulphur analysis suggest that minimal sulphur exists. XRF 2-theta scans, on pressed pellets, from Oxygen upwards in the periodic table, confirm that no undetermined element is abundant, such as C and S, in any great quantity to produce the observed low totals. No collective or single trace element is present in a significant a quantity to lowers totals by 3%. The most common trace element are Zr and Ba and Y which together contribute less than 0.5 wt %, see appendix 4.2.

Analytical conditions for major-element analysis of fusion disks on the University of Leicester Department of Geology ARL8420+ XRF spectrometer.

Element	Line	Crystal	Peak angle	Count time (s)	Background 1 angle	Count time (s)	Background 2 angle	Count time (s)	Collimator	Detector
Goniometer 1										
P	Ka1,2	PET	89.54	50	91.97	25	86.7	25	Fine	FPC
Si	Ka1,2	PET	109.21	20	112.44	5	105.57	5	Std. Coarse	FPC
Al	Ka1,2	PET	145.12	30	148.85	15	140.44	15	Std. Coarse	FPC
Mg	Ka1,2	AX06	20.2	50	22.25	20	18.98	20	Std. Coarse	FPC
Na	Ka1,2	AX06	24.37	50	26.99	20	22.25	20	Std. Coarse	FPC
Goniometer 2										
Fe	Ka1,2	LiF200	57.52	25	60.42	10	55.25	10	Fine	FPC
Ti	Ka1,2	LiF200	86.14	40	88.8	20	84.25	20	Fine	FPC
Ca	Ka1,2	LiF200	113.09	25	115.1	10	110.1	10	Fine	FPC
K	Ka1,2	LiF200	136.69	50	139.36	20	131.67	20	Fine	FPC
Mn	Ka1,2	LiF220	95.2	50	98	25	92.85	25	Fine	FPC

Mean values and 1-sigma standard deviations for the major elements determined on the ARL8420+ from a selection of reference materials

	Sample				BOB-1				NIM-G			
Reference	Mean	Std. dev.	%Std. dev.	Number of runs	Mean	Std. dev.	%Std. dev.	Number of runs	Mean	Std. dev.	%Std. dev.	Number of runs
SiO_2	50.59	0.1	0.2	10	77.75	0.49	0.63	5	66.06	0.27	0.41	5
TiO_2	1.29	0.05	0.35	10	0.1	0	0.2	5	0.88	0	0.57	5
Al_2O_3	16.4	0.04	0.24	10	11.52	0.07	0.63	5	14.35	0.05	0.32	5
Fe_2O_3	8.55	0.01	0.16	10	2.02	0.02	1.04	5	7.05	0.02	0.23	5
MnO	0.14	0	0.96	10	0.01	0	15.38	5	0.14	0	0.71	5
MgO	7.66	0.03	0.34	10	0.09	0.01	13.33	5	1.61	0.02	0.99	5
CaO	11.13	0.02	0.21	10	0.75	0	0.4	5	5.68	0.03	0.48	5
Na_2O	3.12	0.01	0.4	10	2.91	0.01	0.34	5	3.3	0.03	0.88	5
K_2O	0.37	0	0.32	10	4.94	0.01	0.24	5	0.75	0	0.4	5
P_2O_5	0.16	0	0.92	10	0.01	0	6	5	0.17	0	1.21	5
LOI 1	0.73			1	0.63			1	0.38			1
LOI 2					0.59			1	0.34			1

Note: Analyses for BOB-1 were repeated on the same fusion disks and therefore reflect instrumental precision. The analyses are reported on a fully oxidized, volatile-free basis Analyses for NIM-G performed on three separate fusion disks and reflect the precision of the sample preparation proceedures and the instrumental precision.

Analytical conditions for trace-element determinations on the University of Leicester Department of Geology Philips PW1400 and ARL8420+.

Element	Line	Crystal	Peak angle (s)	Count time angle	Background 1 (s)	Count time angle	Background 2 (s)	($) Count time	Collimator	Detector
Nb	Ka1,2	LiF220	30.43	100	33.025	50	29.83	50	Fine	Scint.
Zr	Ka1,2	LiF220	32.115	80	33.025	50	29.83	50	Fine	Scint.
Y	Ka1,2	LiF220	33.925	80	33.025	50	29.83	50	Fine	Scint.
Sr	Ka1,2	LiF220	35.88	80	36.58	50	33.025	50	Fine	Scint.
Rb	Ka1,2	LiF220	38.045	80	38.7	50	36.58	50	Fine	Scint.
Th	La1	LiF220	39.3	100	41.015	50	38.7	50	Fine	Scint.
Ga	Ka1,2	LiF200	38.965	40	39.565	20	38.265	20	Fine	FPC + Scint.
Zn	Ka1,2	LiF200	41.805	40	42.605	20	39.565	20	Fine	FPC + Scint.
Ni	Ka1,2	LiF200	48.625	40	49.885	20	47.125	20	Fine	FPC + Scint.
Ce	Lb1	LiF220	111.64	160	114.07	160	110.14	160	Std. Coarse	FPC
Nd	La1	LiF220	112.67	160	114.07	160	110.14	160	Std. Coarse	FPC
La	La1	LiF220	138.78	160	141.78	80	136.78	80	Std. Coarse	FPC
Ba	La1	LiF220	154.17	100			153.17	100	Std. Coarse	FPC
Fe	Ka1,2	LiF200	57.52	25	60.42	10	55.25	10	Fine	FPC
Ti	Ka1,2	LiF200	86.14	40	88.8	15	84.25	15	Fine	FPC
Co	Ka1,2	LiF200	77.83	100	81.03	40	74.03	40	Fine	FPC
Cr	Ka1,2	LiF200	107.02	100	109.81	40	104.61	40	Fine	FPC
V	Ka1,2	LiF200	123.17	100	126.37	40	121.17	40	Fine	FPC
Sc	Ka1,2	LiF200	97.7	100			95.9	100	Fine	FPC
Ca	Ka1,2	LiF200	113.09	25	115.1	15	110.1	15	Fine	FPC
Cu	Ka1,2	LiF200	45.03	60	45.63	30	44.43	30	Fine	FPC

Precision and accuracy of XRF results based on analyses of three standard rocks: BOB-1, W-1, and BE-N.

	BOB-1		W-1		BE-N	
	Mean	σ	Mean	σ	Mean	σ
Rh X-ray tube trace element program						
Nb	4.5	±0.2	7.5	±0.5	111.2	±0.6
Zr	102.2	±1.0	93.3	±2.0	280.1	±2.6
Y	27.9	±1.0	22.7	±0.7	29.7	±0.1
Sr	194.8	±1.5	188.5	±1.3	1431.9	±9.4
Rb	6.1	±0.9	22.6	±0.5	50.4	±0.4
T	1.6	±1.2	2.5	±1.2	13.7	±0.6
Ga	15.3	±0.7	18.6	±0.7	18.2	±0.7
Zn	68.1	±0.6	90.1	±1.0	132.1	±1.1
Ni	109.9	±3.0	75.8	±1.1	291.6	±3.4
W X-ray tube trace element program						
V	244.0	±4.4	270.9	±3.4	254.2	±1.6
Cr	305.2	±1.7	133.2	±0.8	374.2	±4.0
Ba	37.5	±0.8	166.9	±3.2	1106.0	±12.2
La	5.8	±0.9	11.8	±1.0	85.3	±1.3
Ce	12.8	±1.9	23.8	±1.3	151.4	±1.4
Nd	10.7	±1.0	12.7	±1.8	64.2	±0.4

Appendix 2.0 (cont.) ***analytical techniques***

Microprobe analysis

Polished thin sections, with a < 1 μm finish were made from core chip samples. These were carbon coated by vacuum evaporation and mineral analyses performed using a JEOL 8600S wave-length dispersive (WD) electron microprobe with three automated crystal spectrometers or a LINK 860 Series, energy-dispersive (ED) system.

WD analysis

For the WD system the electron beam was operated at an accelerating voltage of 15kV and probe current of 30 nA with a probe diameter of 5 μm. This was increased to 10-15 μm to minimise damage when analysing beam-sensitive large feldspar crystals. X-ray intensities were standardised against a range of pure elements, synthetic oxides and natural minerals. Dead-time and background corrections were applied to X-ray intensities followed by ZAF correction to the measured oxide concentrations. Software employed was for the routine quantitative analysis of the common silicate minerals by analysis of the elements S1, Ti, Al, Cr, Mn, Mg, Ca, Na, K, Ni and subsequent recalculation to oxide weight percent, White *et., al.*, (1983). Detection limits for each of these elements are variable, depending on background interference, but range between 0.03 wt% (Na - As) and 0.05 wt%(Ge-Bi). Precision is also variable for the same reasons as detection limits. Values from 100% relative at the lower detection limit to 1% relative at higher concentrations (>40%). Precision may be computed from count rate data for each individual analysis.

ED analysis

Ed system was employed for analysis the beam sensitive clay minerals and mica . The system employed was operated using a 15kV accelerating voltage and 3 nA probe current. A 5 micron beam was used, and focused for small grains. Analysis of similar silicate minerals using the same elements as the WD system was performed on LINK ZAF4-FLS+ software. Detection limits are genrally higher than the WD system, 0.2 % for elements except Na (0.5%). For analytical details of the technique refer to Dunham and Wilkinson, (1978).

SEM analysis

SEM was employed to observe the morphology of sandstones and mudstones. A Hitachi 520 scanning electron microscope coupled to a LINK AN1000 energy-dispersive (EDX) detector, were deployed, using vacum coated (gold) core chippings; refer to Goldstein et., al., (1981).

Thin section analysis

Petrographic modal analysis were made on standard thin sections following Chayes (1956). An average of 400 - 600 points being counted per 1.5 cm^2 using a Swift integrating stage and counter (Nb. for 211/18a-a33 used contractors 300 points). Modal analyses were attempted on sandstone samples only; mudstones being much to fine.

Mineralog analysis

Modal estimates were also obtained by Fourier Transform infra-red spectroscopy (FTIR) for some Thistle samples, see Appendix 4.0. Mineralog is a trademark of Core Labs Inc. Samples were reduced to 2μm. The principle of measurement being that molecular vibrations are measured. The frequency of vibration is a function of bond strengh, atomic mass and radius; and crystal structure and FTIR is sensitive to "short range order", whereas XRD is sensitive to "long range order". Accuracy is quoted as similar to XRD (*cf.* approx 5%) and bulk samples can be used to distinguish clay phases, although illite can not be distinguished from mica. Refer to Harville and Hamish 1990.

Leco Analysis (C & S)

Accurate analysis of C and S (to 3 decimal places) were dertermined by a Leco Anayser from powders prepared for XRF analyis.

Appendix 3
XRD mineralogy for the Thistle211/18a-a33 reservoir section

Sample	kaolinite	quartz	K-feldspar	albite	muscovite	siderite	pyrite	rutile	chlorite	Total
10452	4.11	83.64	10.12	1.81	0	0	0	0	0	99.68
10456	4.2	79.19	10.74	3.5	0	0	0	0	0	97.63
10458	0	0	0	0	0	0	0	0	0	0
10469	0	0	0	0	0	0	0	0	0	0
10470	54.4	26.75	4.18	3.5	6.98	2.16	0	1.08	0	99.04
10471	64.39	20.39	5.48	2.13	5.17	3.06	0	2.02	1	102.9
10472	64.05	20.16	4.56	2.19	5.27	1.48	0	2.32	1	100.04
10473	73.28	12.25	1.89	7.75	2.71	2.08	0	2.16	1	101.94
10475	5.61	80	8.93	3.76	0	0	0	0	0	98.3
10479	7.12	78.47	8.99	4.13	0	0	0	0.37	0	99.09
10482	5.38	74.38	9.44	8.8	0	0	0	0	0	98
10483	11	72.35	10.08	4.78	0	0	0	0.51	0	98.73
10484	6.77	79.18	8.75	5.18	0	0	0	0.27	0	100.15
10485	7.86	70.58	11.38	5.42	5.63	0.64	0	0	0	101.92
10486	44.91	28.57	9.5	3.65	4.79	5.62	0	3.44	0	100.47
10487	8.29	70.99	8.96	4.45	0.1	0	0	0	0	92.8
10487	8.68	67.18	9.33	5.11	0.2	0	0	0	0	90.51
10488	6.83	78.13	9.05	2.36	0	0	0	0	0	96.87
10490	6.67	77.48	9.95	3.93	0	0	0	0	0	98.03
10491	8.28	72.31	8.6	4.06	0.58	0	0.52	0	0	94.34
10493	7.56	77.8	8.28	3.84	0.2	0	0	0	0	97.67
10494	25.49	51.13	9.17	4.5	1.44	1.38	0	1.16	0	94.28
10496	65.95	28.32	3.79	0.5	0.46	0	0	1.47	1	100.27
10497	12.77	78.93	6.09	0	0.5	0	0.96	0	0	99.24
10498	9.67	82.9	5.92	0.33	0	0	0.96	0.47	0	100.25
10499	4.85	84.51	8.17	1.49	0	0	0	0	0	99.02
10500	2.85	84.19	8.05	1.65	0	0	0	0	0	96.73
10501	5.14	81.57	8.32	2.21	0.4	0	0	0	0	97.63
10506	10.52	75.96	8.57	3.13	0.4	0	0	0	0	98.58
10507	13.17	70.62	7.57	3.59	0.36	0	0	0.27	0	95.58
10508	11.05	76.36	8.35	3.24	0.4	0	0	0	0	99.4
10511	8.08	77.65	8.62	3.12	0.39	0	0	0	0	97.86
10512	11.67	75.53	8.37	3.67	0.4	0	0	0	0	99.64
10513	11.65	76.34	6.63	3.36	0	0	0	0	0	98
10514	5.45	82.51	11.26	3.76	0.39	0	0	0	0	103.38
10515	16.62	68.28	12.11	3.77	0.61	0	0	1.36	0	102.74
10516	8.24	78.81	9.33	3.01	0.41	0.72	0	0.59	0	101.11
10517	8.53	74.48	7.28	3.91	0.2	0.85	0	0	0	95.24
10518	7.02	74.93	12.06	2.84	0.42	0.81	0	0.49	0	98.57
10526	9.34	73.58	9.12	3.07	0	0.31	0	0.27	0	95.69
10530	6.26	75.13	9.73	7.13	0	0	0	0.26	0	98.52
10536	6.94	75.13	12.32	3.53	1.16	0	0	0	0	99.08
10540	6.59	73.07	15.11	5.54	0.39	0	0	0	0	100.69
10542	6.36	78.22	13.23	4.42	1.2	0	0	0	0	103.43
10543	7.49	69.14	16.72	6.69	1.96	0	0	0	0	101.99
10544	6.9	68.74	17.36	4.94	1.25	0	0	0	0	99.19
10545	7.87	61.33	23.08	6.14	1.88	0.24	0	0	0	100.54
10561	17.47	54.59	13.98	7.34	3.8	0	0	0	0	97.18
10562	13.89	55.83	14.72	7.53	2.88	0	0	0.87	0	95.72
10564	13.32	58.84	14	7.27	3.85	0.88	0	0	0	98.15
10566	15.87	55.15	18.48	8.51	3.31	0.83	0	0	0	102.17
10568	10.95	51.75	19.99	10.45	3.03	1.17	0	0	0	97.33
10570	17.91	52.89	18.7	6.52	2.9	1.01	0	0	0	99.94
10574	19.94	43.08	19.61	8.42	5.19	1.38	0	0	0	97.61
10576	15.55	48.22	15.34	8.9	3.71	1.1	0	0	0	102.94
10578	24.96	40.06	18.33	7.16	5.14	1.79	0	0	0	97.45
10580	16.04	45.71	18.26	7.85	2.36	1.22	0	0	0	91.44
10582	26.5	44.25	17.33	8.84	4.59	1.13	0	0	0	102.63

Appendix 4.0 Thin section point count data and mineralog modal data for 211/18a-a33 reservoir section (wt%)

Thin section analysis (converted to wt%)

ID/DEP	Qtz wt%	Fsp wt%	Musc wt%	Bio wt%	OPaq wt%	lay-m wt%	ement wt%	hm wt%
455	89.85	10.15	0	0	0	0	0	0
480	76.17	5.17	0	0	7.95	9.01	0	1.69
490	75.21	7.42	8.07	0.5	0.83	7.48	0	0.48
492	71.69	15.41	0	0	3.95	8.95	0	0
499	66.49	7.3	0	0	1.7	24.17	0	0.35
501	71.67	9.91	0	0	0	16.47	0	1.94
502	64.39	8.08	1.25	2.58	5.32	18.38	0	0
520	61.15	4.63	0	0	1.77	13.84	12.28	6.13
540	60.59	19.83	1.75	0	0.29	12.42	4.72	0.33
541	59.12	6.35	0	0	4.88	23.2	4.71	1.67
561	43.89	17.49	8.35	9.39	5.04	9.04	4.25	2.48
567	52.72	6.23	7.92	6.96	0	22.75	1.57	1.83
580	44.85	12	13.27	13.6	1.77	13.58	0.73	0.17

Mineralog analysis (wt%)

sample	kaolinite	quartz	K-feldspar	albite	muscovite	siderite	pyrite	rutile	chlorite	Total
10473/m1	42	9	0	2	40	1	0	0	6	100
10482/m1	5	72	10	7	6	0	0	0	0	100
10486/m1	30	21	5	5	26	10	0	0	3	100
10491/m1	4	73	9	7	4	0	0	0	3	100
10545/m1	6	58	15	10	10	1	0	0	0	100
10574/m1	13	44	12	10	15	2	0	0	4	100
repeat analysis										
10473/m2	38	9	0	3	47	3	0	0	0	100
10482/m2	0	69	6	12	12	1	0	0	0	100
10486/m2	29	22	4	5	30	10	0	0	0	100
10491/m2	0	74	9	7	10	0	0	0	0	100
10545/m2	6	58	15	10	10	1	0	0	0	100
10574/m2	11	46	12	10	18	3	0	0	0	100

Appendix 4.1 Mineral compositions used in modelling the Thistle 211/18a-a33 reservoir section (wt%)

Mineral	SiO2	TiO2	Al2O3	Fe2O3	MnO	MgO	CaO	Na2O	K2O	S	total
Specific compositions											
a33-albite	68.14	0	19.64	0	0	0	0.55	11.18	0.54	0	100.1
a33-ksp	64.18	0	18.23	0	0	0	0	1.01	15.52	0	98.94
a33-kaolinite	45.94	0.2	36.83	0.8	0	0.22	0	0	0.23	0	84.22
a33"clay"	45.71	0.25	33.96	2.59	0	1.43	0.16	0	0.9	0	85
a33-muscovite	47.1	0.74	29.68	4.17	0	1.76	0	0.34	10.32	0	94.11
a33-biotite	35.51	3.44	16.08	23.12	70	8.91	0	0.14	9	0	166.2
a33-mica	41.21	2.09	22.88	13.65	0	5.4	0.13	0.5	9.67	0	95.53
a33-siderite	0	0.13	0	54.66	0.3	5.21	5.28	0	0	0	65.58
a33-quartz	98.68	0	0	0	0	0	0.21	0.28	0	0	99.17
Et-albite	68.58	0	19.64	0.06	0	0	0.43	11.08	0.82	0	100.6
Et-kaolinite	46.19	0.25	36.68	0.08	0	0	0	0.08	0.22	0	83.5
Et-k-feldspar	64.22	0	18.27	0	0	0	0	1.01	15.52	0	99.02
Et-muscovite	45.49	0.61	30.44	3.97	0	1.45	0.05	0.23	9.19	0	91.43
Ran-albite	67.47	0	19.62	0.09	0	0	0.73	11.32	0.13	0	99.36
Ran-kaolinite	45.45	0.09	35.77	2.24	0	0.62	0	0	0.24	0	84.41
Ran-k-feldspar	64.07	0	18.12	0.06	0	0	0	1.02	15.51	0	98.78
Ran-muscovite	47.22	0.79	29.4	4.24	0	1.88	0	0.38	10.52	0	94.43
Theoretical compositions											
siderite	0	0	0	66.69	2.86	0.2	0.08	0	0	0	69.83
siderite-1	0	0	0	67.88	1.12	0.13	0.1	0	0	0	69.23
rutile	0	100	0	0	0	0	0	0	0	0	100
quartz	100	0	0	0	0	0	0	0	0	0	100
rutile	0	100	0	0	0	0	0	0	0	0	100
calcite	0	0	0	0	0	0	56.03	0	0	0	
dolomite	0	0	0	0	0	30.41	21.86	0	0	0	
pyrite	0	0	0	67.24	0	0	0	0	0	53	
Mg - chlorite	27.64	0.22	22.48	13.46	0	24.32	0	0.17	0.06	0	88.35
Fe - chlorite	25.62	0.88	21.19	27.83	0	15.28	0.16	0	0	0	90.96
illite-theoretical	56.91	0.81	18.5	5.28	0	2.07	1.59	0.43	5.1	0	90.69
Fithian-illite	51.74	0.68	23.98	5.78	0	1.99	0.97	0.36	5.59	0	91.09
"global" illite	49.78	0.42	26.35	4.98	0	2.75	0.32	0.25	7.02	0	91.87
High -ill/smectite	47.26	0	31.06	2.49	0	2.26	0	0	10.7	0	93.77
Low ill/smectite	53.65	0	22.22	3.1	0	3.89	1.23	0	3.95	0	88.04
smectite-1	53.52	0	18.89	5.08	0	3.9	1.52	0.54	0.51	0	83.96
smectite -2	59.27	0	22.28	2.9	0	4.72	1.79	0.51	0	0	91.47

Notes.

prefix 'a33' - average value of compositions derived from microprobe analysis of minerals from the section.

prefix 'Et' - average value of compositions derived from microprobe analysis of minerals from the Etive Formation

prefix 'Ran' - average value of compositions derived from microprobe analysis of minerals from the Rannoch Formation

All compositions include volatile fractions.

Sample	SiO2	TiO2	Al2O3	Fe2O3	MnO	MgO	CaO	Na2O	K2O	P2O5	LOI	Total	C	S	Nb	Zr	Y	Sr	Rb	Th	Ga	Zn	Ni	Tl	Sc	V	Cr	Co	Cu	Ba	La	Ce	Nd
10452	86.85	0.58	6.23	0.62	0.01	0.15	0.19	0.86	2.33	0.03	2.2	99.86	1.3	0.034	6.2	261.1	7.3	76.8	34.8	0.6	3.1	-0.6	2.5	0.463	3	17.4	37.9	144	30.3	836.7	4	9.6	1
10456	88.75	0.36	4.99	0.7	0.02	0.12	0.12	0.81	1.9	0.02	2.27	100.07	1.15	0.04	7.9	163.5	9	88.8	36.1	4.3	6.9	4.2	10.8	0.387	3.1	20.9	20.5	221.8	2.2	1331.3	13.1	7.2	0
10470	56.92	1.52	20.45	5.61	0.08	1.3	0.25	0.74	2.77	0.13	11.16	97.86	3.556	0.03	38.2	316.7	40.5	172.2	112.9	15	23	141.8	70.6	1.385	17.1	148.5	134.7	39.5	23	545.8	35.5	94.1	35.1
10471	53.75	1.58	21.3	6.72	0.1	1.38	0.34	0.5	2.71	0.17	12.73	98.33	3.1	0.66	36.5	251.9	48.6	181.1	116.2	13.8	27.6	141.3	100.2	1.346	17.6	175.1	152.9	42.5	27.3	477.4	44.8	122.4	50.1
10472	54.58	1.48	22.89	5.6	0.06	1.37	0.28	0.76	2.87	0.16	10.9	98.56	3.1	0.068	35.2	236.1	45.7	193.2	130.5	14	28.3	136.3	81.3	1.319	17.4	182.8	147.8	32.9	27.4	495.2	43.1	108.4	41.9
10473	49.67	1.6	25.5	5.6	0.1	1.42	0.29	0.4	2.82	0.16	13.85	97.44	4.64	0.052	35.6	206.3	45.2	219.2	143.7	17.8	38.5	124.7	92.3	1.369	19.6	202	162	29.8	36.3	493.4	57.4	117.6	46.7
10475	88.81	0.85	4.85	0.58	0.02	0.14	0.15	0.74	1.61	0.26	2.27	99.2	1.25	0.109	11.5	454.8	12.5	106.8	31.8	3.8	3.1	19.6	4.7	0.859	1.6	46.3	46.1	97.3	3.7	2473.4	9.9	2.6	0
10478	88.39	0.91	4.43	0.68	0.01	0.18	0.14	0.68	1.6	0.03	2.96	98.11	1.129	0.082	10.5	494.4	13.8	94.1	32.7	3.5	4	24.7	8.9	0.873	3.4	52.2	49.2	126.6	22.9	1880.2	15	30.9	11.7
10479	87.9	0.48	5.08	0.46	0.01	0.13	0.13	0.98	1.68	0.03	3.23	100.15	1.56	0.118	11.8	494.9	16.9	115.1	31.2	1.5	3.2	20.1	8.4	0.976	3.8	55.3	61.1	115	32.7	2919.9	15.1	14.7	1.1
10482	87.39	0.93	4.87	0.62	0.02	0.19	0.19	0.93	1.56	0.03	3.35	98.75	1.54	0.067	8.3	164.3	14.6	95.2	32.4	0.3	2.9	18.5	0.7	0.524	5.7	51.8	33.2	90.2	33.5	1695.4	16.1	23.7	11.4
10483	88.32	1.09	4.73	0.61	0.01	0.19	0.19	0.79	1.47	0.03	2.6	98.06	1	0.105	13.6	396.2	17.4	107	28.2	2	4.4	15.5	-1.2	1.116	8.7	57.9	64.2	91.1	15.5	2833.9	16.8	11.7	0.4
10484	88.54	0.7	4.02	0.83	0.03	0.16	0.17	0.74	1.43	0.02	3.45	99.56	1.61	0.078	10.6	286.7	14.3	100.1	29.2	2.9	3	13	1.6	0.785	3.6	45.3	41.3	101.9	20.6	2377.3	13.5	14	0.4
10485	85.47	1	5.18	1.7	0.05	0.27	0.19	0.78	1.72	0.04	3.7	98.83	1.45	0.111	12.7	409.6	18.7	107.9	33.2	0.2	5.5	26.5	5.4	1.007	8.5	69.2	79.2	62.9	15.4	2276	14	11.6	0
10486.2	57.92	2.06	16.56	7.68	0.2	1.08	0.41	0.76	2.67	0.11	11.49	97.23	3.85	0.018	30.2	790.9	53.6	179.3	91.8	15.1	28.8	85.5	56.8	1.811	29.6	189	20.9	37.3	20.3	801.1	62.7	139.2	65.9
10486.6	87.21	1.2	4.37	0.5	0.01	0.14	0.1	1.39	1.47	0.01	3.69	98.58	0.5	0.116	16	669.1	19.5	83.6	29.1	0.5	4.2	11.6	16.1	1.288	5.8	56.7	93.4	85.9	7.7	1907	12.6	17	7.3
10487	88.16	0.74	4.97	0.45	0.01	0.13	0.16	0.82	1.54	0.03	3.06	98.98	1.36	0.105	9.3	336	13.4	108	29.1	-0.4	1.8	17	7.9	0.733	6.4	33.3	43.9	128.8	16.3	3271.9	11.6	0	0
10488	88.22	0.62	4.11	0.81	0.03	0.18	0.13	0.79	1.49	0.18	3.7	98.74	1.65	0.092	8.1	279.2	11.6	89.1	29.4	2.5	1.9	16.2	35.1	0.648	5.6	31.3	48.7	112.7	27.3	2084.7	11.1	7	0
10490	88.97	0.65	4.17	0.46	0.02	0.17	0.11	1.01	1.37	0.02	3.17	100.24	1.49	0.071																			
10491	87.89	0.73	4.14	0.87	0.02	0.14	0.15	0.8	1.36	0.02	4.02	99.81	1.69	0.328	10	271.4	11.3	86.6	28.1	1.1	2.7	14.4	8.6	0.756	2.2	42.6	51.7	104.2	6.1	2366.7	8.4	6.9	0
10493	86.71	0.83	4.46	1.24	0.04	0.22	0.19	0.87	1.45	0.02	4.13	99.69	1.49	0.115	12.3	376	15.5	91.2	28.3	2.4	2	20.1	2	0.845	4.5	49.1	59.9	119.5	15.8	2251.1	12.1	2.8	0
10494	73.33	1.21	11.22	3.68	0.08	0.6	0.23	0.71	1.78	0.04	7.65	99.8	2.97	0.137	19.4	623.1	31.3	119.1	50.1	5.1	16.9	77.2	38.1	1.259	18.7	97.8	114.3	45.8	16.1	1430.8	35.1	69.3	30.8
10496	52.89	1.36	24.41	3.69	0.02	0.91	0.17	0.59	2.13	0.06	15.54	97.27	6.2	0.067	24.6	251	54.3	177.8	84.9	17.5	48.4	112.7	96.2	1.237	6.4	76.4	99.1	65.7	7.8	1094.8	18	38.3	18.6
10497	73.08	1.65	7.31	2.14	0.02	0.2	0.11	0.37	1.18	0.02	15.79	97.63	10.04	0.973	24.2	532.8	50.4	71.1	24.2	10	15.6	33.8	104.1	1.263	25.9	157.1	154.5	37.4	30.8	618.7	55.6	113.5	55.9
10498	82.97	1.02	1.88	5.35	0.01	0.12	0.12	0.36	0.63	0.02	8.32	101.5	3.96	4.08	13.6	529.5	21	50.4	10.8	4.8	3.3	12.5	54.6	1.64	20.5	113.2	89	185.8	8.2	793.7	31.3	65.7	33.8
10499	83.68	0.49	7.28	1.38	0.02	0.38	0.14	0.83	3.01	0.03	2.79	98.64	1.54	0.113	14.9	631.8	18.4	95.1	21.3	0.1	2.5	2.5	9.5	1.331	10.9	51.8	55.7	169.5	5.7	2911.5	12.4	10.6	0
10500	89.11	1.12	3.76	0.39	0.01	0.12	0.15	0.63	1.46	0.02	3.23	98.7	1.66	0.077	15.1	540.6	17.6	83	30	3.4	3.5	13.9	0.9	1.172	0.8	43	68.1	154.5	11.1	2153.1	16	23.8	6.9
10501	87.19	1.12	5.16	0.74	0.02	0.19	0.16	0.47	1.71	0.02	3.29	98.56	1.41	0.098	3.29	14.6	476.5	19	96.9	39	3.4	9.3	25.4	1.207	7.8	60.8	58.9	101.7	10.2	1993.5	19.8	26.9	9.6
10506	87.6	0.84	5.38	0.99	0.02	0.19	0.3	0.65	1.3	0.02	2.74	99.23	0.82	0.101	11.4	423.7	20.7	102.1	25	3.4	6.6	29.8	4.2	0.894	6.1	70.5	56	102.3	44.1	2818.9	31.5	44.4	22
10507	74.39	1.07	4.99	1.48	0.03	0.19	0.32	0.56	1.2	0.03	18.47	98.67	0.96	0.145	3.46	16.1	512.3	23.3	140.3	26.3	3.2	6.4	23.8	1.303	5.9	82.1	110	118.8	24.7	4721.2	23.9	15	0
10508	87.61	1.01	5.17	0.76	0.02	0.2	0.26	0.63	1.49	0.03	2.87	98.74	1.22	0.14	3.35	15.5	433.6	18.6	111.9	28	1.8	6.7	15.9	1.052	1.2	66.6	74.4	115.1	15.1	3032.6	18.6	17.9	3.6
10511	89.74	0.4	3.64	0.68	0.01	0.22	0.18	0.74	1.53	0.02	2.9	98.72	1.27	0.11	3.24	5.4	151.5	12.4	107.9	28.8	3.4	5	12.1	0.39	4.1	33.7	24.9	131.2	23.4	2809.1	18.5	14.2	0.8
10512	86.48	1.1	5.64	0.93	0.03	0.2	0.23	0.75	1.47	0.05	3.23	100.17	1.14	0.939	3.29	15.5	387.7	29.6	92.6	27.2	3.2	7	33.4	1.18	14.7	83.1	74.4	102.3	27.5	2103.5	50.4	95.1	48.8
10513	85.17	1.73	5.84	1.5	0.05	0.28	0.33	0.64	1.32	0.036	3.17	98.8	1.02	0.11	3.6	22.2	935.5	39	94.5	25.9	4.5	8.3	31.5	1.828	15.4	98.1	102.7	95.2	18.6	2348.2	45.5	88.7	39.8
10514	90.09	0.37	3.91	0.56	0.02	0.15	0.17	0.58	1.57	0.02	2.63	100.33	0.99	0.336	3.56	29.8	783.7	41.5	87.4	26.1	6.1	9.8	39.8	0.394	1.9	38.3	44.3	137.3	62.2	1975.5	16.6	14.4	4.8
10515	87.14	0.04	4.52	0.28	0.01	0.54	2.18	0.33	1.64	0.04	3.39	101.36	1.05	0.078	3.21	7.4	174.9	11.7	89.1	29.9	1.1	5.7	11.6	2.418	18.1	120.3	135.9	120.2	12.8	1449	37.9	80.2	40.3
10516	86.68	1.14	5.05	1.59	0.06	0.28	0.32	0.69	1.39	0.33	2.82	98.6	0.89	0.122	3.57	15.9	738.4	27.4	101.4	25	3	7	27	1.171	10.9	72.3	98.4	130.8	10.3	2487.6	20.4	36.4	11
10517	87.08	0.74	5.28	0.79	0.02	0.19	0.27	1.11	1.57	0.03	2.98	99.55	1.04	0.095	3.62	12	693.5	24.7	73.2	23.5	6	6.5	17.5	0.918	15.4	57.9	93.1	151.5	44.8	1558.5	17.6	34.9	14.1
10518	85.4	1.21	4.29	1.99	0.07	0.42	0.39	1.62	1.23	0.05	3.44	99.15	1.04	0.095	3.63	15.4	862.4	26.4	78.6	21.5	3.6	6.8	21.2	1.15	8.8	73.4	142.3	106.9	16.3	1851	20	41.8	14.2
10526	87.29	1.17	4.64	0.93	0.03	0.19	0.28	0.84	1.41	0.03	3.25	99.2	1.18	0.12	3.46	14.9	749.9	19.2	88.2	26.1	3.8	6.3	20.6	1.201	9	57.5	66.3	128.9	27.3	2207.9	20.5	27.6	9.5
10530	88.49	0.59	4.2	0.77	0.02	0.17	0.29	0.61	1.52	0.02	3.44	99.64	1.33	0.108	3.5	8.8	232.1	12.6	132.6	29.4	2.3	4.4	7.9	0.611	4.7	33.3	36	218.2	2.7	4054.5	8.8	0	0
10536	87.49	0.28	4.53	0.73	0.01	0.26	0.15	0.68	2.28	0.02	3.6	97.2	2.229	0.149	3.36	6.7	78.5	9.4	123.1	44.9	-1.1	5.2	6.2	0.278	0	28.7	22.5	188.5	1.6	2649	8	0	0
10540	88.13	0.44	4.45	0.34	0.01	0.17	0.07	1.07	1.88	0.02	3.63	99.39	0.56	0.089	3.28	10.9	167.1	13.3	116.1	46.7	1.8	7	10.3	0.634	1.9	44.9	143.4	98.9	1.9	2310.7	10.5	0.2	0
10542	88.11	0.3	5.63	0.55	0.01	0.17	0.1	1.21	2.27	0.03	1.66	100.45	0.51	0.079	3.23	7.3	88.8	9.5	98.6	46.1	2.8	7	9.2	0.33	5.3	23.3	21.7	79.5	23.8	1214.5	9.7	8.1	3.5
10543	84.99	0.43	7.42	0.84	0.02	0.23	0.12	1.1	2.81	0.03	2.06	99.99	0.34	0.026	3.33	11.8	128.9	11.9	115.1	61	3.5	8.4	14.2	0.474	7.2	47	29.3	78.9	9.8	1433.2	13.8	12.2	2.1
10544	86.63	0.37	6.66	0.62	0.01	0.17	0.11	0.9	2.76	0.03	1.78	100.16	0.56	0.096	3.3	10.2	146.6	8.5	116.9	58.7	1.6	7.1	6.5	0.403	2.9	24.2	26	108.9	11.8	1651.9	9.6	2.4	0
10545	82.5	0.46	8.33	1.33	0	0.33	0.13	1.33	3.1	0.03	2.47	98.7	0.471	0.085	3.74	20.5	817.8	21.9	107.4	84.5	6.8	13	56.6	0.977	6.7	46.4	42.9	218.7	12.1	1275.3	23.1	7.2	14.8
10561	75.31	1.14	10.68	2.69	0.06	0.69	0.25	1.15	3.03	0.06	5.12	98.9	3.21	0.019																			
10562	76.15	1.29	10.09	2.39	0.05	0.63	0.25	1.51	2.91	0.05	4.86	98.71	1.78	0.018	3.7	20.5	1162.6	23.6	104.9	77.8	7.9	12.6	57.5	1.388	7.8	76.6	92.5	59.9	6.3	1123.6	20.2	39.4	19.6
10564	78.86	0.82	9.07	2.23	0.04	0.52	0.24	1.63	2.85	0.05	3.81	99.48	1.93	0.033	3.54	16.3	340.8	11.1	98.3	75.4	4.2	11	42.1	0.931	11.4	58.1	49.9	47.8	5.1	1159.7	12.4	21.7	12
10566	78.36	0.81	9.17	2.27	0.03	0.7	0.26	1.35	3.12	0.06	4.29	98.69	0.48	0.079	3.54	16.4	306.2	14.7	105.7	80.9	2.3	11.6	45.3	0.812	9.3	59.9	93	74.3	5.2	1098.5	14.7	21	13.5
10568	72.3	0.74	11.56	3.92	0.07	0.91	0.4	1.24	3.39	0.06	5.76	100.17	0.49	0.015	3.99	16.3	180.4	16	133.8	93	2.2	12.5	59.3	0.761	6.5	60.5	130.7	72.1	9.3	2257.8	15.7	10.3	4.8
10570	71.82	0.88	11.5	3.83	0.05	1.05	0.42	1.79	3.63	0.07	6.15	97.92	3.55	0.124																			
10574	68.27	0.8	14.09	4.64	0.07	1.1	0.45	1.2	3.8	0.08	6.43	98.61	0.56	0.006	4.11	18.4	163.9	15.8	131.6	112.4	3.2	17.6	75.3	0.8.8	15.8	59.5	51.5	54.8	14.1	1526.8	12.8	15.2	11.3
10576	71.91	0.74	11.18	4.04	0	1.07	0.45	1.41	3.47	0.07	5.82	98.83	2.97	0.048	3.98	16.2	103	14.9	119.8	101.3	6.7	15.1	63.8	0.719	10.1	56.3	40.3	72.1	10.3	1388.9	11.8		
10578	67.33	0.77	12.83	5.53	0.07	1.38	0.58	0.93	3.79	0.08	7.1	98.82	2.4	0.028	4.29	18	80.4	15.5	119.6	119.1	4.2	18.9	79.6	0.724	9.6	64.7	55.8	86.8	12.7	1037	12.7		
10580	70.01	0.69	11.59	4.23	0.06	1.07	0.44	2.47	3.67	0.07	6.03	99.64	1.68	0.026	4.39	18.6	77.6	13.3	129.1	108.3	2.5	16.3	64.7	0.679	7.2	61.5	44.2	122.5	13	1117.1	11.7		
10582	71.54	0.65	12.34	4.11	0.06	0.9	0.43	1.25	3.58	0.06	5.32	99.2	1.75	0.053	4.05	15.7	74	13.4	121.1	103.4	2.1	15.5	58.6	0.643	8.3	59.1	38	114.1	11.4	1169.4	13.4		

Appendix 4.2 XRF major and trace element chemistry for Thistle section 211/18a-a33. Major elements in Wt%, trace elements in ppm.
C and S determined by a Leco Analyser. LOI is included in analysis but it is also included here as a seperate column for reference.

Appendix 4.3 Electron microprobe analyses from the Brent Group

Prefix 211/ - Sample from 211/18a-a33

Prefix B41 & B26 - Sample from the Statfjord holes -B26 and- B41

Suffix '*' analysis using energy dispersive probe (ED) probe system

albite

sample	SiO2	TiO2	Al2O3	Fe2O3	MnO	MgO	CaO	Na2O	K2O	total
B26/420	68.25	0.02	19.42	0.07	0.01	0.01	0.70	11.27	0.20	99.98
211/540/1	70.72	0.01	19.44	0.08	0.01	0.00	0.02	11.77	0.21	102.32
211/540/2	70.13	0.01	19.48	0.05	0.03	0.00	0.20	11.71	0.20	101.84
211/485.8	70.60	0.04	19.50	0.07	0.00	0.00	0.06	11.98	0.07	102.38
211/485.8/2	66.85	0.04	21.71	0.18	0.05	0.00	2.51	10.13	0.19	101.68
211/500	67.74	0.02	19.37	0.06	0.02	0.00	0.11	11.69	0.14	99.18
211/580	66.66	0.04	20.82	0.19	0.03	0.00	2.26	10.59	0.08	99.67
211/580/2	68.13	0.02	19.26	0.04	0.02	0.01	0.25	11.58	0.13	99.37
211/580/3	64.92	0.01	21.52	0.06	0.01	0.00	2.70	10.09	0.20	99.54
211/580/4	68.24	0.01	19.21	0.04	0.03	0.00	0.13	11.60	0.10	99.37
211/580/5	68.19	0.01	19.20	0.09	0.03	0.00	0.14	11.63	0.17	99.47
211/580/6	68.26	0.02	18.92	0.06	0.01	0.00	0.09	11.78	0.10	99.25
211/580/7	67.24	0.02	18.75	0.22	0.03	0.00	0.12	11.63	0.16	98.18
211/580/8	68.14	0.22	19.31	0.07	0.02	0.00	0.20	11.65	0.09	99.75
211/512	68.77	0.02	19.39	0.01	0.03	0.00	0.12	11.84	0.20	100.41
211/512/2	69.01	0.02	19.57	0.03	0.03	0.00	0.17	11.83	0.10	100.77
211/512/3	67.04	0.01	18.81	0.02	0.03	0.00	0.13	11.47	0.12	97.64
211/512/4	67.83	0.01	19.57	0.01	0.01	0.01	0.50	11.56	0.09	99.61
b26/575*	68.44	0.00	19.26	0.00	0.00	0.00	0.00	9.15	0.00	96.85
211/512per	66.65	0.01	19.68	0.14	0.03	0.00	0.61	8.54	4.13	99.84
211/512per	66.89	0.01	19.40	0.04	0.02	0.00	0.63	8.85	4.18	100.08

kaolinite

211/500/1	46.54	0.00	37.44	0.00	0.00	0.00	0.00	0.00	0.00	83.99
211/500/2	45.96	0.00	36.48	0.00	0.00	0.00	0.00	0.00	0.00	82.65
211/500/3	44.89	0.53	37.22	0.00	0.00	0.00	0.00	0.53	0.38	83.60
211/500/4	47.97	0.51	38.51	0.00	0.00	0.00	0.00	0.55	0.21	87.54
211/500/5	47.49	0.00	38.01	0.00	0.00	0.00	0.00	0.00	0.23	85.74
211/500/6	47.40	0.00	37.17	0.00	0.00	0.00	0.00	0.00	0.00	84.56
211/500/7	48.18	0.00	38.32	0.00	0.00	0.00	0.23	0.00	0.23	87.50
211/500/8	46.31	3.39	35.71	0.00	0.00	0.00	0.00	0.00	0.00	85.46
211/500/9	48.52	0.00	37.15	0.00	0.00	0.00	0.00	0.00	0.34	86.01
211/500/10	46.15	0.00	36.30	0.00	0.00	0.00	0.00	0.00	0.00	82.45
b26/575	49.56	0.00	38.08	0.00	0.00	0.00	0.00	0.00	0.55	88.18
B41/485	42.17	0.78	30.85	5.52	0.00	2.13	0.00	0.00	1.77	82.67
B41/485/2	43.41	0.31	33.85	3.16	0.00	1.02	0.00	0.00	0.52	81.96
211/580/1	48.83	0.00	38.08	0.00	0.00	0.00	0.00	0.00	0.17	89.02
211/580/2	46.65	0.00	36.84	1.35	0.00	0.00	0.00	0.00	0.00	84.71
211/550	47.89	0.00	37.64	1.70	0.00	0.00	0.00	0.00	0.29	87.35
211/580/3	47.13	0.00	38.03	0.80	0.00	0.00	0.00	0.00	0.00	85.88
211/580/4	41.88	0.00	32.61	7.60	0.00	3.66	0.00	0.00	0.26	85.24
211/580/5	44.53	0.00	35.94	2.87	0.00	0.63	0.00	0.00	0.24	83.83
211/580/6	45.49	0.00	36.79	0.97	0.00	0.00	0.00	0.00	0.00	83.15
211/580/7	44.80	0.60	35.12	2.19	0.00	0.00	0.00	0.00	0.00	82.74
211/502	46.12	0.00	37.42	0.00	0.00	0.00	0.00	0.00	0.21	83.74
B26/404	47.69	0.03	37.61	0.02	0.03	0.00	0.01	0.12	0.33	85.87
B26/420	47.50	0.01	37.27	0.03	0.03	0.01	0.02	0.07	0.16	85.14
211/485.8	45.98	0.02	36.51	0.07	0.01	0.01	0.02	0.11	0.11	82.89
211/500/11	49.04	0.00	39.70	0.00	0.00	0.00	0.00	0.00	0.00	88.73
B41/485	45.00	0.00	35.70	1.54	0.00	0.90	0.09	0.00	0.25	83.23
B41/456	42.58	1.32	24.66	6.86	0.00	2.17	0.46	0.00	4.63	82.04

Kaolinite cont..

sample	SiO2	TiO2	Al2O3	Fe2O3	MnO	MgO	CaO	Na2O	K2O	total
B41/456/2	46.84	0.00	38.21	0.00	0.00	0.00	0.00	0.00	0.00	85.04
B41/456/3	46.20	0.00	35.91	0.68	0.00	0.66	0.00	0.00	1.72	84.33
B41/456/4*	46.3	0.0	35.3	0.6	0.0	0.0	0.0	0.0	0.0	82.08
B41/456/5*	46.9	0.0	36.4	1.3	0.0	0.7	0.0	0.0	0.5	85.67
B41/456/6*	47.5	0.0	35.3	1.9	0.0	1.4	0.0	0.0	1.7	87.63
B41/456/7*	46.0	0.8	32.2	2.4	0.0	2.1	0.0	0.0	2.7	85.98
B41/456/8*	47.4	0.0	36.2	0.7	0.0	1.0	0.0	0.0	1.7	86.96
B41/511*	44.8	0.0	37.1	1.4	0.0	1.6	0.0	0.0	0.0	84.73
B41/511/2*	46.5	0.0	38.5	0.0	0.0	0.6	0.0	0.0	0.3	85.93
B41/511/3*	43.9	0.0	36.5	1.2	0.0	0.8	0.0	0.0	0.0	82.31
b26/575*	47.2	0.0	36.8	0.0	0.0	0.0	0.0	0.0	0.6	84.66
b26/575/2*	47.0	0.0	37.7	0.0	0.0	0.0	0.0	0.0	0.8	85.63
b26/575/3*	45.2	0.0	35.4	0.5	0.0	0.0	0.0	0.0	1.1	82.12

K-feldspar

B26/406	60.71	0.02	17.65	0.08	0.02	0.00	0.05	0.95	18.49	98.00
B41/511	62.06	0.04	18.24	0.03	0.01	0.00	0.17	2.41	16.18	99.19
B26/409	61.14	0.03	17.50	0.03	0.03	0.00	0.03	0.72	19.27	98.77
B26/575	64.70	0.01	15.74	0.02	0.03	0.00	0.02	0.62	16.58	97.75
B26/575	60.59	0.05	17.31	0.03	0.03	0.00	0.01	0.59	19.28	97.96
B26/575	62.00	0.04	17.68	0.18	0.01	0.00	0.01	0.98	18.98	99.91
B26/575	61.75	0.01	17.64	0.22	0.03	0.00	0.09	1.38	17.86	98.99
B26/404	60.76	0.03	17.58	0.04	0.03	0.00	0.01	0.72	18.49	97.69
B26/404	64.44	0.03	18.06	0.06	0.03	0.00	0.01	1.44	16.05	100.14
B26/404	64.13	0.02	17.97	0.03	0.03	0.00	0.05	2.13	16.97	101.36
B26/420	60.87	0.13	17.34	0.11	0.03	0.00	0.00	0.64	18.32	97.48
B26/420	62.69	0.05	17.77	0.03	0.01	0.00	0.01	0.62	19.71	100.89
B26/437	59.79	0.18	26.47	2.83	0.02	0.59	0.05	0.90	8.33	98.89
211/540	65.33	0.01	18.56	0.04	0.04	0.00	0.01	0.97	14.96	99.93
211/540	64.23	0.02	18.23	0.05	0.03	0.00	0.06	0.95	15.58	99.20
211/540	64.10	0.02	18.05	0.01	0.02	0.00	0.01	1.10	14.97	98.28
211/540	64.12	0.02	18.08	0.02	0.05	0.00	0.01	1.04	15.21	98.59
211/540	64.35	0.07	18.10	0.01	0.00	0.00	0.01	0.64	15.79	99.01
211/540	63.43	0.01	17.93	0.10	0.01	0.00	0.04	1.25	14.86	97.67
211/540	64.51	0.01	17.89	0.02	0.01	0.00	0.01	0.61	16.15	99.25
211/540	63.75	0.02	18.11	0.14	0.01	0.00	0.01	1.13	14.87	98.07
211/540	64.07	0.04	18.27	0.10	0.03	0.00	0.01	0.92	15.30	98.77
211/560	64.09	0.01	18.08	0.03	0.02	0.00	0.01	0.76	15.78	98.78
211/540	64.73	0.01	18.27	0.13	0.00	0.00	0.00	0.37	16.77	100.30
211/540	62.83	0.00	18.79	0.01	0.01	0.00	0.03	0.83	15.36	97.90
211/540	65.23	0.01	18.65	0.01	0.03	0.00	0.01	3.10	13.21	100.32
211/500	63.85	0.01	18.42	0.02	0.03	0.00	0.01	0.71	16.26	99.36
211/580/1	64.07	0.19	18.05	0.04	0.01	0.00	0.00	0.97	15.70	98.95
211/580/2	64.58	0.06	18.42	0.14	0.02	0.00	0.16	2.18	13.80	99.39
211/580/3	63.91	0.02	18.02	0.00	0.00	0.00	0.01	1.26	15.40	98.68
211/580/2	63.54	0.04	18.19	0.02	0.01	0.00	0.01	0.54	16.47	98.86
211/580/3	64.15	0.01	18.04	0.03	0.00	0.00	0.01	0.83	16.07	99.15
211/512/1	64.68	0.03	18.06	0.01	0.02	0.00	0.01	0.56	16.43	99.83
211/512/2	64.75	0.00	18.12	0.09	0.01	0.00	0.01	0.75	16.32	100.08
211/512/3	64.71	0.03	18.43	0.07	0.00	0.00	0.16	2.02	14.06	99.50
211/512/4	64.58	0.04	18.41	0.03	0.01	0.00	0.07	1.89	14.43	99.59

K-feldspar cont..

sample	SiO2	TiO2	Al2O3	Fe2O3	MnO	MgO	CaO	Na2O	K2O	total
211/512/5	64.33	0.02	18.36	0.02	0.02	0.00	0.01	1.22	15.28	99.31
211/512/6	64.80	0.04	18.16	0.05	0.02	0.00	0.06	1.13	15.56	99.87
211/512/7	64.78	0.01	18.18	0.04	0.01	0.00	0.03	1.20	15.24	99.52
211/512/8	63.55	0.06	18.42	0.03	0.03	0.00	0.01	0.70	15.92	98.75
211/512/9	64.60	0.01	18.25	0.04	0.01	0.00	0.01	0.51	16.44	99.89
B41/456*	64.0	0.0	19.0	0.0	0.0	0.0	0.6	2.2	13.6	99.39
B41/456*	61.5	0.0	19.0	0.0	0.0	6.4	0.0	0.6	16.0	97.89
B41/456*	62.1	0.0	19.0	0.0	0.0	0.0	0.0	0.8	16.3	98.15
211/500*	65.6	0.0	18.6	0.0	0.0	0.0	0.0	0.0	15.9	100.01
211/502*	62.4	0.0	17.8	0.0	0.0	0.0	0.3	0.6	16.7	98.60

muscovite

B26/575	48.51	0.50	29.17	1.82	0.00	0.84	0.01	3.10	9.53	93.34
B26/437	47.79	0.83	27.80	5.72	0.04	1.92	0.01	0.36	12.79	96.73
B26/437/2	45.62	0.96	29.07	5.10	0.06	1.39	0.00	0.27	11.88	93.88
211/485.8	47.40	0.95	34.81	1.10	0.03	0.76	0.00	0.77	7.93	93.68
211/561	46.47	0.93	30.54	4.34	0.06	1.29	0.01	0.18	8.30	91.77
211/561/2	45.72	1.10	27.16	6.58	0.05	1.81	0.01	0.34	10.44	92.60
211/561/3	46.95	0.96	29.44	5.24	0.04	1.58	0.01	0.44	10.60	94.74
211/500*	44.7	0.1	32.0	4.1	0.0	1.0	0.4	0.0	10.7	93.45
211/500/3*	46.0	0.9	28.7	5.6	0.0	1.6	0.0	0.0	10.3	92.64
b26/575*	46.8	1.6	28.0	5.4	0.0	1.4	0.0	0.0	10.1	92.74
b26/575/2*	47.3	0.5	32.9	2.1	0.0	0.0	0.0	0.0	9.6	92.14
b26/575/3*	45.8	0.8	27.2	6.1	0.0	1.5	0.0	0.0	10.5	91.19
b26/575/4*	46.9	1.0	31.9	2.1	0.0	1.8	0.0	0.0	10.5	94.68
B26/575/5*	46.9	1.0	31.9	2.1	0.0	1.8	0.0	0.0	10.5	93.95
211/580*	48.2	0.9	31.8	4.0	0.0	1.3	0.0	2.8	8.5	94.92
211/580/1*	51.9	0.9	25.4	3.4	0.0	3.3	0.0	0.0	11.3	96.10
211/580/2*	49.7	0.5	30.6	3.0	0.0	1.7	0.0	0.0	10.8	96.77
211/580/3*	47.4	0.5	32.2	1.7	0.0	1.9	0.0	0.8	10.4	94.75
211/580/4*	47.6	0.5	30.3	2.9	0.0	2.3	0.0	0.0	11.2	95.11
211/580/5*	48.2	0.6	28.0	5.0	0.0	2.5	0.0	0.0	11.6	95.43
211/580/6*	51.4	0.0	24.5	4.6	0.0	2.8	0.0	0.0	10.8	93.70
211/580/7*	46.7	0.3	35.8	1.7	0.1	0.8	0.1	1.4	9.9	96.09
211/580/8*	46.7	1.3	29.1	5.1	0.0	1.9	0.0	0.0	11.4	95.01
211/580/9*	48.2	0.9	31.8	4.0	0.0	1.3	0.0	0.0	8.5	94.41
211/580/10'	51.9	0.9	25.4	3.4	0.0	3.3	0.0	0.0	11.3	95.93
211/580/11'	49.7	0.5	30.5	3.0	0.0	1.7	0.0	0.7	10.8	96.62
211/502*	46.0	0.0	34.4	1.2	0.0	0.8	0.0	1.1	8.4	91.75
B41/456*	44.9	0.7	30.2	4.2	0.0	2.1	0.0	0.7	9.7	91.95
B41/511/1*	45.3	0.8	35.7	0.7	0.0	1.4	0.3	1.0	7.5	91.71
B41/511/2*	45.5	0.7	30.9	4.3	0.0	2.0	0.0	0.7	10.8	94.92
B41/511/3*	44.6	0.4	35.9	1.2	0.0	1.3	0.3	1.2	8.3	93.12
B41/511/4*	48.2	0.4	28.3	3.7	0.0	3.6	0.0	0.7	10.1	94.48
B41/511/5*	46.5	0.4	28.2	3.5	0.0	2.8	0.0	0.0	11.0	91.96

biotite

561/1*	35.8	3.3	16.0	22.9	0.5	9.1	0.0	0.1	9.2	94.64
561/2*	34.7	3.2	16.1	23.0	0.5	8.9	0.0	0.1	8.6	93.02
561/3*	35.1	3.8	16.2	23.3	0.6	8.9	0.0	0.1	9.1	94.84
561/4*	35.6	3.5	16.0	23.3	0.5	8.7	0.0	0.2	9.1	94.65

quartz

211/540/1	98.92	0.01	0.14	0.08	0.03	0.28	0.61	0.82	0.08	100.96
211/540/2	98.76	0.01	0.00	0.02	0.03	0.00	0.02	0.01	0.01	98.88
211/561	98.38	0.01	0.00	0.04	0.01	0.00	0.00	0.01	0.01	98.48

chlorite

sample	SiO2	TiO2	Al2O3	Fe2O3	MnO	MgO	CaO	Na2O	K2O	total
561/1*	25.9	0.1	21.8	23.1	0.2	17.3	0.0	0.1	0.1	86.45
561/2*	29.1	1.8	17.4	31.6	0.4	8.1	0.4	0.3	0.7	86.66
561/3*	28.6	1.8	17.4	31.5	0.4	7.8	0.4	0.3	0.6	85.74

siderite

580-1-sid	0.00	0.00	0.00	55.03	0.55	2.09	3.37	0.00	0.00	61.03
580-2	0.00	0.00	0.00	44.36	0.35	7.99	6.43	0.00	0.00	59.13
580-3	0.00	0.00	0.00	48.17	0.00	5.54	6.04	0.00	0.00	59.75
B26-575	0.00	0.00	0.00	51.59	1.00	5.94	2.58	0.00	0.00	61.12

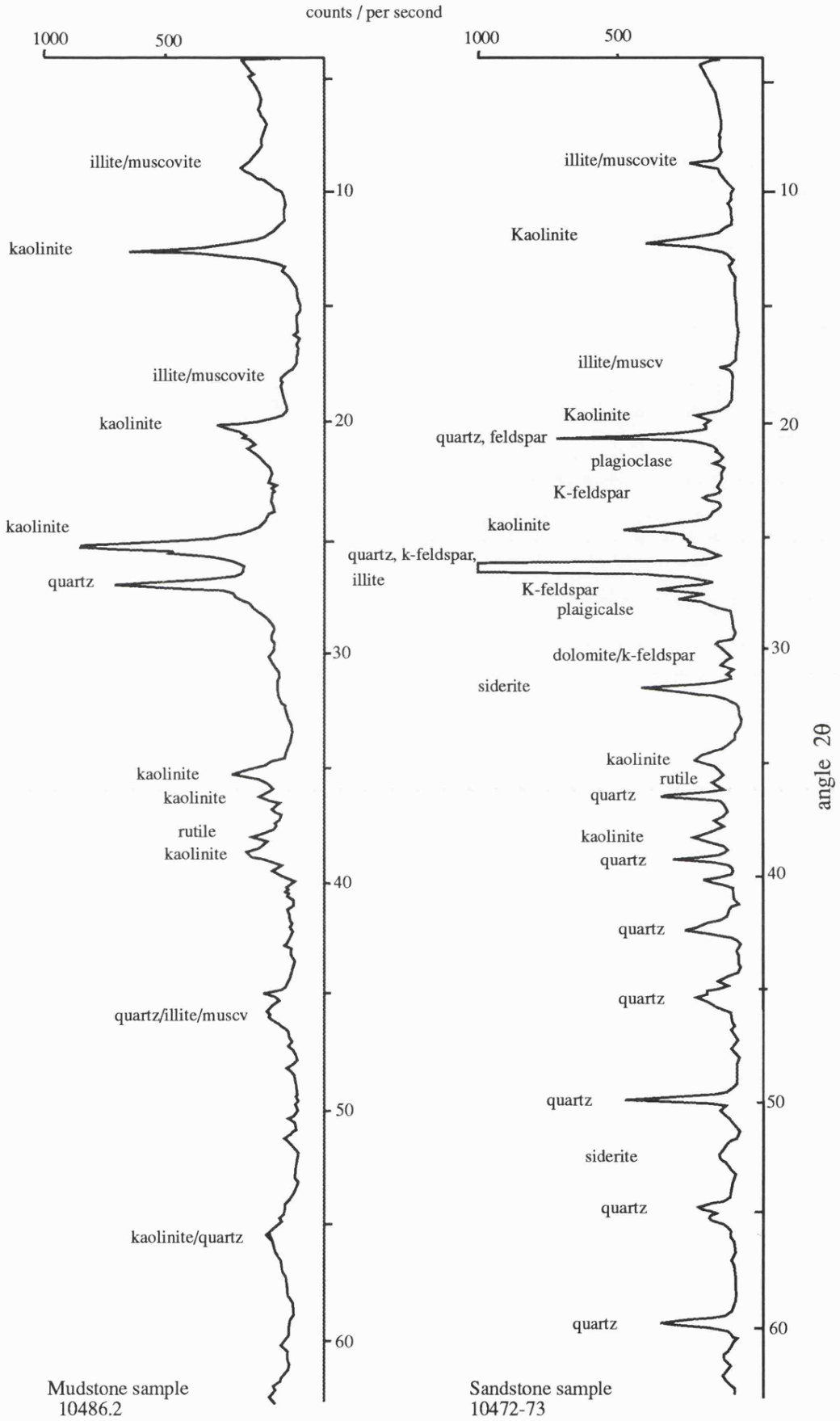

APPENDIX 4.4 Example whole-rock (un-orientated) X-ray diffraction scans of a sandstone (10472-73) and a mudstone (10486.2) from hole 211/18a-a33, Thistle Field.

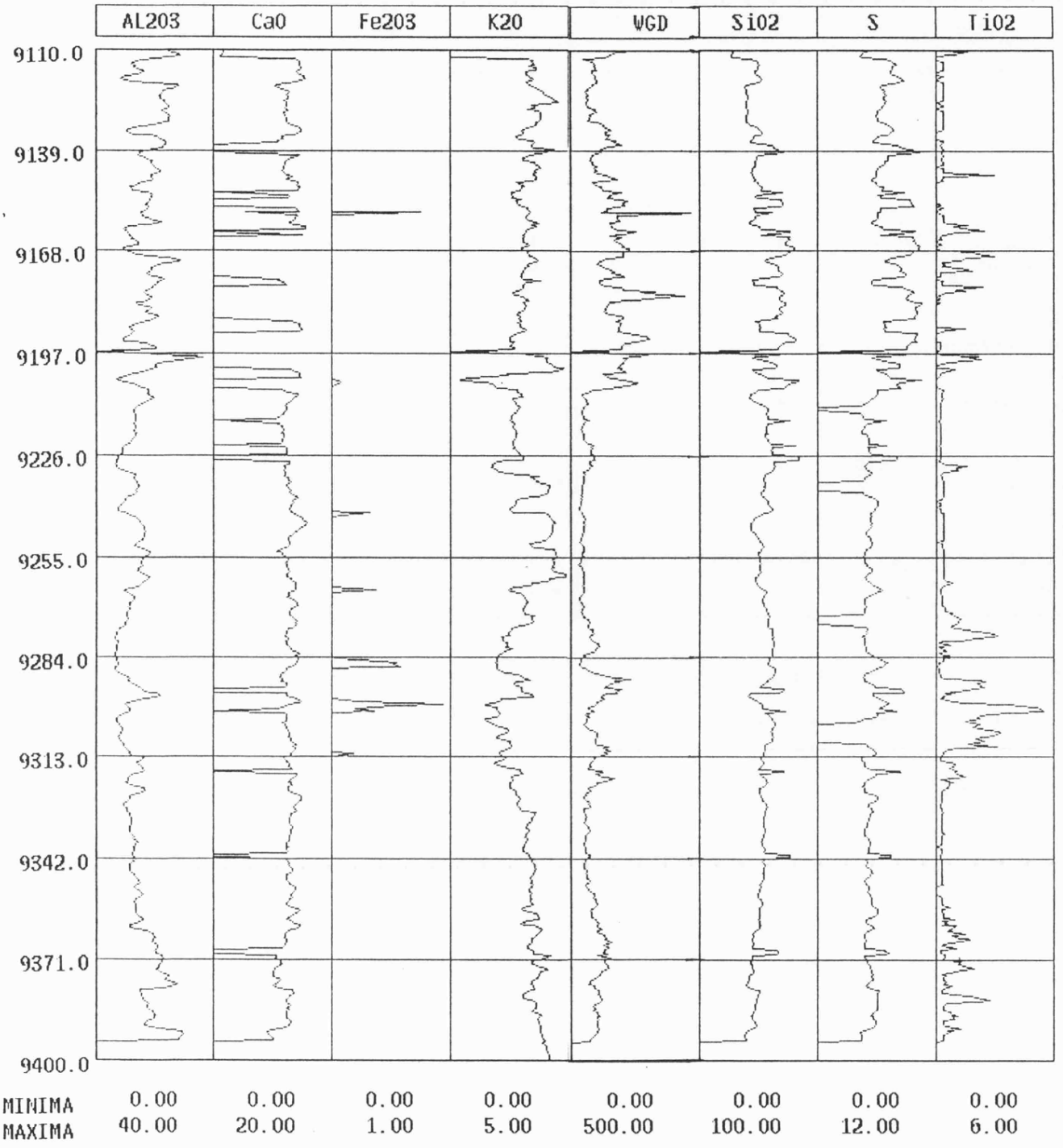

Appendix 5.0 Oxide logs (wt%) from the "Pass 1 processing" of hole 211/18-a50 GLT data, interval 9110 to 9499'. Depth in feet. (log depth)

Appendix 6.0 Compositions (wt%) used in modelling hole 211/18-a50; not-normalsed.

mineral	SiO2	TiO2	Al2O3	Fe2O3	CaO	K2O	S
albite	68.14	0	19.64	0.08	0.55	0.54	0
K-feldspar	64.18	0	18.23	0	0	15.52	0
"feldspar"	66.18	0	18.93	0.04	0.28	8.03	0
kaolinite	45.94	0.2	36.83	0.8	0	0.23	0
muscovite	47.1	0.74	29.68	4.17	0	10.32	0
biotite	35.31	3.44	16.08	23.13	0	9	0
'altered' biotite	34.97	2.73	16.86	20.82	0.25	5.91	0
'altered' mica	41.05	1.73	23.27	12.5	0.12	8.11	0
mica	41.21	2.09	22.88	13.65	0	9.67	0
a33- siderite	0	0.13	0	54.66	5.28	0	0
quartz	98.68	0	0.05	0	0.21	0	0
"a50clay"	47.74	0.19	31.15	3.24	0.43	1.58	0
siderite	0	0	0	66.69	0.08	0	0
siderite-1	0	0	0	67.88	0.1	0	0
rutile	0	100	0	0	0	0	0
calcite	0	0	0	0	56.03	0	0
pyrite	0	0	0	67.24	0	0	53

XRD mineral estimates hole 211/18-a50

Log depth	Core depth	kaolinite	quartz	feldspar	total-mica	siderite	calcite	pyrite
9217.5	9200.8	21.1	52.6	21.1	5.3	0.0	0.0	0.0
9218.0	9201.1	16.7	55.6	22.2	5.6	0.0	0.0	0.0
9221.0	9204.0	12.5	58.3	25.0	4.2	0.0	0.0	0.0
9224.0	9207.0	17.6	47.1	29.4	5.9	0.0	0.0	0.0
9227.0	9210.0	23.8	42.9	28.6	4.8	0.0	0.0	0.0
9230.0	9213.0	5.0	80.0	10.0	5.0	0.0	0.0	0.0
9232.0	9215.0	14.3	57.1	23.8	4.8	0.0	0.0	0.0
9234.0	9217.1	18.2	45.5	31.8	4.5	0.0	0.0	0.0
9236.0	9219.0	23.5	17.6	29.4	11.8	0.0	0.0	17.6
9239.5	9222.0	26.3	31.6	31.6	10.5	0.0	0.0	0.0
9243.0	9226.0	7.7	15.4	23.1	15.4	23.1	15.4	0.0
9246.0	9229.0	33.3	19.0	28.6	19.0	0.0	0.0	0.0
9249.0	9232.0	27.3	22.7	31.8	18.2	0.0	0.0	0.0
9254.0	9237.0	17.6	52.9	23.5	5.9	0.0	0.0	0.0
9257.0	9240.0	22.2	38.9	27.8	11.1	0.0	0.0	0.0
9261.0	9244.0	17.6	29.4	29.4	5.9	17.6	0.0	0.0
9265.0	9248.0	11.8	47.1	23.5	5.9	0.0	11.8	0.0
9269.0	9252.0	17.4	52.2	26.1	4.3	0.0	0.0	0.0
9276.0	9259.0	17.4	43.5	34.8	4.3	0.0	0.0	0.0
9279.0	9262.0	10.5	68.4	21.1	0.0	0.0	0.0	0.0
9285.0	9268.1	5.3	68.4	21.1	0.0	0.0	0.0	5.3
9287.0	9270.0	4.0	79.2	14.9	0.0	0.0	0.0	2.0
9293.0	9276.0	18.3	36.6	24.4	12.2	6.1	0.0	2.4
9302.5	9285.7	2.1	78.9	15.8	3.2	0.0	0.0	0.0
9308.0	9291.0	4.7	70.1	15.9	9.3	0.0	0.0	0.0
9310.0	9293.0	14.3	52.4	19.0	14.3	0.0	0.0	0.0
9313.0	9296.0	30.0	35.0	15.0	20.0	0.0	0.0	0.0
9328.0	9311.0	24.0	43.3	13.5	19.2	0.0	0.0	0.0
9332.0	9315.0	16.1	36.3	28.2	16.1	3.2	0.0	0.0
9335.0	9318.0	23.1	34.6	23.1	19.2	0.0	0.0	0.0
9339.0	9322.0	17.4	43.4	26.0	13.2	0.0	0.0	0.0
9343.0	9326.0	24.3	34.0	29.1	12.6	0.0	0.0	0.0
9345.0	9328.0	22.7	31.8	31.8	13.6	0.0	0.0	0.0
9346.5	9329.9	22.1	14.7	14.7	44.1	4.4	0.0	0.0
9350.0	9333.0	16.4	28.7	36.9	16.4	1.6	0.0	0.0
9351.5	9334.9	32.3	12.1	28.2	24.2	3.2	0.0	0.0
9355.0	9338.0	22.7	31.8	27.3	18.2	0.0	0.0	0.0
9358.0	9341.2	21.2	33.9	25.4	16.9	2.5	0.0	0.0
9378.0	9361.8	14.5	65.2	14.5	2.9	2.9	0.0	0.0

Thin section point-count estimates (porosity included)

quartz	feldspar	total clay	mica	siderite	calcite	pyrite
55.8	19.5	14.3	7.8	0.0	0.0	2.6
59.5	11.9	20.2	7.1	0.0	0.0	1.2
37.6	17.6	23.5	18.8	1.2	0.0	1.2
50.6	16.0	25.9	6.2	0.0	0.0	1.2
42.1	18.9	17.9	7.4	0.0	0.0	13.7
58.4	18.2	15.6	1.3	0.0	5.2	1.3
50.0	23.7	13.2	10.5	0.0	0.0	2.6
35.1	17.5	30.9	11.3	4.1	0.0	1.0
31.9	17.0	16.0	22.3	0.0	0.0	12.8
45.3	18.9	25.3	9.5	0.0	0.0	1.1
11.1	12.1	4.0	12.1	34.3	26.3	0.0
24.2	20.9	13.2	38.5	0.0	0.0	3.3
35.7	17.9	21.4	23.8	1.2	0.0	0.0
63.9	22.2	8.3	5.6	0.0	0.0	0.0
41.0	20.5	24.1	12.0	2.4	0.0	0.0
15.2	14.1	5.4	14.1	50.0	0.0	1.1
47.5	16.2	12.1	13.1	0.0	9.1	2.0
53.7	18.3	18.3	7.3	0.0	0.0	2.4
63.3	15.2	10.1	10.1	0.0	0.0	1.3
71.4	14.3	8.3	3.6	2.4	0.0	0.0
75.3	16.0	6.2	0.0	0.0	0.0	2.5
79.7	16.2	0.0	0.0	0.0	0.0	4.1
45.7	8.5	27.7	13.8	3.2	0.0	1.1
74.1	13.6	9.9	2.5	0.0	0.0	0.0
69.1	12.3	8.6	6.2	2.5	0.0	1.2
50.6	9.4	18.8	17.6	3.5	0.0	0.0
68.6	11.6	16.3	2.3	1.2	0.0	0.0
42.3	11.3	25.8	15.5	4.1	0.0	1.0
51.1	9.1	14.8	12.5	12.5	0.0	0.0
40.2	9.8	9.8	32.6	7.6	0.0	0.0
35.7	9.2	25.5	17.3	12.2	0.0	0.0
45.9	9.4	9.4	24.7	9.4	0.0	1.2
41.5	8.5	6.4	38.3	4.3	0.0	1.1
19.1	8.5	5.3	53.2	13.8	0.0	0.0
50.6	11.5	5.7	24.1	6.9	0.0	1.1
27.1	8.3	10.4	45.8	8.3	0.0	0.0
39.4	9.6	22.3	21.3	7.4	0.0	0.0
58.2	11.0	8.8	13.2	7.7	0.0	1.1
35.9	9.8	18.5	29.3	6.5	0.0	0.0

Appendix 6.1. XRD and Thin section data from hole 211/18-a50.

Data from Russel,1987. XRD data re-normalised if total > 5% from 100;
Thin section data re-calculated with porosity excluded, (wt%).

Appendix 6.2 GLT elemental data from Thistle 211/18-a50 interval 9199 - 9872.5 (wt% oxide form)

Depth (log)	Depth (core)	SiO2	TiO2	Al2O3	CaO	Fe2O3	K2O	S	WMIN
9216	9199	78.86	0.53	12.14	0	0.71	2.36	0.35	1.24
9216.5	9199.5	77.88	0.48	12.45	0	0.68	2.27	0.95	0.95
9217	9200	74.81	0.46	12.18	1.26	0.66	2.31	2.06	0.23
9217.5	9200.5	78.28	0.48	11.51	0.04	0.66	2.41	1.75	0.5
9218	9201	74.4	0.44	11.53	2.04	0.93	2.42	1.68	0.18
9218.5	9201.5	76.02	0.46	11.72	1.01	0.92	2.36	1.63	0.01
9219	9202	77.01	0.49	11.93	0.53	0.63	2.32	1.6	0
9219.5	9202.5	78.14	0.43	12.17	0	0.61	2.38	1.18	0.7
9220	9203	74.28	0.31	12.4	1.97	0.82	2.37	1.02	0.55
9220.5	9203.5	74.95	0.36	12.96	1.28	0.77	2.33	0.81	0
9221	9204	72.29	0.26	13.12	2.44	1.15	2.37	0.7	0
9221.5	9204.5	72.48	0.19	13	2.6	1.09	2.45	0.54	0.44
9222	9205	72.17	0.34	12.55	2.65	1.42	2.54	0.73	1.8
9222.5	9205.5	73.62	0.25	11.86	2.3	1.55	2.56	0.8	2.01
9223	9206	78.31	0.43	10.89	0	1.92	2.54	0.91	2.67
9223.5	9206.5	80.96	0.35	9.84	0	1.94	2.56	0	2.85
9224	9207	81.47	0.36	8.8	0	2.13	2.49	0.68	3.24
9224.5	9207.5	83.38	0.29	8.15	0	2.08	2.42	0	2.62
9225	9208	76.9	0.35	7.98	3.05	2.5	2.38	0.54	4.11
9225.5	9208.5	75.94	0.29	7.84	3.95	2.66	2.36	0	4.25
9226	9209	73.21	0.2	7.53	5.26	2.83	2.43	0.6	6.5
9226.5	9209.5	75.41	0.25	6.98	4.18	2.92	2.41	0.92	6.67
9227	9210	74.33	0.32	6.84	4.34	3.13	2.49	1.41	8.01
9227.5	9210.5	78.18	0.35	6.74	2.52	2.81	2.49	1.42	7.38
9228	9211	78.84	0.45	6.64	2.88	2.41	2.47	0.85	7.8
9228.5	9211.5	79.85	0.5	6.05	2.61	2.45	2.26	1.14	6.86
9229	9212	81.27	0.57	5.3	2.98	2.3	2.07	0.51	6.68
9229.5	9212.5	83.8	0.65	4.9	2.02	1.97	1.97	0.72	5.18
9230	9213	88.01	0.69	5.23	0	1.56	1.97	0.25	4.14
9230.5	9213.5	86.25	0.62	5.83	0.89	1.29	2.07	0	3.03
9231	9214	84.39	0.5	7.1	0.91	1.29	2.14	0	2.38
9231.5	9214.5	82.61	0.45	8.8	0.66	1.06	2.38	0	1.95
9232	9215	79.55	0.52	10.98	0.55	0.92	2.68	0	1.74
9232.5	9215.5	72.56	0.61	12.88	2.53	1.11	3.28	0	3.1
9233	9216	72.21	0.79	13.6	1.4	1.77	3.57	0	4.35
9233.5	9216.5	70.25	0.84	13.86	2.27	1.73	3.65	0	4.83
9234	9217	68.31	0.58	14.06	3.41	1.58	3.29	0.22	4.07
9234.5	9217.5	64.3	0.48	15.23	4.42	1.55	3.29	0.76	2.57
9235	9218	64.74	0.51	16.48	2.3	2.11	3.5	1.24	2.23
9235.5	9218.5	61.68	0.53	17.05	3.28	2.19	3.79	1.39	2.32
9236	9219	61.82	0.53	16.55	3.69	2.53	3.88	0.81	3.21
9236.5	9219.5	64.48	0.63	15.18	2.45	3.26	3.87	1.17	3.94
9237	9220	67.35	0.67	14.14	1.57	3.62	3.91	0.86	4.24
9237.5	9220.5	68.76	0.63	13.72	1.41	3.81	3.87	0.2	4.05
9238	9221	65.84	0.5	13.3	2.41	5.24	3.77	0.04	4.09
9238.5	9221.5	66.95	0.57	12.33	1.22	6.77	3.37	0.32	5.32
9239	9222	61.55	0.39	10.56	4.51	8.68	3.04	0.01	6.34
9239.5	9222.5	56.45	0.16	9.61	7.03	10.32	2.64	0	6.61
9240	9223	50.96	0.44	9.11	9.95	10.87	2.49	0	5.27
9240.5	9223.5	49.32	0.38	8.51	11.21	10.89	2.38	0.31	4.32
9241	9224	42.55	0.25	7.66	15.36	11.08	2.33	0.76	4.11
9241.5	9224.5	43.78	0.28	6.95	15.37	11.08	2.32	0.58	5.51
9242	9225	41.03	0.46	6.8	15.93	11.56	2.28	1.55	7.06
9242.5	9225.5	39.73	0.45	6.91	16.73	11.85	2.34	0.88	7.45
9243	9226	41.41	0.46	7.66	15.56	11.43	2.42	0.77	7.56
9243.5	9226.5	49.1	0.34	8.82	11.74	10.1	2.86	0.14	7.95
9244	9227	54.41	0.41	10.19	8.98	8.36	3.4	0	8.35
9244.5	9227.5	56.91	0.15	11.61	8.17	6.21	3.97	0	7.24
9245	9228	62.84	0.33	12.83	3.82	5.43	4.26	0.79	6.95
9245.5	9228.5	64.99	0.22	13.65	3.77	3.86	4.39	0	6.8
9246	9229	63.47	0.42	13.74	4.49	3.76	4.37	0.03	7.25
9246.5	9229.5	64.24	0.2	13.71	4.67	3.3	4.19	0	6.52
9247	9230	66.6	0.15	13.74	3.75	2.84	4.09	0.01	6.07
9247.5	9230.5	68.34	0.26	14.22	2.43	2.68	4.15	0	5.4
9248	9231	68.05	0.44	14.69	1.88	2.82	4.27	0.11	4.66
9248.5	9231.5	70.98	0.45	15.36	0.15	2.29	4.26	0.08	4.61
9249	9232	70.36	0.5	15.6	0	2.24	4.21	0.58	4.87
9249.5	9232.5	67.93	0.47	15.16	1.75	2.12	4.11	0.77	5.32
9250	9233	65.71	0.44	14.8	3.53	2.19	4.04	0.35	4.46
9250.5	9233.5	69.99	0.48	14.34	1.66	2.29	3.95	0	4.48
9251	9234	69.82	0.23	13.27	2.95	2.14	3.8	0	4.23
9251.5	9234.5	71.13	0.28	11.77	3.58	2.05	3.53	0	4.45
9252	9235	76.41	0.36	10.43	1.85	1.94	3.28	0	5.2
9252.5	9235.5	76.79	0.37	10.87	1.47	1.74	3.18	0	4.32
9253	9236	73.48	0.51	13.2	1.27	1.38	3.52	0.38	2.51
9253.5	9236.5	68.57	0.65	16.72	0.82	1.24	3.94	0.69	0.14
9254	9237	65.32	0.67	18.45	1.08	1.27	4.21	0.72	0
9254.5	9237.5	64.29	0.88	18.43	0.86	1.74	4.24	1.2	0.69
9255	9238	65.99	0.92	17.07	0.47	2.18	4.3	1.44	1.8
9255.5	9238.5	66.82	0.91	15.91	0.61	2.34	4.42	1.78	2.77
9256	9239	67.51	0.79	15.31	1.74	2.17	4.39	0.48	2.71
9256.5	9239.5	67.9	0.63	15.12	1.76	2.37	4.37	0.28	3.48
9257	9240	66.55	0.38	14.89	3.31	2.02	4.34	0	3.61
9257.5	9240.5	62.26	0.55	14.96	5.3	2.22	4.32	0.15	2.78
9258	9241	61.17	0.51	15.21	5.3	2.77	4.09	0.22	2.4
9258.5	9241.5	58.68	0.69	15.53	4.86	4.48	3.98	0.33	1.08
9259	9242	54.88	0.75	15.59	4.8	6.56	3.85	0.98	1.24
9259.5	9242.5	52.56	0.71	15.27	4.86	8.43	3.79	0.97	2.82
9260	9243	54.71	0.6	15.29	2.83	9.16	3.72	1.39	6.16
9260.5	9243.5	54.11	0.43	16.07	3.42	8.47	3.9	0.94	8.25
9261	9244	56.49	0.52	16.55	2.59	6.67	4.06	1.77	8.48
9261.5	9244.5	60.16	0.71	17.14	2.02	4.59	4.4	1.05	6.88
9262	9245	61.29	0.79	17.59	2.65	3.32	4.49	0.03	5.06
9262.5	9245.5	64.29	1.08	16.72	1.68	2.87	4.57	0.33	3.94
9263	9246	65.93	1.28	14.8	2.36	3.07	4.27	0.03	4.53
9263.5	9246.5	64.7	1.39	12.91	4.19	3.45	4.05	0.21	4.46
9264	9247	63.72	1.31	11.5	6.14	3.37	3.66	0.19	3.9
9264.5	9247.5	66.01	1.07	9.39	6.32	3.46	3.27	0.9	2.32
9265	9248	67.67	0.85	7.43	8	3.03	2.74	0.32	1.82
9265.5	9248.5	68.23	0.58	7.08	8.45	2.38	2.38	0.81	0.93
9266	9249	69.58	0.34	7.74	8.23	1.67	2.29	0.28	1.38
9266.5	9249.5	72.14	0.35	8.78	6.03	1.3	2.37	0.59	1.54
9267	9250	76.24	0.34	9.37	3.72	0.87	2.5	0.33	1.24
9267.5	9250.5	77.14	0.37	9.77	2.9	1.06	2.56	0	0.56
9268	9251	79.04	0.5	10.22	1.3	1.13	2.7	0	0
9268.5	9251.5	77.57	0.53	10.51	1.7	1.29	2.85	0	0
9269	9252	76.54	0.57	10.55	2.2	1.27	2.98	0	0.08
9269.5	9252.5	75.49	0.4	10.42	2.82	1.46	3.07	0	0.45
9270	9253	76.37	0.67	10	2.38	1.63	3.06	0	1
9270.5	9253.5	76.83	0.53	9.8	2.37	1.61	3.1	0	0.71
9271	9254	77.38	0.74	9.9	1.59	1.74	3.14	0.24	0
9271.5	9254.5	78.5	0.96	9.96	0.19	1.88	3.24	0.96	0
9272	9255	77.51	1.19	10.28	0	1.96	3.39	1.34	0
9272.5	9255.5	77.65	1.14	10.43	0.1	2.02	3.36	0.85	0
9273	9256	76.45	1.23	10.48	0.5	2.22	3.28	0.9	0.39
9273.5	9256.5	77.16	1.15	10.2	0.62	1.98	3.13	0.89	1.71
9274	9257	73.23	0.92	9.62	3.89	2.11	3.15	0	3.38
9274.5	9257.5	73.14	0.84	9.05	4.35	2.23	3.2	0	4.11
9275	9258	74.42	0.93	8.84	3.31	2.29	3.13	0.65	4.08
9275.5	9258.5	78.34	0.91	8.71	1.23	2.18	2.89	0.91	3.76
9276	9259	75.24	0.96	8.42	3.12	2.28	2.66	0.96	3.8
9276.5	9259.5	78.81	0.97	7.66	2.05	2.07	2.48	0.84	4.84
9277	9260	83.24	1.11	6.85	0	2.05	2.39	1.17	4.97
9277.5	9260.5	79.13	1.2	6.32	2.71	1.99	2.27	1.25	4.73

Appendix 6.2 (cont..)

Depth (log)	Depth (core)	SiO2	TiO2	Al2O3	CaO	Fe2O3	K2O	S	WMIN
9278.5	9261.5	80.64	1.45	5.14	2.07	2.14	2.11	2.14	2.54
9279	9262	80.32	1.31	4.84	1.94	2.53	2.02	2.68	1.53
9279.5	9262.5	78	1.03	5.11	2.58	2.93	1.9	3.14	2.97
9280	9263	76.01	0.96	5.95	2.32	3.79	2.11	3.07	3.94
9280.5	9263.5	66.93	0.8	7.35	4.98	5.72	2.38	2.53	6.46
9281	9264	65.11	0.68	7.98	3.53	7.55	2.65	3.21	9.36
9281.5	9264.5	61.72	0.54	7.79	4.69	8.69	2.69	3.23	11.24
9282	9265	63.21	0.61	7.48	4.01	8.78	2.84	3.14	12.18
9282.5	9265.5	66.64	0.52	7.1	4.09	7.1	2.86	2.77	12.3
9283	9266	75.09	0.56	6.53	1.78	4.95	2.65	2.56	10.01
9283.5	9266.5	76.75	0.45	5.9	3.09	3.24	2.07	2.45	3
9284	9267	77.93	0.54	5.66	4	2.08	1.61	1.91	0
9284.5	9267.5	83.31	0.52	5.29	2.04	1.36	1.39	1.77	0
9285	9268	83.91	0.49	5.18	2.2	0.81	1.29	1.92	0
9285.5	9268.5	83.41	0.4	5.03	2.97	0.68	1.28	1.62	0
9286	9269	85.02	0.4	4.93	2.13	0.77	1.24	1.52	0
9286.5	9269.5	83.03	0.25	4.99	2.77	0.92	1.3	2.11	0
9287	9270	80.27	0.21	5.48	3.79	1.12	1.39	2.04	0
9287.5	9270.5	80.74	0.3	6.26	2.8	1.51	1.53	1.5	0.08
9288	9271	77.69	0.26	7.33	2.48	2.04	1.85	2.5	0
9288.5	9271.5	79.18	0.45	8.37	0	3.32	2.2	1.75	2.83
9289	9272	72.69	0.41	10.25	0	4.25	2.74	3.62	5.52
9289.5	9272.5	65.6	1.06	13.03	0	5.4	3.31	3.93	7.44
9290	9273	57.04	1.23	15.22	0	8.37	3.7	4.4	8.57
9290.5	9273.5	51.03	1.07	17.16	0	11.07	3.66	3.78	10.85
9291	9274	45.97	0.88	16.2	0.74	14.68	3.11	4.02	8.76
9291.5	9274.5	38.84	1.04	14.8	2.4	18.1	2.39	5.24	6.86
9292	9275	37.88	1.03	14.51	3.29	18.32	2.12	4.9	7.05
9292.5	9275.5	40.24	1.05	14.82	3.42	16.58	2.12	4.45	9.9
9293	9276	41.9	0.92	16.12	3.03	14.63	2.48	4.4	9.44
9293.5	9276.5	50.73	0.81	15.8	0	12.6	2.65	4.49	10.23
9294	9277	54.6	0.69	15.73	0	10.75	2.76	3.65	10.72
9294.5	9277.5	50.89	0.62	16.99	2.31	9.4	2.91	3.37	10.14
9295	9278	55.55	0.82	18.58	0	7.69	3.11	2.8	8.76
9295.5	9278.5	53.69	0.95	20.79	0	6.94	3.38	2.3	7.43
9296	9279	54.18	0.94	21.05	0	6.14	3.46	2.55	7.71
9296.5	9279.5	63.38	0.62	16.52	0	5.41	3.22	1.69	8.38
9297	9280	72.17	0.73	11.57	0	4.38	2.59	1.95	8.52
9297.5	9280.5	73.39	0.49	7.88	3.61	3.14	1.92	2.14	7.93
9298	9281	83.99	0.72	6.21	0	2.5	1.41	1.5	5.82
9298.5	9281.5	82.14	0.97	5.97	1.74	1.57	1.27	1.77	2.89
9299	9282	82.28	1.2	6.44	1.52	0.93	1.33	2	0.51
9299.5	9282.5	79.84	1.18	7.12	2.54	0.78	1.46	1.81	0
9300	9283	83.63	1.42	7.43	0	0.79	1.56	1.78	0
9300.5	9283.5	82.39	1.37	7.72	0	1.25	1.64	1.92	0
9301	9284	82.17	1.18	7.66	0	1.71	1.7	1.73	0.06
9301.5	9284.5	79.86	1.05	7.22	1.81	2.33	1.65	0.81	1.15
9302	9285	78.11	0.74	6.6	3.43	2.61	1.52	0.57	2.15
9302.5	9285.5	80.23	0.63	6.36	2.87	2.42	1.37	0.29	2.6
9303	9286	79.63	0.62	6.25	3.81	2.04	1.36	0	2.4
9303.5	9286.5	77.05	0.49	6.58	5.33	1.68	1.42	0	1.71
9304	9287	77.35	0.56	6.76	4.99	1.22	1.56	0.52	0.77
9304.5	9287.5	77.38	0.84	7.34	4.03	0.94	1.7	1.32	0.29
9305	9288	74.39	1.06	8.08	4.3	1.8	1.88	1.18	0.89
9305.5	9288.5	71.74	1.22	8.9	4.07	2.21	2.09	2.04	2.13
9306	9289	72.54	1.41	9.47	2.57	2.93	2.26	1.76	2.95
9306.5	9289.5	71.24	1.4	9.69	1.54	4.34	2.28	2.42	3.75
9307	9290	66.84	1.35	9.39	2.29	6.3	2.08	3.04	5.61
9307.5	9290.5	65.54	1.12	8.7	2.54	7.86	1.83	2.98	8.51
9308	9291	66.9	0.95	7.84	2.15	8.44	1.66	2.98	10.05
9308.5	9291.5	67.59	0.77	7.37	2.44	8.62	1.71	2.43	10.16
9309	9292	68.35	0.67	7.79	3.39	7.58	1.81	1.12	9.29
9309.5	9292.5	70.51	1	8.43	2.71	6.5	1.99	0.49	8.17
9310	9293	77.11	1.1	8.92	0	4.99	2.1	0.14	8
9310.5	9293.5	77.41	1.13	9.16	0	4.4	2.21	0.27	6.81

Depth (log)	Depth (core)	SiO2	TiO2	Al2O3	CaO	Fe2O3	K2O	S	WMIN
9311.5	9294.5	73.45	1.23	9.1	0.16	6.73	2.16	0.48	6.78
9312	9295	72.17	1.02	9.28	0	7.7	2.11	0.54	7.54
9312.5	9295.5	66.1	0.89	9.79	2.09	8	2.05	1.72	8.16
9313	9296	68.82	0.63	9.91	0	8.27	2.08	2.3	7.64
9313.5	9296.5	64.85	0.57	11.19	1.47	7.49	2.2	2.84	4.76
9314	9297	61.9	0.52	14.57	2.11	5.08	2.51	3.06	0
9314.5	9297.5	54.58	0.56	19.16	3.82	3.6	2.81	2.61	0
9315	9298	58.44	0.57	18.52	3.42	2.94	2.62	1.59	0
9315.5	9298.5	62.46	0.63	15.69	4.2	2.42	2.2	1.31	0
9316	9299	65.56	0.64	14.33	3.86	2.48	1.94	0.93	0
9316.5	9299.5	67.19	0.72	14.96	2.5	2.66	2	0.47	0
9317	9300	66.66	0.9	14.99	2.61	2.95	2.19	0.1	0.28
9317.5	9300.5	68.71	0.9	14.62	1.21	3.64	2.36	0	4.45
9318	9301	66.91	0.94	14.06	2.17	4.18	2.5	0	6.23
9318.5	9301.5	62.73	1.04	15.24	3.36	4.07	2.75	0.23	0.45
9319	9302	64.38	1.15	15.07	1.89	4.48	2.95	0.6	0
9319.5	9302.5	66.18	0.99	14.83	1.5	4.4	3.05	0.16	0
9320	9303	61.43	1.11	14.02	2.54	5.15	3.03	2.73	0
9320.5	9303.5	60.87	0.99	12.81	3.36	5.4	3.09	3.23	0
9321	9304	61.82	1.25	11.72	3.8	4.86	3.11	3.6	0
9321.5	9304.5	61.31	1.15	10.34	6.21	4.71	3.03	2.39	1.51
9322	9305	65.49	1.15	9.89	4.99	4.29	2.8	1.87	5.49
9322.5	9305.5	68.53	0.79	10.96	3.81	3.59	2.77	0.85	5.73
9323	9306	66.99	0.78	12.69	3.73	3.14	2.7	0.7	4.85
9323.5	9306.5	66.88	0.56	13.31	3.67	3.2	2.66	0.21	3.83
9324	9307	68.32	0.34	12.46	3.39	3.1	2.51	0.9	3.06
9324.5	9307.5	69.7	0.26	11.21	3.71	3.38	2.47	0.53	3.9
9325	9308	69.88	0.27	9.68	4.51	3.64	2.55	0.73	4.53
9325.5	9308.5	72.68	0.29	8.88	3.46	3.87	2.62	0.61	5.41
9326	9309	75.3	0.56	8.54	1.78	4.16	2.65	0.75	4.91
9326.5	9309.5	75.78	0.65	8.37	1.7	4.3	2.64	0.42	4.94
9327	9310	78.46	0.63	8.08	0	4.45	2.71	0.91	4.7
9327.5	9310.5	78.33	0.72	7.68	0	4.55	2.8	1.3	5.83
9328	9311	77.24	0.62	7.74	1.01	4.65	2.82	0.54	6.34
9328.5	9311.5	73.9	0.39	7.9	2.85	4.69	2.77	0.54	6.75
9329	9312	71.99	0.19	8.29	4.35	4.29	2.88	0	6.66
9329.5	9312.5	72.15	0.19	8.62	3.85	4.41	3.06	0	7.14
9330	9313	73.46	0.33	8.99	2.94	4.1	3.2	0	7.24
9330.5	9313.5	74.82	0.2	9.61	1.48	4.45	3.13	0	6.91
9331	9314	74.68	0.29	10.46	0.97	4.23	3.12	0	5.92
9331.5	9314.5	72.77	0.62	11.36	1.36	3.91	3.18	0	5.5
9332	9315	70.53	0.67	11.91	1.83	4.1	3.27	0.17	5.65
9332.5	9315.5	66.63	0.52	12.4	3.41	4.09	3.26	0.67	6.42
9333	9316	66.49	0.47	12.55	2.75	4.42	3.21	1.26	7.22
9333.5	9316.5	68	0.56	12.33	2.25	4.5	3.16	0.84	6.66
9334	9317	69.48	0.48	11.69	1.37	4.8	3.18	1.41	5.91
9334.5	9317.5	71.55	0.5	10.94	1.91	4.15	3.14	0.58	5.39
9335	9318	75.48	0.63	10.2	0	4.2	3.09	0.93	5.34
9335.5	9318.5	76.92	0.73	9.7	0	3.62	3	1.02	4.81
9336	9319	77.46	0.77	9.37	0	3.27	2.91	1.45	5.64
9336.5	9319.5	78.29	0.69	9.64	0	2.78	2.84	1.09	4.95
9337	9320	77.04	0.84	10.26	0	2.91	2.8	1.1	5.15
9337.5	9320.5	75.21	0.68	11.63	0	2.91	2.93	1.01	4.04
9338	9321	73.85	0.58	12.87	0	3.22	3.02	0.22	4.71
9338.5	9321.5	73.18	0.64	13.1	0	3.46	3.08	0.13	5.31
9339	9322	71.48	0.45	12.74	0.97	3.97	3.12	0.06	5.92
9339.5	9322.5	68.89	0.34	12.52	2.54	4.13	3.21	0.02	6.43
9340	9323	66.05	0.31	12.54	4.19	4.06	3.2	0.01	6.06
9340.5	9323.5	66.81	0.35	13.09	3.55	3.75	3.18	0	4.87
9341	9324	68.08	0.31	13.03	3.1	3.52	3.16	0.01	3.57
9341.5	9324.5	68.45	0.36	12.89	2.82	3.44	3.3	0.33	3.32
9342	9325	69.69	0.31	11.73	3.18	3.34	3.36	0.32	3.47
9342.5	9325.5	75.49	0.55	10.32	0.66	3.52	3.43	0.54	3.19
9343	9326	77.05	0.56	9.92	0	3.4	3.4	0.9	1.87
9343.5	9326.5	76.79	0.51	10.21	0.31	3.2	3.32	0.58	1.5

Appendix 6.2 (cont..)

Depth (log)	Depth (core)	SiO2	TiO2	Al2O3	CaO	Fe2O3	K2O	S	WMIN
9344.5	9327.5	74.51	0.64	10.9	0.92	3.46	3.12	0.36	1.98
9345	9328	71.43	0.63	12.84	0.9	3.73	3.08	0.25	1.85
9345.5	9328.5	66.84	0.59	13.59	2.36	4.2	3.1	0.44	3.43
9346	9329	66.65	0.82	13.98	0.61	5.3	3.08	1.23	5.43
9346.5	9329.5	61.1	0.72	14.1	3.3	6.15	3.14	0.65	8.4
9347	9330	64.88	0.99	14.83	0	6.82	3.04	0.49	10.01
9347.5	9330.5	55.76	0.64	15.68	4.22	7.19	3.09	0.59	10.58
9348	9331	56.1	0.66	15.11	4.02	7.89	3	0.44	10.51
9348.5	9331.5	59.17	0.67	12.8	3.73	8.27	3.01	0.72	10.65
9349	9332	64.64	0.73	9.59	3.71	7.76	3.01	0.75	10.5
9349.5	9332.5	66.77	0.4	8.08	4.41	7.11	3.03	0.87	9.61
9350	9333	68.8	0.52	8.55	4.08	5.66	3.05	0.77	6.7
9350.5	9333.5	68.28	0.41	9.61	3.31	5.64	3.08	1.16	5.01
9351	9334	66.24	0.27	10.76	3.96	5.31	3.1	0.98	4.91
9351.5	9334.5	62.47	0.3	13.01	4.27	5.42	3.16	0.67	3.64
9352	9335	57.73	0.4	15.06	4.28	5.99	3.15	1.34	5.14
9352.5	9335.5	57.76	0.34	14.5	3.79	7.11	3.17	1.38	6.99
9353	9336	56.06	0.35	13.52	4.85	7.95	3.01	1.46	9.27
9353.5	9336.5	57.52	0.31	12.82	4.54	7.68	2.85	2.05	10.08
9354	9337	56.21	0.47	13.41	5.27	6.83	2.76	2.27	10.35
9354.5	9337.5	62.21	0.49	13.58	2.05	6.84	2.94	1.72	9.69
9355	9338	64.88	0.71	14.14	0	6.81	3.16	1.61	9.19
9355.5	9338.5	65.68	0.87	14.11	0	7	3.33	0.46	8.93
9356	9339	63.22	0.92	14.55	1.13	7.17	3.37	0	8.66
9356.5	9339.5	62.59	0.82	14.84	1.45	6.99	3.37	0	9.14
9357	9340	55.77	0.99	14.8	3.95	8.28	3.12	0.39	9.02
9357.5	9340.5	53.93	0.71	14.59	5.5	8.46	2.79	0	9.44
9358	9341	55.42	0.7	13.9	3.61	9.94	2.44	0.78	8.78
9358.5	9341.5	54.78	0.88	13.34	3.23	11.01	2.43	1.15	9.31
9359	9342	56.03	0.78	13.23	3.44	10.9	2.59	0	9.44
9359.5	9342.5	58.91	0.86	11.8	2.58	11	2.84	0.37	10.63
9360	9343	60.59	0.91	9.05	2.66	12.05	2.96	0.89	10.09
9360.5	9343.5	61.04	0.94	8.57	2.91	11.9	2.95	0.92	10.36
9361	9344	58.82	0.84	8.62	3.54	12.65	2.77	1	10.13
9361.5	9344.5	56.52	0.77	8.98	5.13	11.9	2.68	1.15	11.3
9362	9345	56.68	0.98	8.98	4.01	13.06	2.76	1.02	11.24
9362.5	9345.5	56.9	0.98	10.28	3.18	12.78	2.97	0.71	11.71
9363	9346	54.98	0.98	13.11	2.13	12.51	3.08	0.68	10.65
9363.5	9346.5	54.62	0.89	15.88	1.54	10.96	3.03	0.41	10.15
9364	9347	59.52	0.85	14.93	0	10.3	2.92	0.73	10.25
9364.5	9347.5	61.93	0.87	14.45	0	9.69	2.87	0	10.98
9365	9348	62.67	1.23	14.81	0	8.04	2.92	0.7	11.57
9365.5	9348.5	61.59	0.89	16.38	0	7.73	3.03	0.27	10.16
9366	9349	53.39	1.17	19.59	1.85	7.06	3.33	0.9	8.81
9366.5	9349.5	55.96	1.11	19.82	0	7.18	3.46	1.08	8.4
9367	9350	56.33	0.99	19.24	0.19	7.7	3.43	0.65	10.6
9367.5	9350.5	59.77	0.77	17.92	0	7.41	3.1	0.35	10.71
9368	9351	58.17	0.98	17.78	0.81	7.7	2.84	0.21	10.16
9368.5	9351.5	59.34	0.83	18.3	0	7.47	2.77	0.23	9.38
9369	9352	55.75	0.79	18.83	1.01	7.88	2.83	0.62	10.34
9369.5	9352.5	54.3	0.89	19.73	0.28	8.19	2.96	1.31	10.62
9370	9353	51.63	0.83	20.22	1.04	8	3.11	2.09	10.98
9370.5	9353.5	54.6	0.69	19.92	0	8.15	3.15	1.39	9.48
9371	9354	54.33	0.77	20.45	0	7.42	3.16	1.81	9.34
9371.5	9354.5	55.04	0.7	20.57	0	6.62	3.21	2.1	8.01
9372	9355	57.65	0.72	18.5	0	7.52	3.33	1.27	8.11
9372.5	9355.5	57.12	0.94	17.76	0	8.24	3.34	1.56	8.67
9373	9356	52.75	1	17.84	2.22	7.92	3.22	2.24	9.36
9373.5	9356.5	54.61	0.96	17.62	1.57	7.63	3.06	2.4	8.68
9374	9357	50.62	0.96	18.82	3.15	7.27	2.93	2.36	8.4
9374.5	9357.5	45.16	0.75	21.3	5.24	5.74	2.89	2.87	8.34
9375	9358	45.62	0.5	20.97	6.2	5.29	2.88	2.19	8.92
9375.5	9358.5	52.77	0.53	20.23	2.48	6.03	2.81	1.74	8.44
9376	9359	55.15	0.59	19.16	1.73	6.74	2.71	1.29	8.27
9376.5	9359.5	61	0.62	16.02	0	7.89	2.54	1.5	8.9

Depth (log)	Depth (core)	SiO2	TiO2	Al2O3	CaO	Fe2O3	K2O	S	WMIN
9377.5	9360.5	57.74	0.9	19.04	0	6.17	2.37	2.51	8.83
9378	9361	56.53	1.06	18.37	0	6.36	2.53	4	9.28
9378.5	9361.5	57.37	1.17	16.93	0	7.09	2.75	4	10.66
9379	9362	59.75	1.21	14.02	0	8.44	3.02	3.79	10.92
9379.5	9362.5	63.6	1.07	12.94	0	7.86	3.12	2.64	10.45
9380	9363	64.68	0.88	11.15	0	8.81	3.11	2.96	10.27
9380.5	9363.5	60.6	0.92	11.43	2.77	8.81	2.99	1.85	9.79
9381	9364	60.58	0.78	12.3	2.9	8.21	2.91	1.43	9.49
9381.5	9364.5	57.78	0.88	15.51	1.85	7.65	2.96	1.99	9.09
9382	9365	56.09	0.95	17.09	1.65	7.2	3.07	2.22	9.13
9382.5	9365.5	54.38	1.14	17.11	2.68	7.02	3.04	2.15	9.28
9383	9366	55.44	1.29	17.07	1.43	7.2	2.96	2.93	10.09
9383.5	9366.5	57.21	1.26	17	0.9	6.76	2.97	2.9	10.17
9384	9367	59.03	0.93	16.7	0.81	6.8	3.02	2.05	10.14
9384.5	9367.5	59.94	0.66	16.46	1.29	6.22	3.06	1.75	9.34
9385	9368	60.2	0.5	16.84	1.35	5.79	3.07	1.64	9.56
9385.5	9368.5	59.33	0.52	17.35	1.54	5.72	3.06	1.51	9.18
9386	9369	56.44	0.41	17.8	3.43	5.7	3.1	0.6	9.39
9386.5	9369.5	56.44	0.59	17.76	3.26	5.79	3.13	0.64	9.02
9387	9370	58.01	0.66	17.66	1.72	6.26	3.24	1.08	10.25
9387.5	9370.5	61.12	0.84	17.32	0	6.55	3.32	0.93	10.71
9388	9371	62.32	0.89	16.79	0	6.9	3.41	0	11.38
9388.5	9371.5	61.15	0.79	17.3	0	6.88	3.46	0.47	10.69
9389	9372	60.87	0.91	17.02	0	7.04	3.56	0.72	10.85
9389.5	9372.5	57.73	0.7	16.19	3.26	6.75	3.51	0.04	10.05

Appendix 6.3

Modelled mineral estimates from compositions that represent the upper and lower limits of uncertainty (precision) of GLT derived chemistry. Four synthetic rocks modelled. High- upper estimates, low- lower estimates

	quartz	albite	K-felspar	kaolinite
Mix1	59.976	19.330	10.929	9.765
low	50.037	27.445	19.429	3.089
high	67.904	17.628	2.606	11.862

	quartz	muscovite	kaolinite
Mix2	30.62	24.39	44.97
low	25.54	34.85	39.60
high	35.51	14.32	50.16

	quartz	K-feldspar	Dolomite	kaolinite	muscovite
arenite	74.99	16.24	4.19	4.55	0.00
low	52.21	29.06	7.23	11.49	0.00
high	81.17	0.00	0.56	0.00	18.26

	quartz	K-feldspar	Dolomite	kaolinite	muscovite
pelite	20.47	14.56	4.74	13.54	46.67
low	8.11	35.85	9.41	24.46	22.14
high	30.70	0.00	1.03	4.19	64.06

Compositions used in precision modelling, Chapter 6.

	SiO2	TiO2	Al2O3	Fe2O3	MgO	CaO	Na2O	K2O
Mix1								
actual	85.384	0.020	10.044	0.140	0.060	0.420	2.331	1.600
(low)	87.386	0.000	8.551	0.000	0.066	0.000	2.571	1.426
(High)	81.438	0.338	10.473	0.652	0.054	3.283	2.073	1.691
arenite								
actual	90.005	0.124	4.437	0.514	0.522	1.492	0.949	1.957
(low)	93.526	0.000	2.994	0.000	0.583	0.000	1.059	1.838
(high)	85.532	0.315	5.505	0.989	0.464	4.263	0.844	2.017
Mix2								
actual	67.921	0.111	27.460	1.073	0.192	0.071	0.039	3.131
(low)	67.855	0.010	28.300	0.489	0.212	0.000	0.043	3.100
(high)	65.805	0.404	25.905	1.504	0.170	3.122	0.034	3.056
Pelite								
actual	61.406	0.136	25.514	1.733	1.386	1.688	0.854	7.283
(low)	61.785	0.000	26.625	1.250	1.558	0.000	0.959	7.823
(high)	60.051	0.423	24.200	2.084	1.228	4.526	0.756	6.732

Appendix 7.1 Statfjord holes 33/12-b26, 33/12-b41

Model calculated mineral estimates and core XRD estimates (wt%)

Section b26

Mineral Modes for two sections

Depth	quartz	kaolinite	ζ-feldspa	albite	mica	siderite	rutile	calcite	pyrite
4174	85.8	1.01	6.41	5.36	0	1	0.42	0	0
4175	88.8	1.39	5.08	3.71	0.31	0.19	0.29	0.23	0
4176	85.11	1.56	3.63	3.39	0	5.45	0.85	0	0
4177	77.08	11.65	5.48	3.23	1.5	0.39	0.53	0.14	0
4178	62.42	12.54	9.83	9.11	4.19	0.88	0.8	0.23	0
4179	68.75	7.76	8.92	9.07	2.44	2.31	0.56	0	0.19
4180	36.78	20.85	13.72	9.68	4.04	11.04	1.09	0	2.81
4180	78.19	4.21	6.77	7.91	0.15	2.29	0.44	0.04	0
4181	87.53	1.54	5.28	4.97	0	0.51	0.16	0	0
4182	86.81	1.37	5.33	5.79	0.07	0.4	0.13	0.1	0
4184	83.92	0.81	5.66	8.17	0	1.16	0.28	0	0
4186	88.18	1.53	4.68	4.19	0	1.19	0.22	0	0
4187	84.73	1.64	5.46	5.74	0	2.12	0.3	0	0
4188	85.14	1.44	5.3	6.44	0	1.39	0.29	0	0
4188	84.92	1.45	4.61	5.7	0	3.1	0.22	0	0
4189	85.45	2.24	5.38	5	0	1.7	0.23	0	0
4193	41.07	27.57	15.3	8.75	0	5.83	1.47	0	0
4193	77.39	5.09	7.25	7.41	0	1.7	1.16	0	0
4194	64.34	9.28	11.21	8.14	3.91	2.51	0.49	0.11	0
4195	47.53	19.87	11.06	7.26	5.82	5.63	0.93	0	1.89
4195	57.39	14.55	12.13	8	3.47	3.6	0.73	0.13	0
4196	45.12	18.3	13.22	7.14	5.58	8.69	0.82	0	1.13
4198	22.98	24.73	4.55	4.59	14.8	21.9	1	0	5.44
4199	37.94	25.49	8.42	6.62	12.93	3.1	0.99	0	4.51
4201	15.4	32.31	16.41	6.43	6.47	21.61	1.2	0.18	0
4202	38.4	18.73	12.1	9.24	14.22	5.66	0.5	0	1.15
4202	54.67	12.91	13.01	9.09	6.12	3.69	0.46	0.06	0
4203	58.96	11.18	13.39	9.42	2.2	3.95	0.79	0.12	0
4204	65.68	5.35	8.87	7.86	0.09	7.55	0.42	0	4.18
4205	59.8	10.67	12.73	8.57	0.62	6.5	1.12	0	0
4206	63.67	9	12.16	9.47	2.13	2.15	1.22	0.19	0
4206	61.59	10.09	13.28	8.43	1.76	3.7	1.01	0.13	0
4207	56.33	12.1	12.79	8.23	5.22	4.62	0.67	0.04	0
4208	54.07	13.57	13.44	10.16	4.74	2.81	0.95	0.25	0
4208	36.47	24.54	13.27	7.58	10.45	6.69	0.91	0.08	0
4208	23.49	7.57	2.11	4.49	12.33	35.63	0.09	14.3	0
4209	29.6	19.11	7.5	5.03	12.1	20.27	0.55	5.83	0
4209	44.94	20.19	14.18	8.02	7.52	4.13	0.7	0.32	0
4210	43.81	19.22	13.41	9.82	9.08	3.74	0.73	0.19	0

XRD estimates, where present.

kaolinite	quartz	ζ-feldspa	albite	dolomite	mica	siderite	rutile	pyrite	calcite
2.75	86.72	7.9	2.83	0	0.38	0	0	0	0
4.24	85.04	7.38	2.76	0	0.39	0	0	0	0
30.51	43.14	8.02	6.94	0.49	9.45	6.65	0	0	0
2.37	86.38	7.99	4.23	0	0.39	0	0	0	0
3.78	84.31	7.6	5	0	0.3	1.02	0	0	0
31.53	43.14	13.35	6.55	0.37	2.64	0.16	0	1.22	0
8.25	67.45	13.8	8.5	0	3.05	0.82	0	0	0
19.36	50.67	16.29	9.99	0.18	7.59	3.03	0	0	0
31.11	44.43	9.39	5.72	0	6.68	4.43	0	0	0
42.82	21.91	8.62	4.3	0	22.19	4.61	0	0.49	0
15.23	63.17	12.09	6.63	0	1.93	2.79	0	0	0
13.49	59.74	16.2	7.55	0	3.28	1.69	0	0	0
19.92	26.32	10.23	3.99	1.55	5.67	21.95	0	0	9.98

Section b41

4137	68.23	9.71	10.21	7.49	0	1	3.36	0	0
4144	46.9	27.35	12.17	7.15	0	1.34	5.08	0	0
4145	61.79	11.01	10.29	7.05	0	0.92	8.94	0	0
4145	81.86	2.41	7.35	6.48	0	0.61	1.28	0	0
4146	81.46	2.83	7.58	6.38	0	0.52	1.24	0	0
4147	83.07	1.48	6.68	7.68	0	0.25	0.83	0	0
4148	74.51	4.72	10.39	8.34	0	0.55	1.49	0	0
4149	84.42	1.7	6.37	6.51	0	0.31	0.69	0	0
4156	41.63	5.31	21.2	12.95	0	4.44	14.46	0	0
4157	78.79	3.56	8.4	6.85	0	0.57	1.83	0	0
4157	78.79	3	8.52	8.42	0	0.45	0.8	0	0
4157	76.62	2.99	9.23	9.51	0	0.5	1.14	0	0
4158	76.12	2.77	9.66	9.78	0	0.48	1.2	0	0
4160	80.64	2.04	7.06	9.38	0	0.38	0.5	0	0
4161	72.45	4.86	11.15	8.55	0	0.75	2.24	0	0
4162	71.1	4.43	10.55	11.71	0	0.47	1.74	0	0
4162	63.91	7.47	12.23	11.9	0	0.74	3.75	0	0
4162	63.44	6.75	12.78	12.36	0	0.92	3.75	0	0
4163	72.28	3.88	11.12	11.2	0	0.33	1.19	0	0
4167	84.62	2.82	6.32	3.58	0	0.23	2.43	0	0
4168	50.78	16.81	14.17	7.12	4.21	0.75	5.77	0	0.38
4169	58.68	12.19	15.21	8.99	0	0.75	4.18	0	0
4170	86.29	2.6	7.15	3.07	0.54	0.22	0.01	0	0.11
4171	72.29	6.64	12.38	6.91	0	0.62	1.16	0	0
4172	72	6.71	11.73	7.22	0	0.72	1.62	0	0
4172	72.99	6.02	11.4	7.43	0	0.58	1.57	0	0
4173	68.12	7.97	12.89	7.76	0	0.74	2.52	0	0
4174	64.6	10.52	12.19	7.9	0	1.28	3.52	0	0
4175	69.27	7.72	10.93	8.07	0	1.49	2.52	0	0
4175	62.44	10.95	12.22	8.2	0	0.82	5.37	0	0
4176	70.74	5.97	11.28	9.32	0	0.77	1.92	0	0
4177	63.55	11.46	12.43	7.31	0	0.86	4.39	0	0
4177	55.2	15.65	14.15	7.28	0	0.98	6.74	0	0
4178	47.36	21.67	14.84	6.58	0.68	0.82	8.05	0	0

kaolinite	quartz	ζ-feldspa	albite	dolomite	mica	siderite	rutile	pyrite	calcite
11.62	64.05	12.38	6.9	0	1.66	1.04	0	0	
21.17	57.36	12.7	4.43	0.26	4.31	0.98	0	0	
2.36	85.48	7.53	4.64	0	0	0	0	0	
2.35	83.92	8.25	4.46	0	0.58	0	0	0	
3.63	83.51	9.82	5.61	0	0.58	0	0	0.49	
2.82	79.17	12.25	7.95	0	0.68	0	0	0	
3.05	77.88	9.81	11	0	0.58	0	0	0	
6.62	65.85	14.38	12.01	0	1.02	0.91	0	0	
3.25	87.81	6.63	2.4	0	0.4	0	0	0.99	
18.85	53.98	17.5	6.41	0	3.78	1.21	0	0	
4.21	71.39	16.59	5.7	0.28	0.79	0	0	0	
8.09	72	12.53	5.49	0.22	1.02	0.51	0	0	
9.47	61.64	16.78	7.18	0.31	1.08	1.76	0	0	
11.85	68.97	13.76	5.72	0	1.55	1.09	0	0	
22.79	49.49	14.65	8.44	0	4.52	2.82	0	0	

Appendix 7.2. Petrohysical data from hole 211/18-a50.

Density in g/cm3, porosity in percent.

Prefix - "core" means calculated on core samples in the laboratory.

Prefix-"calculated" estimate is derived GLT derived estimates of mineralogy.

Depth	calculated grain density	core porosity	core grain density	RHOB	Calculated porosity	core calc-bulk density	Depth	calculated grain density	core porosity	core grain density	RHOB	Calculated porosity
9216	2.65	26.00	2.64	2.25	24.29	2.24	**9251**	2.68	16.80	2.66	2.36	18.93
9216.5	2.66	25.20	2.65	2.24	25.75	2.26	**9251.5**	2.67			2.36	19.05
9217	2.69			2.22	27.82		**9252**	2.67	28.10	2.65	2.35	19.54
9217.5	2.65			2.21	26.56		**9252.5**	2.67			2.30	22.02
9218	2.69	24.50	2.64	2.21	28.28	2.26	**9253**	2.67	27.50	2.65	2.24	25.64
9218.5	2.68			2.21	27.98		**9253.5**	2.66			2.20	28.11
9219	2.68			2.22	27.55		**9254**	2.66	18.30	2.65	2.21	27.20
9219.5	2.67			2.23	26.48		**9254.5**	2.69			2.25	25.66
9220	2.67	22.40	2.65	2.24	25.68	2.30	**9255**	2.70	16.40	2.67	2.32	22.62
9220.5	2.66			2.27	23.89		**9255.5**	2.71			2.34	21.79
9221	2.67	18.90	2.66	2.29	23.06	2.37	**9256**	2.69	17.80	2.65	2.35	19.83
9221.5	2.66			2.30	21.73		**9256.5**	2.69			2.34	20.36
9222	2.68			2.33	20.79		**9257**	2.67	18.10	2.66	2.34	19.63
9222.5	2.68			2.34	20.34		**9257.5**	2.69			2.32	21.81
9223	2.69	21.70	2.65	2.34	21.04	2.31	**9258**	2.70	22.10	2.65	2.31	23.22
9223.5	2.67			2.33	20.41		**9258.5**	2.74			2.29	25.88
9224	2.70			2.32	22.34		**9259**	2.80	15.40	2.78	2.30	28.07
9224.5	2.67			2.31	21.42		**9259.5**	2.85			2.33	27.99
9225	2.71	17.80	2.65	2.31	23.37	2.37	**9260**	2.86	17.70	2.97	2.40	24.61
9225.5	2.71			2.31	23.42		**9260.5**	2.84			2.50	18.24
9226	2.72	14.30	2.70	2.34	22.07	2.47	**9261**	2.81	15.70	2.67	2.54	14.68
9226.5	2.72			2.37	20.73		**9261.5**	2.76			2.52	13.95
9227	2.74	17.20	2.64	2.39	20.45	2.38	**9262**	2.71			2.44	15.56
9227.5	2.73			2.37	20.89		**9262.5**	2.70			2.41	17.51
9228	2.71	14.60	2.66	2.34	21.63	2.43	**9263**	2.72	16.10	2.68	2.40	18.69
9228.5	2.72			2.35	21.87		**9263.5**	2.73			2.41	18.47
9229	2.71	25.60	2.67	2.33	22.47	2.27	**9264**	2.74	12.60	2.67	2.42	18.19
9229.5	2.71			2.30	24.00		**9264.5**	2.74			2.43	17.76
9230	2.68	27.70	2.64	2.23	27.02	2.21	**9265**	2.73			2.45	16.15
9230.5	2.68			2.20	28.45		**9265.5**	2.72			2.49	13.36
9231	2.67	22.70	2.65	2.19	28.61	2.30	**9266**	2.69	24.90	2.65	2.51	10.59
9231.5	2.67			2.21	27.18		**9266.5**	2.68			2.47	12.40
9232	2.66		2.65	2.25	24.38	2.27	**9267**	2.66	19.00	2.67	2.38	16.78
9232.5	2.66			2.31	20.83		**9267.5**	2.66			2.31	20.92
9233	2.67	21.10	2.66	2.35	19.11	2.33	**9268**	2.66	27.40	2.65	2.27	23.67
9233.5	2.67			2.34	19.60		**9268.5**	2.66			2.24	25.27
9234	2.67	25.00	2.63	2.33	20.52	2.25	**9269**	2.66		2.66	2.23	26.08
9234.5	2.68			2.29	23.55		**9269.5**	2.66			2.23	25.86
9235	2.70	14.80	2.70	2.27	25.19	2.46	**9270**	2.67	24.60	2.66	2.24	26.11
9235.5	2.70			2.29	24.21		**9270.5**	2.67			2.23	26.53
9236	2.70	16.00	2.65	2.35	21.02	2.40	**9271**	2.68	24.10	2.65	2.21	28.20
9236.5	2.73			2.40	19.41		**9271.5**	2.70			2.21	28.65
9237	2.73	16.30	2.66	2.40	18.74	2.41	**9272**	2.71			2.22	28.67
9237.5	2.73			2.40	19.03		**9272.5**	2.70			2.24	27.07
9238	2.76	14.50	2.67	2.40	20.58	2.44	**9273**	2.71			2.28	25.46
9238.5	2.80			2.42	21.49		**9273.5**	2.71			2.31	23.13
9239	2.85	18.60	2.89	2.44	22.14	2.56	**9274**	2.69	22.70	2.66	2.34	20.72
9239.5	2.89			2.45	23.03		**9274.5**	2.69			2.35	20.47
9240	2.91	19.70	2.83	2.45	24.16	2.49	**9275**	2.71	22.80	2.66	2.33	22.06
9240.5	2.92			2.44	24.90		**9275.5**	2.71			2.31	23.50
9241	2.93	20.90	2.84	2.48	23.01	2.48	**9276**	2.72	24.60	2.65	2.29	25.03
9241.5	2.93			2.56	19.18		**9276.5**	2.71			2.29	24.65
9242	2.95	16.30	2.92	2.63	16.55	2.62	**9277**	2.72			2.28	25.26
9242.5	2.96			2.65	15.74		**9277.5**	2.72			2.27	26.24
9243	2.94	9.70	2.97	2.68	13.68	2.79	**9278**	2.74	23.50	2.66	2.26	27.52
9243.5	2.89			2.68	11.08		**9278.5**	2.75			2.26	28.12
9244	2.84	14.30	2.66	2.63	11.65	2.44	**9279**	2.74	15.60	2.67	2.26	27.85
9244.5	2.78			2.53	14.33		**9279.5**	2.78			2.25	29.57
9245	2.77	12.70	2.68	2.46	17.25	2.48	**9280**	2.80			2.26	30.11
9245.5	2.72			2.45	15.46		**9280.5**	2.84			2.31	28.88
9246	2.72	16.00	2.67	2.46	15.23	2.42	**9281**	2.87			2.38	26.23
9246.5	2.70			2.45	14.99		**9281.5**	2.89			2.46	23.18
9247	2.69	19.30	2.65	2.42	15.94	2.35	**9282**	2.90	23.70	2.66	2.40	26.06
9247.5	2.69			2.39	17.78		**9282.5**	2.85			2.31	29.48
9248	2.70	16.40	2.66	2.38	18.73	2.40	**9283**	2.81	23.10	2.65	2.20	33.68
9248.5	2.68			2.38	17.64		**9283.5**	2.77			2.17	33.74
9249	2.68	17.90	2.66	2.39	17.44	2.38	**9284**	2.73	22.60	2.65	2.19	31.38
9249.5	2.69			2.39	17.51		**9284.5**	2.71			2.21	29.31
9250	2.68	18.40	2.65	2.37	18.58	2.36	**9285**	2.70			2.22	28.29
9250.5	2.68			2.37	18.22		**9285.5**	2.69			2.21	28.37

Appendix 7.2 cont..

Depth	calculated grain density	core porosity	core grain density	RHOB	Calculated porosity	core calc-bulk density
9286.5	2.70			2.22	28.20	
9287	2.71	23.50	2.65	2.23	28.22	2.29
9287.5	2.71			2.24	27.51	
9298	2.73			2.41	18.67	
9298.5	2.72			2.34	22.27	
9299	2.71			2.27	25.68	
9299.5	2.71			2.24	27.65	
9300	2.71			2.23	27.93	
9300.5	2.72			2.24	27.77	
9301	2.72	21.90	2.64	2.26	26.75	2.30
9301.5	2.73			2.29	25.42	
9302	2.72	24.90	2.65	2.32	23.49	2.26
9302.5	2.72			2.34	21.89	
9303	2.70			2.34	21.52	
9303.5	2.69			2.31	22.51	
9304	2.69	20.10	2.68	2.27	24.71	2.36
9304.5	2.70			2.25	26.46	
9305	2.72	19.50	2.77	2.24	27.62	2.44
9305.5	2.74			2.25	28.18	
9306	2.76	26.50	2.65	2.27	27.52	2.24
9306.5	2.81			2.31	27.56	
9307	2.87	25.20	2.65	2.37	26.92	2.26
9307.5	2.89			2.45	23.22	
9308	2.90	24.80	2.66	2.54	19.06	2.27
9308.5	2.89			2.59	15.77	
9309	2.84	18.90	2.68	2.58	14.56	2.38
9309.5	2.82			2.51	16.66	
9310	2.77	17.50	2.67	2.47	17.14	2.40
9310.5	2.76			2.43	18.66	
9311	2.78	16.20	3.08	2.42	20.02	2.76
9311.5	2.82	20.70	2.68	2.38	24.17	2.35
9325.5	2.74			2.33	23.30	
9326	2.75	21.70	2.65	2.33	23.89	2.31
9326.5	2.75			2.34	23.44	
9327	2.77	18.50	2.68	2.35	23.63	2.39
9327.5	2.77			2.37	22.88	
9328	2.76	19.10	2.68	2.38	21.90	2.38
9328.5	2.76			2.38	21.91	
9329	2.74	19.90	2.67	2.37	21.47	2.36
9329.5	2.74			2.38	21.08	
9330	2.74	18.10	2.68	2.39	20.02	2.39
9330.5	2.74			2.39	20.16	
9331	2.73	17.90	2.68	2.38	20.73	2.40
9331.5	2.74			2.37	21.13	
9332	2.74	18.30	2.68	2.38	21.01	2.39
9332.5	2.74			2.38	20.99	
9333	2.76	13.10	2.69	2.37	21.87	2.48
9333.5	2.75	16.60	2.67	2.39	20.89	2.41
9334	2.77			2.41	20.03	
9334.5	2.74			2.42	18.78	
9335	2.75	23.50	2.65	2.40	20.08	2.29
9335.5	2.74			2.38	20.77	
9336	2.74	19.70	2.66	2.37	21.27	2.35
9336.5	2.72			2.34	22.20	
9337	2.73	14.90	2.67	2.31	24.20	2.44
9337.5	2.72			2.29	25.24	
9338	2.72	18.50	2.67	2.29	24.87	2.38
9338.5	2.72			2.31	23.75	
9339	2.73	19.60	2.67	2.36	21.60	2.36
9339.5	2.73			2.37	20.73	
9340	2.73	20.10	2.67	2.38	20.34	2.35
9340.5	2.72			2.35	21.44	
9341	2.72	19.30	2.67	2.34	21.86	2.37
9341.5	2.72			2.33	22.40	
9342	2.72	18.70	2.67	2.34	21.86	2.38
9342.5	2.73			2.34	22.14	
9343	2.73			2.34	22.62	
9343.5	2.72			2.35	21.68	
9344	2.72	11.80	2.60	2.35	21.92	2.42
9344.5	2.73			2.34	22.10	
9345	2.73	11.10	2.70	2.33	22.96	2.52
9345.5	2.74			2.35	22.38	
9346	2.78	9.50	2.73	2.41	20.91	2.58
9346.5	2.79			2.46	18.59	
9347	2.82	9.70	2.77	2.51	16.95	2.61
9347.5	2.81			2.51	16.53	
9348	2.83	19.70	2.67	2.53	16.41	2.36
9348.5	2.85			2.55	15.96	
9349	2.84	20.20	2.67	2.56	15.13	2.35
9349.5	2.82			2.53	16.33	
9350	2.79	10.10	2.74	2.42	20.31	2.57
9350.5	2.78			2.35	24.13	

Depth	calculated grain density	core porosity	core grain density	RHOB	Calculated porosity
9351	2.77	10.80	2.73	2.35	23.54
9351.5	2.77			2.32	25.63
9352.5	2.82			2.39	23.56
9353	2.84	11.20	2.68	2.48	19.79
9353.5	2.84			2.54	16.69
9354	2.83	15.10	2.65	2.54	15.85
9354.5	2.82			2.50	17.66
9355	2.82	10.20	2.69	2.49	18.46
9355.5	2.82			2.48	18.51
9356	2.81	9.30	2.70	2.49	17.91
9356.5	2.81			2.49	17.71
9357	2.85	14.50	2.68	2.49	19.27
9357.5	2.85			2.51	18.36
9358	2.89	12.20	2.72	2.53	19.19
9358.5	2.92			2.56	18.52
9359	2.90	11.00	2.72	2.58	16.70
9359.5	2.91			2.62	14.92
9360	2.95			2.60	18.13
9360.5	2.95			2.56	19.69
9361	2.97	16.80	2.53	2.54	21.58
9361.5	2.95			2.53	21.27
9362	2.98	13.10	2.80	2.53	22.83
9362.5	2.95			2.52	22.05
9363	2.95			2.52	22.25
9363.5	2.91			2.50	21.09
9364	2.90			2.48	21.91
9364.5	2.86	11.80	2.72	2.48	20.64
9365	2.85			2.49	19.34
9365.5	2.83			2.43	21.92
9366	2.82			2.38	24.19
9366.5	2.82			2.37	25.04
9367	2.83			2.43	22.02
9367.5	2.82			2.45	20.70
9368	2.82			2.48	18.85
9368.5	2.82			2.45	20.17
9369	2.82			2.43	21.86
9369.5	2.85			2.40	24.13
9370	2.86			2.39	25.01
9370.5	2.85			2.37	25.72
9371	2.83			2.36	26.01
9371.5	2.81			2.36	25.34
9372	2.83			2.40	23.78
9372.5	2.86			2.45	21.71
9373	2.86			2.43	22.86
9373.5	2.85			2.36	26.88
9374	2.87			2.30	30.51
9374.5	2.83			2.29	29.86
9375	2.81			2.31	27.34
9375.5	2.79			2.32	26.49
9376	2.81			2.32	26.88
9376.5	2.85			2.35	27.00
9377	2.82			2.38	24.06
9377.5	2.82			2.46	19.90
9378	2.87	15.80	2.73	2.50	19.69
9378.5	2.88			2.54	18.15
9379	2.91			2.53	20.03
9379.5	2.87			2.52	18.48
9380	2.89	26.10	2.92	2.52	19.62
9380.5	2.88			2.52	19.41
9381	2.86	9.90	2.77	2.53	17.91
9381.5	2.85			2.52	17.92
9382	2.86			2.51	19.10
9382.5	2.86			2.51	19.04
9383	2.88			2.52	19.16
9383.5	2.87			2.52	18.40
9384	2.83			2.52	16.98
9384.5	2.80			2.51	16.22
9385	2.79			2.51	15.34
9385.5	2.79			2.50	15.87
9386	2.77			2.50	15.07
9386.5	2.77			2.49	16.22
9387	2.80			2.47	18.01
9387.5	2.81			2.47	18.43
9388	2.81			2.49	17.46
9388.5	2.81			2.52	15.91
9389	2.82			2.53	16.10
9389.5	2.80			2.52	15.28
9390	2.79			2.53	14.47

References.

Albarede, F., & Provost, A. (1977). Petrological and geochemical mass-balance equations: an algorithm for least-squares fitting and general error analysis. Computers & Geosciences, 3, 309-326.

Albright, W. A., Turner, W. L., & Williamson, K. R. (1980). Ninian Field, UK sector, North Sea. In M. T. Halbouty (Ed.), Giant Oil and Gas fields of the decade:1968-1978. pp. 173-194. Tulsa, Oklahoma.: Amer. Assoc. Petrol. Geol.

Anderson, R., & Dove, R. (1988). The determination of heat flow in a wellbore in South Eugene Island area of offshore Louisana: implications for fluid migration and hydrocarbon location in the subsurface. International geochemistry and spectroscopy conference,Paper K. Schlumberger-Doll Research, Ridgefield, CT.

Anderson, R. N., Alt, J. C., Malpas, J., Lovell, M. A., Harvey, P. K., & Pratson, E. L. (1988). Geochemical Well Logging in Basalts: The Palisades Sill and the Ocean Crust of Hole 504B. Jn. of Geophysical Research, 95, 9265-9292.

Archie, G. E. (1942). The electrical resistivity log as an aid to determining some reservoir characteristics. Jn. Pet. Technology, 5, 1-8.

Banks, R. (1979). The use of Linear Programming in the Analysis of Petrological Mixing Problems. Contributions to Mineralogy and Petrology, 70, 237-244.

Barth, T. F. W. (1959). Principles of classification and norm calculation of metamorphic rocks. Journal of Geology, 67, 135-152.

Bateman, R. M. (1985). Log quality control. Dordrecht: Reidel, 398.

Biscaye, P. E. (1965). Mineralogy and sedimentation of of recent deep sea clay in the Atlantic Ocean and adjacent seas and oceans. Geol. Soc. of Am. Bull., 76, 803-832.

Bjerhammer, A. (1973). Theory of errors and generalised matrix inverses. Amsterdam: Elsevier, 420.

Bjorlykke, K., & Brendsel, A. (1986). Diagenesis of the Brent sandstone in the Statfjord Field, North Sea. Jn. Sed. Petrology, 56, 157-167.

Blanche, J. B., & Whitaker, J. H. M. (1978). Diagenesis of part of the Brent Sand Formation (Middle Jurassic) of the northern North Sea Basin. Jn, Geol. Soc. Lond., 135, 73-82.

Blatt, H., Middelton, G., & Murray, R. (1980). Origin of sedimentary rocks. New Jersey: Prentice-Hall, 782.

Bowen, J. M. (1975). The Brent Oil Field. In A. W. Woodland (Ed.), Petroleum Geology and the continental shelf of North West Europe. pp. 353-362. Barking: Applied Science Publishers.

Brenand, T. P. (1984). Petroleum Geology in North Sea exploration 1964-1983. In K. W. Glennie (Ed.), Introduction to the Petroleum Geology of the North Sea. pp. 1-16. Oxford: Blackwell.

Brennand, T P., & Siri, J. B. (1975). The geology of the Northern North Sea. Proc. Offshore Conf. OE-75. Aberdeen: Spearhead Pulications

Brewer, T. S., Lovell, M. A., Harvey, P. K., Pelling, R., Atkin, B. P., & Adamson, A. (1990). Preliminary geochemical results from DSDP/ODP hole 504B: a comparison of core and log data. Geol. Soc. Spec. Pubs., 48, 177-195.

Brindley, G. W., & Brown, G. (1980). Crystal structure of clay minerals and their X-ray identification, Monograph 5. London: Mineralogical Society, 450.

Bristow, J. F., & Broglia, C. (in press). Geochemical logging results from ODP Leg 134. Proc. ODP Scientific Results, 134, Pt 1 College Stn. Tx.: Ocean Drilling Program.

Bristow, J. F., Broglia, C., deMenocal, P. B., & Pratson, E. L. (1992). Geochemical logging results from the Sea of Japan: Sites 798 & 799. In Proc. ODP Scientific Results, 127/128, Pt 2. pp. 1395-1410. College Stn. Tx.: Ocean Drilling Program.

Bristow, J. F., & deMenocal, P. B. (1992). Evaluation of the quality of geochemical log data in Hole 798B. In Proc. ODP Scientific Results, 127/128. pp. 1021-1036. College Stn. TX.: Ocean Drilling Program.

Brown, R. C., Richards, P. C., & Thompson, A. R. J. (1987). Patterns in the deposition of the Brent Group (Middle Jurassic) UK North Sea. In J. Brooks, & K. W. Glennie (Ed.), Petroleum Geology of North West Europe. pp. 899-913. London: Graham & Trotman.

Bryan, W. B., Finger, L. W., & Chayes, F. (1969). Estimating proportions in Petrographic Mixing Equations by Least-Squares Approximation. Science, 163, 926-927.

Budding, M. C., & Inglin, H. F. (1981). A reservoir geological model of the Brent Sands in the southern Cormorant. In L. V. Illing, & G. D. Hobson (Ed.), Petroleum Geology of the continental shelf of North-West Europe. pp. 326-34. London: Heyden.

Burri, C. (1964). Petrochemical Calculations based on equivalents (Methods of Paul Niggli). Israel Program for Scientific Translations, Sivan Press, Jerusalem., 304.

Carpenter A. B., Ryan, P. (1991). Accuracy and Precision of mineralogical determinations from borehole elemental analyses. . SPWLA, Ann. Log. Symp. Oklahoma.(abstract)

Carmichael, R. S. (1989). Practical handbook of physical properties of rocks and minerals. Florida: CRC, 741.

Chapman, S., Colson, J. L., Flaum, C., Hertzog, R. C., Pirie, G., Scott, H., Everett, R., Herron, M. M., Schweitzer, J., LaVigne, J., Quirein, J., & Wendlandt, R. (1987). The emergence of Geochemical Well Logging. The Technical Review, 35(2), 27-35.

Chauvin, A. L., & Valachi, L. Z. (1980). Sedimentology of the Brent and Statfjord Formations of the Statfjord field. In:The sedimentation of the North Sea Reservoir Rocks, Geilo: Norway, 16/1-17.

Chayes, F. (1956). Petrographic modal analysis. New York: John Wiley and Sons Inc., 113.

Clark, I. (1984). Practical geostatistics. New York: Elsevier applied science publishers, 129.

Cohen, D., and Ward, C. R. (1991). SEDNORM - a program to calculate a normative mineralogy for sedimentary rocks based on chemical analyses. Computers & Geosciences, 17(9), 1235-1253.

Cross, W., Iddings, J.P., Pirsson, L.V. and Washington, H.S. (1902). Quantitative classification of igneous rocks. University of Chicago, Chicago. 286.

Davies, R. A., & Watts, T. R. (1977). The Murchison Oil Field. In: Mesozoic Northern North Sea Symposium. Oslo, Norway: Norw. Petrol. Soc., 1-24.

Davis, J. C., (1986). Statistics and data analysis in geology. New York: John Wiley & Sons.

Deer, W. A., Howie, R. A., & Zussman, J. (1966). Introduction to the rock forming minerals. London: Longmans, 528.

Degan, C. E., & Skull, B. J. (1977). A standard lithostratigraphic nomenclature for the central and northern North Sea. Report for the Institute Geol. Sci., 77/25. 36.

deMenocal, P. B., Bristow, J. F., & Stein, R. (1992). Paleoclimatic applications of downhole logs: Plio-Pleistocene results from Hole 798B, Sea of Japan. In Proc. ODP Scientific Results, 127/128, (Pt. 2). pp. 393-408. College Stn. TX: Ocean Drilling Program.

Dove, R. E., & Williams, C. F. (1988). Thermal conductivity estimated from elemental concentration logs. Schlumberger-Doll Research, Ridgefield, CT

Doveton, J. (1986). Log Analysis of Subsurface Geology: Concepts and Computer Methods. New York: Wiley-Interscience Publication, John Wiley & Sons, 273.

Dunham, A., & Wilkinson, K. (1978). Accuracy, precision and detection limits of energy-dispersive electron-microprobe analyses of silicates. Jn. X-ray spectrometry, 7(No. 2), 50-56.

Edmunson, H., & Raymer, L. L. (1979). Radioactive logging parameters for common minerals. Log Analyst, 20, 38-47.

Ehrlich, R., & Full, W. (1987). Sorting out geology - Unmixing mixtures. In W. B. Sixe (Ed.), Use and abuse of Statistical methods in the Earth Sciences. pp. 169. New York, Oxford: Oxford University Press.

Ellis, D. V. (1987). Well logging for Earth Scientists. New York: Elsevier, 532.

Ellis, D. V.,Howard, J., Flaum, C., McKeon, D., Scott, H., Serra, O., (1988). Mineral Logging parameters: Nuclear and acoustic. The Technical Review, 36, 38-52.

Eynon, G. (1981). Basin development and sedimentation in the Middle Jurassic of the northern North Sea. In L. V. Illing, & G. D. Hobson (Ed.), Petroleum Geology of the continental shelf of North-west Europe. pp. 196-204. London: Heyden.

Falt, L. M., Helland, R., Jacobsen, V. W., & Renshaw, D. (1989). Correlation of transgressive-regressive depositional sequences in the Middle Jurassic Brent/Vestland Group Megacycle, Viking Graben, Norwegian North Sea. In J. D. Collinson (Ed.), Correlation in hydrocarbon exploration. pp. 191-200. London: Graham & Trotman, Norwegian Pet. Soc.

Falt, L. M., & Steel, R. (1990). A new palaeogeographic reconstruction for the Middle Jurassic of the northern North Sea: a disscussion. Jn. of the Geol. Soc. Lond., 147, 10485-90.

Folk, L. L. (1968). Petrology of sedimentary rocks. Austin, Texas: Hemphills, 170.

Forsythe, G., & Moler, C. B. (1967). Computer solution of linear algebraic systems. Englewood, Cliffs, NJ: Prentice-Hall, 345.

Fox, L. (1964). An introduction to numerical linear algebra. Oxford: Oxford Univ. Press, 201.

Fuh, T. M. (1973). The principle of Constituent Analysis with Special Reference to the Calculation of Weight Percentages of Minerals in metamorphic Rocks. Canadian Journal of Earth Science, 10, 657-669.

Full, W. E., Ehrlich, R., & Bezdek, J. C. (1982). FUZZY Q-MODEL: A new approach for linear unmixing. Jn. Math. Geol., 14(3), 259-270.

Full, W. E., Ehrlich, R., & Klovan, J. E. (1981). EXTENDED Q-MODEL-Objective definition of external end members in analysis of mixtures. Jn. Math. Geol., 13(4), 331-334.

Garrels, L. M., & Mackenzie, F. T. (1971). Evolution of sedimentary rocks. New York: W. W. Norton & Co, 397.

Gass, S. I. (1975). Linear programming: methods and applications. New York: McGraw-Hill,

Gatto, H., & Lauterjung, J. (1990). Quantitative and qualitative determination of minerals in crystalline rocks. Trans. 13th European Formation Evaluation Symposium, SPWLA, Paper N. Budapest, Hungary

Georgi, D. T. (1991). Application of time series analysis to induced gamma-ray spectroscopy logs from two cold lake heavy-oil observation wells. SPE Formation Evaluation, 6, 505-512.

Gold, C. M., Cavell, P. A., & Smith, D. G. W., (1983). Clay minerals in mixtures: sample preparation, analysis and statistical interpretation. Clays and Clay Minerals, 31. pp 191-199.

Goldstein, J. I., Newbury, D. E., Echlin, P., Joy, D., Fiori, C., & Lifshin, E. (1981). Scanning electron microscopy of authigenic clay minerals in sandstone. Clay and clay minerals, 30, 232-236.

Grau, J. A., & Herron, M. M. (1987). Absolute elemental concentration estimated from geochemical well logging using neutron-induced gamma-ray spectroscopy and a geological model. Am. Assoc. Pet. Geol. Bull., 71, 561.

Grau, J. A., & Schweitzer, J. S. (1989). Elemental concentrations from thermal neutron captivation gamma-ray spectra in geological formations. Nucl. Geophys., 1, 157-165.

Grau, J. A., Schweitzer, J. S., Ellis, D. V., & Hertzog, R. C. (1988). A geological model for gamma-ray spectroscopy logging measurements. Nucl. Geophys., 3, 351-359.

Grau, J. A., Schweitzer, J. S., & Hertzog, R. C. (1980). From spectra to elemental yields in 256 easy steps. Technical Review, No 28(No 3), 43-50.

Grau, J. A., Schweitzer, J. S., & Hertzog, R. C. (1990). Statistical uncertainties of elemental concentrations extracted from neutron-induced gamma-ray measurements. IEEE Trans. Nuc Sci., 37, 2175-2178.

Graue, E., Helland-Hansen, W., Johnson, J., Lomo., L., Nottvedt, A., Ronning, K., Ryseth, K., & Steel, R. J. (1987). Advance and retreat of the Brent Delta system, Norwegian North Sea. In J. Brooks, & K. W. Glennie (Ed.), Petroleum Geology of North West Europe. pp. 915-1037. London: Graham & Trotman.

Hallett, D. (1981). Refinement of the geological model of the Thistle Field. In L. V. Hobson, & J. D. Hobson (Ed.), Petroleum geology of the continental shelf of North-West Europe. pp. 315-325. London: Heydon.

Harbaugh, J. W., & Bonham-Carter, G. (1981). Computer simulation in geology. Malabar, FL.: R. E. Krieger Publishing Co., 450.

Harvey, P. K., Lovell, M.A. & Bristow, J.F. (1991). The Interpretation of Geochemical Logs from the Oceanic Basement: Mineral Modelling in Ocean Drilling Program (ODP) Hole 735B. Nuclear Geophysics, 5(3), 267-277.

Harvey, P. K., Lofts, J. C. and Lovell, M. A. (1992). Mineralogy logs: element to mineral transforms and compositional colinearity in sediments. SPWLA 33rd. Ann. Log. Symp, Paper M. Oklahoma City, Oklahoma.

Harvey, P. K., J. F, B., & M. A, L. (1990). Mineral transforms and downhole geochemical measurements. Scientific Drilling, 1, 163-176.

Harvey, P. K., & Lovell, M. A. (1992a). Downhole mineralogy logs: mineral inversion methods and the problem of compositional colinearity. In A. Hurst, Griffiths, C. M., Worthington, P. F., (Ed.), Geologicial applications of wireline logs II. Geol. Soc. Spec. Pubs. No. 65. London: Geol. Soc.

Harvey, P. K., & Lovell, M. A. (1992b). Nuclear Logging and Mineral Inversion in Sedimentary Sequences. Conference record of the IEEE Nuc. Sci. symp. Santa Fe, New Mexico: 1103-1113.

Harvey, P. K., & Lovell, M. A. (un published). Evaluation of mineral transforms from core and GLT data in the Welton and Gyda Fields, North Sea. Report to BP. Dec. 1989.

Harville, D. G., & Hamish, G. (1990). Comparison of XRD and FTIR analyses. SPWLA Intl. Symposium, Midland. TX. (abstract and overheads)

Hastings, A. F. (1988). Using the derived elemental concentrations to improve the accuracy of fluid saturations determined from well logs. International geochemistry and spectroscopy conference, Schlumber-Doll Research, Ridgefield, CT. Paper T.

Hay, J. T. C. (1977). Structural development in the northern North Sea. Jn. Pet. Geology, 1, 65-77.

Helland-Hansen, W., Ashton, M., Lomo, L., & Steel, R. (1992). Advance and retreat of the Brent Delta: recent contributions to the depositional model. In A. C. Morton, R. S. Haszeldine, M. R. Giles, & S. Brown (Ed.), Geol. Soc. Spec. Pub. No. 61: Geology of the Brent Group. pp. 109-127. London: The Geol. Soc. of London.

Herron, M. M. (1986). Mineralogy from geochemical well logging. Clays and Clay Minerals, 34, 204-213.

Herron, M. M. (1987). Estimating the intrinsic permeability of clastic sediments from geochemical data. SPWLA 28th Ann. Log. Symp. Paper HH.

Herron, M. M. (1987 (b)) Future applications of elemental concentrations from geophysical logging. Nucl. Geophysics. 1 (3), 197-211.

Herron, M. M. (1988). Geochemical classification of terrigenous sands and shales from core and log data. Jn. of Sedimentary Petrology, 58, 820-829.

Herron, M. M., & Herron, S.L. (1990). Geological applications of geochemical well logging. In A. Hurst, M. M. Lovell, & A. Morton (Ed.), Geological application of wireline logs. Geol. Soc. Spec. Pub. No. 48. London: Geol. Soc. London.

Herron, M. M., & Grau, J. A. (1987). Clay and framework mineralogy, cation exchange capacity, matrix density and porosity from well logging in Kern County California. Am. Assoc Petroleum Geologists, 71, 567-575.

Herron, M. M., Herron, S. L., Everett, R., & Macdonald, K. (1990). Enhanced resistivity interpretation in three wells using geochemical data. 31st Ann. Log. Symp., Paper U. Lafayette, Louisiana.

Herron, S. (1987). A total organic carbon log for source rock evaluation. Log Analyst, 28, 520-527.

Herron, S. L., Herron, M. M., Grau, J. A., & Ellis, D. V. (in press). Interpretation of chemical concentration logs and applications in the petroleum industry. In C. Pieters, & P. Englert (Ed.), Remote geochemical analysis: Elemental and mineralogical composition Cambridge: Lunar & Planetary Insitute and Cambridge University Press.

Hertzog, R., Soran P. D., & Schweitzer, J. S. (1976). Applications of cross section data for nuclear geochemical well logging. Radiation Effects. 96,1-4.

Hertzog, R. (1979). Laboratory and field evaluation of inelastic neutron scattering and capture gamma-ray spectroscopy tools. Soc. Pet. Eng. AIME, Paper 7430.

Hertzog, R., Colson, L., Seeman, B., O'Brian, M., Scott, H., McKeon, D., Grau, J. A., Ellis, D., Schweitzer, J., & Herron, M. M. (1989). Geochemical logging with spectrometry tools. SPE Formation Evaluation, 4, 153-162.

Hertzog, R. C., & Herron, M. M. (1990). Applications of Elemental Measurements in Geochemical Logging. Trans. 13th Ann. European Formation Evaluation Symposium, Paper DD. Budapest, Hungary: Society of Professional Well Log Analysts.

Hertzog, R. C., & Plasek, R. E. (1979). Neutron-excited gamma-ray spectroscopy for well logging. IEEE Transactions on Nuclear Science, NS-26(No 1), 1558-1563.

Hodgson, M., & Dudeney, A.W.L. (1984). Estimation of clay proportions in mixtures by X-ray diffraction and computerised chemical mass balance. Clays and Clay Minerals, 32, 19-28.

Hodson, G., Fertl, W. H., & Hammack, G. W. (1976). Formation evaluation in Jurassic sandstones of the northern North Sea. The Log Analyst, 22.

Hodson, G. M. (1975). Some aspects of geology of the middle Jurassic in the North Sea with particular reference to electro-physical logs. Nor. Pet. Soc, Stavanger: 1-39.

Humphries, B., & Lott, G. K. (1990). An investigation into nuclear log responses of North Sea Jurassic sandstones using mineralogical analysis. In A. Hurst, M. A. Lovell, & A. Morton (Ed.), Geologicial applications of wireline logs. Geol. Soc. Spec. Pubs. No. 48. pp. 223-240. London: Geol. Soc. London.

Hurst, A. (1990). Natural gamma-ray spectroscopy in hydrocarbon-bearing sandstones from the Norwegian continental shelf. In A. Hurst, M. M. Lovell, & A. Morton (Ed.), Geological application of wireline logs. Geol. Soc. Spec. Pub. No. 48 London: Geol. Soc. London.

Hurst, A., Lovell, M. A., & Morton, A. (1990). Geological Applications of Wireline Logs. Geological Society Special Publication No. 48., 357.

Imbrie, J., & Poldervaart, A. (1959). Mineral compositions calculated from chemical analyses of sedimentary rocks. Journal of Sedimentary Petrology, 29, 588-595.

Jackson, D. D. (1976). Most-squares inversion. Jn. Geophys. Res., (81), 1027-1030.

Jarrard, R. D., & Lyle, M. L., (1991). High-resolution geochemical variations at ODP sites 723, 728 and 731: a comparison of X-ray fluorescence and geochemical logs. In W. L. Prell, N. Niitsuma, & e. al. (Ed.), Proc. ODP, Sci. Results, 117. pp. 473-498. College Station, TX.: Ocean Drilling Program.

Johnson, R. J., & Stuart, D. J. (1985). Role of clastic sedimentology in the exploration and production of oil and gas in the North Sea. In P. J. Brenchley, & B. P. J. Williams (Ed.), Geol. Soc. Spec. Pub. 18 :Sedimentology: Recent developments and applied aspects. pp. 249-310. Oxford: Blackwell.

Kaye, M. J., Dunham, A. C., & Hirst, D. M. (1968). A comparison of two methods of quantitative mineralogical analysis of sedimentary rocks. Jn. Sed. Pet. (June, 1968).

Kelsey, C. H. (1965). Calculation of the C.I.P.W. norm. Mineralogical Magazine, 34, 276-282.

Klovan, J. E., & Miesch, A. T. (1986). EXTENDED CABFAC and Q-MODEL computer programs for Q-model factor analyis of compositional data. Comput. Geosci., 1, 161-178.

Kornder, S. C., & Carpenter, J. R. (1984). Application of a linear unmixing algorithm to the normal alkane patterns from recent salt marsh sediments. Org. Geochem., 7(1), 61-71.

Leeder, M. (1983). Lithostratigraphic stretching and North Sea Jurassic clastic source lands. Nature, 305, 510-13.

LeMaitre, R. W. (1982). Numerical Petrology. Amsterdam: Elsevier, 281.

Lock, G. A., & Hoyer, W. A. (1971). Natural gamma-ray spectral logging. Log Analyst, 12, 3-9.

Lofts, J. C., Harvey, P. K., Lovell, M. A., & Locke, J. (in press). The application of induced gamma-ray spectroscopy measurements: Characterisation of a North Sea reservoir. IEEE Trans. Nucl. Sci., 39.

Marquardt, D. W. (1962). An algorithm for least squares estimation of non-linear parameters. Jour. Soc. Indust. Appl. Math., 11, 431-441.

Marrett, G., & Kimminau, S. (1990). Logs, charts and computers - the history of log interpretation modelling. Log Analyst, 31(6), 33-354.

Mathews, M. A., Bowman, R., Huang, L., Lavelle, M. J., Smith, A. R., Hearst, J. R., Wollenberg, H. A., & Flexser, S. (1987). A Low radioactive spectral gamma-ray calibration facility. Log Analyst, 28, 462-469.

Meju, M. A. (1992). An effective ridge regression procedure for resistivity data inversion. Computers and Geoscience, 18(2/3), 99-118.

Meju, M. A., & Hutton, R. S. (1992). Iterative most-squares inversion: application to magnetotelluric data. Geophys. Jn. Int., (108), 758-766.

Merodio, J. C., Spalletti, L. A., & Bertone, L. M. (1992). A Fortran program for the calculation of normative composition of clay minerals and pelitic rocks. Computers & Geosciences, 18(1), 47-61.

Middelton, G. V. (1960). Chemical composition of sandstones. Geol. Soc. America Bull., 71, 1011-1026.

Miesch, A. T. (1962). Computing mineral compositions of sedimentary rocks from chemical analyses. Jn. of Sedimentary Petrology, 32, 217-225.

Miesch, A. T. (1976). Q-mode factor analysis of geochemical and petrologic data matrices with constant row sums. US Geol Surv. Prof., (paper 574-G), 47.

Moiola, R. J., Jones, E. L., & Shanmugam, G. (1986). Sedimentology and diagenesis of the Brent Group (Middle Jurassic), Statfjord Field, Norway-UK (abstract).

Moore, D. M., & Jr., R. C. Reynolds (1989). X-ray diffraction and the identification and analysis of clay minerals. Oxford: Oxford University Press, 332.

Morton, A. (1985). A new approach to provenance studies: electron microprobe analysis of detrital garnets from Middle Jurassic sandstones of the northern North Sea. Sedimentology, 32, 553-566.

Morton, A. C., Haszeldine, R. S., Giles, M. R., & Brown, S. (1992). Geology of the Brent Group: Introduction. In A. C. Morton, R. S. Haszeldine, M. R. Giles, & S. Brown (Ed.), Geol Soc. Spec.Pubs. No. 61: Geology of the Brent Group. pp. 1-2. London: The Geol. Soc. of London.

Morton, A. C., & Humphries, B. (1983). Petrology of the Middle Jurassic sandstones from the Murchison Field, North Sea. Jn. Pet. Geol., 5, 245-260.

Moss, B., (1992). The petrophysical characteristics of the Brent sandstones. In A. C. Morton, R. S. Haseldine, M. R. Giles, & S. Brown (Ed.), Geol. Soc. Spec. Pub. No. 61: Geology of the Brent Group. pp. 471 - 496. London: The Geol. Soc. of London.

Nicholls, G. D. (1962). A scheme for recalculating the chemical analyses of argillaceous rocks for comparative purposes. American Mineralogist, 47, 34-46.

Nyberg, O., Lein, K., Lindberg, P. A., & Smistad, J. K. (1978). Mineral composition, an aid in classical log analysis used in the Jurassic sandstones of the North Sea. SPWLA 19th Ann. Symp. 1-35.

Pearson, M. J. (1978). Quantitative clay mineralogical analyses from the bulk chemistry of sedimentary rocks. Clays and Clay Minerals, 26, 423-433.

Pelling, R., Harvey, P. K., & Lovell, M. A. (1989). Statistical analysis of Geochemical Logging Data from ODP Boreholes in Oceanic Basement. Proceedings of the Third MLGS International Symposium on Borehole Geophysics for Minerals, Geotechnical and Groundwater Applications, Las Vegas, Nevada, 1, 349-383.

Pelling, R., P.K., H., M.A., L., & D., G. (1992). Statistical analysis of geochemical logging tool data from Hole 735B, Atlantis II Fracture Zone, southwest Indian Ocean. In Proc of the Ocean Drilling Program. Scientific Results.118. pp. 271-284. College Stn.: Ocean Drilling Program.

Pelling, R.,(un published) Integrated geochemical - geophysical studies of the earth crust. PhD. Thesis (June 1992), University of Nottingham. UK.

Perry, K. (1967). An application of linear algebra to petrologic problems: Part 1. Mineral classification. Geochimica et Cosmochimica Acta., 31, 1043-1078.

Pettijohn, F. J. (1975). Sedimentary Rocks. New York: Harper & Row.

Pettijohn, F. J., Potter, P. E., & Siever, R. (1972). Sand and sandstone. New York: Springer-Verlag, 618.

Pevararo, R. C., & Russel, K. J. (1984). Interpretation of wireline and core data from a mid-Jurassic sand/shale sequence. Clay and clay minerals, 19, 483-505.

Pickering, K. T., Marsh, N. G., & Dickie, B. (in press). Data report. Inorganic major,trace and rare earth element analysis of the muds and mudstones from site 808. In I. Hill, A. Taira, & J. V. Firth (Ed.), Proc. of the Ocean Drilling Program, Scientific results. 131. College Stn. TX.: Ocean Drilling Program.

Pollack, S. S. (1979). Estimating mineral matter in coal from its major inorganic elements. Fuel., 58, 76-78.

Primmer, T. J., Kerr, S. A., & Myers, K. J. (1990). Feasability of in situ elemental analysis in mudrock evaluation. 195-203. In A. Hurst, M. M. Lovell, & A. Morton (Ed.), Geological application of wireline logs. Geol. Soc. Spec. Pub. No. 48 London: Geol. Soc. London.

Proctor, C. V. (1980). Distribution of Middle Jurassic facies in the East Shetlands Basin and their control on reservoir capability. In N. P. S. Geilo (Ed.), The sedimentation of the North Sea Reservoir Rocks. pp. 15/1-22. Norway: Geilo.

Quirein, J. A., Kimminau, S., LaVigne, J., Singer, J., & Wendel, F. (1986). A coherent framework for development and application of multiple formation evaluation models. SPWLA 27th Ann. Log. Symp. Paper DD.

Reid, M. J., Gancarz, A. J., & Albee, A. L. (1973). Constrained least squares analysis of petrological mixing problems with an application to lunar sample 12040. Earth & Planet. Sci. Letters, 17(4), 433-445.

Rhys, G. H. (1974). A proposed standard lithostratigraphic nomeclature for the southern North Sea and outline structural nomenclature for the whole of the (U.K) North Sea. Rept. Inst. Geol. Sci., 74/8, 14.

Richards, P. C. (1990). The early to mid-Jurassic evolution of the northern North Sea. In R. P. F. Hardman (Ed.), Tectonic events responsible for britain's oil and gas reserves. Geol Soc. Spec. Pubs. No 55. pp. 191-205. London: Geol. Soc. London.

Richards, P. C., & Anderton, R. (1988). A new palaeogeographic reconstruction for the middle Jurassic of the northern North Sea. Jn. of the Geol. Soc., London, 147, 1085-90.

White, S. H., Shaw, H. F., & Hugget, J. M. (1983). The use of back-scattered electron imaging for the petrographic study of sandstones and shales. Jn. Sed. Petrology, 54(2), 487-494.

Willard, H. H., Merit, L. L., Dean, J. A., & Settle, F. A. (1988). Instrumental methods of analysis. Belmont, CA.: Wadsworth.

Wright, T. L., and Doherty, P.C. (1970). A Linear Programming and Least Squares Computer Method for Solving Petrological Mixing Problems. Geological Society of America Bulletin, 81, 1995-2008.

Ziegler, P. A. (1982). Geological Atlas of Western and Central Europe. The Hague: Shell.
